Analysis of Silicon Wafer Damage Due to Nanoindentation by Micro-Raman Spectroscopy and White Beam Synchrotron X-Ray Topography

DISSERTATION SUBMITTED IN FULFILMENT OF THE REQUIREMENTS FOR THE AWARD OF DOCTOR OF PHILOSOPHY (PH.D.)

DUBLIN CITY UNIVERSITY
SCHOOL OF ELECTRONIC ENGINEERING

David Allen
B.Eng. (Hons.)
February 2014

Supervised by Prof. P. McNally

Acknowledgements

I would like to acknowledge the support given to me by Prof. Patrick McNally both for allowing me the opportunity to complete this dissertation and for his mentorship and guidance during my time at DCU.
I would also like to thank the entire SiDAM team, Prof. Brian Tanner, Prof. Keith Bowen Dr. Elizalde, Dr. Danilewsky, Jorge Garagorri, Eider Gorostegui-Colinas, Matteo Fossati, Daniel Hanschke and Zhi Juan Li for their help and fun days out at the SiDAM meetings.

I want to say thanks to Jochen Wittge and Thomas Jauss for discussions and fun times whiling away long hours at the synchrotron, without you guys the work would not have been half as much fun

I would like to acknowledge the staff at the ANKA Topo-Tomo beamline for their support and help.
A big thank you to all my colleagues at DCU, Aidan, Ken, Evgueni, Jen, Ameera, Jithin, Rajani and Yang for being there to bounce ideas off and get the data and math straight in my head.

The biggest thank you has to go to my wonderful family, Lisa my wife and supporter and best friend and to my wonderful children Darragh and Brónagh, without their support I would not have been able to complete this dissertation. This work is my tribute to them.

Declaration

I hereby certify that this material, which I now submit for assessment on the programme of study leading to the award of Ph.D. is entirely my own work, that I have exercised reasonable care to ensure that the work is original, and does not to the best of my knowledge breach any law of copyright, and has not been taken from the works of others save and to the extent that such work has been cited and acknowledged within the text of this work.

Signed: ....

ID No. ……………………………………………..

Date: ....

Abstract

In the semiconductor industry, wafer handling introduces micro-cracks at the wafer edge and the causal relationship of these cracks to wafer breakage is a difficult task. By way of understanding the wafer breakage process, a series of nano-indents were introduced to both 20 x 20mm (100) wafer pieces and into whole 200mm wafers as a means of introducing controlled strain. The indents were introduced to the silicon by way of a Berkovich tip with applied forces of 100mN to 600mN and with a Vickers tip with applied forces of 2N to 50N. The samples were subjected to an array of both *in situ* and *ex situ* anneal in order to simulate a production environment. The samples were analysed using both micro-Raman spectroscopy and white beam x-ray topography to study the strain fields produced by the nano-indentation and the effect of annealing on the strain fields which was then compared to FEM models of the indents. A novel process for the creation of three dimensional x-ray images, 3D-XRDI, was defined using ImageJ, a freely available image processing tool. This allowed for the construction of three dimensional images and the ability to rotate these images to any angle for ease of viewing. It will be shown how this technique also provided the ability to travel through the sample to view the dislocation loops at any point within the sample. It was found that the temperature profile across the annealing tool had an effect on the strain fields, the growth and movement of dislocation loops and slip bands and on the opening and propagation of cracks. The behaviour of the cracks during rapid thermal anneal was also observed and from this data a parameter was defined that could predict the possibility of wafer breakage.

Table of Contents

ACKNOWLEDGEMENTS .... **II**

DECLARATION .... **III**

ABSTRACT .... **IV**

TABLE OF CONTENTS .... **VI**

LIST OF COMMONLY USED SYMBOLS AND CONSTANTS .... **X**

LIST OF COMMONLY USED SI AND SI DERIVED UNITS .... **X**

CHAPTER 1 INTRODUCTION **1**

1.1 BACKGROUND 1

1.1.1 Problem *1*

1.1.2 DCU Contribution *1*

1.2 EQUIPMENT 2

1.2.1 Micro-Raman spectroscopy *2*

1.2.2 White Beam X-Ray Topography *4*

1.3 SUMMARY 5

1.4 REFERENCES 6

CHAPTER 2 –SILICON CRYSTAL **7**

2.1 INTRODUCTION 7

2.2 SINGLE CRYSTAL SILICON 8

2.3 HIGH PRESSURE PHASES OF SILICON 9

2.3.1 Nanoindentation of Silicon *11*

2.4 SAMPLE PREPERATION 14

2.4.1 Berkovich Tip *15*

2.4.2 Vickers Tip *16*

2.5 DISLOCATIONS IN SILICON 17

2.6 GEOMETRY OF DISLOCATIONS 19

2.6.1 Edge Dislocations *19*

2.6.2 Screw Dislocations *20*

2.7 BURGERS VECTOR AND BURGERS CIRCUIT 21

2.7.1 Burgers Vector *21*

2.7.2 Burgers Circuit ... *22*
2.8 Dislocation Energy ... 23
2.9 Frank-Read Sources ... 24
2.10 References ... 26
CHAPTER 3 – MICRO-RAMAN SPECTROSCOPY ... 33
3.1 Introduction ... 33
3.2 Micro-Raman Spectroscopy ... 33
3.2.1 History of Raman Spectroscopy ... *33*
3.2.2 Principles of Raman Spectroscopy ... *35*
3.2.3 Polarisability and Symmetry ... *40*
3.3 Principle of Stress Measurment ... 41
3.4 Experimental Setup ... 44
3.5 Spatial Resolution and Spot Size ... 47
3.6 Penetration Depth of Laser in Silicon ... 48
3.7 Summary ... 50
3.8 References ... 51
CHAPTER 4 – WHITE BEAM X-RAY TOPOGRAPHY ... 54
4.1 Introduction ... 54
4.2 X-Ray Topography ... 54
4.2.1 History of X-ray Topography ... *54*
4.2.2 Synchrotron White Beam X-ray Topography ... *56*
4.3 Production of Synchrotron X-Rays ... 56
4.3.1 Operation of a Synchrotron Facility ... *59*
4.4 X-ray Scattering Theories ... 60
4.4.1 Kinimatic Theory ... *60*
4.4.2 Dynamic Theory ... *62*
4.5 Experimental Setup ... 62
4.5.1 Large Area Transmission ... *63*
4.5.2 Section Transmission ... *65*
4.5.3 Large Area Back Reflection ... *65*
4.6 Resolution ... 66
4.7 Penetration depth ... 67
4.8 Contrast Formation ... 68

4.8.1 Orientational Contrast ... *68*
4.8.2 Extinction Contrast ... *69*
4.9 REFERENCES ... 73
CHAPTER 5 – THREE DIMENSIONAL X-RAY DIFFRACTION IMAGING ... 78
5.1 INTRODUCTION ... 78
5.2 SAMPLE PREPERATION ... 78
5.2.1 Sample Heating ... *79*
5.3 THREE DIMENSIONAL X-RAY DIFFRACTION IMAGING ... 81
5.3.1 History of Three Dimensional X-ray Diffraction Imaging ... *81*
5.3.2 ImageJ ... *82*
5.3.3 Image Acquisition ... *82*
5.3.4 Image Formation ... *84*
5.3.5 3D Rendering ... *86*
5.4 RESULTS ... 88
5.4.1 K-means Clustering ... *94*
5.5 PRODUCTION OF 3D PHYSICAL MODELS ... 97
5.6 SUMMARY ... 97
5.7 REFERENCES ... 99
CHAPTER 6 – MICRO-RAMAN SPECTROSCOPY RESULTS ... 102
6.1 INTRODUCTION ... 102
6.2EXPERIMENTAL SETUP ... 102
6.3 SYSTEM CALIBRATION AND ERROR COMPENSATION ... 104
6.3.1 System Calibration ... *104*
6.3.2 Error Compensation ... *105*
6.4 RAMAN RESULTS ... 107
6.4.1 Line Scan ... *107*
6.4.2 Map Scan ... *129*
6.4.3 Impact of Thermal Annealing ... *137*
6.5 CORRELATION WITH FEM ... 144
6.6 SUMMARY ... 149
6.7 REFERENCES ... 150
CHAPTER 7 – SYNCHROTRON X-RAY TOPOGRAPHY RESULTS ... 152

7.1 INTRODUCTION 152
7.2 EXPERIMENTAL SETUP..... 152
7.3 X-RAY RESULTS 154
7.3.1 Pre Thermal Annealing 154
7.3.1.1 Large Area Back Reflection Topography 154
7.3.1.2 Large Area Transmission Topography..... 156
7.3.2 Post Thermal Annealing 160
7.3.3 Plateau Annealing 163
7.3.5 Slip Band Development 168
7.4 SUMMARY 179
7.5 REFERENCES 180
SUMMARY 183
FUTURE WORK..... 185
PUBLICATIONS..... 186
APPENDIX 1 188
APPENDIX 2 197
APPENDIX 3 198

List of Commonly used Symbols and Constants

k_B	Boltzmann's Constant	$1.3806504 \times 10^{-23}$ J/K
h	Planck's Constant	$6.62606896 \times 10^{-34}$ Js
ħ	Dirac Constant	$1.054571628 \times 10^{-34}$ Js
c	Speed of Light	299,792,458 ms^{-1}
eV	Electron Volt	$1.60217653 \times 10^{-19}$ C
π	pi	3.141592653589793
λ	Wavelength	nm
G	Giga	10^{9}
M	Mega	10^{6}
k	Kilo	10^{3}
c	Centi	10^{-2}
m	Milli	10^{-3}
μ	Micro	10^{-6}
n	Nano	10^{-9}

List of Commonly used SI and SI derived Units

Metre	Length	m
Kilogram	Mass	Kg
Second	Time (t)	s
Kelvin	Temperature (T)	K
Pascal	Pressure	Pa
Tesla	Magnetic Field	T
Joule	Energy	J
Coulomb	Electric Charge	C
Newton	Force	N
Mole	Amount of a substance	mol

Chapter 1 Introduction

1.1 Background

1.1.1 Problem

In the semiconductor manufacturing industry a typical wafer flow has several hundred individual processing steps and can visit up to 250 process tools. The wafer must be transported not only within a bay but also from one bay to another resulting in a travel journey of approximately 13 - 16 km [1]. This makes wafer handling a critical operation during which damage to silicon wafers can be caused by the introduction of micro-cracks at the wafer edge. This damage can be caused by the transport cassettes or the handling grippers. During thermal processing these can produce slip bands, which can produce larger, long-range cracks and these can cause catastrophic failure during subsequent manufacturing. Dense slip bands can also lead to yield loss by causing boron segregation and retarded phosphorus diffusion [2]. Micro-cracks and slip bands are visible through X-Ray Topography [3]; but, as yet, it is unknown which of the defects imaged are those that will result in yield or wafer loss. Estimates of the loss suffered by a single fabrication plant, due to wafer breakage, puts the proportion of wafers breaking prior to completion at 0.2% leading to a total loss of ~$7.2M per annum per typical fab line [4]. This figure will also increase as the industry moves to the 450 mm wafer size, which is projected to have start-up costs in excess of $20 Billion [5]. The work reported herein is part of a collaborative study along with CEIT (Spain), Kristallographisches Institut, Universität. Freiburg (Germany), Jordan Valley Semiconductors (UK) Ltd., and University of Durham (UK) under the European Community Research Infrastructure Action FP7 ‘‘Structuring the European Research Area’’ programme which aims to discover how to derive quantitative, predicative information to enable a breakthrough metrology for wafer inspection.

1.1.2 DCU Project Contribution

The Dublin City University portion of this programme and the subject of this thesis is to study nano-indentations on silicon samples using both micro-Raman Spectroscopy and White Beam X-Ray Topography and to study both the phases of silicon (Si) and the strain fields produced by nanoindentation in order to derive both qualitative and quantitative information that will allow the semiconductor industry to predict when damage to a silicon wafer will cause catastrophic failure. Defined defects, i.e. nano-indents, were introduced into silicon (100) samples, by CEIT, by the use of a nano-indenter equipped with a Berkovich tip; figure 1.1. Numerous samples were produced, including samples with a 5x5 array. Figure 1.2 shows a Nomarski Interference Contrast image of a sample showing a 5x5 array of nano-indents. The array was produced using vertical applied forces of 500 mN, 400 mN, 300 mN, 200 mN and 100 mN, respectively, the indents being 100µm apart. Other samples were produced with a single line of 15 indents each 1 mm apart

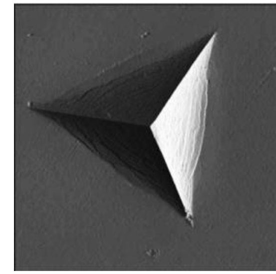

Figure 1.1: Pyramidal tip of a Berkovich nano-indenter.

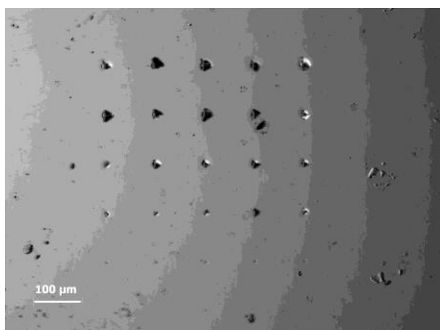

Figure 1.2: Nomarski Interference Contrast Microscopy image of nano-indents, Courtesy of A. Danilewsky and J. Wittge, University of Freiburg

1.2 Equipment

1.2.1 Micro-Raman Spectroscopy

Micro-Raman Spectroscopy (µRS) is known as a highly selective and advantageous tool for the investigation of both the silicon phase transitions and the strain fields produced by nanoindentation [6,7]. The technique has the advantage of being non-destructive and the

probe depth can be controlled by changing the wavelength of the exciting laser. The Raman spectra of the indents were recorded with a Horiba Jobin-Yvon LabRam® HR800 Raman imaging microscope using Labspec 5 software as supplied by the manufacturer; figure 1.3.

1.2.2 White Beam X-Ray Topography

White beam synchrotron X-ray topography (SXRT) is a non-destructive imaging technique, using synchrotron radiation that is widely used for the characterisation of both long range and short range strain in single crystals [3,8]. Figure 1.5 shows a schematic of the TOPO-

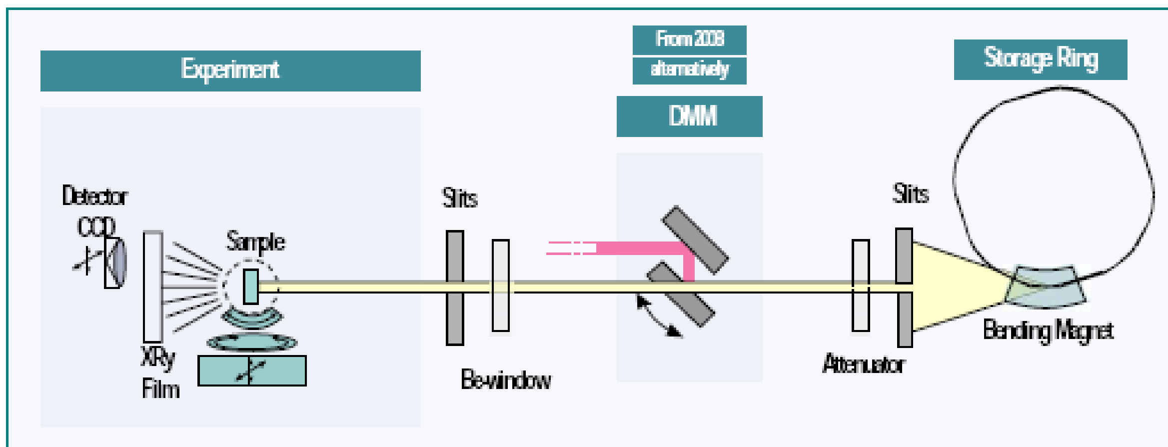

Figure 1.5 Schematic layout of TOPO-TOMO beamline at the ANKA Facility. [14].

TOMO beam line at the ANKA Facility in Karlsruhe, Germany. Figure 1.6 shows a typical set-up for back reflection topography. The technique employs X-ray film upon which a full Laue pattern of the crystal is collected. A pco.4000 14 bit CCD camera system was positioned to capture the 220 reflection.

1.3 Thesis Organisation

The thesis is organised as follows.

Chapter 1 presents an introduction to the thesis and the motivation behind the work

Chapter 2 presents a synopsis of silicon from its discovery. It derives the elastic constants that will be used in later chapters to correlate Raman data to strain in silicon. The chapter will also deal with the various high pressure phases of silicon and the effect of nanoindentation. It will give an introduction to the different tips used for nanandentation and talk about the different dislocation types and how the dislocation energy can be calculated.

Chapters 3 and 4 will deal with the tools used in this thesis. Chapter 3 will deal with micro-Raman spectroscopy, it will trace the development of Raman spectroscopy and show the principles behind Raman spectroscopy and how it can be used for stress measurement, while chapter 4 will deal with White Beam Synchrotron X-Ray Topogrophy. These chapters will also explain the experimental setup and the equipment setup used for this work.

Chapter 5 deals with 3D X-Ray Diffraction Imaging, the history of the technique and the developments to the technique that resulted from the work herein, particularly the creation of 3D software images that can be manipulated to show defects from any desired angle and the ability to step through a sample to trace the formation and spread of dislocation loops.

Chapter 6 and 7 then show the analysis of nanoindents in silicon using the techniques mentioned above.

1.3 Summary

This thesis show the effects of controlled nanoindentation on Silicon wafer breakage. The nano-indents are studied and their induced strain fields examined using both μRS and SXRT. It will be shown that micro Raman spectroscopy and X-Ray topography (X-Ray Diffraction Imaging) can be used as complimentary techniques to study strain in silicon. It will also show techniques developed within the study – particularly the use and implementation of 3D X-Ray Diffraction Imaging.

1.3 References

[1] G. K. Agrawal and S. S. Heragu, IEEE T. Semiconduct. M. **19**, 112 (2006).

[2] H. Park, K. S. Jones, J. A. Slinkman, and M. E. Law, Int. Elec. Dev. Meet., 303 (1993).

[3] A. N. Danilewsky, J. Wittge, A. Rack, T. Weitkamp, R. Simon, T. Baumbach, and P. J. McNally, J. Mater. Sci. **19**, 269 (2008).

[4] P. Y. Chen, M. H. Tsai, W. K. Yeh, M. H. Jing, and Y. Chang, Jpn. J. Appl. Phys. **48**, 1 (2009).

[5] S. Myers, *Standards Taskforce Established on 450 mm Wafer Handling*, 2009.

[6] D. C. Mahon, P. J. Mahon, and D. C. Creagh, Nuc. Instrum. Meth. Phys. Res. A **580**, 430 (2007).

[7] C. Himcinschi, I. Radu, R. Singh, W. Erfurth, A. P. Milenin, M. Reiche, S. H. Christiansen, and U. Gösele, Mat. Sci. Eng. B **135**, 184 (2006).

[8] A. N. Danilewsky, R. Simon, A. Fauler, M. Fiederle, and K. W. Benz, Nuc. Instrum. Meth. Phys. Res. B **199**, 71 (2003).

Chapter 2 Silicon Crystal

2.1 Introduction

Silicon (Si) is a group (IVA) element with an atomic number of 14 and a molecular weight of 28.09 kg/mol, it has a covalent atomic radius of 0.118 nm and a melting point of 1685 K and makes up ~25.7% of the Earth's crust by mass [1,2]. It does not occur free in nature but occurs chiefly as an oxide or as silicates.

Silicon, as a substance, was first discovered by Joseph Louis Gay-Lussac and Louis Jacques Thenard of the École Polytechnique in 1811 by heating potassium and silicon tetrafluroide.

$$SiF_4 + 4K => Si + 4KF \quad (2.1)$$

This technique was then perfected by Friherre Jöns Jacob Berzelius of the Karolinska Institute in 1824, where he repeatedly washed the resultant mass first produced by Guy-Lussac and Thenard in water to produce amorphous silicon. Crystalline silicon was first discovered by Henri Sainte-Claire Deville in 1854 through the electrolysis of sodium-aluminium chloride with 10% silicon [3].

Although research into semiconductor properties began with Michael Faraday in 1833 [4] it was not until a 1948 paper by Bardeen *et al.* [5] and then a 1949 paper by Shockley [6], wherein he published his theory on the use of semiconductors to create *p-n* junctions, that the semiconductor revolution took off. Initially the semiconductor of choice was Germanium (Ge) but then in 1952 Gordon Teal moved from Bell Laboratories to Texas Instruments to develop Si as a transistor material as Ge did not meet the military specifications for temperature stability [4]. In 1961 Robert Noyce of Fairchild Semiconductors [7] filed a patent application for the fabrication of integrated circuits (IC) using Si and the Silicon era took off. Noyce, along with Jack Kilby of Texas Instruments are considered the inventors of the IC. In

2000 Kilby was awarded the physics Nobel Prize for his contributions; sadly, by this time, Noyce had passed away.

Single crystal silicon (c-Si) is the dominant substrate material used in the semiconductor industry at present [8-10] and has become the most important and characteristic material of the silicon age [1,11]. The majority of the wafers come from ingots grown using the Czochralski (Cz) method to produce dislocation free ingots [12] which are then wafered by an inner diameter (ID) diamond saw blade [1,13,14]. The wafers are then lapped, polished and then shipped to the manufacturing companies. As mentioned in section 1.1.1, this shipping process can induce mechanical damage at the edge of the Si.

For this reason the deformation characteristics of c-Si under indentation have been extensively studied [10,15-39]. This chapter will deal with the structure of c-Si, the methods of nanoindentation and the resulting phases of Si produced.

2.2 Single Crystal Silicon

Single crystal Silicon, of the type used by the semiconducting manufacturing industry, exists in a cubic diamond (cd) form known as Si-I [11,40,41], as shown in figure 2.1.

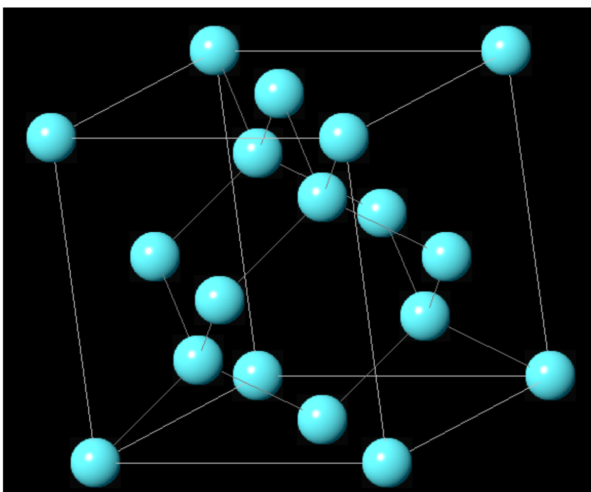

Figure 2.1: Representation of Cubic Diamond Silicon

It is a face centred cubic (fcc) structure with 8 atoms per unit cell and a density ρ_{si} of $2.329\ g/cm^3$ at $298K$ [42,43]. The second order elastic constants for pure Si-I at room temperature and atmospheric pressure are [44]:

$$C_{11} = 1.6564 \times 10^{11}\ Pa \quad (2.2)$$

$$C_{12} = 0.6394 \times 10^{11}\ Pa \quad (2.3)$$

$$C_{44} = 0.7951 \times 10^{11}\ Pa \quad (2.4)$$

Using these figures the elastic compliance tensors (S_{ij}) used in section 3.3 can be resolved from the following equations [54]:

$$S_{11} = \frac{C_{11} + C_{12}}{(C_{11} - C_{12})(C_{11} + 2C_{12})} \quad (2.5)$$

$$S_{12} = \frac{-C_{12}}{(C_{11} - C_{12})(C_{11} + 2C_{12})} \quad (2.6)$$

Eqn. (2.2) and eqn. (2.3) can now be used to find, not only the bulk modulus (B) of Si-I, but also can be used to estimate the change in volume (ΔV) due to hydrostatic pressure [43]:

$$B = -\frac{P}{(\Delta V/V)} = \frac{1}{3}(C_{11} + 2C_{12}) \quad (2.7)$$

where B is the bulk modulus, P is the hydrostatic compression applied and V is the volume of the Si-I.

2.3 High Pressure Phases of Silicon

The static high pressure behaviour of Silicon (Si) has been studied since Minomura *et al*. first published their paper '*Pressure induced phase transitions in silicon, germanium and some III-V compounds*' in 1962 [46] where they found significant changes in the electrical resistivity of c-Si as a result of static compression to 20 GPa. They concluded that this was the result of a solid-solid phase transition from a semiconducting to a metallic state and showed that in the presence of a large uniaxial stress this transition occurred at 13.5 to 15 GPa. This was confirmed in 1963 when Jamieson used X-ray diffraction to show the transition from c-Si to a

white tin structure with a 22% volume reduction at pressures of less than 16 GPa [47]. That same year Wentorf *et al*. found the transition to be sensitive also to temperature and time of pressure and also discovered a second body centred cubic (bcc) phase, identified as Si-III, after release from pressure [48].

In 1966 Wittig discovered that the high pressure phases of Si become superconducting with a superconducting transition temperature of 6.7 K when under a pressure of 12 GPa [49]. Then in 1970 Anastassakis *et al*. produced a paper which showed how the effects of static uniaxial stress on Si would shift the Raman peak of the triply degenerate optical phonon linearly with respect to the applied stress and showed how it was possible to use Raman scattering to obtain data on the strain dependant spring constants of optical phonons which are Raman active [50]. Anastassakis's paper also provided the values for S_{ij}, the elastic compliance constants, that are used in determining $\Delta\omega$ from section 3.3. This was followed up by Weinstein *et al*. where they used Raman scattering and infrared microscopy to observe the c-Si transition to a metallic phase. They found that the transition occurred at 12.5 GPa and was not a gradual change (in time) but appeared first in a shallow portion of the bulk Si and then spread throughout the sample [41]. In contrast to Wentorf's electrical experiments, where the transformation appeared sluggish [48], the transformation observed by Weinstein occurred in approximately 5 minutes [41]. Their conclusion was that the speed of transformation was dependent upon the loading conditions. Later that same year, Welber *et al*. studied the dependence of the indirect energy gap of Si on hydrostatic pressure and showed that the sample became opaque at an applied pressure of between 11.5 and 12.6 GPa [51], a phase they attributed to the same metallic phase observed by Minomura *et al*., though they could not explain the discrepancy between their observed critical pressures and those observed by Minomura. This was later accounted for by Gupta *et al*. where Minomura's figures were corrected for their calibration point and showed a critical pressure of approximately 13 GPa

[34]. Work on identifying high pressure phases of Si has continued to the present day and there are currently 13 known phases (as well as the amorphous phase) [20,40]. These are shown in figure 2.2:

Designation	Structure	Space Group	Pressure region (GPa)	Raman Peaks (cm^{-1})
Si-I	diamond cubic	Fd3m	0-12.5	301, **520**
Si-II	body centred tetragonal (β-Sn)	$I4_1/amd$	8.8-16	480
Si-III (or BC8)	body centred cubic (basis of 8 atoms)	$Ia\bar{3}$	2.1-0	458, 447, **431**, 413, 384, 354, 162
Si-IV	diamond hexagonal (lonsdaleite)	$P6_3/mmc$	-	500-510
Si-V	primitive hexagonal	P6/mmm	14-35	
Si-VI	Orthorhombic	Cmca	34-40	
Si-VII	hexagonal close packed	$P6_3/mmc$	40-78.3	
Si-VIII	tetragonal (~ 30 atoms per unit cell)	$P4_12_12$	14.8-0	
Si-IX	tetragonal (12 atoms per unit cell)	$P4_222$	12-0	
Si-X	face centred cubic	Fm3m	78.3 → 230	
Si-XI (or Imma)	body centred orthorhombic	Imma	13/15	
Si-XII (or R8)	rhombohedral (8 atoms per unit cell)	$R\bar{3}$	12-2.0	514, 440, 395, 382, **350**, 165
Si-XIII	unidentified			200, 330, 475, 497
a-Si	random tetrahedral network			160, 300, 390, **470**

Figure 2.2: High pressure Phases of Si. [40]

2.3.1 Nanoindentation of Silicon

It is known that the indentation of Si can create areas of high stress that result in phase changes to the crystal structure [35] and that in the core region of the indent, where the stresses are highest, the c-Si structure may become unstable and transforms to either an amorphous phase or a high pressure polymorph of the type outlined above [27]. Indentation can be performed with a 'blunt' indenter, such as a spherical indenter, or a 'sharp' indenter, such as Vickers or Berkovich types. This study concentrates on indentations performed with a 'sharp' indenter as it is these indenters that are considered to be the most dangerous and pertinent to real life damage [65]. Indentation studies began in the late 1970's with papers by

Lawn *et al*. wherein they tried to find simple approximations for the tensile stress distribution in the elastic/plastic indentation fields to determine the critical conditions for the growth of cracks [66]. While this paper did show the existence of cracks under indentation the equations derived were for a Vickers tip and were not easily transferable to a Berkovich tip as they relied upon experimental observations of the impression diagonal as well as the intensity and extent of the tensile field [66]. The paper also made no assumptions regarding the nature of starting flaws other than to state that they exist and have some effective dimension. It was not until the late 1990's that work began in earnest on the mechanics and physics of silicon under nanoindentation [17] and how nanoindentation produces phase transformations in Si [11,27,28,35,36,39,63,67-70]. Si-I requires a minimum pressure of 8.8 GPa to initiate transformation into Si-II which is required before any other high pressure polymorph phases can be realised [53]. Later work by Kailer *et al*. [28], Domnich *et al*. [11] and Rao *et al*. [21] plotted out the phase transformations of Si under pressure. The phase transformations were shown to follow a distinct path as shown in figure 2.3.

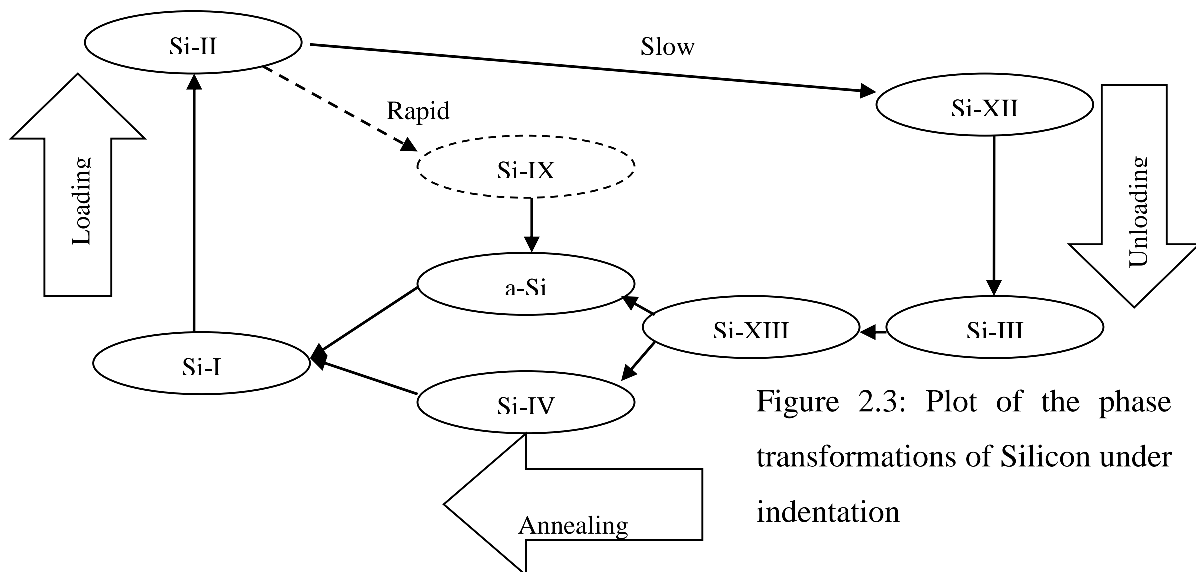

Figure 2.3: Plot of the phase transformations of Silicon under indentation

Slow unloading of the indenter first produces a rhombohedral structure, r8 (Si-XII) at ~ 12 GPa [28,63,64]. On further release there is a reversible transition from Si-XII to the bcc

structure, bc8, (Si-III) at ~ 2 GPa [52,53,56]. This produces a mixture of Si-III and Si-XII at ambient pressure [63]. Upon heating, to above 470 K, the Si-III/Si-SII structure changes first to an as yet unidentified phase of silicon known as Si-XIII [38] and then to a diamond hexagonal structure Si-IV [23,56] before reverting back to the cubic diamond structure, Si-I.

With rapid unloading of the sample Si-II transforms to a-Si [11]. This transformation produces a phase of silicon known as Si-IX, believed to be a tetragonal phase of silicon. This phase was reported by Zhao *et al*. [60] though this result has not been reproduced by any other group.

High pressure transformations involve a volume change in the silicon. The different volumes are shown in figure 2.4 below.

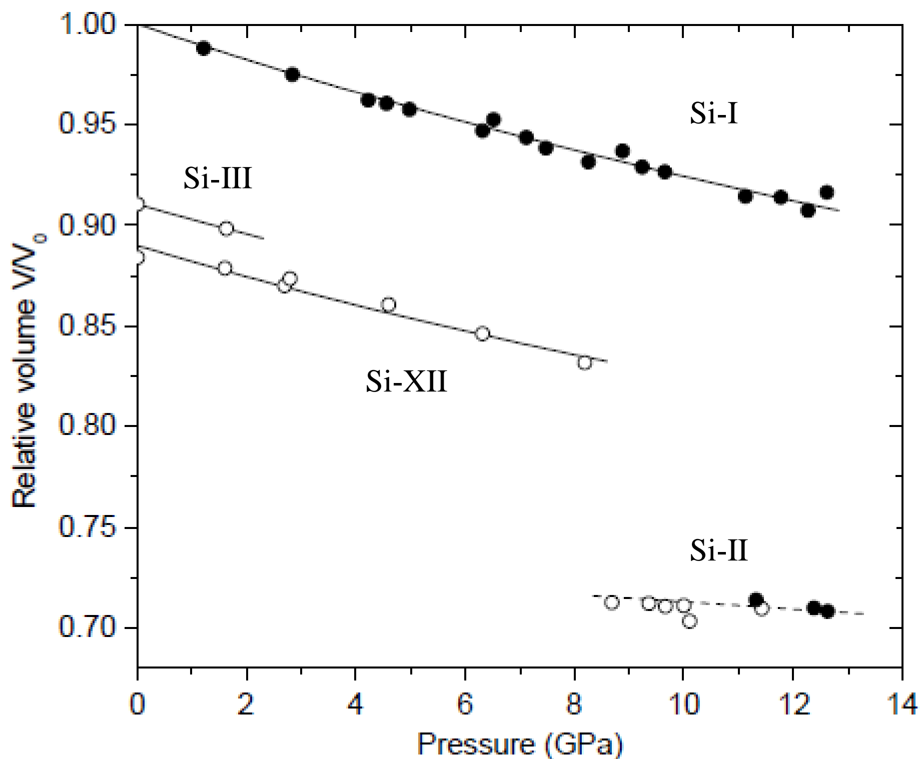

Figure 2.4: Relative volumes of the high pressure phases of Si. Filled Circles are increasing pressure and open circles are decreasing. [38]
Data for Si-I and Si-II are from Hu *et al*.[53]. Data for Si-III and Si-XII are from Pilz *et al*. [64]

As stated in section 2.3, Si undergoes a ~22% volume reduction upon transformation from Si-I to Si-II. Si-XII is ~11% denser than Si-I [64,71] while Si-III is ~9% denser than Si-I [48,72]. The densification of the c-Si into Si-II upon loading can, but not always, lead to a discontinuity in the load curve called a 'pop-in'; this event is thought to be as a result of the sudden yielding of the material under load. A similar event can be seen on unloading and is called a 'pop-out'. This event is thought to be due to a large volume change from Si-II to less dense metastable phases such as Si-III or Si-XII [28]. These events are shown in figure 2.5 courtesy of J. Garagorri, CEIT:

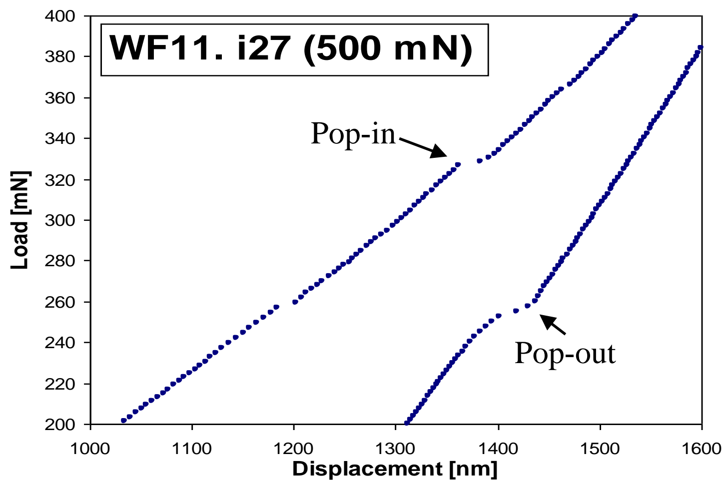

Figure 2.5: Pop-in and Pop-out events on a 500mN indent
(Courtesy of J. Garagorri, CEIT, Spain)

2.4 Sample Preparation

All nanoindented samples utilised in this study were produced by Jorge Garagorri at CEIT and TECNUN (University of Navarra, San Sebastian, Spain). Because of the requirements to create a wide range of load conditions a number of tools were used to create the indents. A NTS Nanoindenter II equipped with a Berkovich tip was used to create indents ranging from 100mN to 600mN, a LECO M-400G2 hardness tester equipped with a Vickers tip was used

to create indents with loads from 600mN to 10N while a Mitutoyo AVK-C2 hardness tester was used for loads ranging from 10N to 200N.

2.4.1 Berkovich Tip

The Berkovich tip is a three sided pyramidal diamond indenter used to create indentations with loads typically ranging from 100mN to 600mN. It has a centre to face angle, α, of 65.3° and produces a triangular shaped indent as shown in fig. 2.7, with one edge parallel to the [110] direction.

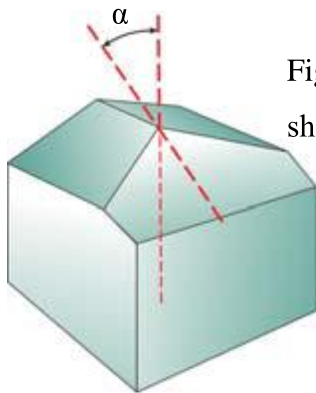

Figure 2.6: Schematic of a Berkovich tip showing the centre to face angle, α.

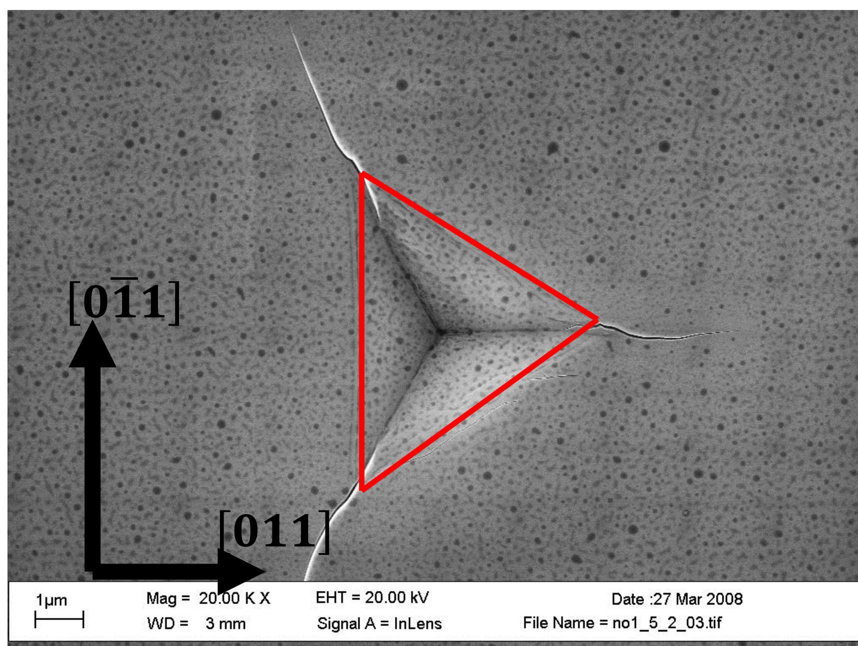

Figure 2.7: Triangular indent from a Berkovich tip. Courtesy of J. Wittge (Crystallography Institute of Geoscience, Albert-Ludwigs-University, Freiburg)

2.4.2 Vickers Tip

The Vickers tip is a four sided pyramidal square diamond indenter used to create indents with loads ranging from 600mN to 200N. It has a centre to face angle, α, of 68.5°. A schematic of the indenter and the resulting indent is shown below. The tip produces a square indent as shown in fig. 2.9.

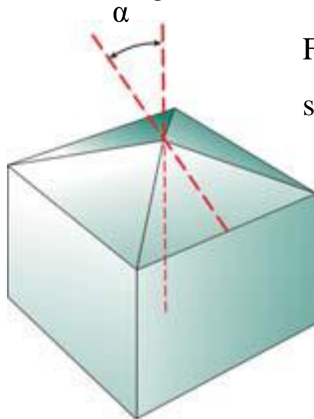

Figure 2.8: Schematic of a Vickers tip showing the centre to face angle, α.

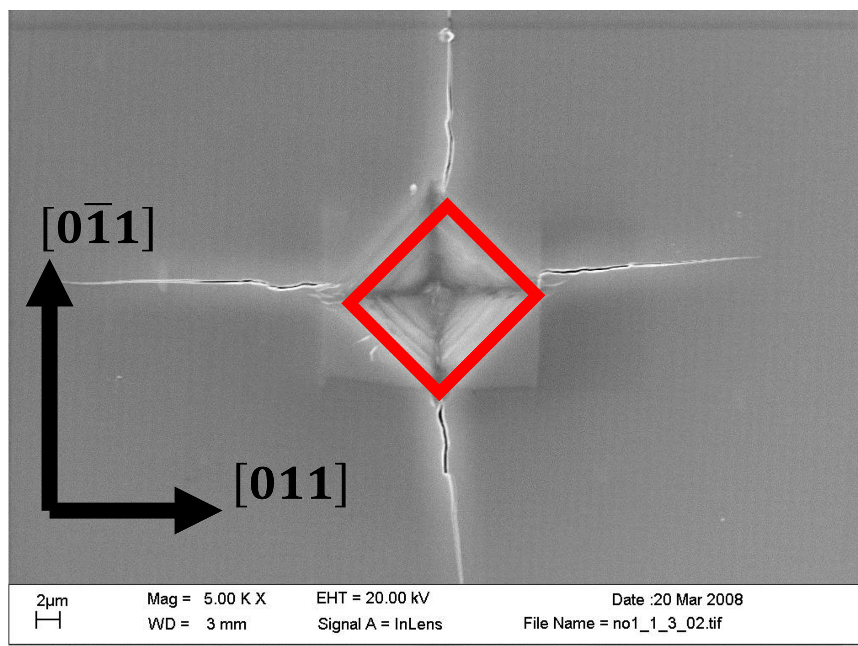

Figure 2.9: Square indent produced from a Vickers tip. Courtesy of J. Wittge (Crystallography Institute of Geoscience, Albert-Ludwigs-University, Freiburg)

2.5 Dislocations in Silicon

Dislocations in semiconductors are of great interest because of their effect on devices and also because they serve as a model for the study of plastic deformation [73]. The deformation and strength of crystalline materials are determined by the various crystal defect types, i.e. vacancies, interstitials, dislocations, etc. Most often, dislocations define the plastic yield and flow behaviour of the crystal [74].

The most studied material studied with respect to dislocations is silicon [75] even to the extent that individual kink migration has been studied. [76]

Dislocations were first observed in the early twentieth century, for example Ewing *et al*. [77] noticed that the plastic deformation of metals occurred by the formation of slip bands or slip packets [78]. The idea of a dislocation as a line defect was introduced as a mathematical concept by Volterra in 1907 [79], where the elastic properties of a cut cylinder were considered. In 1926 Frenkel first calculated the shear stress required for this form of plastic deformation [80].

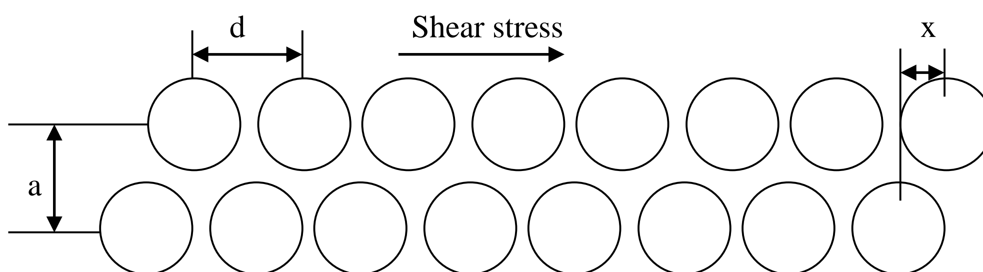

Figure 2.10: Representation of atom positions used to estimate the theoretical critical shear stress for slip [80].

Frenkel assumed that there was a periodic shearing force required to move one row of atoms across another row (fig. 2.10), and that this relationship is given by:

$$\tau = \tau_{th} \sin\frac{2\pi x}{d} \qquad (2.8)$$

where τ is the applied shear stress, τ_{th} the theoretical shear stress, d is the spacing between the atoms in the direction of the shear stress and x the shear translation of the two rows away from the low energy equilibrium position. For small strains, $\frac{x}{a} < 1$, where a is the interplaner spacing, Hookes' law applies in the form:

$$\tau = \mu\frac{x}{a} \qquad (2.9)$$

where μ is the shear modulus. At the small-strain limit:

$$\sin\frac{2\pi x}{d} \cong \frac{2\pi x}{d} \qquad (2.10)$$

And eqn. 2.8 now becomes:

$$\tau \approx \left(\frac{\mu x}{a}\right)\left(\frac{2\pi x}{d}\right) \qquad (2.11)$$

This now gives a maximum value of τ to be:

$$\tau = \frac{\mu d}{2\pi x a} \qquad (2.12)$$

Since $d \cong a$, it can be stated that:

$$\tau \cong \frac{\mu}{5} \qquad (2.13)$$

This, however, is in marked disagreement with experimental findings that showed that the shear stress required to initiate plastic flow was in the range of 10^{-3} to 10^{-4} μ [78,81].

This discrepancy was not explained until 1934 when Orowan [82], Polanyi [83] and Taylor [84,85] independently accounted for it by the presence of edge dislocations. This was followed up in 1939 when Burgers advanced the description of the screw dislocation [86]. These findings were then confirmed experimentally by Dash [87] and Hirsch *et a*l. [88] in the 1950's.

2.6 Geometry of Dislocations

Dislocations are line defects representing the boundary of a region where slip between adjacent atomic planes has occurred. As such, a single dislocation must either be a closed loop within the crystal or terminate on the surface at both ends [73]. The dislocation is described by its line sensor or line of dislocation ξ and Burgers vector $\boldsymbol{b}$. The Burgers vector has two distinct components: normal to the line of dislocation and perpendicular to the line of dislocation [78,81,89]. This gives the two fundamental dislocation types: edge and screw [2,90].

2.6.1 Edge Dislocations

An edge dislocation is one where the Burgers vector is normal to the line of the dislocation. It is produced when the applied stress results in a localised lattice distortion that exists along the end of an extra half plane of atoms 'wedged' into the top half of a crystal, Fig. 2.11.

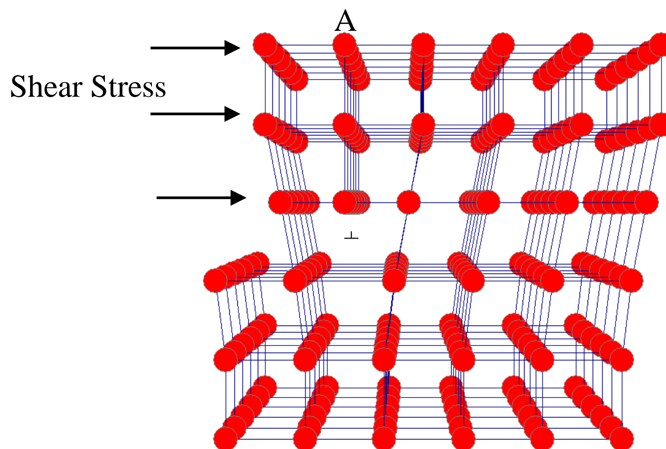

Figure 2.11: Atomic arrangement of an edge dislocation. The extra half plane of atoms is labeled A

A consequence of this type of dislocation is that the top half of the crystal experiences compression on either side of the dislocation while the region below the dislocation experiences significant dilatation or tension. By convention fig 2.11 shows a 'positive' edge dislocation and is represented symbolically by '⊥'. Had the extra half plane been introduced

into the bottom of the crystal, the localised compression and dilatation would have been reversed and would be defined as a 'negative' edge dislocation and be represented by ' ┬ ' .

Clearly, if a crystal contains both positive and negative edge dislocations lying in the same plane, it would result in mutual annihilation and the elimination of two high energy regions of lattice distortion [91]. The movement of an edge dislocation is most clearly explained in terms of considering its Burgers circuit. This will be discussed later. Suffice it to say that an edge dislocation has two forms of motion: conservative and nonconservative motion. Conservative motion occurs when the dislocation moves in the same direction as its Burgers vector ***b***, the direction of slip. Nonconservative motion occurs when the dislocation moves out of its normal glide plane, through the removal of a row of atoms. This results in the dislocation climbing from one plane to another where conservative motion can occur once again [78,81,91].

2.6.2 Screw Dislocations

A screw dislocation is one where the Burgers vector is parallel to the line of dislocation and can be defined as the displacement of one part of the crystal relative to the other, fig. 2.12. The Burgers circuit about the screw dislocation assumes the shape of a helix; a 360° rotation produces a translation equal to one lattice vector in a direction parallel to the

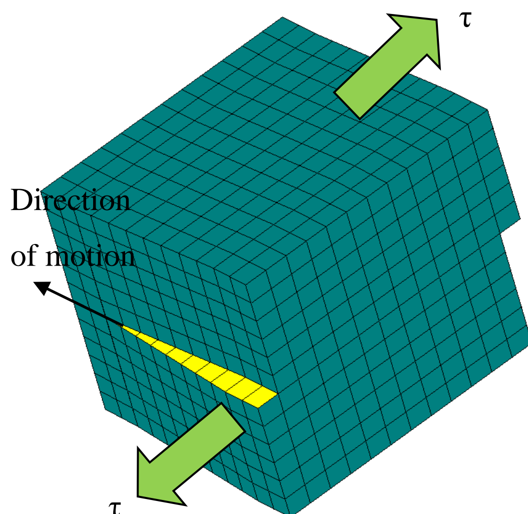

Figure 2.12. Screw dislocation: τ is the direction of the applied shear stress

dislocation line. Looking down the dislocation line, if the helix advances one plane when a clockwise circuit is made, it is referred to as a 'right hand screw' dislocation; if the reverse is true then it is called a 'left hand screw' dislocation [81]. While the slip direction is parallel to ***b***, the direction of movement is perpendicular to ***b***. The movement of a screw dislocation is not confined to a single slip plane: this movement takes place through a process known as 'cross-slip'. If the movement of a screw dislocation on a particular plane is impeded by some obstacle, the dislocation can cross over to another equivalent plane and continue its movement. As the Burgers vector is unchanged the slip continues on in the same direction. A table of the differences is shown in fig 2.13 [78].

Dislocation Characteristic	**Type of Dislocation**	
	Edge	**Screw**
Slip Direction	Parallel to ***b***	Parallel to ***b***
Relationship between dislocation line and ***b***	Perpendicular	Parallel
Direction of dislocation line movement relative to ***b***	Parallel	Perpendicular
Process by which dislocations may leave glide plane	Nonconservative climb	Cross-slip

Fig 2.13: Characteristics of Dislocations [78]

2.7 Burgers Vector and Burgers Circuit

The most useful definition of a dislocation can be given in terms of its Burgers vector and Burgers circuit, both of which will be explained here [81].

2.7.1 Burgers Vector

The Burgers vectors defined for a simple crystal is defined as the shortest lattice translation vector that joins two points in a lattice. The diamond cubic structure of silicon is face centred cubic (fcc) with a basis of two atoms giving a ***b*** of a/4[111] [92]. It can be thought of as two

interpenetrating fcc lattices, one of which is displaced by (¼,¼,¼) with respect to the other [73].

The Burgers vector of a dislocation is a crystal vector, specified by Miller indices that specifies the difference between the distorted lattice around a dislocation and the perfect lattice. It also defines the direction and magnitude of the atomic displacement that occurs when a dislocation moves [93].

2.7.2 Burgers Circuit

A Burgers circuit is any atom-to-atom path taken in a crystal containing dislocations that forms a closed loop, fig. 2.14. If the same circuit is then taken in a perfect crystal containing no dislocations, and the circuit does not close, fig. 2.15, the first circuit must contain a dislocation. It can be seen that the movement sequence of the circuit '*abde*' in the perfect crystal, fig 2.15, is the same as in the crystal containing the dislocation, fig. 2.14. The closure failure '*bc*' is the Burgers vector. This construction implies two rules: first, when looking along the dislocation line the circuit is drawn clockwise; second, the Burgers vector is taken to run from the finish to the start point of the reference system [81].

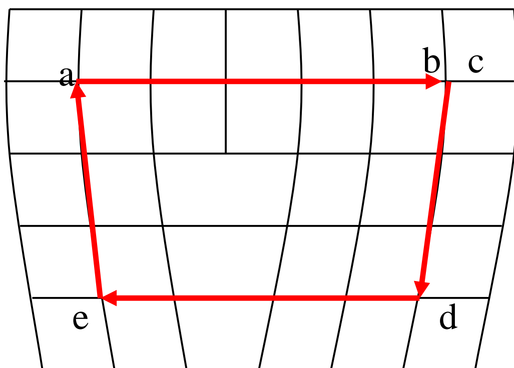

Figure 2.14: Burgers circuit around an edge dislocation

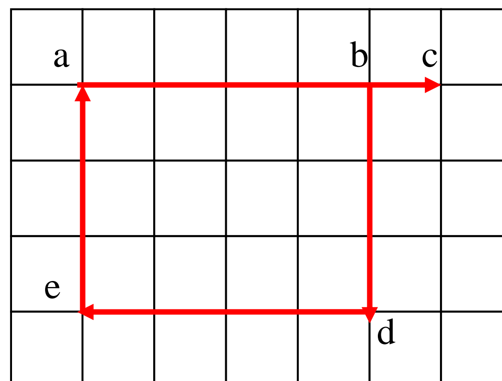

Figure 2.15: Equivalent circuit in a perfect crystal

It was mentioned earlier that a dislocation must form a closed loop and cannot end inside a crystal. Another possibility is that the dislocation can branch into other dislocations. When three or more dislocations meet at a point a node is formed and it is a necessary condition that the Burgers vector is conserved [90]. In other words the sum of the Burgers vectors must be zero:

$$b_1 + b_2 + b_3 = 0 \qquad (2.14)$$

Furthermore, when the dislocations are of the same sense then:

$$b_1 = b_2 + b_3 \qquad (2.15)$$

This holds true when one dislocation dissociates into two additional dislocations or two dislocations combine into one [91]. In general for n-dislocation branches it can be said [81,94]:

$$\sum_{i=1}^{n} b_i = 0 \qquad (2.16)$$

2.8 Dislocation Energy

The existence of lattice distortion around a dislocation implies that the crystal is no longer in its lowest energy state and now contains some elastic energy from the dislocation. The formula for this energy was derived in 1949 by F.C. Frank [95]. The derivation will not be performed here but the formulae for the energy are given by:

$$E_{screw} = \frac{Gb^2}{4\pi} \ln\frac{r_1}{r_0} \qquad (2.17)$$

$$E_{edge} = \frac{Gb^2}{4\pi(1\text{-}v)} \ln\frac{r_1}{r_0} \qquad (2.18)$$

where G is the shear modulus, $\boldsymbol{b}$ is the magnitude of the Burgers vector in the slip direction, r_1 is the outer boundary of the crystal, r_0 the region outside the core of the dislocation and v the Poisson's ratio [78,81,91]. In general a crystal will contain both edge and screw

dislocations and the energy will be intermediate between the limiting factors of eqn. (4.17) and (2.18). This gives rise to the general formula:

$$E = \alpha G b^2 \qquad (2.19)$$

where α is a geometrical factor taken to be between 0.5 and 1. A consequence of this is that a dislocation with a Burgers vector ***b*** will find it energetically favourable to dissociate into dislocations whose Burgers vectors are as small as the structure of the crystal lattice permits. In general the Frank criteria for dissociation is a split will occur only if [78,90]:

$$b_1^2 > b_2^2 + b_3^2 \qquad (2.20)$$

2.9 Frank-Read Sources

In 1950 Frank *et al*. noticed that, on a typical active slip plane there was ~10^3 times more slip than could be accounted for by the passage of a single dislocation [96]. Frank considered a dislocation segment AB as shown in fig. 2.16 whose ends are pinned. When there is applied stress the segment bows out by glide; as the bow-out proceeds the radius of the curvature of the line decreases and the line tension forces try to restore the line to a straight configuration. As long as the expanding loop neither jogs out its original glide plane because of intersections with other dislocations nor is obstructed from rotating about the pinning point, it will create a completed closed loop.

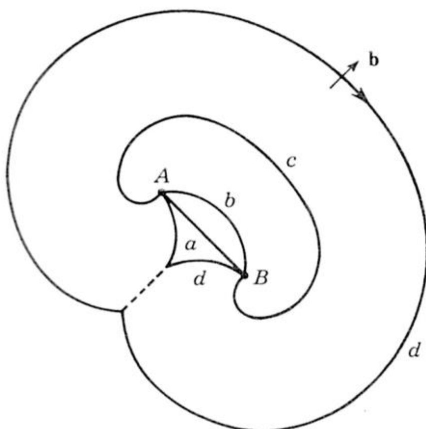

Figure 2.16: Dislocation segment (a) pinned at A and B, (b) bowing out of its glide plane, and (c) and (d), operating as a Frank-Read source. [77]

A sequence of loops then continues from the source until sufficient internal stresses are generated for the net resolved shear stress at the source to drop below the critical stress limit for a dislocation defined as [78]:

$$\sigma^{*} = \frac{\alpha Gb}{L} \qquad (2.21)$$

where L is the straight segment length. However it was not until 1956 that Dash first produced the classical picture of a Frank-Read source in silicon decorated with copper [87]. An image of a Frank-Read source is shown in fig. 2.17. This image is from a 200mm wafer indented with 500mN load and imaged using a Bedescan™ High Resolution X-Ray Diffraction tool by our research team.

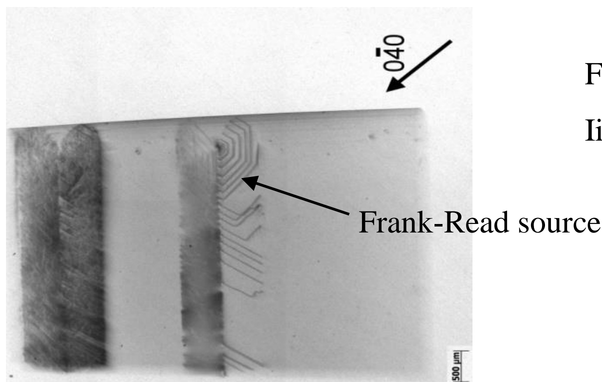

Figure 2.17: $0\bar{4}0$ X-ray diffraction Iimage of a Frank-Read source

2.10 References

[1] W. C. O'Mara, R. B. Herring, and L. P. Hunt, *Handbook of Semiconductor Silicon Technology* (Noyes Publications, New Jersey, 1990), p. 795.

[2] W. D. Callister, *Materials Science and Engineering An Introduction*, edited by W. Anderson and K. Santor (John Wiley & Sons, Inc., New York, 2003), p. 820.

[3] M. E. Weeks, J. Chem. Educ. **9**, 1386 (1932).

[4] J. Orton, *The story of semiconductors* (Oxford University Press, Oxford, 2004), p. 510.

[5] J. Bardeen and W. H. Brattain, Phys. Rev. **74**, 230 (1948).

[6] W. Shockley, Bell. Syst. Tech. J., 435 (1949).

[7] R. Noyce, *Semiconductor Device and Lead Structure* (H01L 23/485, USA, 1961), 257/587, p. 1.

[8] D. E. Kim and S. I. Oh, Nanotech. **17**, 2259 (2006).

[9] J. Yan, J. Appl. Phys. **95**, 2094 (2004).

[10] I. Zarudi, L. C. Zhang, W. C. D. Cheong, and T. X. Yu, Acta Materialia **53**, 4795 (2005).

[11] V. Domnich and Y. Gogotsi, Rev. Adv. Mater. Sci. **3**, 1 (2002).

[12] W. C. Dash, J. Appl. Phys. **29**, 736 (1958).

[13] K. A. Jackson, *Silicon devices : structures and processing* (Weinheim, Chichester, 1998).

[14] G. Harbeke and M. Schultz, *Semiconductor silicon : materials science and technology* (Berlin, New York, 1988).

[15] I. Zarudi, J. Zou, and L. C. Zhang, Appl. Phys. Lett. **82**, 874 (2003).

[16] I. Zarudi and L. C. Zhang, Trib. Int. **32**, 701 (1999).

[17] L. C. Zhang and H. Tanaka, JSME International Journal **42**, 546 (1999).

[18] F. Yang and P. Fei, Semicond. Sci. Tech. **19**, 1165 (2004).

[19] T. Vodenitcharova and L. C. Zhang, Int. J. Sol. Struct. **40**, 2989 (2003).

[20] T. Vodenitcharova and L. C. Zhang, Int. J. Sol. Struct. **41**, 5411 (2004).

[21] R. Rao, J. E. Bradby, S. Ruffell, and J. S. Williams, J. Microelec. **38**, 722 (2007).

[22] P. Puech, F. Demangeot, P. S. Pizani, V. Domnich, and Y. Gogotsi, J. Phys. Condens. Mat. **16**, 39 (2004).

[23] R. J. Needs and A. Mujica, Phys. Rev. B **51**, 9652 (1995).

[24] S. Narayanan, S. R. Kalidindi, and L. S. Schadler, J. Appl. Phys. **82**, 2595 (1997).

[25] D. Lowney, T. S. Perova, M. Nolan, P. J. McNally, R. A. Moore, H. S. Gamble, T. Tuomi, R. Rantamaki, and A. N. Danilewsky, Semicond. Sci. Tech. **17**, 1081 (2002).

[26] S. J. Lloyd, J. M. Molina-Aldareguia, and W. J. Clegg, J. Mater. Res. **16**, 3347 (2001).

[27] A. Kailer, K. G. Nickel, and Y. Gogotsi, J. Raman Spec. **30**, 939 (1999).

[28] A. Kailer, Y. Gogotsi, and K. G. Nickel, J. Appl. Phys. **81**, 3057 (1997).

[29] T. F. Juliano, Y. Gogotsi, and V. Domnich, J. Mater. Res. **18**, 1192 (2003).

[30] T. F. Juliano, V. Domnich, T. E. Buchheit, and Y. Gogotsi, Mat. Res. Soc. Symp. Proc. **791**, 191 (2004).

[31] J. Jang, M. J. Lance, S. Wen, T. Y. Tsui, and G. M. Pharr, Acta Materialia **53**, 1759 (2005).

[32] M. Hebbache, Mat. Sci. Eng. A **387-389**, 743 (2004).

[33] S. J. Harris, A. E. O'Neill, W. Yang, P. Gustafson, J. Boileau, W. H. Weber, B. Majumdar, and S. Ghosh, J. Appl. Phys. **96**, 7195 (2004).

[34] M. C. Gupta and A. L. Ruoff, J. Appl. Phys. **51**, 1072 (1980).

[35] Y. Gogotsi, A. Kailer, and K. G. Nickel, Mat. Res. Innovat. **1**, 3 (1997).

[36] Y. Gogotsi, C. Baek, and F. Kirscht, Semicond. Sci. Tech. **14**, 936 (1999).

[37] D. Ge, V. Domnich, and Y. Gogotsi, J. Appl. Phys. **93**, 2418 (2003).

[38] D. Ge, V. Domnich, and Y. Gogotsi, J. Appl. Phys. **95**, 2725 (2004).

[39] B. Galanov, V. Domnich, and Y. Gogotsi, Exp. Mech. **43**, 303 (2003).

[40] A. George, *High Pressure Phases of c-Si* (Inspec, London, 1999), 20, p. 104.

[41] B. A. Weinstein and G. J. Piermarini, Physical Review B **12**, 1172 (1975).

[42] G. F. Cerofolini and L. Meda, *Physical chemistry of, in, and on silicon* (Springer-Verlag, Berlin ; New York, 1989), 8.

[43] Y. Okada, *Diamond Cubic Si: structure, lattice parameter and density* (INSPEC, London, 1998), p. 91.

[44] J. J. Hall, Phys. Rev. **161**, 756 (1967).

[45] A. George, *Elastic constants and elastic moduli of diamond cubic si* (INSPEC, London, 1997), p. 98.

[46] S. Minomura and H. G. Drickamer, J. Phys. Chem. Solids **23**, 451 (1962).

[47] J. C. Jamieson, Science **139**, 762 (1963).

[48] R. H. Wentorf Jr. and J. S. Kasper, Science **139**, 338 (1963).

[49] J. Wittig, Z. Phys. **195**, 215 (1966).

[50] E. Anastassakis, A. Pinczuk, E. Burstein, F. H. Pollak, and M. Cardona, Solid State Comm. **8**, 133 (1970).

[51] B. Welber, C. K. Kim, M. Cardona, and S. Rodriguez, Solid State Comm. **17**, 1021 (1975).

[52] J. Z. Hu, L. D. Merkle, C. S. Menoni, and I. L. Spain, Phys. Rev. B **34**, 4679 (1986).

[53] J. Z. Hu and I. L. Spain, Solid State Comm. **51**, 263 (1984).

[54] H. Olijnyk, S. K. Sikka, and W. B. Holzapfel, Phys. Lett. A **103**, 137 (1984).

[55] W. H. Weber and R. Merlin, *Raman Scattering in Materials Science* (Springer-Verlag, New York, 1950), p. 492.

[56] G. Weill, J. L. Mansot, G. Sagon, C. Carlone, and J. M. Besson, Semicond. Sci. Tech. **4**, 280 (1989).

[57] S. J. Duclos, Y. K. Vohra, and A. L. Ruoff, Phys. Rev. B **41**, 12021 (1990).

[58] R. J. Needs and R. Martin, Phys. Rev. B **30**, 5390 (1984).

[59] S. J. Duclos, Y. K. Vohra, and A. L. Ruoff, Phys. Rev. Lett. **58**, 775 (1987).

[60] Y. X. Zhao, F. Buehler, J. R. Sites, and I. L. Spain, Solid State Comm. **59**, 679 (1986).

[61] M. I. McMahon and R. J. Nelmes, Phys. Rev. B **47**, 8337 (1993).

[62] M. I. McMahon, R. J. Nelmes, N. G. Wright, and D. R. Allan, Phys. Rev. B **50**, 739 (1994).

[63] J. Crain, J. R. Maclean, G. J. Ackland, R. O. Piltz, P. D. Hatton, and G. S. Pawley, Phys. Rev. B **50**, 13043 (1994).

[64] R. O. Piltz, J. R. Maclean, S. J. Clark, G. J. Ackland, P. D. Hatton, and J. Crain, Phys. Rev. B **52**, 4072 (1995).

[65] B. R. Lawn and E. R. Fuller, J. Mater. Sci. **10**, 2016 (1975).

[66] B. R. Lawn and A. G. Evans, J. Mater. Sci. **12**, 2195 (1977).

[67] W. H. Gust and E. B. Royce, J. Appl. Phys. **42**, 1897 (1971).

[68] W. C. D. Cheong and L. C. Zhang, J. Mater. Sci. Lett. **19**, 439 (2000).

[69] W. C. D. Cheong and L. C. Zhang, Nanotech. **11**, 173 (2000).

[70] V. Domnich, Y. Gogotsi, and S. Dub, Appl. Phys. Lett. **76**, 2214 (2000).

[71] B. G. Pfrommer, M. Cote, S. G. Louie, and M. L. Cohen, Phys. Rev. B **56**, 6662 (1997).

[72] R. Biswas, R. Martin, R. J. Needs, and O. H. Nielsen, Phys. Rev. B **30**, 3210 (1984).

[73] N. Lehto and M. I. Heggie, *Modelling of dislocations in c-Si* (INSPEC, USA, 1998), p. 357.

[74] H. M. Zbib, M. Hiratani, and M. Shehade, *Multiscale Discrete Dislocation Dynamics Plasticity* (Wiley, USA, 2004), p. 201.

[75] A. George and J. Rabier, Rev. Phys. Appl. **22**, 941 (1987).

[76] H. R. Kolar, J. C. H. Spence, and H. Alexander, Phys. Rev. Lett. **77**, 4031 (1996).

[77] J. A. Ewing and W. Rosenhain, Phil. Trans. Roy. Soc. **193**, 353 (1900).

[78] J. P. Hirth and J. Lothe, *Theory of Dislocations* (Krieger Publishing Company, Florida, 1982), p. 857.

[79] V. Voltera, Ann. École Norm. Super **24**, 401 (1907).

[80] J. Frenkel, Z. Phys. **37**, 572 (1926).

[81] D. Hull and D. J. Bacon, *Introduction to Dislocations* (Butterworth-Heinmann, London, 2002), p. 242.

[82] E. Orowan, Z. Phys. **89**, 614 (1934).

[83] M. Polanyi, Z. Phys. **89**, 660 (1934).

[84] G. I. Taylor, Proc. Roy. Soc. **145**, 362 (1934).

[85] G. I. Taylor, Phil. Trans. Roy. Soc. **145**, 388 (1934).

[86] J. M. Burgers, Proc. Kon. Ned. Akad. Wet. **42**, 293 (1939).

[87] W. C. Dash, *The Observation of Dislocations in Silicon* (Wiley, New York, 1956), p. 57.

[88] P. B. Hirsch, R. W. Horne, and M. J. Whelan, *Direct Observations of the Arrangment and Motion of Dislocations in Aluminium* (Wiley, New York, 1956), p. 92.

[89] W. Chen, *White Beam Synchrotron X-ray Topography and micro-Raman Spectroscopy Characterization of Crystal Materials* (Dublin City University, Dublin, 2003).

[90] J. Weertman and J. R. Weertman, *Elementary Dislocation Theory* (Oxford University Press, USA, 1992).

[91] R. W. Hertzberg, *Deformation and Fracture Mechanics of Engineering Materials* (John Wiley & Sons, USA, 1996), p. 786.

[92] A. George, *Core Structures and energies of dislocations in Si* (INSPEC, USA, 1997), p. 108.

[93] University of Cambridge, [online], http://www.doitpoms.ac.uk/tlplib/dislocations/burgers.php,*Burgers Vector*, (Accessed 08/04/09).

[94] Y. Xiang, Comm. Comput. Phys. **1**, 383 (2006).

[95] F. C. Frank, Proc. Phy. Soc. **62**, 131 (1949).

[96] F. C. Frank and W. T. Read, Phys. Rev. **79**, 722 (1950).

Chapter 3 Micro-Raman Spectroscopy

3.1 Introduction

Spectroscopy can trace its history back to the 1860s with work performed by Tyndall which was then elaborated upon by Lord Rayleigh. Then in the 1920s the theories of inelastic scattering of light were presented by Raman and Smekal [2-4].

This chapter will look at the history of micro-Raman Spectroscopy (μRS) and then present the principles of μRS and how this technique can be used for stress measurement. The chapter will also look at how the probe laser spot size is determined and the formulae for determining the penetration depth of the laser.

The chapter will also examine the experimental setup used for this study.

3.2 Micro-Raman Spectroscopy

3.2.1 History

The history of the study of light scattering can be traced as far back as John Tyndall in 1868. He discovered that white light, scattered at 90° to the incident light source by fine particles, was partially polarised and slightly blue in colour. This work was followed up by Lord Rayleigh in 1899, where, by observing the scattering of light by spherical particles of relative permittivity κ suspended in a medium of relative permittivity κ_o, he derived the formula for the intensity of scattered light:

$$I_s = I\frac{9\pi^2 N d^2}{2\lambda^4 r^2}\left(\frac{\kappa\text{-}\kappa_0}{\kappa + 2\kappa_0}\right)^2 (1+\cos^2\phi) \quad (3.1)$$

where I is the intensity of the unpolarised incident light, N is the number of scattering particles of volume d, r is the distance to the point of observation, and ϕ is the angle through

which the light is scattered. This became known as Rayleigh's law and was published in 1899 in the Philosophical Magazine in an article entitled *"On the calculation of the frequency of vibration in its gravest mode, with an example from hydrodynamics"*.[1]

The phenomenon of inelastic scattering of light was then first postulated on theoretical grounds by Brillouin in 1922 and Smekal in 1923 and was observed experimentally by Raman and Krishna in 1928 [2-4]. The initial experiment consisted of a beam of sunlight filtered through a telescope and focused onto a sample of purified liquid and used the human eye as a detector. Around this time Landsberg and Mandelstam discovered a similar phenomenon in quartz. Later Raman recorded the spectra of several liquids using a mercury lamp and a spectrograph, but as the Raman effect is a weak effect, of the order of $\sim 10^{-8}$ of the intensity of the incident exciting light source, they required a 24 hour exposure [2].

It was not until the early 1960s when the laser was invented, [5,6] that there was a renaissance in Raman spectroscopy. A monochromatic coherent source was now available that allowed spectra to be easily recorded from small samples. Further advances included the fabrication of high-quality holographic gratings, improved detectors and computers.

However, it was not until 1974 that the first results of practical Raman microscopy were reported by two independent groups at the IVth International Conference on Raman Spectroscopy, namely Rosasco *et al*. [7] from the National Bureau of Standards (NBS) and Delhaye *et al*. [8] from the Laboratoire de Spectrochimie Infrarouge et Raman at Lille University. The NBS system was effective in demonstrating the capture of Raman spectra from micrometre and sub-micrometre particles but had limitations in its ease of use, particularly in sample mounting and alignment, while the Lille University group described a spectrometer based around an optical microscope which allowed single point analysis and Raman imaging/mapping [2]. This system was subsequently commercialized [3].

3.2.2 Principles of Raman Spectroscopy

When light interacts with matter it can either be absorbed or scattered. The Raman effect results from the scattering of this light. If the light is scattered elastically, i.e. it retains its incident energy, a Rayleigh peak is observed. When the light is scattered inelastically it can occur in two distinct ways: either the photon loses energy, which gives rise to Stokes scattering, or the photon gains energy, which gives rise to anti-Stokes scattering. Both of the inelastic scattering peaks are due to the Raman effect, i.e. if ω_0 is the frequency of the incident light then the inelastic scattering frequencies (ω_s) are at $\omega_0 \pm \omega_s$; see figure 3.1.

$$\omega = \omega_0 \pm \omega_s \quad (3.2)$$

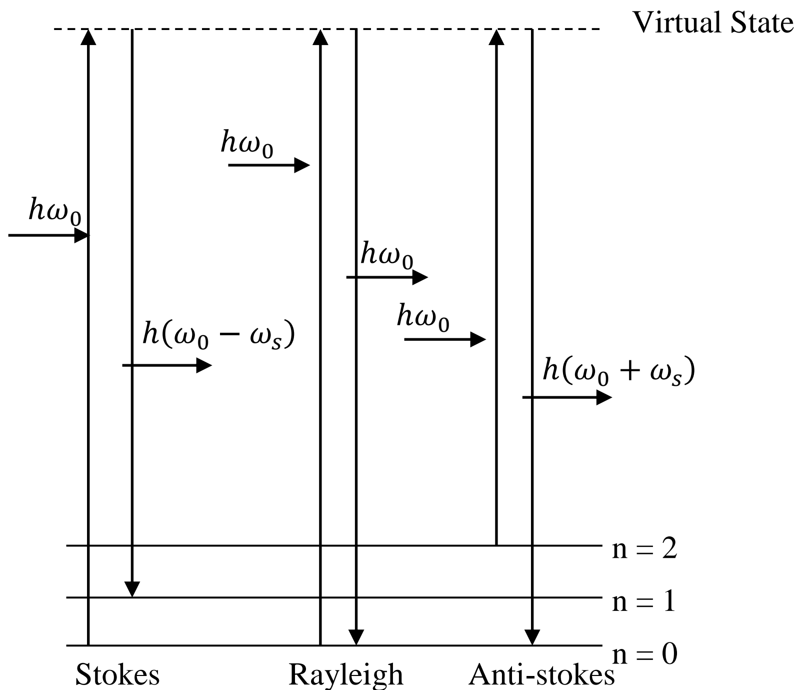

Figure 3.1: Idealised diagram of Raman and Rayleigh scattering. [2]

This scattering results from the interaction of crystalline vibrational modes (phonons) of the sample with the electromagnetic radiation [1-3]. This chapter will deal with optical phonon interactions and not acoustical phonons, this interaction leading to a low temperature spectroscopy known as Brillouin spectroscopy. An idealised scattering experiment is shown in figure 3.2.

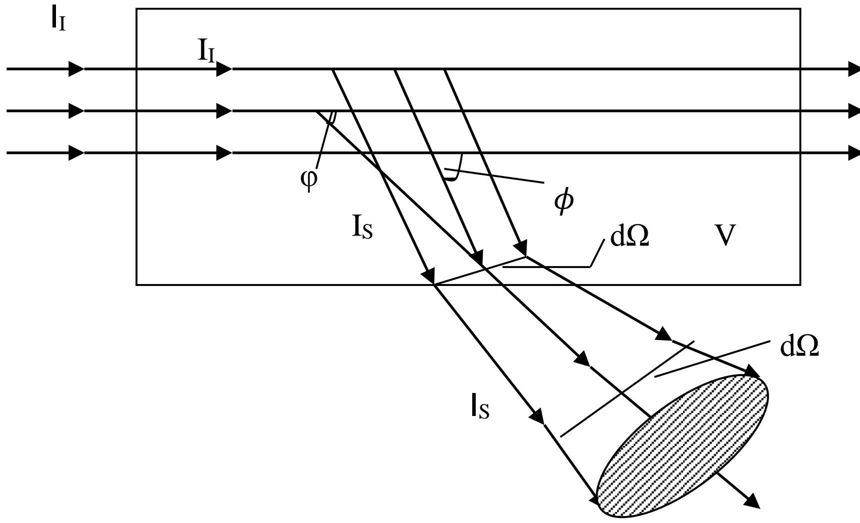

Figure 3.2. Idealised Scattering Experiment. [1]

The incident beam from a laser source, of intensity I_I, passes through a sample of volume *V* and is scattered in all directions. A detector, shown as a lens here, is set up to study the light scattered at an angle φ to the direction of the incident beam in the sample. The range of acceptance of the detector is limited to a small solid angle $d\Omega$ by the lens. I_I and I_S are the intensities of the incident and scattered beams outside the sample respectively and ϕ is the scattering angle inside the sample. As the frequency of the scattered light, ω_s, has a value in the order of 10^{12} s^{-1}, the frequency values are usually divided by the speed of light, expressed as $cm.s^{-1}$, to give a resulting quantity in wave numbers or cm^{-1}. [3]

$$\bar{v}_v = \frac{v_v}{c} = \frac{1}{\lambda} \quad (3.3)$$

The scattering process involves at least two quanta acting simultaneously in the light-matter system, while the scattering efficiency or intensity *I* is given by:

$$I = C\sum_j \left|\hat{e}_i . R_j . \hat{e}_s\right|^2 \quad (3.4)$$

C is a constant, R_j is the Raman tensor of the phonon j, $\hat{e}_j$ and $\hat{e}_s$ are the polarisation vector of the incident and scattered light, respectively. The Raman tensors for a silicon crystal with the coordinate system X=[100], Y=[010] and Z=[001] are given by [9,10]:

$$R_x = \begin{pmatrix} 0 & 0 & 0 \\ 0 & 0 & a \\ 0 & a & 0 \end{pmatrix}, R_y = \begin{pmatrix} 0 & 0 & a \\ 0 & 0 & 0 \\ a & 0 & 0 \end{pmatrix}, R_z = \begin{pmatrix} 0 & a & 0 \\ a & 0 & 0 \\ 0 & 0 & 0 \end{pmatrix} \quad (3.5)$$

The subsequent Raman effect can then be described in both classical and quantum theory. Both theories will be expanded here:

Classical theory:

The interaction of light with any material can be thought of as the interaction of the incident light upon the charges in the material. For simplicity this section concentrates on the interaction of the incident electromagnetic field upon a single molecule, as this will show the mathematical formula that defines both Rayleigh and Raman scattering.

In one dimension (1D) the effect of an electric field E on a molecule is to polarize the electron distribution. This induced moment is given by:

$$\mu = \alpha E \quad (3.6)$$

where α is the polarisability constant. A fluctuating electric field will produce a fluctuating dipole moment of the same frequency. Electromagnetic radiation produces an electric field which is expressed as:

$$E = E_0 \cos 2\pi t v_0 \quad (3.7)$$

Here E_0 is the equilibrium field strength and v_0 the frequency of vibration of the molecule. Assuming a simple harmonic motion, the internuclear distance can be written as:

$$q_v = q_0 \cos 2\pi v_v t \quad (3.8)$$

where q_0 is the amplitude of vibration. The polarisability can now be expanded in a Taylor series in q_v, where the higher order terms are neglected for small atomic displacements:

$$\alpha = \alpha^0 + \left(\frac{d\alpha}{dq_v}\right)_0 q_v + \ .... \quad (3.9)$$

Substituting Eq. (3.8) into Eq. (3.9) gives:

$$\alpha = \alpha^0 + \left(\frac{d\alpha}{dq_v}\right)_0 q_0 \cos 2\pi v_v t \quad (3.10)$$

Substituting Eq. (3.7) into Eq. (3.6) results in:

$$\mu = \alpha E_0 \cos 2\pi v_0 t \quad (3.11)$$

Now substituting Eq. (3.10) into Eq. (3.11) yields:

$$\mu = \alpha_0 E_0 \cos 2\pi v_0 t + E_0 \left(\frac{d\alpha}{dq_v}\right)_0 q_0 \cos 2\pi v_0 t \cos 2\pi v_v t \quad (3.12)$$

Rearranging Eq. (3.12) gives:

$$\mu = \alpha_0 E_0 \cos 2\pi v_0 t + E_0 \left(\frac{d\alpha}{dq_v}\right)_0 q_0 \{\cos[2\pi(v_0 \text{-} v_v)t] + \cos[2\pi(v_0 + v_v)t]\} \quad (3.13)$$

The first term of Eq. (2.13) describes Rayleigh scattering and states that the frequency of the scattered light is v_o. The second term of Eq. (3.13) describes Raman scattering with a frequency of $v_o \pm v_v$. An important note is that the second term also contains the factor $(d\alpha/dq_v)_0$, which shows that the Raman intensity not only depends on the derivative of the polarisability with respect to the molecular coordinate q_v, but also that Raman scattering can only occur when $(d\alpha/dq_v)_0 \neq 0$.

Quantum Theory:

As opposed to the classical model, the quantum theory of Raman emission assumes that the vibrational energy of a molecule or the equivalent photonic excitation is quantised according to the relationship:

$$\varepsilon = (n + ½)\hbar\omega \quad (3.14)$$

where n is the vibrational quantum number controlling the energy of the particular vibration and having values of $n = 0,1,2,3,...$ and ω is the angular frequency. Figure 3.1 shows an

idealised model of both Raman and Rayleigh scattering where the atom is excited to a virtual energy level by an incoming photon. In these processes the crystal is initially in an electronic ground state. The incoming photon (ω_o) is absorbed causing the excitation of an electron-hole pair leading to the creation of an optical phonon (ω) and a scattered photon (ω_s), fig. 3.3.

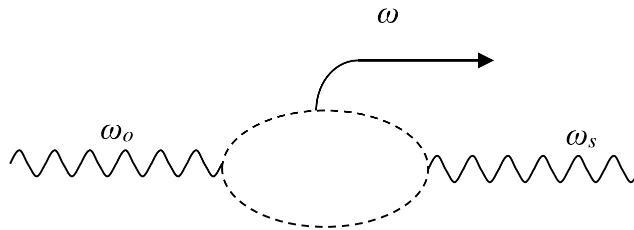

Fig. 3.3. Raman scattering process [12]

The transition time from the electronic ground state to the virtual intermediate state and back again occurs quickly, in the order of 10^{-12} s for Stokes scattering and 10^{-9} s for anti-Stokes scattered radiation. [3,4,11,12]

In figure 2.1 it can also be seen that the Stokes scattering arises from transitions that start at the ground vibrational level ($n = 0$) while anti-Stokes scattering arises from a vibrationally excited state. Since at room temperature, the majority of electrons are in the ground vibrational state, the majority of the Raman scattering will be Stokes scattering [2,4]. The ratio of intensity of Stokes to anti-Stokes scattering is dependent on the number of molecules in the ground and excited vibrational states and can be calculated from Boltzmann's equation [4]:

$$\frac{N_n}{N_m} = \frac{g_n}{g_m} \exp\left[\frac{-(E_n - E_m)}{k_B T}\right] \quad (3.15)$$

where N_n is the number of molecules in the excited vibrational level (n), N_m is the number of molecules in the ground vibrational level (m), and E_n-E_m is the difference in energy between the vibrational energy levels. g is the degeneracy of the levels n and m and occurs because some vibrations can occur in more than one way due to the symmetry of vibrations. As the

energies are the same the individual components cannot be separately identified. The Boltzmann distribution has to take into account all possible vibrational states and g corrects for this. This can then be used to give the relative strengths of the anti-Stokes to Stokes lines [13]:

$$\frac{I_{AS}}{I_S} = e^{\frac{\hbar\Omega}{k_B T}} \quad (3.16)$$

where I_{AS} is the intensity of the anti-Stokes line, I_S is the intensity of the Stokes line, k_B is Boltzmann's constant, T is the temperature, $\hbar$ is Dirac's constant and Ω is the phonon frequency.

3.2.3 Polarisability and Symmetry

When linearly polarised light is incident on a molecule, the electron cloud is distorted by an amount that is related to the ability of the electrons to polarise with respect to the positively charged nucleus. This is defined in Eq. (3.6). However, although the polarised light is in one plane, the effect on the electron cloud is three dimensional in each of the three Cartesian coordinates x, y and z. To allow for this the polarisability components of a molecule are normally labelled as:

$$\alpha_{ij} \quad (3.17)$$

The first index i denotes the direction of the polarisability of the molecule and the second index j refers to the polarisation direction of the incident light [2,4,14]. This allows for Eq. (3.6) to be expanded to take into account the three Cartesian planes and results in:

$$\mu_x = \alpha_{xx}E_x + \alpha_{xy}E_y + \alpha_{xz}E_z \quad (3.18)$$

$$\mu_y = \alpha_{yx}E_x + \alpha_{yy}E_y + \alpha_{yz}E_z \quad (3.19)$$

$$\mu_z = \alpha_{zx}E_x + \alpha_{zy}E_y + \alpha_{zz}E_z \quad (3.20)$$

Eq. (3.18) to Eq. (3.20) can then be written in matrix form giving:

$$\begin{pmatrix}\mu_x\\ \mu_y\\ \mu_z\end{pmatrix} = \begin{pmatrix}\alpha_{xx} & \alpha_{xy} & \alpha_{xz}\\ \alpha_{yx} & \alpha_{yy} & \alpha_{yz}\\ \alpha_{zx} & \alpha_{zy} & \alpha_{zz}\end{pmatrix}\begin{pmatrix}E_x\\ E_y\\ E_z\end{pmatrix} \quad (3.21)$$

If a crystal possesses a Centre of Symmetry then it follows the Mutual Exclusion Rule. This rule states that any vibrations that are Raman active (symmetric, *g*) will not be infra-red active and any vibrations that are infra-red active (anti-symmetric, *u*) will not be Raman active. As Silicon possesses a Centre of Inversion Symmetry, it is Raman active. [3,11]

3.3 Principle of Stress Measurement

Micro-Raman spectroscopy is a technique, used in the semiconductor industry and others, where the light of the exciting laser is typically focused on the sample through a microscope lens, allowing for analysis of samples with micron spatial resolution [15]. Micro-Raman Spectroscopy is used for the non-destructive study of mechanical stresses in silicon as any stress or strain will affect the frequencies of the Raman bands and lift their degeneracies [9,10,16-25].

In the absence of strain, the first order Stokes Raman spectrum of silicon shows a peak which corresponds to the triply degenerate Transverse Optical (TO) phonon and has a wave number shift, with respect to the excitation light source, of ~ 520 cm^{-1}; Figure 3.4.

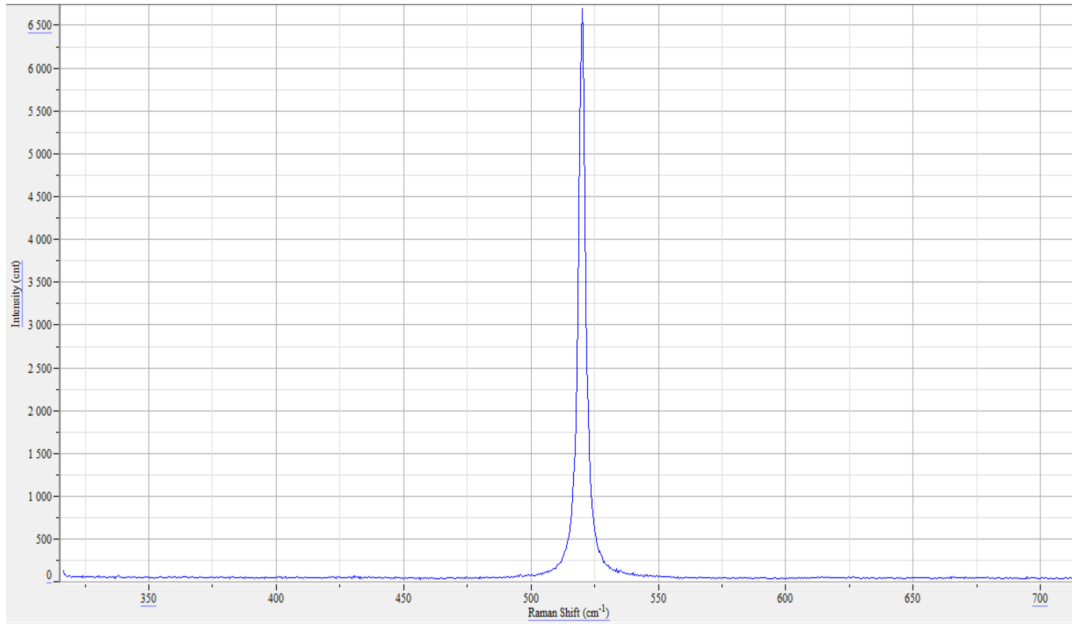

Figure 3.4: Raman Spectrum of unstrained Silicon showing triply degenerate TO phonon at 520.053 cm^{-1}.

The effect of strain on the crystal lattice can be explained by considering the lattice structure as a regular lattice of atoms connected to each other by 'springs', fig 3.5.

These 'springs' have a fundamental frequency of vibration or spring constant. Any strain or deformation of the lattice, such as that due to nano-indentation, causes the 'springs' to either elongate or contract.

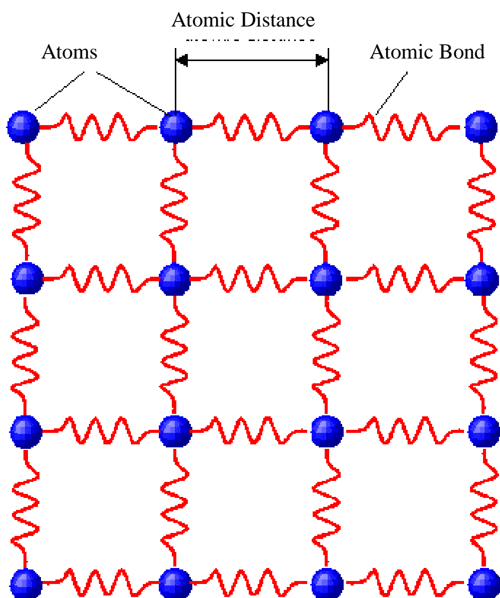

Fig. 3.5: Depiction of a crystal lattice structure with the interatomic bonds visualised as springs. Image courtesy of Prof. P. McNally

This induces a change in the normal modes of vibration, i.e. the phonon modes in a crystalline semiconductor, thus leading to changes in the frequencies.

The Raman shifts in the presence of strain can be obtained by solving the following secular equation [19]:

$$\begin{vmatrix} p\varepsilon_{11} + q(\varepsilon_{22} + \varepsilon_{33}) - \lambda & 2r\varepsilon_{12} & 2r\varepsilon_{13} \\ 2r\varepsilon_{12} & p\varepsilon_{22} + q(\varepsilon_{33} + \varepsilon_{11}) - \lambda & 2r\varepsilon_{23} \\ 2r\varepsilon_{13} & 2r\varepsilon_{23} & p\varepsilon_{33} + q(\varepsilon_{11} + \varepsilon_{22}) - \lambda \end{vmatrix} = 0 \quad (3.22)$$

$$\lambda_j = \omega^2 - \omega_0^2 \quad (3.23)$$

Rearranging Eq. (3.23) gives:

$$\lambda_j = (\omega+\omega_0)(\omega-\omega_0) \quad (3.24)$$

As ω is usually very close to ω_0, Eq. (3.24) becomes:

$$\lambda_j = 2\omega_0(\omega - \omega_0) \text{ or } \Delta\omega = \frac{\lambda_j}{2\omega_0} \quad (3.25)$$

In Eq. (3.22) p, q and r are the phonon deformation potentials, which describe the changes in the 'spring constant' of the triply degenerate optical phonon with strain and ε_{ij} are the strain tensor components. These can be determined experimentally by applying external stress to a sample. By calculating the eigenvalues λ_j $(j=1, 2, 3)$, the Raman frequency shift in the presence of stress (ω) relative to the absence of stress (ω_0) can be calculated from Eq. (3.23) and Eq. (3.24) [10]. To calculate the impact of a uniaxial stress along a [100] plane, the strain tensor components are calculated using Hooke's law. This gives $\varepsilon_{11} = S_{11}\sigma$ and $\varepsilon_{22} = \varepsilon_{33} = S_{12}\sigma$, where S_{ij} are the elastic compliance tensor elements of silicon [10]. Solving Eq. (3.22) and Eq. (3.25) gives:

$$\Delta\omega_1 = \frac{\lambda_1}{2\omega_0} = \frac{1}{2\omega_0}[pS_{11} + 2qS_{12}]\sigma \quad (3.26)$$

$$\Delta\omega_2 = \frac{\lambda_2}{2\omega_0} = \frac{1}{2\omega_0}[pS_{12} + q(S_{11} + S_{12})]\sigma \quad (3.27)$$

$$\Delta\omega_3 = \frac{\lambda_3}{2\omega_0} = \frac{1}{2\omega_0}[pS_{12} + q(S_{11} + S_{12})]\sigma \quad (3.28)$$

For backscattering from a [001] plane, it can be shown from eqn. (3.4) and eqn. (3.5), that only the third Raman mode is observed [10,26] and the relation between the shift of this mode and stress is given by Eq. (3.28). Using figures developed by Anastassakis *et al.* S_{11} = 76.8x10^{-14} cm^2/dyne = 7.68x10^{-12} Pa^{-1}, S_{12} = -21.4x10^{-14} cm^2/dyne = -2.14x10^{-12} Pa^{-1}, p = -1.43ω_0^2, q = -1.89ω_0^2 [27] and taking the Raman peak of unstressed silicon as ω_0 = 520 cm^{-1} [10] it can be seen that:

$$\Delta\omega_3 = -2x10^{-9}\,\sigma\ (\text{Pa}) \qquad (3.28)$$

In the case of biaxial strain in the X - Y plane, the stress components are σ_{xx} and σ_{yy}, and Eq. (3.28) becomes:

$$\Delta\omega_3 = -4x10^{-9}\left(\frac{\sigma_{xx}+\sigma_{yy}}{2}\right)(\text{Pa}) \qquad (3.29)$$

Assuming $\sigma_{xx} = \sigma_{yy}$ Eq. (3.29) can be rewritten as:

$$\sigma_{xx} = \sigma_{yy} = \frac{\Delta\omega}{-4}\,\text{GPa} \qquad (3.30)$$

where $\Delta\omega$ is expressed in units of cm^{-1}. This shows that both uniaxial and biaxial compressive stress will result in an increase of the Raman frequency (i.e. a blue shift) and tensile stress will result in a decrease (i.e. a red shift).

3.4 Experimental Setup

As mentioned earlier in this dissertation, the µRS system used is a Horiba-Jobin Yvon LabRam® HR800 system employing manufacturer supplied Labspec® 5 software. It is a single monochromator spectrometer wherein the incident monochromatic laser beam is reflected by a beam splitter and a flip mirror into a microscope objective. Figure 3.6 shows the beam setup for the system used.

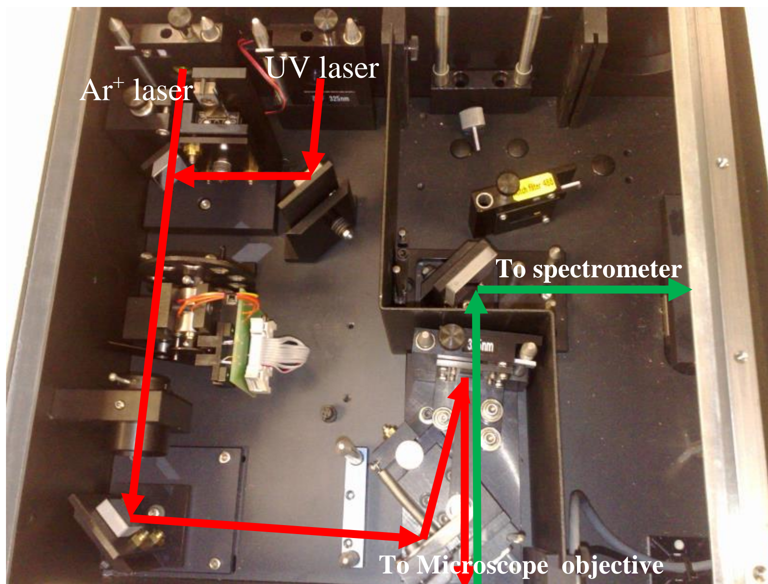

Figure 3.6: Internal setup for LabRam® HR800 System.

The red line shows the path of the laser beam, while the green line shows the path of the Raman scattered beam. The microscope objective is used to focus the probe beam onto the sample surface and is equipped with a number of lenses allowing different optical magnifications and spot sizes; Figure 3.7. The lenses available are x10, x50 and x100 for the Ar^+ laser and x40 for the UV laser.

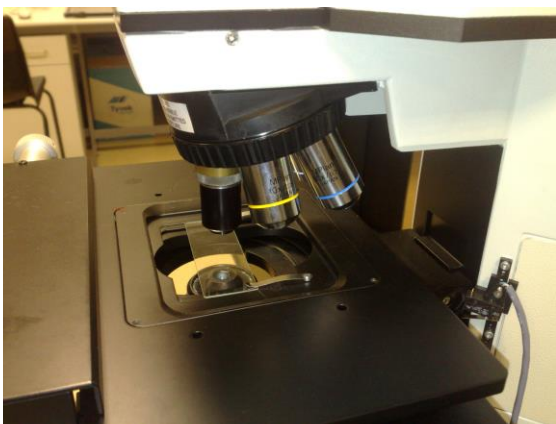

Figure 3.7: Microscope lenses attached to the LabRam® HR800 System.

The scattered light is collected through the same objective using backscattering geometry. This then passes through a beam splitter and is focused onto the entrance slit of the

spectrometer that disperses the light onto a Charge-coupled Device (CCD) detector. For the LabRam® HR800 this detector is cooled with liquid Nitrogen (N_2) and kept at 77K. The spectrum is analysed by the host PC using the Labspec® 5 software. The use of a flip mirror enables the specimen under the microscope objective to be visualised using a TV camera. An advantage of this system is that the laser spot can be directly observed by the camera allowing precise positioning of the laser beam onto the area of interest.

In this study each Raman spectrum was acquired as three accumulations of 10s each. A grating of 2,400 grooves/mm was used with the exciting laser source being focused through an Olympus® 100x microscope objective for the 488 nm Ar^+ laser and an OFR® Near Ultraviolet (NUV) 40x lens for the 325 nm He-Cd laser. Holographic edge and notch filters reject the Rayleigh light and an interference filter rejects the plasma lines of the laser.

The LabRam HR800 uses a confocal technique at the entrance to the microscope objective. Figure 3.8 shows a schematic of this arrangement.

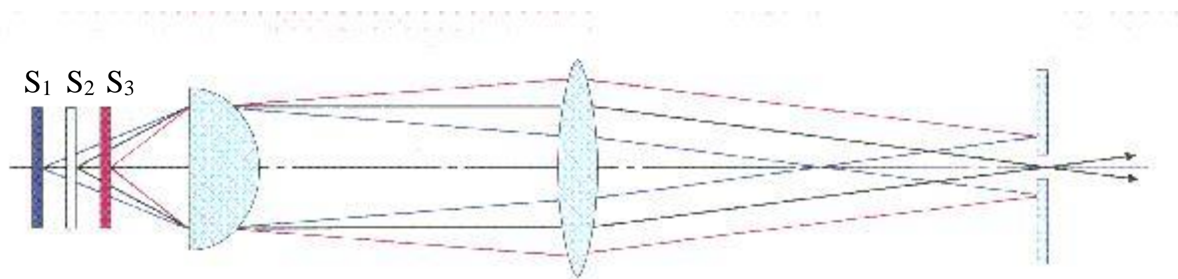

Figure 3.8: Schematic of the confocal optics for the LabRam HR800 [28]

The principle of confocal imaging was first patented by Marvin Minsky in 1961 [28]. The system allows the rejection of radiation that originates away from the focal point conjugate to the confocal aperture. The radiation from the S_1 and S_3 planes (coloured Blue and Red here) do not pass through the aperture as they are not focused in the confocal plane. The only radiation to pass through the aperture is from S_2. This means that Raman radiation originating

away from the sample depth of interest never reaches the entrance to the spectrometer and the Raman spectrum observed is specific to the depth of the sample in focus. As previously mentioned, for Si, this depth is ~ 569 nm for the Ar^+ laser and ~9 nm for the He-Cd UV laser. The LabRam® HR800 allows for software control of the confocal pinhole diameter and has pinholes of 50 μm, 100 μm, 150 μm and 200 μm diameters.

3.5 Spatial Resolution and Spot Size

In applications where a μRS setup is being used for microanalysis it is important to know the spatial resolution of the Raman map. For a Raman system this resolution depends on the focused beam diameter or spot size.

For light of wavelength λ passing through a lens of focal length F and diameter D, the diameter of the minimum size spot, d, which can be formed is [13]:

$$d \approx 1.22\frac{F\lambda}{D} \quad (3.31)$$

F/D can be expressed as an f-number; the f-number of a lens can be expressed as:

$$f\# = \frac{1}{2N.A.} \quad (3.32)$$

where *N.A.* is the Numerical Aperture of the lens. Combining Eq. (3.31) and Eq. (3.32) we get the Rayleigh Criterion for microscope lenses:

$$d \approx \frac{1.22\lambda}{2N.A.} \quad (3.33)$$

Eq. 2.33 now allows for the calculation of the minimum spot size achievable, ignoring the diffraction limit. For the Ar^+ laser with wavelength $\lambda = 488\ nm$, focused through the 100x lens, this lens has a N.A. = 0.90 and Eq. (3.33) yields a theoretical minimum achievable spot size of 0.33 μm. Eq. (3.33) would suggest that the use of a light source with a shorter wavelength should decrease the spot size and increase the spatial resolution of the μRS. However, in practice this is not the case due to the lack of near ultraviolet (NUV) objectives

with high N.A. The He-Cd laser has a wavelength λ = *325 nm* and is focused through a 40x NUV lens with a N.A. of 0.65 which yields a theoretical minimum spot size of 0.305 µm.

In reality these are ideal values and in practice the focal point of the exciting beam is limited by aberration defects and by the diffraction limit. It is more realistic to consider the focal region to be cylindrical as shown in figure 3.9 [2].

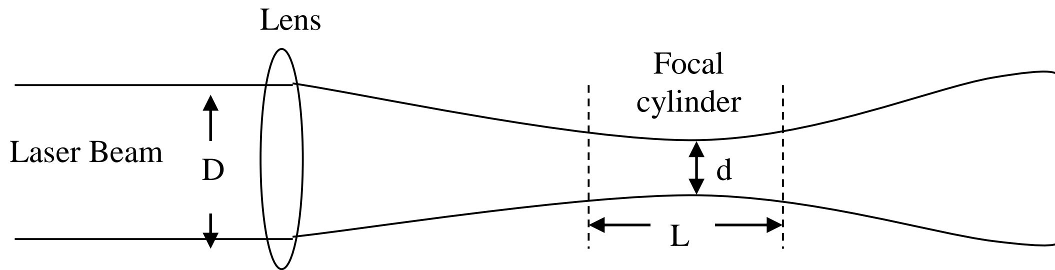

Fig. 3.9: Focusing of a laser beam

The diameter of this focal cylinder is given by [2,29]:

$$d = \frac{4\lambda f}{\pi D} \quad (3.34)$$

where λ is the wavelength of the incident light, f is the focal length of the lens and D is the diameter of the laser beam. The values for f, and D are obtained from the manufacturers' specification sheets. For the Ar^+ laser focused through an Olympus® Mplan 100x lens, $f = 1.8$ *mm* and $D = 0.7$ *mm*. For the UV laser focused through an OFR® Near Ultraviolet (NUV) lens, $f = 2$ *mm* and $D = 1$ *mm*. This gives an effective spot size of ~1 µm for the Ar^+ laser and 0.8 µm for the UV laser.

3.6 Penetration Depth of Laser in Silicon

When light passes through silicon its intensity decreases due to photoelectric absorption of the material. When passing through Silicon to a depth d the intensity can be defined as [13]:

$$I_d = I_i e^{-\alpha d} \quad (3.35)$$

where I_d is the intensity at the depth d, I_i is the incident intensity and α is the absorption coefficient of the material at a specific wavelength. The penetration depth is then defined as the distance over which the intensity of the incident light has dropped to *1/e* of its original intensity.

$$\frac{I_d}{I_0} = \frac{1}{e} \quad (3.36)$$

This now gives a penetration depth d_p as:

$$d_p = \frac{1}{\alpha} \quad (3.37)$$

The value of α can be found in the literature [10,13,30].

Takahashi *et al.* [31] and deWolf *et al.* [10] take a more rigorous approach to calculating the intensity at depth. The total scattered light intensity integrated from the surface to a depth d, can be expressed as:

$$I_s = I_0 R \int_0^d e^{-2\alpha x}\, dx = \left(\frac{I_0 R}{2\alpha}\right) [1 - e^{-2\alpha d}] \quad (3.38)$$

where I_0 is the incident light intensity and R is the Raman scattering cross section. The scattered light intensity from d to infinity is then given by:

$$I_d = I_0 R \int_d^{\infty} e^{-2\alpha x}\, dx = \left(\frac{I_0 R}{2\alpha}\right) [e^{-2\alpha d}] \quad (3.39)$$

From the data supplied by deWolf and Takahashi it can be seen that as the wavelength of the incident light decreases, so the photoabsorption coefficient increases and therefore the penetration depth of the laser becomes shallower. If we are then to assume that the penetration depth d_p of a specific laser is defined as the depth d at which the following relationship is satisfied:

$$\frac{I_d}{I_s + I_d} = 0.1 \quad (3.40)$$

By substituting Eq. (3.38) and Eq. (3.39) into Eq. (3.40) the penetration depth becomes:

$$d_p = \frac{-\ln 0.1}{2\alpha} = \frac{2.3}{2\alpha} \quad (3.41)$$

Eq. (3.41) is the equation that has been used to calculate the penetration depth in this study. Using data from Aspnes *et al*. [30], for the relevant α values, one arrives at a penetration depth in Si of 556 nm for the Ar^{+} laser and 9.33 nm for the UV laser.

3.7 Summary

This chapter discussed the theory and operation of the micro-Raman spectrometer, in particular the LabRam® HR800 used in this study. The chapter also dealt with the principle behind Si stress measurments using μRS, laser spot size estimation and the penetration depths of the probe laser beams of different wavelengths.

3.8 References

[1] W. Hayes and R. Loudon, *Scattering of Light by Crystals* (Wiley-Interscience, USA, 1978), p. 360.

[2] D. J. Gardiner and P. R. Graves, *Practical Raman Spectroscopy* (Springer-Verlag, Berlin, 1989), p. 157.

[3] G. Turrell and J. Corset, *Raman Microscopy : Developments and Applications* (Academic Press, New York, NY ; London, 1996), p. 463.

[4] E. Smith and G. Dent, *Modern Raman Spectroscopy - A Practical Approach* (John Wiley & Sons Ltd., England, 2005), p. 210.

[5] A. L. Schawlow and C. H. Townes, Phys. Rev. **112**, 1940 (1958).

[6] T. H. Maiman, Nat. **187**, 493 (1960).

[7] G. J. Rosasco, E. S. Etz, and W. A. Cassatt, *Investigation of the Raman Spectra of Individual Micron Sized Particles* (Int. Conf. Raman Spec., 1974).

[8] M. Delhaye and P. Dhamelincourt, *Laser microprobe and microscope* (Int. Conf. Raman Spec., 1974).

[9] Y. Kang, Y. Qiu, Z. Lei, and M. Hu, Opt. Las. in Eng. **43**, 847 (2005).

[10] I. De Wolf, Semicond. Sci. Tech. **11**, 139 (1996).

[11] W. H. Weber and R. Merlin, *Raman Scattering in Materials Science* (Springer-Verlag, New York, 1950), p. 492.

[12] R. Loudon, Adv. Phy. **50**, 813 (2001).

[13] S. Perkowitz, *Optical Characterization of Semiconductors; Infrared, Raman and Photoluminescence Spectroscopy*, edited by N. H. March (Academic Press, London, 1993), p. 213.

[14] G. S. Smith, E. B. Tadmore, and E. Kaxiras, Phys. Rev. Lett. **84**, 1260 (2000).

[15] M. J. Pelletier, *Analytical applications of Raman spectroscopy* (Wiley-Blackwell, 1999), p. 478.

[16] Y. Gogotsi, C. Baek, and F. Kirscht, Semicond. Sci. Tech. **14**, 936 (1999).

[17] E. Anastassakis, A. Cantarero, and M. Cardona, Phys. Rev. B **41**, 7529 (1990).

[18] J. Chen and I. De Wolf, IEEE Transactions on Components and Packaging Technologies, **28**, 484 (2005).

[19] I. De Wolf, J. Raman Spec. **30**, 877 (1999).

[20] I. De Wolf, G. Pozzat, K. Pinardi, D. J. Howard, M. Ignat, S. C. Jain, and H. E. Maes, Microelectron. Rel. **36**, 1751 (1996).

[21] K. F. Dombrowski, B. Dietrich, I. De Wolf, R. Rooyackers, and G. Badenes, Microelectron. Rel. **41**, 511 (2001).

[22] T. Wermelinger, C. Borgia, C. Solenthaler, and R. Spolenak, Acta Mater. **55**, 4657 (2007).

[23] J. Zi, H. Buscher, C. Falter, W. Ludwig, K. Zhang, and X. Xie, Appl. Phys. Lett. **69**, 200 (1996).

[24] S. J. Harris, A. E. O'Neill, W. Yang, P. Gustafson, J. Boileau, W. H. Weber, B. Majumdar, and S. Ghosh, J. Appl. Phys. **96**, 7195 (2004).

[25] E. Bonera, M. Fanciulli, and D. N. Batchelder, Appl. Phys. Lett. **81**, 3377 (2002).

[26] I. De Wolf, H. E. Maes, and S. K. Jones, J. Appl. Phys. **79**, 7148 (1996).

[27] E. Anastassakis, A. Pinczuk, E. Burstein, F. H. Pollak, and M. Cardona, Solid State Comm. **8**, 133 (1970).

[28] M. Minsky, *Microscopy Apparatus* (G02B21/00; G02B21/00, Mass./USA, 1961), US19570695107 19571107.

[29] J. J. Barrett and N. I. Adams, J. Opt. Soc. Am. **58**, 311 (1968).

[30] D. E. Aspnes and A. A. Studna, Phys. Rev. B **27**, 985 (1983).

[31] J. Takahashi and T. Makino, J. Appl. Phys. **63**, 87 (1988).

Chapter 4 White Beam Synchrotron X-Ray Topography

4.1 Introduction

White Beam Synchrotron X-ray topography is a non-destructive characterisation method for the analysis of defects and strain in bulk silicon. Every diffraction vector $\boldsymbol{g}$, which satisfies Bragg's law, will result in a topograph. By comparison of several topographs the Burgers vector $\boldsymbol{b}$ of dislocation can be obtained by the invisibility criterion as given by the equation [1]:

$$b \cdot g = 0 \qquad (4.1)$$

This chapter will deal with the history of topography, the main theoretical approaches the kinematical and dynamical theories and will detail the setup used at the synchrotron facilities at ANKA, Karlsruhe, Germany.

4.2 X-Ray Topography

4.2.1 History of X-ray Topography

X-ray topography can trace its origins back to 1895 when W. Röntgen, working with a 'Crookes tube' wrapped in heavy black paper, noticed that the tube was causing a platinobarium tube 2.5 metres away to glow. He concluded that the tube must be emitting an invisible ray and further experimentation showed that this x-ray, called such as 'x' stands for an unknown in mathematics, would penetrate most substances including the soft tissue of the human body [2].

Work continued on studying these new Röntgen rays and in 1905 and then again in 1906 Barkla released two innovative papers detailing experiments into polarisation of x-rays [3,4].

This was followed up by Barkla and Sadler in 1909 with work on characteristic radiation for which Barkla won a Nobel prize in 1917 [5,6].

However it was not until 1912, after a conversation between Ewald and von Laue [7] that von Laue started to think about lattice spectra; this resulted in Friedrich, Knipping and von Laue producing a paper '*Interferenz-Erscheinungen bei Röntgenstrahlungen*' in Proceedings of Akademie der Wissenschafften, Munich, where they obtained x-ray diffraction patterns of rock salt and the study of materials by diffraction started to take place [8]. This was advanced in 1913 when father and son W.H. and W.L. Bragg, using perhaps the world's first x-ray spectrometer, took reflections of x-rays of crystals and concluded that they were the reflections of the x-rays on families of lattice planes [9,10]. This also led to a simple and useful description of crystal diffraction, namely Bragg's law [11] which states that

$$n\lambda = 2d\sin\theta \qquad (4.2)$$

where n is an integer representing the order of diffraction, λ is the x-ray wavelength, d the interplanar spacing of the diffracting plane and θ is the angle of incidence and diffraction of the radiation relative to the reflecting plane fig. 4.1.

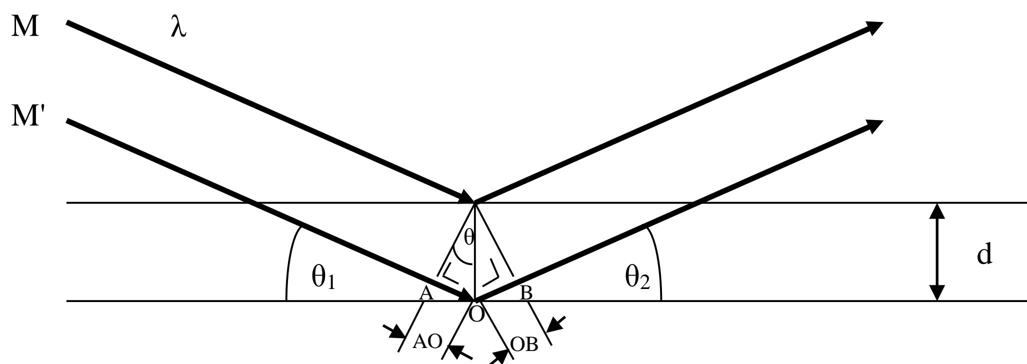

Figure 4.1. Schematic diagram of Bragg's Law $n\lambda=2d\sin\theta$. Constructive interference leading to strong diffraction only occurs when $\theta_1 = \theta_2$ and the extra path length AOB,travelled by parallel x-ray beam, *M'*, with respect to the x-ray beam, *M*, equals $n\lambda$

X-ray topography is a non-destructive, non-invasive technique of diffraction imaging based on Bragg's Law that is capable of providing information on the character and distribution of crystallographic defects [12]. It traces its origins back to early work performed by Berg [13] and then by Barrett [14]. This produced the Berg-Barrett X-ray extinction contrast method of dislocation observation, the simplest high resolution technique for laboratory use [8,15,16]. This was then followed up by Ramachandran in 1944 [17] and Guinier and Tennevin in 1949 [18] where white x-ray beams were first used. In 1958 Lang produced a method for observing dislocations via transmission mode and then in 1959 he produced a method for section topography [19].

4.2.2 Synchrotron X-ray topography

Synchrotron x-rays were first observed in the late 1940's when a group of scientists working for General Electric built the world's first 70MeV synchrotron [20-23], where it was noticed that high energy electrons which are subjected to large accelerations normal to their velocity would radiate electromagnetic energy, this energy being emitted in a narrow cone tangential to the electron orbit with a spectrum that would extend into the visible range, the theory of which would be developed by Schwinger in 1949 [24].

In 1974 a paper by Tuomi *et al*. [25] showed how synchrotron radiation could be utilised to produce x-ray topographs, a process which was confirmed a year later by Hart [26].

4.3 Production of Synchrotron X-rays

According to classical electrodynamics, every charged particle in an accelerated motion emits electromagnetic radiation [21,25,27,28]. Synchrotron radiation occurs when these particles are confined to a circular orbit at relativistic speeds [6,8]. The charged particles are kept in this orbit by the use of a magnetic field, B, perpendicular to the plane of the orbit. In order to achieve this, the Lorentz force applied to the particles travelling at relativistic speeds

$$F = ecB \qquad (4.3)$$

must equal the centripetal force experienced by the particles in their orbit [29],

$$F = \frac{mc^2}{R} \qquad (4.4)$$

Equating eqn. (4.3) and (4.4) the applied magnetic field is expressed as

$$B = \frac{mc}{Re}\gamma \qquad (4.5)$$

where e is the charge on the particle, m the rest mass of the particle, R the radius of the orbit, c the speed of light and γ is the maximum obtainable energy in the synchrotron [27].

As the particle is travelling at relativistic speeds the radiation emitted is perpendicular to the orbital plane and is folded into a cone with an opening angle of [8,30,31], see fig. 4.2 and 4.3.

$$\theta = \frac{mc^2}{E} \qquad (4.7)$$

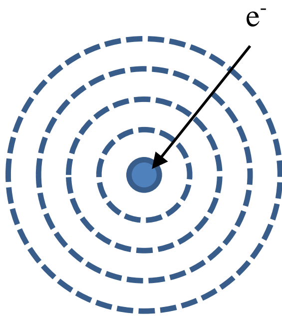

Figure 4.2: Radiation emission from a relativistic particle from the inertial reference frame of the electron [8]

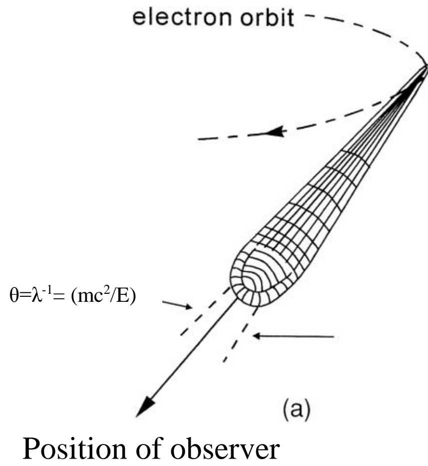

Fig. 4.3: Radiation emission viewed in the rest frame of the observer [8]

To calculate the power radiated, we use Larmor's formula for the power radiated from a single non-relativistic accelerating particle [31],

$$P = \frac{2e^2}{3c^3} a^2 \qquad (4.8)$$

where *a* is the acceleration that must be expended to take account of relativistic motion. For this eqn. 4.8 becomes [24,31,32]:

$$P = \frac{2e^2 c}{r^2} \beta^4 \gamma^4 \qquad (4.9)$$

where *r* is the radius of curvature and *β* is the normalised velocity of the particle given by:

$$\beta = \frac{v}{c} \qquad (4.10)$$

This derivation is covered in Schwinger's 1949 paper "*On the Classical Radiation of Accelerated Particles*" referenced herein [24].

One consequence of this is that as the mass of the charged particle increases the radiated power decreases, and for this reason synchrotron facilities use electrons or positrons as their injected particles [6]. The ANKA facility (Karlsruhe, Germany) uses electrons [33] while the DORIS III facility at HASYLAB (Hamburg, Germany) used positrons [34].

4.3.1 Operation of a Synchrotron Facility

The basic components of a synchrotron facility are the injector and the storage ring; figure 3.4 shows a schematic of the ANKA synchrotron. Charged particles from an electron gun, with an energy of 70keV are injected into a microtron race track, this comprises a 5.2MV linac through which the particles pass 10 times, thus boosting the particles to an energy of ~50MeV [33].

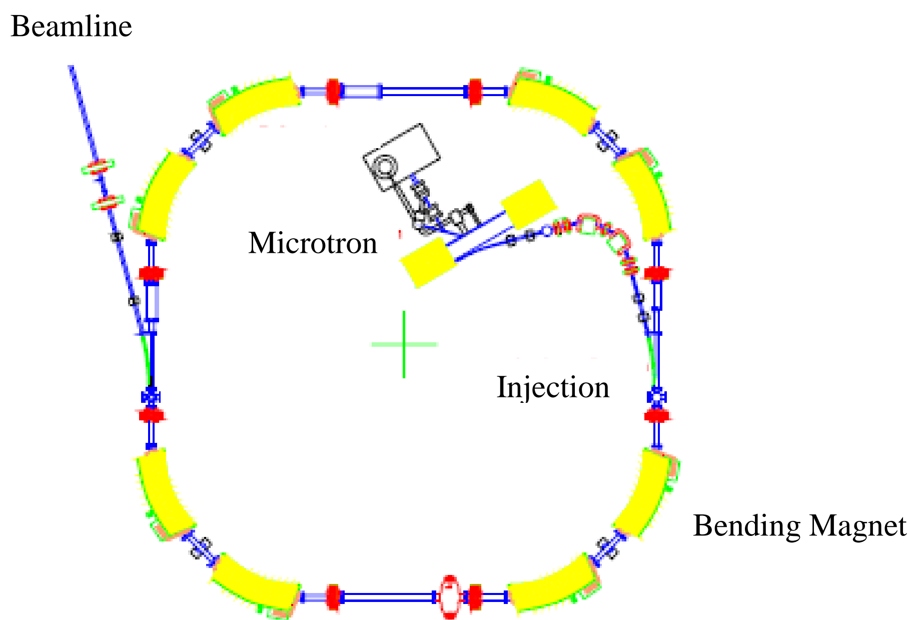

Figure 4.4: Schematic of storage ring at the ANKA facility

The charged particles are then injected into the storage ring. The ring itself consists of dipole bending magnets separated by straight sections in which the injectors are situated. Each injector consists of rows of magnets with alternating polarity installed in the straight sections of the ring. There are two main types of magnet, namely wigglers and undulators [31]. The wiggler magnets enhance the flux and brightness of the radiation by a factor approximately

equalling the number of poles. The undulators, which produce a quasi-monochromatic beam of radiation, are effectively tuneable [8,30,31].

The storage ring needs to be held at a high vacuum, typically 10^{-9} mbar. This high vacuum ensures that collisions between the charged particles and gas atoms are rare and gives approximately 10 hours of continuous operation before re-injection is required [30,31,33,34]. A third type of magnet, the bending magnet, is used in the storage ring itself and allows the particles to run in a circular path, and it is at these magnets that the topographic beamlines are installed [6].

4.4 X-ray Scattering Theories

X-ray scattering theory falls into two main theories. The kinematical theory is the simplest of the theories where a negligible amount of energy transference to the diffracted beam is assumed, and is accurate for weak scattering, i.e. thin crystals, surface scattering and diffuse scattering. The dynamical theory is employed when there is strong scattering, i.e. the diffracted intensities and rocking curves of near perfect crystals.

4.4.1 Kinematical Theory

The kinematical theory assumes that each atom scatters a fraction of the optical wave that passes over it and so now becomes a spherical wave source with double and multiple scattering being neglected. This assumption seems to be justified at first but the biggest problem with the theory is that it violates the law of conservation of energy, as the secondary waves appear from nowhere because the primary beam is assumed to be undiminished by its passage through the crystal [35].

This problem was noted by Darwin in 1914 [36] where, although he ignored the possibility of constructive interference of wavelets, he did note that the measured reflected intensity over the Bragg angle was approximately 10 times greater than what could be expected from pure

kinematical theory. This, he assumed was due to the fact that an imperfect crystal, composed of slightly misorientated crystalline sub-units, would give stronger reflections than a perfect crystal. In this case the primary beam would be weakened from sub-unit to sub-unit as the primary beam is deflected from its original direction.

In any discussions on kinematical theory the first quantity that needs to be considered is the structure factor, F_{hkl}, and the assumptions made to form this quantity; for a full derivation of the structure factor see Wallwork [37]. This fundamental quantity is calculated as follows: Waves with wave vector $\boldsymbol{k}$ scattered from two points in a unit cell separated by a vector $\boldsymbol{r}$ (fig. 3.5) will have the following phase difference [8,38]

$$e^{-2\pi j k\cdot r} = e^{-2\pi j(hu+kv+lw)} \qquad (4.11)$$

where u,v and w are the fractional coordinates within the unit cell of the vector $\boldsymbol{r}$ for an atom of type i and h,k and l are the Bravais-Miller indices.

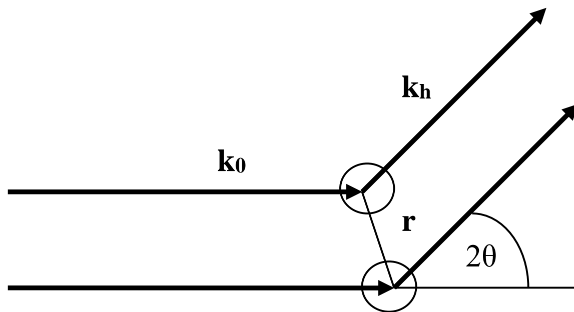

Figure 4.5: Waves with wave vectors $\boldsymbol{k_0}$ and $\boldsymbol{k_h}$, representing the incident and diffracted beams respectively, are scattered by two points on a unit cell which are separated by a vector $\boldsymbol{r}$.[8]

When waves scattered by all the atoms over a unit cell are summed up Eqn. 3.11 becomes

$$F_{hkl} = \sum_i f_i e^{-2\pi j(hu+kv+lw)} \qquad (4.12)$$

The assumptions made for eqn. 4.12 are:

1. The scattered intensity is very small with no or negligible loss of intensity due to re-scattering and the refractive index is unity.

2. The observation point is at a very large distance compared with the dimensions of the scattering volume.
3. Scattered waves from different atoms, labelled $\boldsymbol{k_h}$, are parallel.

If the assumption is taken that there is a continuous distribution of diffracting centres, then eqn. 4.12 must be adjusted to take this into account and becomes

$$F_{hkl} = \int_{-\infty}^{\infty} \rho_o(r) e^{(2\pi j Q \cdot r)} d\tau \qquad (4.13)$$

where $\boldsymbol{Q} = \boldsymbol{k_h} - \boldsymbol{k_o}$ [39] and $\rho(\boldsymbol{r})d\tau$ is the probability that an electron lies in a volume element $d\tau$ at a vector $\boldsymbol{r}$ from the origin.

This is the Darwin spherical-wave theory, published in his first paper in 1914 [36,40], which led to the dynamical theory of x-ray diffraction [41].

4.4.2 Dynamical Theory

Dynamical theory deals with the interaction between scattered or diffracted rays and must be taken into account when dealing with diffraction from large crystals. This theory will not be expanded here but is described in appendix 1. The theory describes the propagation of an x-ray field outside and inside a crystal using Maxwell's equations but will not be required for an examination of the results presented in this thesis.

4.5 Experimental Setup

This section will deal with the two main geometries used in this study: Transmission and Back Reflection Topography, each of which can be employed in two modes, large area and section.

3.5.1 Large Area Transmission

In Large Area Transmission (LAT) topographs the sample is mounted so that the incident beam passes through the sample. A Laue pattern of topographs is then recorded upon a recording film. The sample (for (100) silicon) is tilted typically between 12° to 20° to ensure that the 220 and 004 reflections appear equidistant from the centre of the recording film and that they are far enough away from the direct transmitted beam not to suffer from loss of contrast due to the high x-ray background associated with this direct beam [25,42]. Fig 4.6 shows a typical setup for LAT topography.

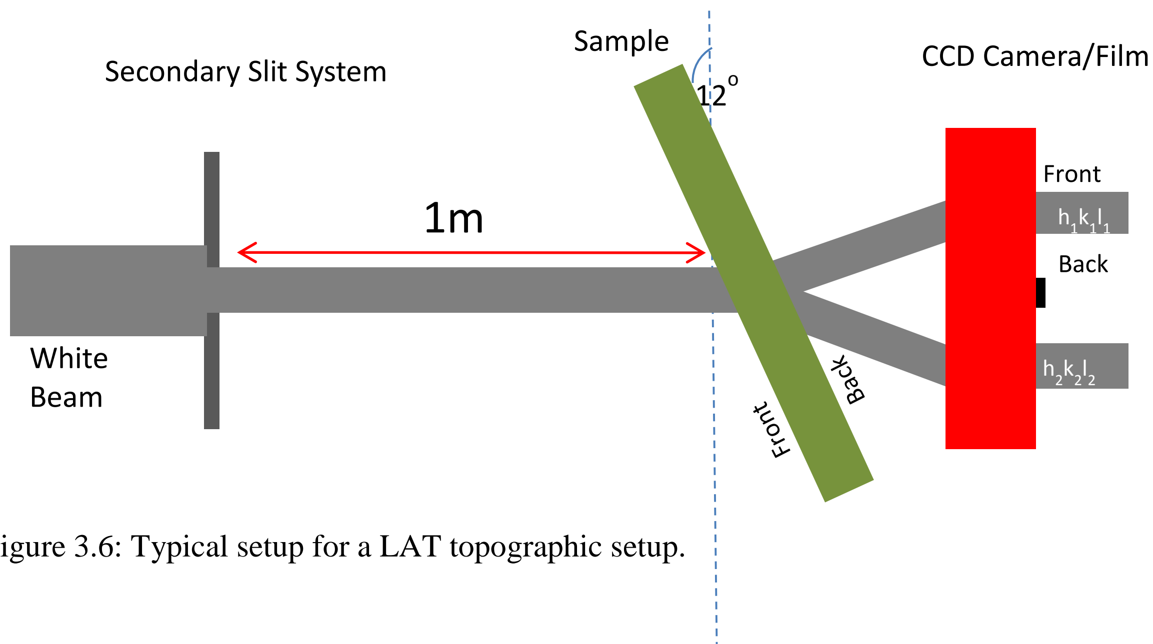

Figure 3.6: Typical setup for a LAT topographic setup.

There are many different diffraction directions that will satisfy Bragg's law, eqn. 4.2, but not all of them will be visible as some will be structure factor forbidden. The intensity of the individual reflections is given by [25]

$$\frac{|F_{hkl}|\lambda^3}{\sin^2\theta_B} e^{-\mu t} \qquad (4.14)$$

where F_{hkl} is the structure factor given in section 3.4.1, μ the absorption coefficient and t the thickness of the crystal.

In silicon

$$|F_{hkl}| = 4\sqrt{2}f_{si}(\theta_B) \qquad (4.15)$$

where all Miller indices h,k,l are odd and

$$|F_{hkl}| = 8f_{si}(\theta_B) \qquad (4.16)$$

where all Miler indices are even and $h+k+l=4n$ *(n=±1, ±2,....).*

$F_{hkl}=0$ for all other indices [25], and $f_{si}(\theta_B)$ is the atomic scattering factor for Si.

The resulting Laue pattern of topographs are captured on high resolution holographic film [43,44]. Film has the advantage of a large field of view allowing the capture of a large number of topographs with one exposure. High resolution films also have high sensitivity that allows for the detailed analysis of defects and strain, however they suffer the drawback that they have a low duty cycle, poor dynamic range and they are gradually disappearing from the market [43,45].

At the ANKA facility a Charged Coupled Device (CCD) camera, imaging via a scintillator plate, can now also be employed to capture topographs. The CCD has the advantage of high duty cycles, high spatial resolution and high dynamic range.

The CCD camera system, positioned 16cm from the sample, comprises a pco.4000 14 bit cooled CCD camera system from PCO Imaging®. The CCD has a resolution of 4008 x 2672 pixels with a pixel size of 9 x 9 µm [56]. The CCD was run with 3.6x Rodenflex® "TV-Heliflex" magnification optics leading to an effective pixel size of 2.5 x 2.5 µm and utilised a scintillating screen 22mm x 4mm in size fabricated from 300µm thick Ce doped $Lu_3Al_5O_{12}$ crystal polished on both sides to optical quality [42,55] The CCD was positioned to capture the $2\bar{2}0$ reflection.

4.5.2 Section Transmission

The section transmission (ST) setup is similar to LAT, the difference being that the incoming beam is collimated to a narrow ribbon by a slit, typically ~10 mm in length and ~15μm in height. As with LAT a Laue pattern of topographs is produced and, providing that the Bragg angle is not too small, the image gives detailed information about the energy flow within the crystal and direct depth information on defects present within the sample [46,47]. A typical setup is shown in fig. 4.7.

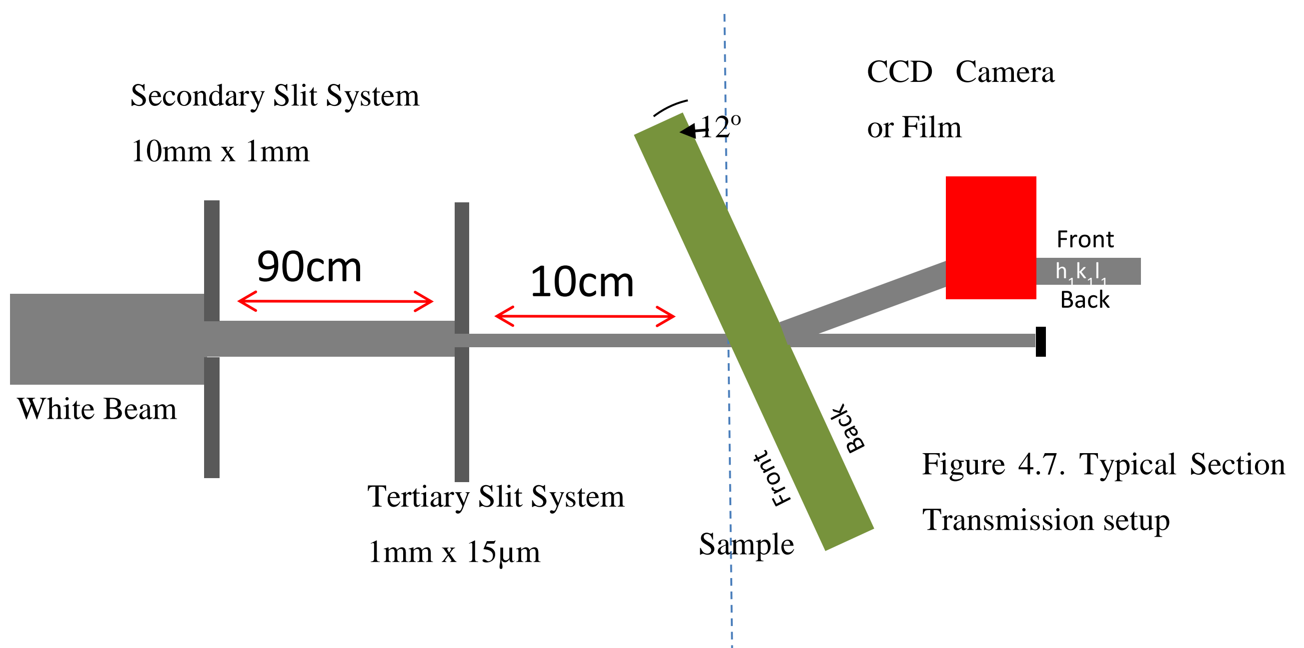

Figure 4.7. Typical Section Transmission setup

4.5.3 Large Area Back Reflection

In large area back reflection topography (LABRT), the incoming beam is collimated to approximately the same size as that for LAT. The beam passes through a hole in the film cassette and impacts perpendicularly on the sample, fig. 4.8. As this is a reflection geometry, the Bragg diffraction criterion is typically satisfied by lower energy photons and therefore the penetration depths for this geometry are quite shallow [48], in the order of tens of microns.

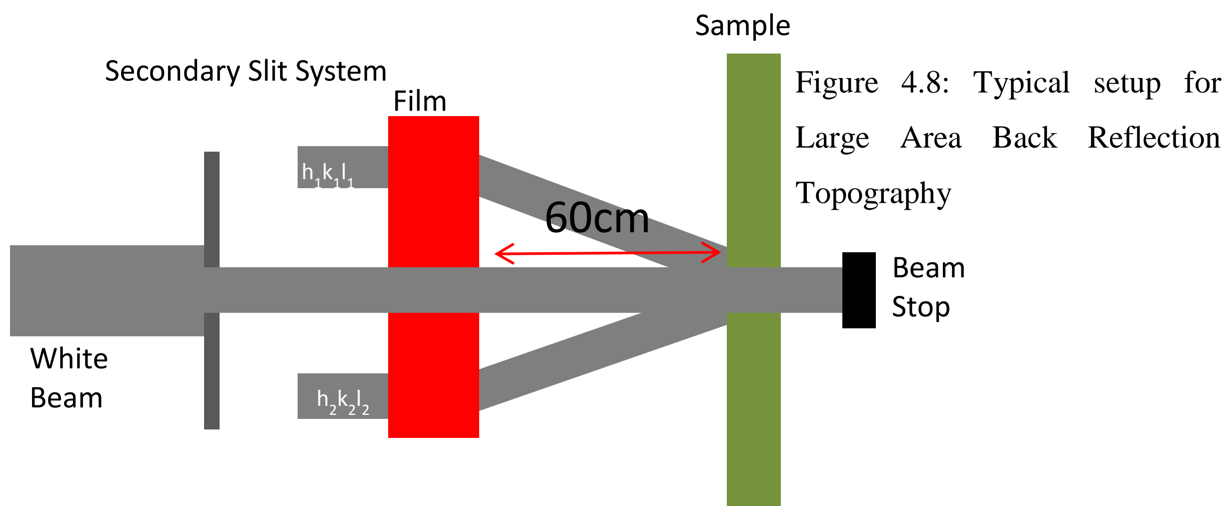

Figure 4.8: Typical setup for Large Area Back Reflection Topography

4.6 Resolution

The resolution on a topographic image is determined by the spatial resolution or minimum strain field size that can be measured, and the geometrical resolution which is due to the displacement of the sample from the x-ray source, fig 4.9.

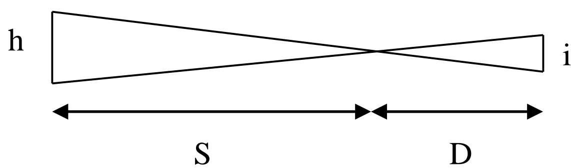

Figure 4.9. Resolution of a topograph, *i* is the image on a photographic plate or CCD chip

Spatial Resolution

Spatial resolution depends upon the angular divergence of the incident beam and the sample to detector distance. It is found from the equation

$$i = \omega D \qquad (4.17)$$

where ω is the divergence of the incident beam and D is the sample to detector distance. If the natural divergence of the beam Ω is smaller than ω, as is the case for synchrotron radiation, then eqn. 4.17 becomes [6]

$$i = \Omega D \qquad (4.18)$$

Geometrical Resolution

Another factor that affects the resolution is the sample to source distance. This is found from

$$i = \frac{hD}{S} \qquad (4.19)$$

where h is the source size and S is the source to sample distance. For the Topo beamline at ANKA, $S = 30m$, $h = 800\mu m$ and $D = 80mm$ [49] giving a geometrical resolution of approx. $2.13\mu m$.

4.7 Penetration Depth of X-Rays

When the incident and exit beam angles are greater than the critical angle ϕ_c for total reflection, then the kinematical penetration depth, t_p is the depth at which the intensity of the reflected beam falls to 1/e times that of the incident beam and it can be expressed as [50]

$$t_p = \left[\mu\left(\frac{1}{\sin\phi_0} + \frac{1}{\sin\phi_n}\right)\right]^{-1} \qquad (4.20)$$

where μ is the wavelength dependent linear absorption coefficient for the material, the value of which can be obtained from the literature [51], ϕ_0 is the incident beam angle and ϕ_n is the exit angle. For the back reflection geometry

$$\phi_0 = 90^o \qquad (4.21)$$

and

$$\phi_n = 90^o - \tan^{-1}\frac{H}{L} \qquad (4.22)$$

where H is the distance from the centre of the film to the topograph being examined and L is the sample to film distance, fig. 4.10.

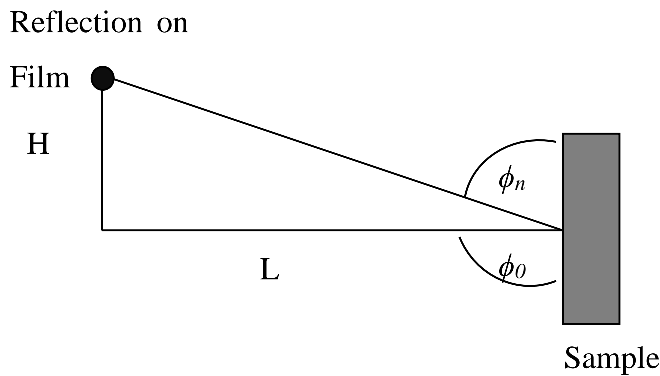

Figure 4.10. Schematic of back reflection topograph.

Rearranging eqn. 4.20 one gets

$$t_p = \left[\mu\left(1 + \frac{1}{\sin\phi_n}\right)\right]^{-1} \qquad (4.23)$$

4.8 Contrast Formation

X-ray topographs provide a picture of the distribution of the defects in a crystal [8]. Information from the topograph is obtained in the form of x-ray contrast variations on the film as local changes in orientation and spacing of the crystal lattice planes will give rise to local differences in either the diffracted beam direction or intensity [52]. The fundamental mechanisms for contrast formation in a topograph will be discussed here.

4.8.1 Orientational Contrast

Orientational contrast occurs when the orientation or spacing of the lattice planes is different from that of the surrounding regions. For monochromatic beams, if the misorientation of the crystal is larger than the beam divergence then there will be no diffracted intensity for the area out of reflection, fig. 4.11, when the Bragg condition is satisfied for the rest of the crystal. This region will then produce a white image (i.e. loss of intensity) on the photographic plate [6,8].

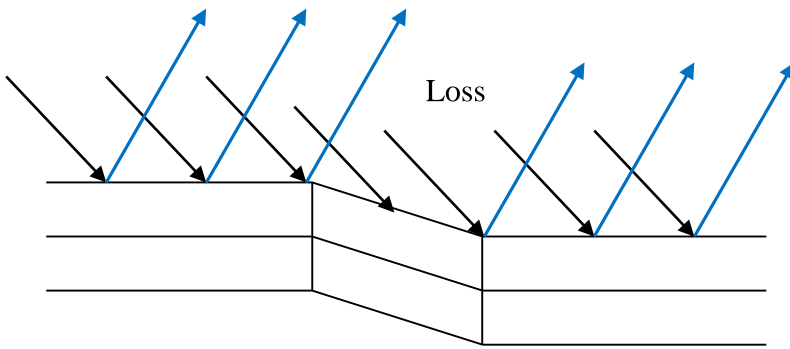

Figure 4.11. Schematic showing Orientation Contrast with monochromatic radiation. [53]

When continuous or white beam radiation is used the diffracted beams from the two parts of the crystal assume different directions in space, fig. 4.12, and there is a loss or gain of intensity in regions corresponding to the boundary of the misoriented region.

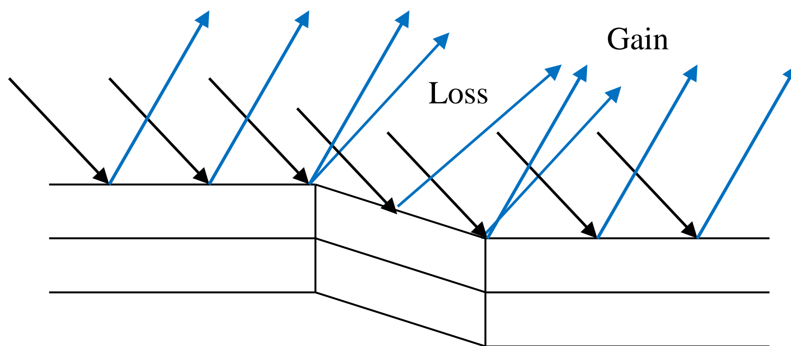

Figure 4.12. Schematic showing Orientation Contrast with synchrotron radiation. [53]

Orientational contrast also arises from the presence of twins and sub-grains [8].

The width of the region of intensity loss or gain is determined by both the angle of misorientation and the sample to film distance [53]. When the beams converge the result is an overlap of the images or conversely one obtains a separation of the images if the beams diverge. The degree of misorientation can determined by measuring the image angular shifts as a function of sample - to - film distance [52].

4.8.2 Extinction Contrast

Extinction contrast arises when the scattering power around a defect in a crystal is different to that of the surrounding region [8,53]. In all cases it arises from a breakdown or change in the

dynamical diffraction of the perfect crystal. The topographs consist of *direct, dynamic* and *intermediary* images, shown in fig. 4.13, corresponding to the three different types of extinction contrast. In transmission geometry the three types of images that can be observed are dependent upon the absorption conditions. The absorption condition is defined as the product

$$\mu_0 t \qquad (4.24)$$

where μ_0 is the linear absorption coefficient of the material and t is the thickness of the crystal.

For topographs recorded under low absorption conditions

$$\mu_0 t < 1 \qquad (4.25)$$

the image is dominated by the direct image contribution, for intermediate absorption conditions

$$5 \geq \mu_0 t > 1 \qquad (4.26)$$

all three components contribute while for high absorption cases

$$\mu_0 \geq 6 \qquad (4.27)$$

the dynamical contribution dominates [52,54]. Fig 4.13 shows all three images. The image is a transmission topograph dislocations in an aluminium nitride (AlN) single crystal under intermediate absorption ($\boldsymbol{g}$ = 1010, λ = 0.75Å) [52].

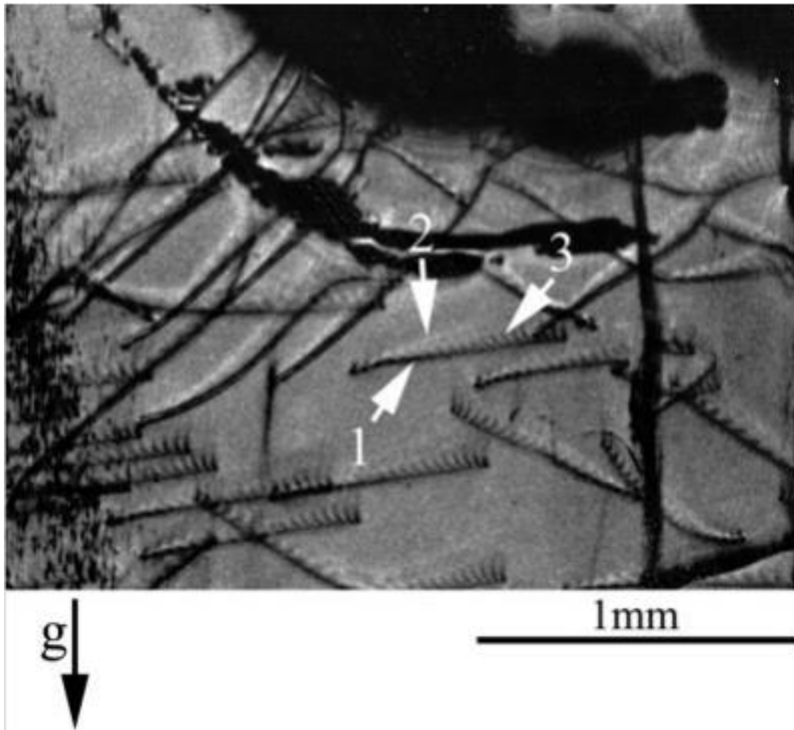

Fig. 4.13. 1010 transmission x-ray topograph of an AlN single crystal under intermediate absorption (μt = 4). (1) Direct Image, (2) Dynamical Image, (3) Intermediate Image of a dislocation. (Image courtesy of Dr. B. Raghothamachar.)

Direct Image

The direct image is the most common image observed in X-ray topographs and is formed when the incident X-ray beam intercepts the defect within the crystal (see fig. 4.14). If the defect region is small in size, then the region will diffract kinematically and will not suffer from the extinction effects that the diffracted beams from the perfect regions of the crystal are subjected to, the result of which is that the beams from the distorted regions will have an enhanced diffracted intensity so giving rise to topographic contrast. Direct images will appear black (i.e. enhanced intensity) [52-54] on the X-ray film due to the diffracted intensity from the defect, D, being greater than that for perfect crystal.

Dynamical Image

The dynamical image arises from the change of wavefield intensity due to a defect. This contrast appears as white shadows cast along the direction of propagation of the wavefields impinging on the defect and is due to the curvature of the wavefields away from their normal path by the strain field surrounding the defect (see fig. 4.14). New wavefields are then created

within the crystal most of which are strongly absorbed. This gives rise to a loss in intensity as these wavefields cannot propagate to the exit surface and so appear white on the topographs [6,52,53].

Intermediary Image

The final diffraction imaging mechanism is termed the intermediary image. This image arises from the interference at the exit surface between the new wavefields, created below the defect, and the original wavefield propagating in the perfect regions of the crystal. Generally these images appear as a bead like contrast along the direct image of the defect. Under moderate absorption conditions, if the defect is inclined to the surface, this type of image forms a fan within the intersections of the exit and entrance surfaces of the defect (Bormann fan) and has an oscillatory contrast, alternating black and white, with depth periodicity [53,54].

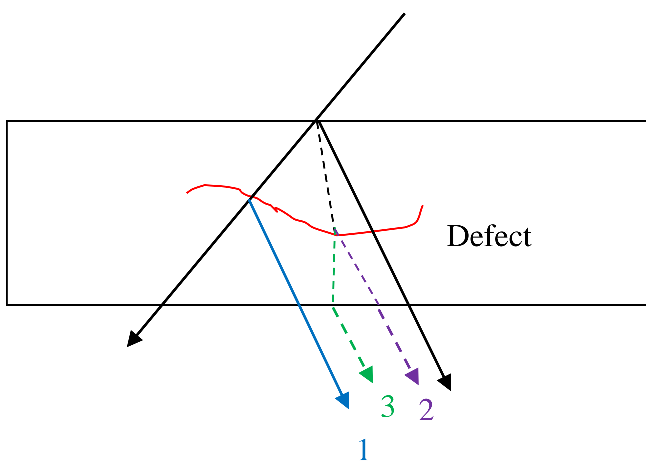

Figure 4.14: Types of extinction Contrast. 1 Direct Image, 2 Dynamical Image and 3 Intermediary Image

4.9 References

[1] A. N. Danilewsky, R. Simon, A. Fauler, M. Fiederle, and K. W. Benz, Nuc. Instrum. Meth. Phys. Res. B **199**, 71 (2003).

[2] A. Chodos, *This Month in Physics History* (APS, 2001), 2009, p. 8.

[3] C. G. Barkla, Phil. Trans. Roy. Soc. **204**, 467 (1905).

[4] C. G. Barkla, Proc. Roy. Soc. **77**, 247 (1906).

[5] C. G. Barkla, *Charateristic Rontgen Radiation - Nobel Lecture*, 1920), 2009, p. 8.

[6] A. Authier, *Dynamical Theory of X-Ray Diffraction* (Oxford University Press, Oxford, 2004), p. 674.

[7] M. von Laue, *Concerning the detection of X-ray interferences*, 1915), 2009, p. 9.

[8] D. K. Bowen and B. K. Tanner, *High resolution X-ray Diffractometry and Topography* (Taylor & Francis, London, 1998), p. 252.

[9] W. H. Bragg and W. L. Bragg, Proc. Roy. Soc. **88**, 428 (1913).

[10] W. H. Bragg and W. L. Bragg, Proc. Roy. Soc. **89**, 277 (1913).

[11] W. L. Bragg, Proc. Roy. Soc. **89**, 248 (1913).

[12] M. Dudley, *X-Ray Topography* (MRS, USA, 1993), 307, p. 213.

[13] W. Berg, Naturwissenschaften **19**, 391 (1931).

[14] C. S. Barrett, Tranactions American Institute of Mining, Metallurigal and petroleum Engineers **161**, 50 (1945).

[15] A. P. L. Turner, T. Vreeland, and D. P. Pope, Acta Cryst. **24**, 452 (1968).

[16] J. B. Newkirk, Phys. Rev. **110**, 1465 (1958).

[17] G. N. Ramachandran, Proc. Indian Acad. Sci. **19**, 599 (1944).

[18] A. Guinier and J. Tennevin, Acta Cryst. **2**, 133 (1949).

[19] A. R. Lang, Acta Cryst. **12**, 249 (1959).

[20] J. P. Blewett, J. Appl. Phys. **18**, 976 (1947).

[21] F. R. Elder, A. M. Gurewitsch, R. V. Langmuir, and H. C. Pollock, Phys. Rev. **71**, 829 (1947).

[22] F. R. Elder, A. M. Gurewitsch, R. V. Langmuir, and H. C. Pollock, J. Appl. Phys. **18**, 810 (1947).

[23] H. C. Pollock, Phys. Rev. **69**, 125 (1946).

[24] J. Schwinger, Phys. Rev. **75**, 1912 (1949).

[25] T. Tuomi, K. Naukkarinen, and P. Rabe, Phys. Stat. Sol. **25**, 93 (1974).

[26] M. Hart, J. Appl. Cryst. **8**, 436 (1975).

[27] D. Iwanenko and I. Pomeranchuk, Phys. Rev. **65**, 343 (1944).

[28] J. P. Blewett, Phys. Rev. **69**, 87 (1946).

[29] W. Chen, *White Beam Synchrotron X-ray Topography and micro-Raman Spectroscopy Characterization of Crystal Materials* (Dublin City University, Dublin, 2003).

[30] H. Winick, *Synchrotron Radiation Sources A Primer* (World Scientific, Singapore, 1994), 1, p. 507.

[31] H. Winick and S. Doniach, *Synchrotron Radiation Research* (Plenum Press, New York, 1980).

[32] F. R. Elder, R. V. Langmuir, and H. C. Pollock, Phys. Rev. **74**, 52 (1948).

[33] M. Cholewa and A. Rack, *ANKA Instrumentation Book* (ANKA Angstroemquelle Karlsruhe, Germany, 2007), 2009, p. 84.

[34] W. Drube and W. Laasch, *Photon Science 2008. Highlights and HASYLAB Annual Report* (Heigener Europprint, Germany, 2008).

[35] P. P. Ewald, Rev. Mod. Phys. **37**, 46 (1965).

[36] C. G. Darwin, Phil. Mag. **27**, 675 (1914).

[37] S. C. Wallwork, *Introduction to the Calculation of Structure Factors* (International Union of Crystallography, Wales, 1980), 3, p. 12.

[38] D. K. Bowen and B. K. Tanner, *X-Ray Metrology in Semiconductor Manufacturing* (CRC Press, USA, 2006), p. 270.

[39] A. Authier and C. Malgrange, Acta Cryst. **54**, 806 (1998).

[40] S. M. Durbin, Acta Cryst. **A**, 258 (1995).

[41] P. P. Ewald, *50 Years of X-ray Diffraction* (International Union of Crystallography - http://www.iucr.org/publ/50yearsofxraydiffraction, Scotland, 1960), p. 733.

[42] A. N. Danilewsky, J. Wittge, A. Rack, T. Weitkamp, R. Simon, T. Baumbach, and P. J. McNally, J. Mater. Sci. **19**, 269 (2008).

[43] A. N. Danilewsky, A. Rack, J. Wittge, T. Weitkamp, R. Simon, H. Riesemeier, and T. Baumbach, Nuc. Instrum. Meth. Phys. Res. B **266**, 2035 (2008).

[44] D. Allen, J. Wittge, A. Zlotos, E. Gorostegui-Colinas, J. Garagorri, P. J. McNally, A. N. Danilewsky, and M. R. Elizalde, Nuc. Instrum. Meth. Phys. Res. B **268**, 383 (2010).

[45] N. E. Lanier, J. S. Cowan, and J. Workman, Rev. Sci. Instrum. **77**, 043504-1 (2006).

[46] P. J. McNally, T. Tuomi, D. Lowney, K. Jacobs, A. N. Danilewsky, M. O'Hare, and L. Considine, Phys. Stat. Sol. **185**, 373 (2001).

[47] B. K. Tanner, J. Electrochem. Soc. **136**, 3438 (1989).

[48] D. Lowney, *Analysis of the Structural and Optoelectrical Properties of Semiconductor Materials and Devices using Photoacoustic Spectroscopy and Synchrotron X-ray Topography* (Dublin City University, Dublin, 2002).

[49] Topo Beamline at ANKA, KIT, [online], http://ankaweb.fzk.de/website.php?page=instrumentation_beam&id=4&field=2 (Accessed 7/12/2009).

[50] R. Rantamaki, T. Tuomi, P. J. McNally, and A. N. Danilewsky, J. X-ray Sci. Tech. **8**, 159 (1998).

[51] Optical Constants, Gullikson,E., [online], http://henke.lbl.gov/optical_constants/ (Accessed 7/12/2009).

[52] B. Raghothamachar, G. Dhanaraj, J. Bai, and M. Dudley, Microsc. Res. Technique **69**, 343 (2006).

[53] B. K. Tanner, *Contrast of Defects in X-ray Diffraction Topographs* (Plenum Press, London, 1996), 357, p. 147.

[54] F. Zontone, L. Mancini, R. Barrett, J. Baruchel, J. Härtwig, and Y. Epelboin, J. Synchrotron Rad. **3**, 173 (1996).

[55] L. Nagornaya, G. Onyshchenko, E. Piroqov, N. Starzhinskiy, I. Tupitsyna, V. Ryzhikov, Y. Galich, Y. Vostretsov, S. Galkin, E. Voronkin, Nuc. Instrum. Meth. Phys. Res. A. **537**, 163 (2005)

[56] pco. imaging, PCO AG, [online], http://www.pco.de/ (Accessed 26/02/10).

Chapter 5 Three Dimensional X-Ray Diffraction Imaging

5.1 Introduction

Three Dimensional X-Ray Imaging (3D-XRDI) is a characterisation technique that utilises Section Transmission (ST) topography to produce three dimensional images of defects such as dislocation loops in silicon. The technique involves the capture of a series of spatially sequential ST topographs onto the CCD camera system described in section 3.5.1. The images are then rendered into three dimensions using medical tomographic algorithms found in *ImageJ*, a freeware image processing program written and developed by Wayne Rasband at the United States National Institute of Health.

5.2 Sample Preparation

Defined defects were introduced into the crystalline silicon with a (100) surface orientation with the notch parallel to the [110] direction. Indents were introduced to full 200 mm diameter polished double sided 725 µm thick wafers and also to 20x20 mm^2 Silicon samples. The 20x20 mm^2 samples were cut from a polished double sided 775 µm thick 300 mm diameter silicon wafer. The first 12 samples were numbered 1 to 12, and thereafter the following naming convention was used:

SiDAM _ wafer # _ piece #

where SiDAM is the project name, wafer # is the wafer number, 0 was the first 300 mm wafer used and all samples come from this wafer, piece # indicates where on the wafer the sample was cut from, as shown below in fig. 5.1.

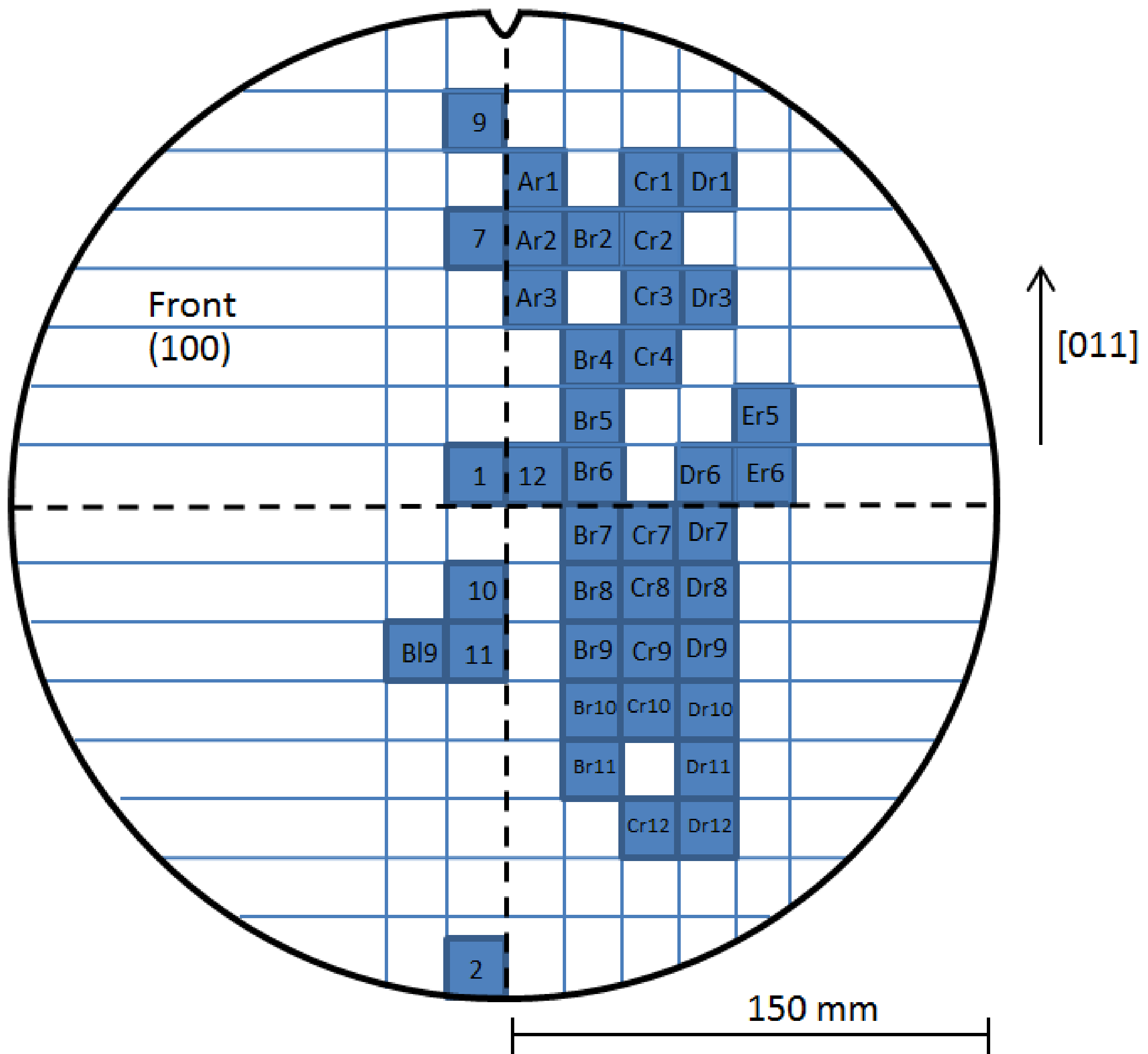

Figure 5.1: Location of 20x20 mm^2 samples cut from a 300 mm diameter wafer

A full matrix of the samples and the experiments carried out on them is shown in appendix 2

5.2.1 Sample Heating

In order to fully simulate an industrial manufacturing process the indented samples were subjected to selected thermal annealing processes. For the small samples this process was accomplished *in situ* by use of a double ellipsoidal mirror furnace. This furnace consisted of 2 elliptical mirror half shells with a middle section that contained the sample holder and thermocouples [1]. The power to the heating lamps was controlled using a Knick precision voltage controller and the temperature was recorded using two 0.5 mm diameter NiCrNi

thermocouples attached to a Testo 735 data logger [2]. When connected together the half shells have a common focal point at the centre of the furnace as shown in figure 5.2.

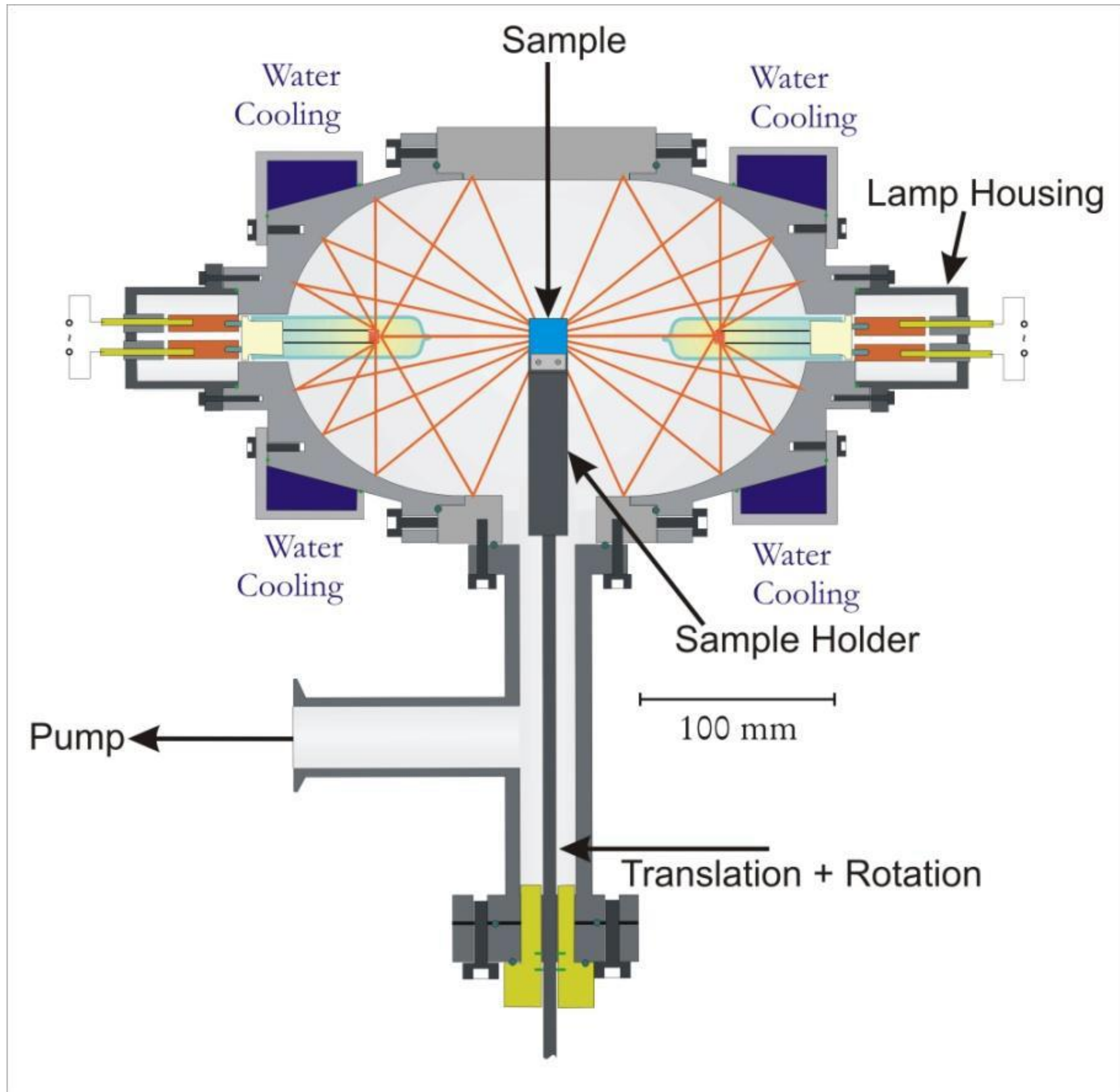

Figure 5.2: Schematic of the double ellipsoid mirror furnace (Danilewsky 2010)

5.3 Three Dimensional X-ray Diffraction Imaging

5.3.1 History of Three Dimensional X-ray Diffraction Imaging

Three dimensional characterisation techniques began with the use of stereo topographs recorded as a pair of hkl and $\bar{h}\bar{k}\bar{l}$ reflections, which are then studied under a stereo viewer. A problem with this technique is that the stereoscopic effect is exaggerated [3,4]. Later on in 1979 Kawado and Aoyama developed a system to gain the full information on the long range strain fields in a crystal. This technique used a system combining the step scan technique created by Andersen and Gerward [5] with an automatic Bragg angle control (ABAC). This technique overcame the problems associated with Andersen's solution, the difficulty of taking a series of section topographs over long range strain fields, by correcting for the deviation of the diffraction angle between steps [6]. The major drawback of this procedure was the time taken to take the individual topographs, ~2 hours per exposure. Later techniques pioneered by Ludwig [7] and Kawado [8,9] used an approach combining both diffraction topography and microtomography. This approach involves the recording of a series of images while rotating the sample around its diffraction vector. While this technique did allow for the formation of 3D images it had a drawback in that it required that the crystal orientation of the sample to be precisely adjusted to the rotation of the goniometer [10].

The application of imaging software was introduced in 2006 by Mukaide *et al*. [11] and now for the first time the researcher was freed from the tedious pen and pencil approach used previously. This was further enhanced when Kvardakov *et al*. [12] produced 3D reconstructions of a series of ST topographs showing defects in quartz crystals.

5.3.2 *ImageJ*

ImageJ is a Java based public domain image processing tool developed by Wayne Rasband at the U.S. National Institutes of Health [13]. It was inspired by NIH Image, a medical image processing and analysis program originally designed for the Mackintosh at the Research Services Branch of the National Institute of Mental Health [14]. Since it is Java based *ImageJ* runs on multiple platforms as a downloadable application and in addition to the image processing capabilities already present within its source code, the functionality can be extended by downloading and installing additional plugins. This study utilised *ImageJ* V. 1.46e for Windows and bundled with 64-bit Java. *ImageJ* was loaded onto a custom built computer incorporating an Intel® Core™ i7 CPU 920 @ 2.67GHz with a 2.66GHz Front Side Bus and 24GB RAM with 6.25TB of hard drive space running 64 Bit Windows 7©.

5.3.3 Image Acquisition

Samples that required 3D-XRDI were imaged at the ANKA synchrotron light source, Institute for Synchrotron Radiation, Karlsruhe Institute of Technology, Germany. The experiments were carried out at the Topo-Tomo beamline using a white x-ray beam sourced from a 1.5 T bending magnet and fed by a 2.5GeV electron storage ring [15,16]. The beamline is 30m in length with a 0.5mm thick polished Beryllium window positioned in front of the sample. Image capture for 3D-XRDI utilised a set of slits positioned at 4.8m from the source. This allows for pre-definition of the beam, control over the beam divergence and a reduction of the heat load on subsequent components. A second set of Tungsten (W) slits are positioned 28m from the source, which are used to collimate the beam to 10mm x 1mm [16-20]. This setup ensures that the images are obtained using Section Transmission (ST) topography as described in section 3.5.2.

A final set of slits are positioned 30cm from the sample to further collimate the beam to 10mm x 15μm as shown in figure 5.3.

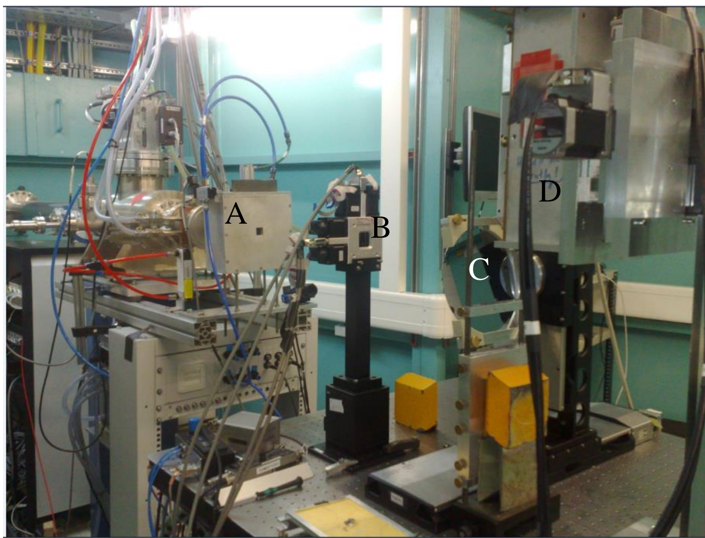

Figure 5.3: 3D-XRDI experimental setup. 'A' is the fast shutter; collimating the beam to 10mm x 1mm. 'B' is the final slit system used to collimate the beam to 10mm x 15μm. 'C' Sample holder containing a 200mm diameter wafer. 'D' CCD camera system

The sample under test was mounted on a goniometer capable of *x-z* translation movement and φ swivel movement. Using the φ translation the sample was tilted to 12° and the CCD positioned to capture the $\bar{2}20$ reflection [18,21], as shown in fig. 5.4.

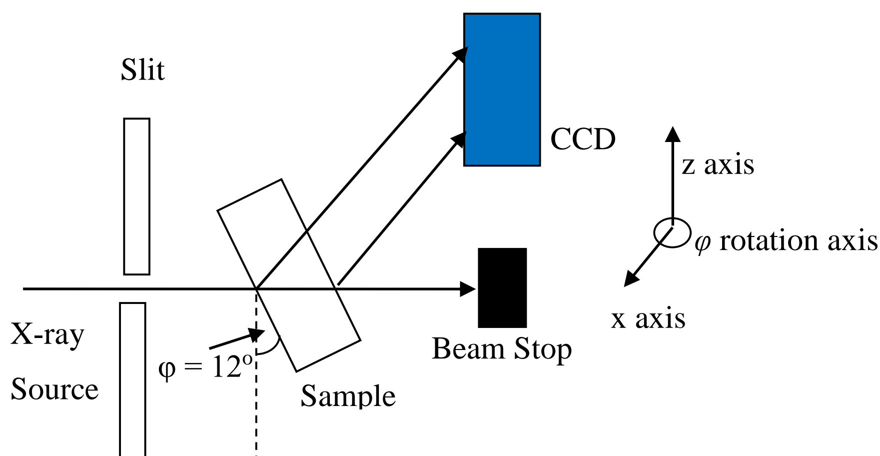

Figure 5.4: Schematic illustration of the experimental arrangement for ST topography. φ rotation occurs around the x axis. Sample is mounted so the features of interest are facing the CCD

The sample was then stepped vertically using the z translation motors in 15µm steps [20], resulting in a series of sequential ST topographs being taken across the area of interest. The images were captured on the CCD camera system as described in section 3.5.1, and were normalised using both darkfield and flatfield images to eliminate machine induced artefacts. After normalisation the images were stacked using the *ImageJ* software [22] this stack being the basis of the 3D rendering.

5.3.4 Image Formation

As mentioned in section 3.8.2, image formation, in transmission geometry, is dependent upon the absorption conditions as given by $\mu_0 t$.

For the samples referenced in this work μ_0 is the linear absorption coefficient of silicon, 22.5 cm^{-1} [23], while t is the sample thickness, 775µm, which gives:

$$\mu_0 t = 1.7 \qquad (5.1)$$

This ensures that there is a direct projection of the defect onto the CCD and consequently the depth information is preserved [24-27].

A $\bar{2}20$ reflection is depicted in figure 5.5 showing the formation of dislocation loops around a series of three 600mN indents from sample 9. The sample was subjected to an *in situ* thermal anneal as described by Wittge *et al*. [28]. At the end of the thermal processing regime, which resulted in the loop structure being "frozen" in the sample, the beam was stepped across the line A – A' shown on fig. 5.5 in 15µm steps and an ST topograph was taken at each step.

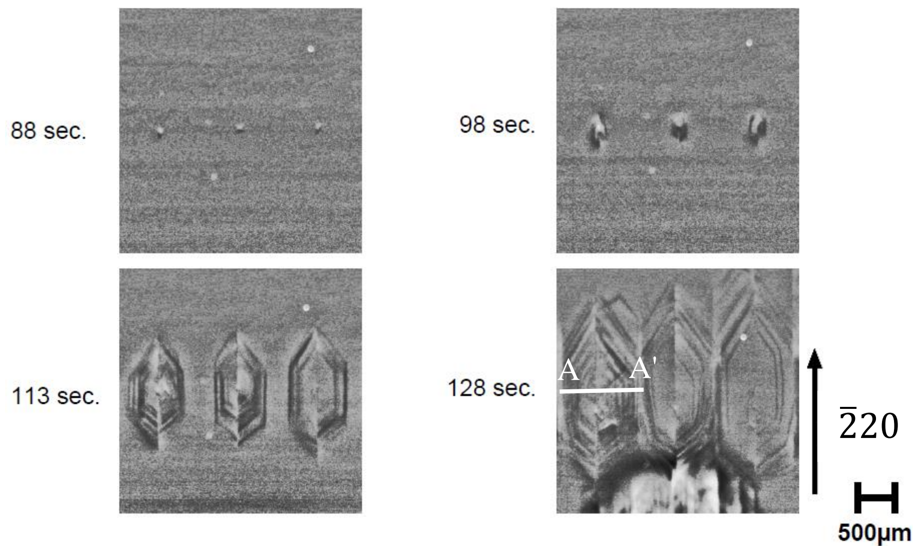

Figure 5.5: A series of time stamped Large Area Transmission (LAT) topographs of 3 600mN indents showing the growth of dislocation loops. A – A' is the line showing the position for the ST topographs

One of the topographs is shown in fig. 5.6 with the individual dislocation loops visible on the left hand portion of the image. The individual loops cannot be seen on the right hand side of the image as the dislocation density is too large.

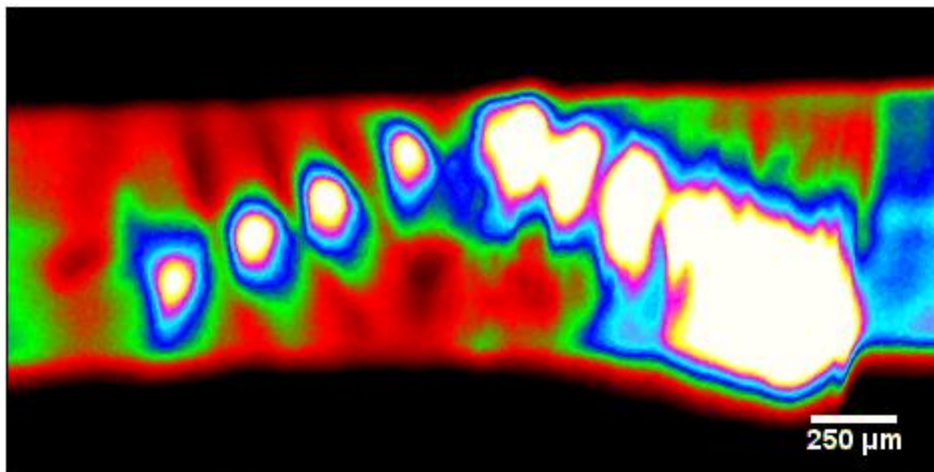

Figure 5.6: Single $\bar{2}20$ ST topograph taken at position A – A' (fig. 3). False colour is added to enhance the appearance of the dislocation loops

The images were normalised using a darkfield image in order to remove machine induced artefacts and any noise removed using the despeckle script in *ImageJ*. The images were

subsequently stacked together using *ImageJ* with the stack being the basis of the 3D rendering.

5.3.5 3D Rendering

Once they are stacked the images need to be converted from 16-bit to 8-bit tiff images and the brightness and contrast settings adjusted to enhance the area of interest. The images were then registered using *StackReg*, a plugin that allows for the images to be aligned on top of each other. This feature allows for the compensation of image drift on the CCD. Manual registration of the images was then performed, if needed, using a macro written by J. Wittge from the University of Freiburg [2].

An animation sequence is then generated using the *3D Project* plugin written by Michael Castle and Janice Keller of the University of Michigan. This plugin offers three linear projection methods. Nearest Point is a method where a ray passes normal to the volume plane through every point of the projection plane. The value of the nearest non-transparent point which is encountered by the ray is then stored in the image. Brightest Point projection projects the brightest point encountered along each ray while Mean Value sums the values of all the transparent points and projects their mean value [14, 22].

In order to accurately construct a 3D image the spacing between each successive ST image needs to be known in pixels. This can be calculated as the image size is a known value, i.e. it is the thickness of the silicon sample. The equivalent image height in pixels can be measured using *ImageJ* and the image spacing can be found using:

$$S = \frac{k}{v} \qquad (5.2)$$

where S is the image spacing, k is the step size in μm and v is the image resolution in μm/pixel [20].

Once the animation sequence is complete the image is ready for viewing. This is facilitated by the use of the *ImageJ 3D Viewer* plugin which produces a 3D image that can be rotated and viewed from any angle. Figure 5.7 below shows a rendering of 45 ST topographs, one of which is shown in fig. 5.6 above. Rotation of the image allows for the visualisation of the individual dislocation loops as they progress through the sample.

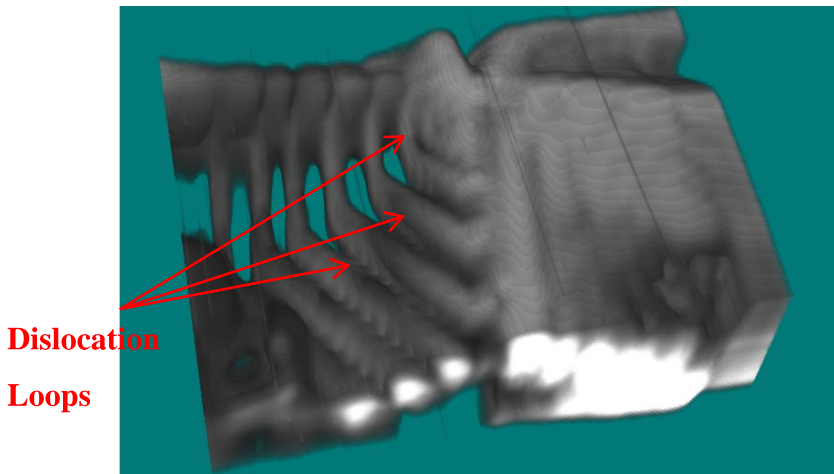

Figure 5.7: 3D rendering of 45 ST topographs. The individual dislocations loops are visible gliding from the top surface to the bottom surface

The 3D Viewer plugin utilises Java 3D to create a universe to hold the rendering. The stack, which has been volume rendered in the previous step is put into this universe and a transparency value is assigned to each voxel depending upon its intensity; black voxels are fully transparent while white ones are opaque [29]. An example of this rendering is shown in fig. 5.8 below. This image is a rendering of 667 separate ST topographs taken across a wafer laser mark. The image not only shows the laser mark but also shows a strain fields extending from the mark into the bulk silicon.

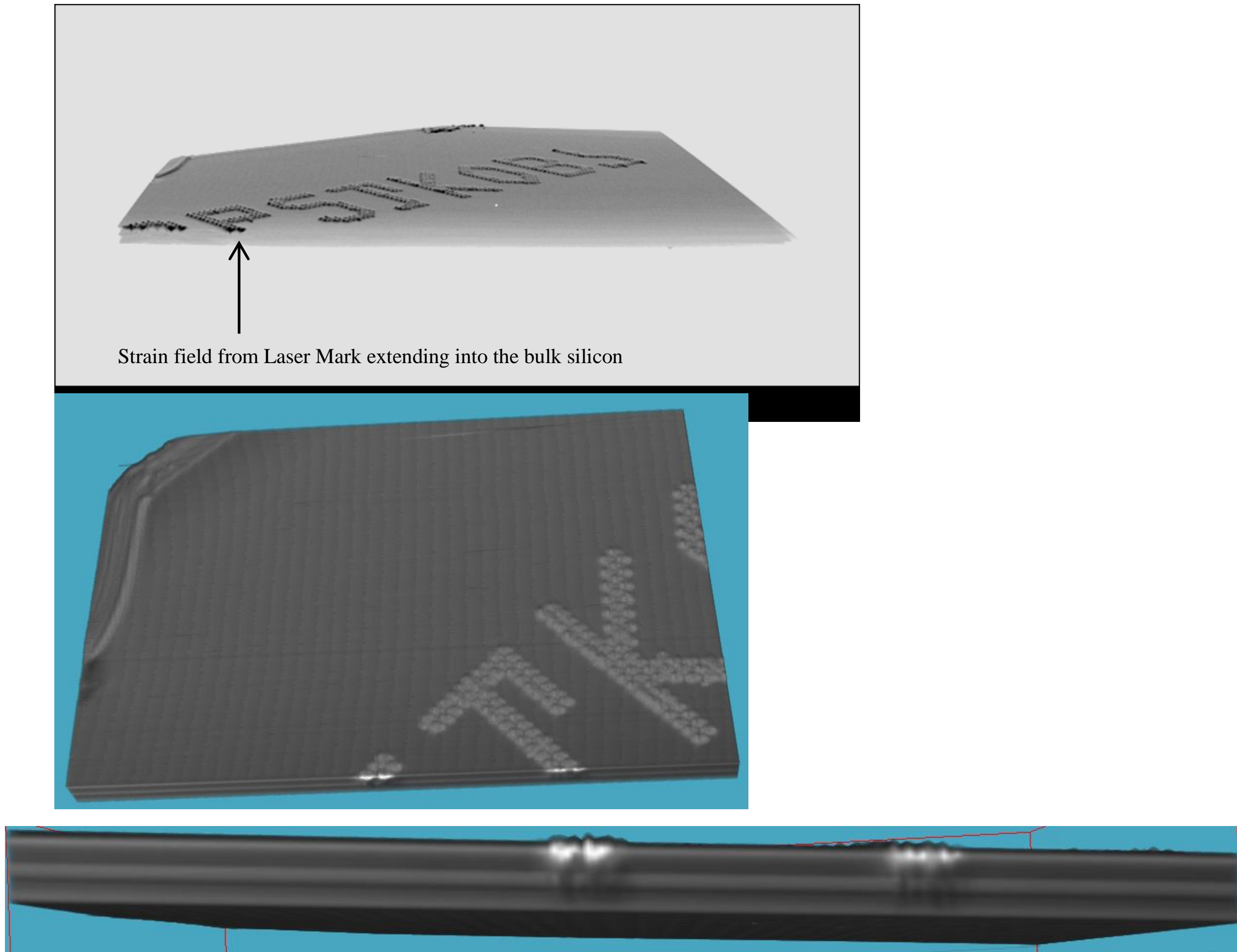

Figure 5.8: 3D-XRDI rendering of 667 individual ST topographs taken across the laser mark on a 200mm wafer. A) shows the laser mark with the accompanying strain field extending into the bulk silicon. B) shows a close up of part of the lasermark, C) shows the strain field in close up of the strain fields

5.4 Results

It is known that the preferred glide plane for (100) silicon is along the {111} series of glide planes [30] and the angle that these planes make to the surface of (100) silicon can be calculated from:

$$\theta = \cos^{-1}\frac{\boldsymbol{a}\cdot\boldsymbol{b}}{|\boldsymbol{a}||\boldsymbol{b}|} \qquad (5.4)$$

where $\boldsymbol{a}$ and $\boldsymbol{b}$ are the {100} and {111} Miller indexed planes, respectively, and θ is the angle between them, giving a theoretical angle of glide of 54.75°. Measurement of the angle that the

dislocation loops make with the surface of the silicon sample confirms that they are gliding at 54°, fig. 5.9.

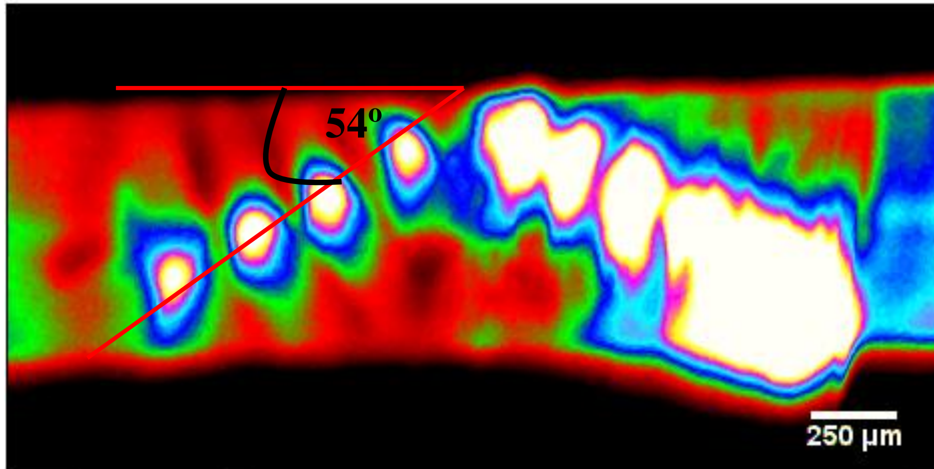

Figure 5.9: Single 220 ST topographic image showing dislocation loops gliding at 54° with respect to the (100) Si surface corresponding to the {111} series of glide planes

In total there are four (111) planes that can be activated and upon which the dislocation loops can glide. This is shown in the schematic fig. 5.10.

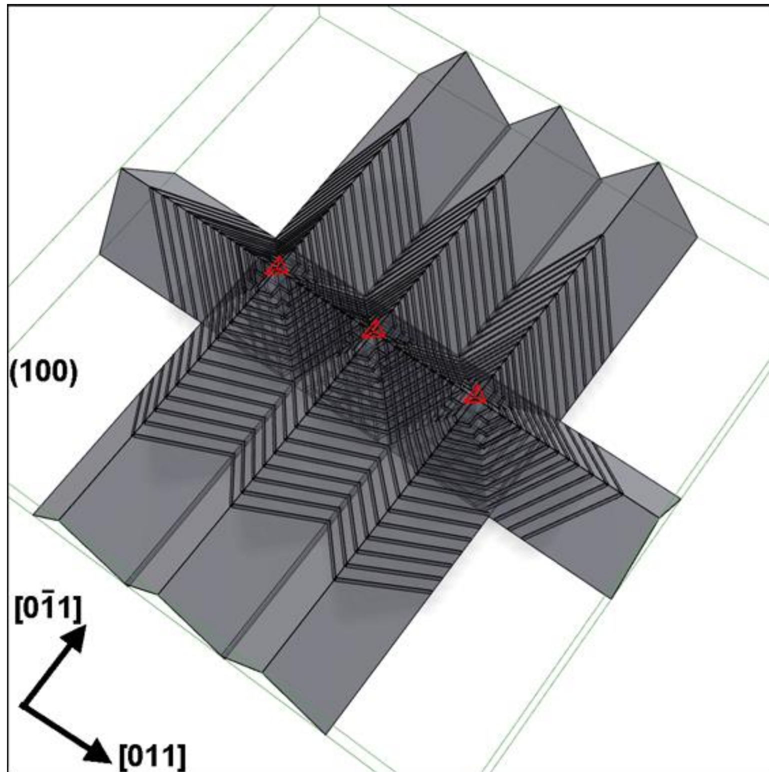

Figure 5.10: Schematic of the {111} series of glide planes. Image courtesy of J. Wittge, University of Frieburg.

Using conventional x-ray topography it is not possible to see the activation of all four glide planes but the application of 3D-XRDI does allow this.

Fig. 5.11 shows a 220 topographic image of a 2N indented region from sample SiDAM_0_Cr4. This sample has been spike annealed 10 times to 1000ºC to allow for the formation of slip planes.

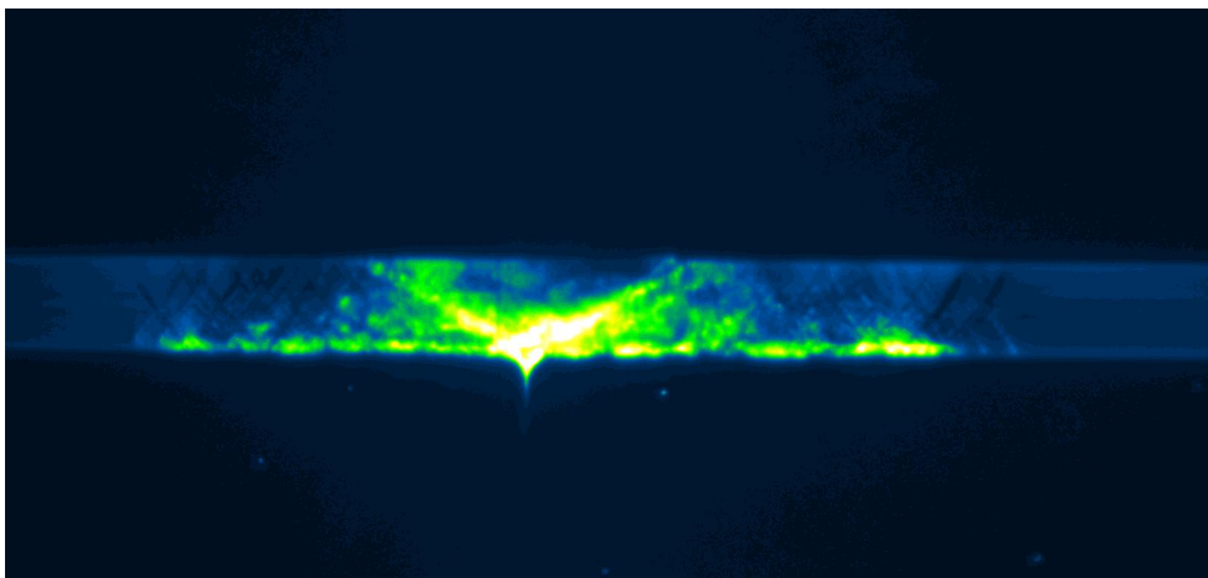

Figure 5.11: Single 220 ST topograph of a 2N indented region post thermal anneal. False colour is added to enhance contrast around the slip bands.

A series of 134 ST topographs was taken across the indent and these were rendered into 3D, see fig. 5.12.

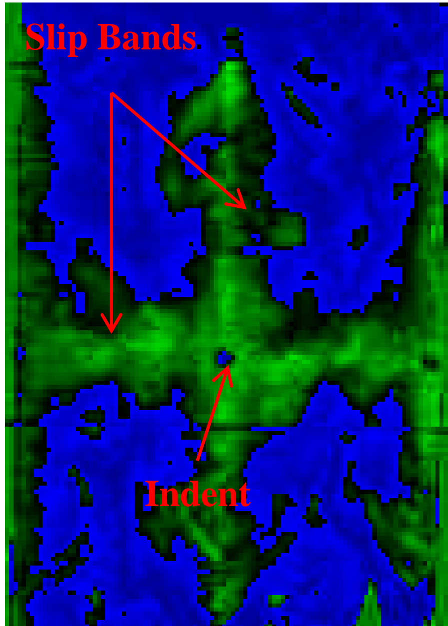

Figure 5.12: 3D XRDI image of 2N indented region shown in fig. 5.10. False colour again added to enhance the contrast around the slip bands.

When the image is rotated through 180° it can be seen that all four of the (111) planes had been activated and that within the square formed by these planes there were no dislocations or slip bands. Measurement of the distance between the slip bands showed them to be 1060 μm apart which again corresponded to an angle of 54°, fig. 5.13.

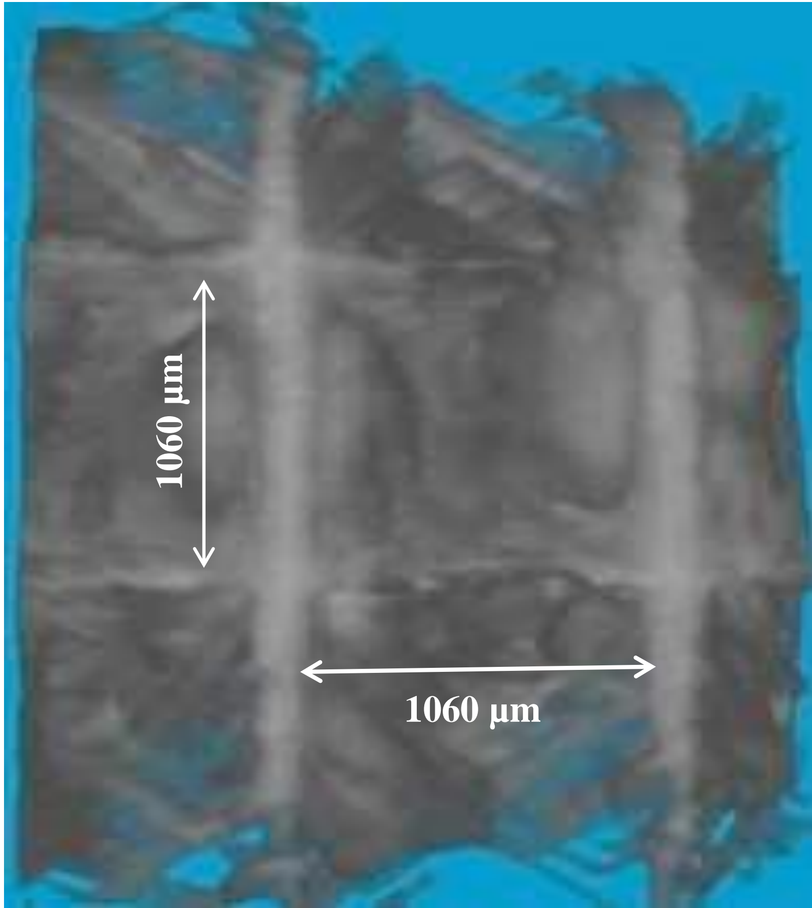

Figure 5.13: Rotation of 3D rendering shown in fig. 5.12 by 180°. Four slip bands are visible 1060 µm apart proving they are the (111) glide planes.

Fig. 5.14 shows the same indented region, albeit covering three 2N indents, imaged using the Bedescan High Resolution X-ray Diffraction (XRD) tool taken at Jordan Valley Semiconductors Ltd, Durham, England. This tool is a stand-alone lab based XRD imaging tool

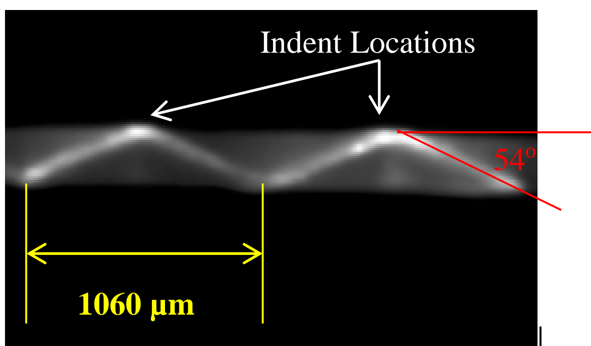

Figure 5.14: 220 ST topograph of sample SiDAM_0_Cr4. Taken on a BedeScan XRD tool using the Cu kα_1 beam

The results from the lab based tool correspond well with the synchrotron results. This shows that for defect identification a lab based tool can now be used that will provide comparable results to that of the synchrotron

Another feature of the 3D rendering is the ability it provides to take a virtual "step through" the bulk silicon and track the progression of the defect. This arises from the fact that depth information is preserved as mentioned in section 5.3.4. Fig. 5.15 shows a sequence of images taken while stepping through the rendering shown in fig. 5.12 and fig. 5.13.

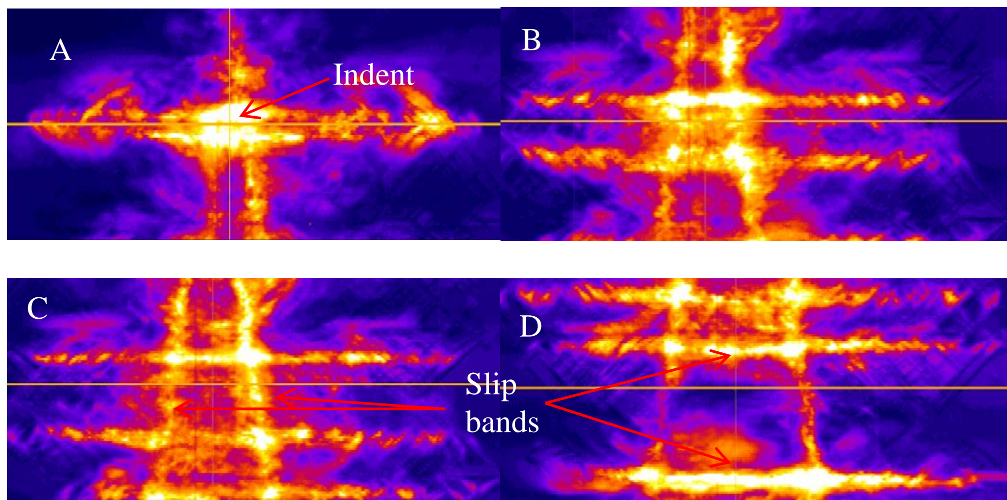

Figure 5.15: Sequence A to D are taken at different depths through sample SiDAM_0_Cr4. The progression of the slip bands can be seen emanating from the indent

The 4 slip bands can be seen moving away from the surface of the silicon sample. The bands then progress through the sample to the bottom of the sample as can be seen in fig. 5.12. This then demonstrates the strength of this technique as an analysis tool in that it is now possible to observe defects at various depths within the sample and to do so completely non-destructively.

5.4.1 K-means Clustering

An unfortunate consequence of topographic imaging is that the raw images are in shades of grey (i.e. only x-ray intensity is recorded) that can be difficult to interpret using the human eye. This means that subtle changes in strain field intensities cannot be easily distinguished. Fig. 5.16 shows the rendering of a series of a Si sample (Sample 1) of five, 2N Vickers indents created from 25 individual 220 ST topographs.

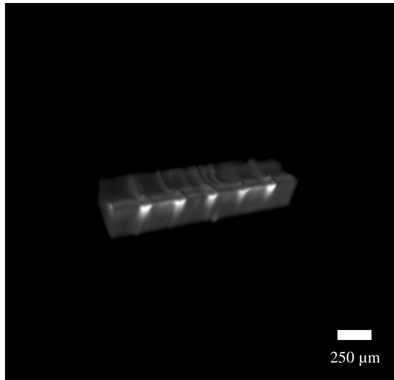

Figure 5.16: 3D rendering of a series of five, 2N indents. Sample 1

This sample was not subject to annealing in order to observe the unchanged 3D strain distributions around the indents.

A powerful method to help with this is to use a technique known as *K-means clustering* together with the application of false colour. *K-means clustering* is an image segmentation process that can highlight or enhance the differences in images that result from the changing strain field within the sample and give a graphical indication of the areas of greatest strain related intensities. The clustering algorithm used is of the form:

$$J = \sum_{j=1}^{k} \sum_{i=1}^{n} \left\| x_i^{(j)} - c_j \right\|^2 \qquad (5.5)$$

where *k* is the number of clusters or segments into which the image will be divided, this being set initially by the user, *n* is the number of data points and $\left\| x_i^{(j)} - c_j \right\|^2$ is the distance between a data point $x_i^{(j)}$ and the cluster centre c_j. *K-means clustering* is a two-step iterative process where each data point *n* is initially assigned to the nearest mean, *k*. Next, the means

are adjusted to match the sample means. This process is then iterated until all the means match the sample, at which point the iteration stops [31].

The use of K-means clustering will then allow for the differentiation of areas of different strain. When used in conjunction with false colouring the strain fields present within the sample can be seen progressing from areas of high strain to those of low strain, fig. 5.17.

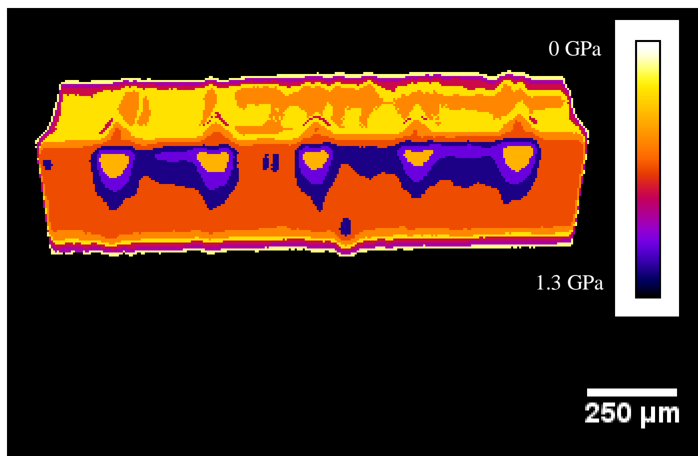

Figure 5.17: K-means cluster with false colour showing areas of strain from sample 1. Strain measurements were obtained using micro-Raman Spectroscopy

While XRT images such as this cannot give quantitative strain data, its use combined with complementary techniques, e.g. micro-Raman Spectroscopy (µRS), can give the location and magnitude of strain seen within the sample. The one major drawback of this technique is that it will only give an absolute value for the strain and will not differentiate between compressive and tensile strain. However this can be done using µRS which will be discussed in section 6.

The use of ST topography in low absorption conditions allows for the preservation of direct depth data, as mentioned in section 5.3.4. Using this property it is possible to segment or slice the image in fig. 5.17 and split the image, see fig 5.18 below. Using this technique the progression of the strain field through the bulk silicon can be observed.

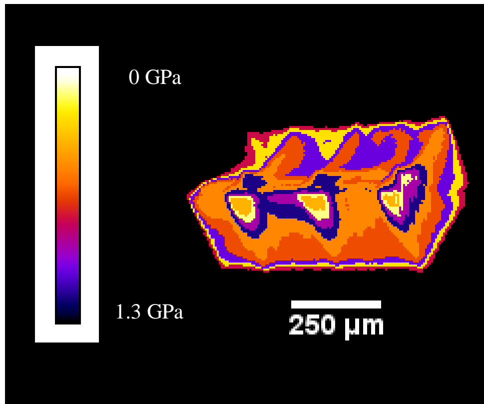

Figure 5.18: Fig. 5.17 after slicing through an indent. Strain field is visible propagating through the bulk silicon

Analysis of fig. 5.18 shows that the strain field extends approx. 120µm into the silicon confirming that this technique will give information on defects inside the bulk silicon and is yet completely non-destructive.

Fig. 5.19A and B show how the data derived from *K-means clustering* can be used to enhance our µRS data. Fig. 5.19A is a *K-means cluster* of the 220 ST topography for a 600 mN indented Si sample (Sample 9, Indent 1), and this has been matched to fig. 5.19B which is a 2D Raman map of the same indented region with the outline of the indent drawn in.

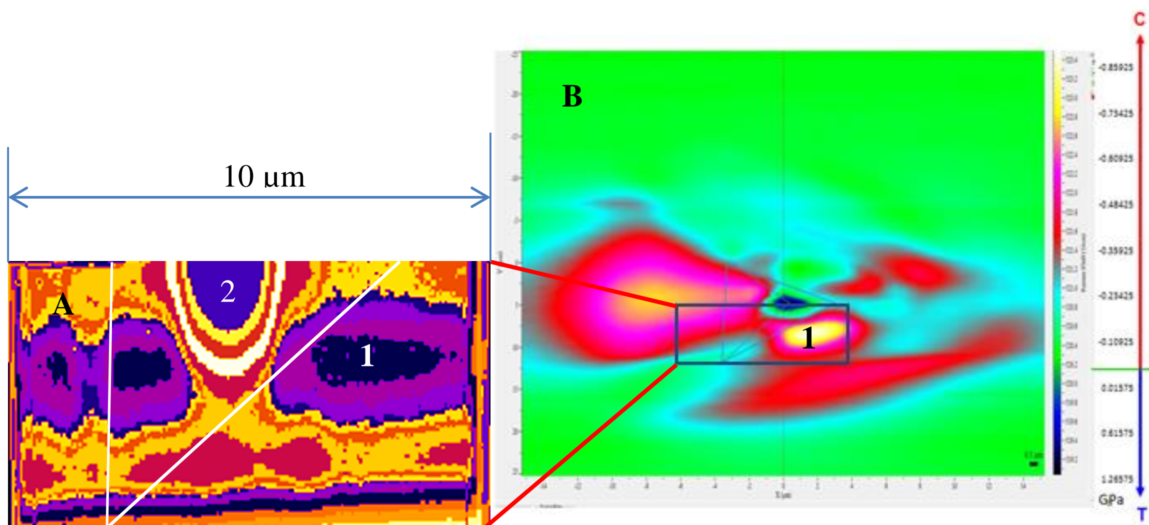

Figure 5.19: Correlation between µRS and XRT. Fig. 5.19A is a *K-means cluster* of 220 ST topography for a 600 mN indent (Sample 9, Indent 1). False colouring is added to highlight areas of highest strain. Fig. 5.19B is a 2D Raman map of the same indent.

In fig. 5.19A the strain resulting from the indent can be seen in the area marked ‘2’ above. The area marked ‘1’ in both images are areas of high compressive strain, approx. 0.8 GPa.

5.5 Production of 3D Physical Models

A physical representation of the image shown in fig. 5.7 was created using two different methods. *Mimics version 13.1 x64* was utilised to threshold the images and to create a binary mask of the volume data. This binary mask was sent to *Advanced Design Consultants*, a company specialising in Stereolithography (SLA). This process uses Ultra Violet (UV) light to solidify light sensitive epoxy resin. The UV laser is directed by a computer guided mirror. The light then hardens the resin. The model is built up layer by layer of 0.1mm thickness. The model is then cured in a UV oven.

The SLA material is a low viscosity liquid photopolymer, Watershed XC, which produces a tough water resistant physical representation of the image, fig. 5.20.

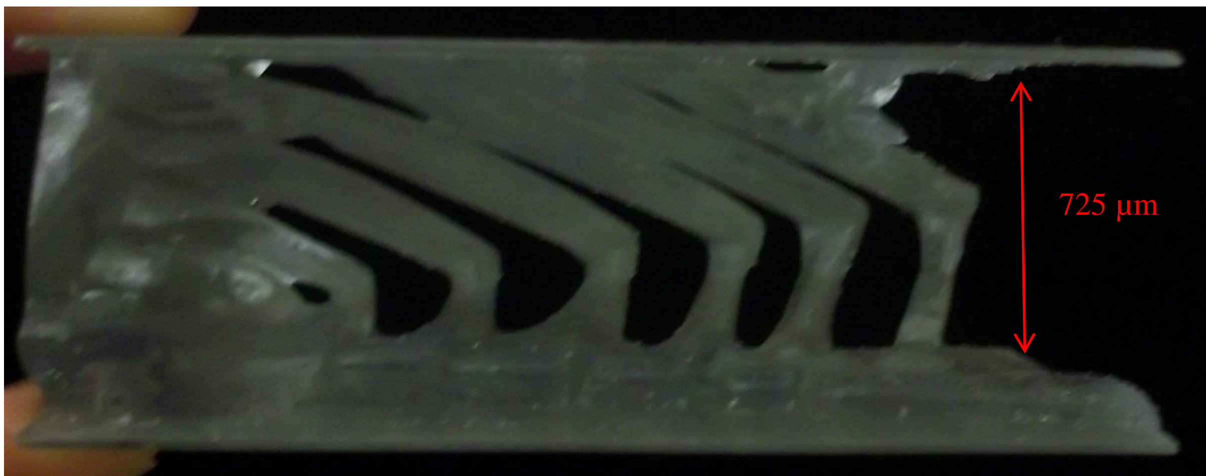

Figure 5.20: Physical representation of the dislocation loops from fig. 5.7. Part created using SLA technology from Advanced Design Consultants.

The second process takes the binary mask and uses it to control a laser etching system and was created by *Gruner Laser Products*. This is typically accomplished by using a high frequency Nd:YAG laser. The laser is focused into a block of laser glass and at the point of focus the heat generated causes the glass to fracture at the focal point, fig. 5.21.

Fig. 5.21: 3D laser blown crystal engraving of dislocation loops from fig. 5.7

5.6 Summary

This section of the thesis detailed the process that was used to create three dimensional images from ST topographs. It showed how these images could be used to non-destructively examine defects, in particular, dislocation loops within a silicon sample. It also showed how physical models of these defects could be produced. The section showed how one can now travel through the sample and observe the progression of the loops.

5.7 References

[1] A. N. Danilewsky, J. Wittge, A. Hess, A. Cröll, D. Allen, P.J. McNally, P. Vagovič, A. Cecilia, Z. Li, T. Baumbach, E. Gorogostegui-Colinas, M.R. Elizalde, Nuc. Instrum. Meth. Phys. Res. B **268**, 399 (2010).

[2] J. Wittge, *In Situ Investigation of Defects in Semiconductors*, PhD thesis (Albert-Ludwigs-Universität Freiburg, Germany, 2012).

[3] A. R. Lang, Acta Cryst. **12**, 249 (1959).

[4] A. R. Lang, J. Appl. Phys. **30**, 1748 (1959).

[5] A. L. Andersen and L. Gerward, Phys. Stat. Sol. A **23**, 537 (1974).

[6] S. Kawado and J. Aoyama, Appl. Phys. Lett. **34**, 428 (1979).

[7] W. Ludwig, P. Cloetens, J. Härtwig, J. Baruchel, B. Hamelin, and P. Bastie, J. Appl. Cryst. **34**, 602 (2001).

[8] S. Kawado, T. Tishi, S. Iida, Y. Suzuki, Y. Chikaura, and K. Kajiwara, J. Synchrotron Rad. **11**, 304 (2004).

[9] S. Kawado, T. Taishi, S. Iida, Y. Suzuki, Y. Chikaura, and K. Kajiwara, J. Phys. D **38**, 17 (2005).

[10] K. Kajiwara, S. Kawado, S. Iida, Y. Suzuki, and Y. Chikaura, Phys. Stat. Sol. **204**, 2682 (2007).

[11] T. Mukaide, K. Kajiwara, T. Noma, and K. Takada, J. Synchrotron Rad. **13**, 484 (2006).

[12] V. V. Kvardakov, K. M. Podurets, S. A. Schetinkin, J. Baruchel, J. Härtwig, and M. Schlenker, Nuc. Instrum. Meth. Phys. Res. A **575**, 140 (2007).

[13] T. A. Ferreira and W. S. Rasband, *The ImageJ User Guide Version 1.43*, (2010).

[14] W. S. Rasband, *ImageJ Documentation*.

[15] M. Cholewa and A. Rack, *ANKA Instrumentation Book* (ANKA Angstroemquelle Karlsruhe, Germany, 2007), 2009, p. 84.

[16] A. Rack, T. Weitkamp, S. Bauer Trabelsi, P. Modregger, A. Cecilia, T. dos Santos Rolo, T. Rack, D. Haas, R. Simon, R. Heldele, M. Schulz, B. Mayzel, A.N. Danilewsky, T. Waterstradt, W. Deite, H. Riesemeir, B.R. Müller, T. Baumbach, Nuc. Instrum. Meth. Phys. Res. B **267**, 1978 (2009).

[17] A. N. Danilewsky, R. Simon, A. Fauler, M. Fiederle, and K. W. Benz, Nuc. Instrum. Meth. Phys. Res. B **199**, 71 (2003).

[18] A. N. Danilewsky, A. Rack, J. Wittge, T. Weitkamp, R. Simon, H. Riesemeier, and T. Baumbach, Nuc. Instrum. Meth. Phys. Res. B **266**, 2035 (2008).

[19] R. Simon and A. N. Danilewsky, Nuc. Instrum. Meth. Phys. Res. B **199**, 550 (2003).

[20] D. Allen, J. Wittge, J. Stopford, A. N. Danilewsky, and P. McNally, J. Appl. Cryst. **44**, 526 (2011).

[21] T. Tuomi, K. Naukkarinen, and P. Rabe, Phys. Stat. Sol. **25**, 93 (1974).

[22] M. D. Abramoff, P. J. Magalhaes, and S. J. Ram, Biophoton Int. **11**, 36 (2004).

[23] G. Hildebrandt, Acta Cryst. A **35**, 696 (1979).

[24] A. Authier, S. Lagomarsino, and B. K. Tanner, *X-Ray and Neutron Dynamical Diffraction Theory and Applications* (Plenum Press, USA, 1996), 357, p. 419.

[25] D. K. Bowen and B. K. Tanner, *High resolution X-ray Diffractometry and Topography* (Taylor & Francis, London, 1998), p. 252.

[26] P. J. McNally, T. Tuomi, D. Lowney, K. Jacobs, A. N. Danilewsky, M. O'Hare, and L. Considine, Phys. Stat. Sol. **185**, 373 (2001).

[27] B. K. Tanner, J. Electrochem. Soc. **136**, 3438 (1989).

[28] J. Wittge, A. N. Danilewsky, D. Allen, P.J. McNally, Z. Li, T. Baumbach, E. Gorostegui-Colinas, J. Garagorri, M.R. Elizalde, D. Jacques, M.C. Fossati, D.K. Bowen, B.K. Tanner, J. Appl. Cryst. **43**, 1036 (2010).

[29] B. Schmid, J. Schindelin, A. Cardona, M. Longair, and M. Heisenberg, BMC Bioinformatics **11**, 274 (2010).

[30] F. Vallino, A. Jacques, and A. George, Phys. Stat. Sol. **222**, 51 (2000).

[31] D. MacKay, *An Example Inference task: Clustering* (Cambridge University, UK, 2003), 1, p. 284.

Chapter 6 Micro-Raman Spectroscopy Results

6.1 Introduction

As part of the overall SiDAM project, micro Raman Spectroscopy (μRS) was used to measure the strain produced by nanoindentation of silicon samples. Two different lasers were employed giving different penetration depths: a 488nm Ar+ visible laser with a penetration depth of ~569nm and a 325nm He-Cd UV laser with a penetration depth of ~9nm, as discussed in section 2.6.

The scans consisted of two modes as discussed below, the line scan and the map scan. The line scan gives not only a measure of the strain observed in a line across the area of interest but also an indication of the different high pressure polymorphs of silicon present within the indented silicon under test.

The map scan is a 2D scan across an area of interest and gives a complete map of the area showing the extent of the areas of high strain, one can also measure crystalline disorder via Raman peak width measurements, or track the spatial location of a Raman peak corresponding to a specific polymorph. Scans of the indents were also compared both pre and post thermal anneal.

6.2 Experimental Setup

The system used in this study is the Jobin-Yvon Horiba LabRam HR800 system running LabSpec 5 software. The system is integrated with a microscope confocally coupled to an 800mm focal length spectrometer. The samples are mounted on a high precision table capable of x-y and z translation. The table can be moved manually and is also motorised and can be

controlled by either a joystick or directly from the LabSpec software. A diffraction grating of 1800 groves per millimetre is used to split the Raman signal into individual wavelengths, which are then directed onto a CCD detector.

The HR800 uses two different CCD detectors: a liquid nitrogen cooled CCD3000 system and an air cooled Synapse CCD system. The CCD3000 is required when there is a need for acquisition times of greater than 120s, as the Synapse system will saturate for these longer times. Two lasers were connected to the Raman system through a periscope: a Uniphase 2014 488nm Argon ion (Ar^+) visible laser with a maximum output power of 20mW, fig. 6.1A, a Kimmon Koha IK3201IR-F 325nm Helium Cadmium (He-Cd) ultraviolet (UV) laser with a max. output power of 22.4mW, fig. 6.1B, a third laser, a Spectra-Physics Stablite 2017 364nm Ar^+ UV laser with a max. output power of 100mW, fig. 6.1C was added later but not used for this study..

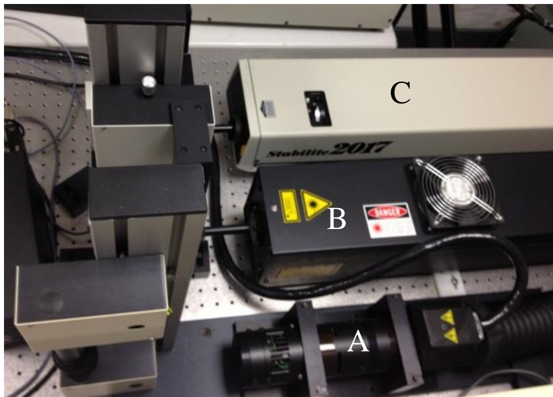

Figure 6.1: Three lasers attached to the Raman system. A is the 488nm visible Ar^+ laser, B is the 325nm He-Cd UV laser and C is the 364nm Ar^+ UV laser (not used).

As mentioned in section 2.6 each laser will give a different penetration depth depending on the laser wavelength. The penetration depth in silicon for the 488nm laser is ~569nm, for the 325nm laser it is ~9nm and for the 364nm laser the penetration depth is ~15nm.

6.3 System Calibration and Error Compensation

In order to be able to accurately measure local strain in silicon it is essential to ensure that the Raman system is properly calibrated before measuring. In order to do this and to ensure that there is reproducibility in results the following steps were used.

6.3.1 System Calibration

Before any measurements were taken the lasers were switched on and allowed to stabilise for an hour. The CCD3000 was given time to cool down to -125°C and this could take up to 3 hours.

The zero position of the spectrometer then needs to be set. This is accomplished using a white light source and with the spectrometer units set to nanometres. Using the "Zero" parameter the spectrum is then adjusted to the zero position.

Once the Zero position is set the spectrometer needs to be centred on the Raman line of the TO Raman phonon peak shift for unstrained silicon at 520.07 cm^{-1} [1]. A piece of unstrained reference (100) silicon is placed on the sample table and the laser is focused on the sample. The spectrometer units are set to cm^{-1} and the spectrum is taken. Using the "Koeff" parameter the spectrum is adjusted until it lies at 520.07 cm^{-1}, fig. 6.2. As mentioned in section 3.3, compressive stress leads to an increase in Raman frequency and for this reason all the subsequent graphs in this section will show compressive strain as a positive stress and tensile as negative.

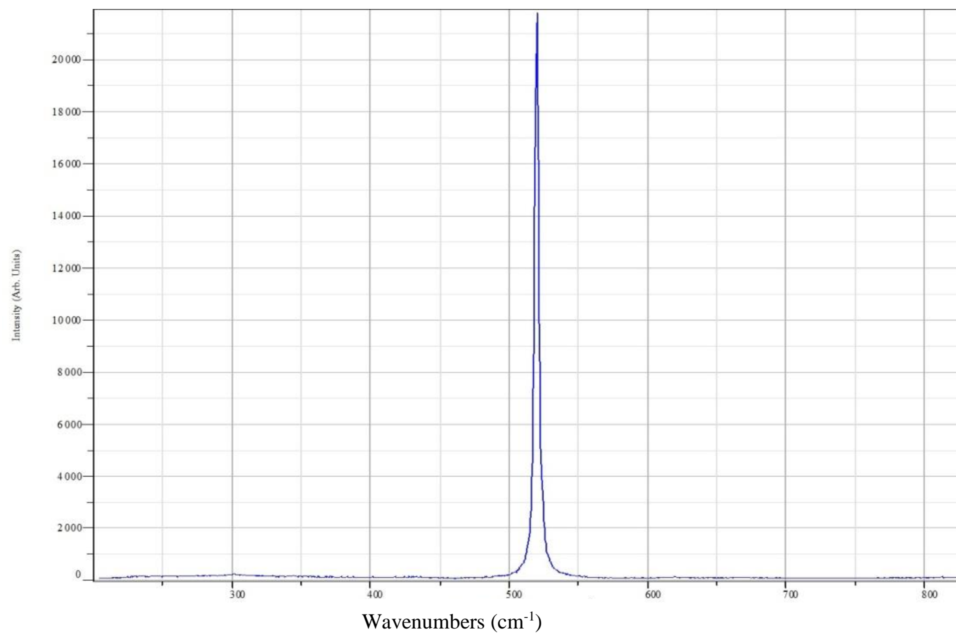

Figure 6.2: Calibration peak taken from a piece of unstrained reference silicon with a sharp peak at 520.07 cm^{-1}. The sharp peak is characteristic of a crystalline substance.

Once achieved this spectrum is recorded to be used as a calibration spectrum against which the Raman shifts of the samples under test will be calculated.

6.3.2 Error Compensation

Large spatial area, and temporally long scans, especially those that are required for 2D Raman maps can take from a number of hours to a number of days to complete. In addition to the local stresses in the sample under test, on long scans, the Raman spectrum can be affected by external factors. Of particular impact are temperature and laser stability. In order to compensate for these factors and to eliminate the drift caused by these, the plasma lines of the laser are recorded, fig 6.3.

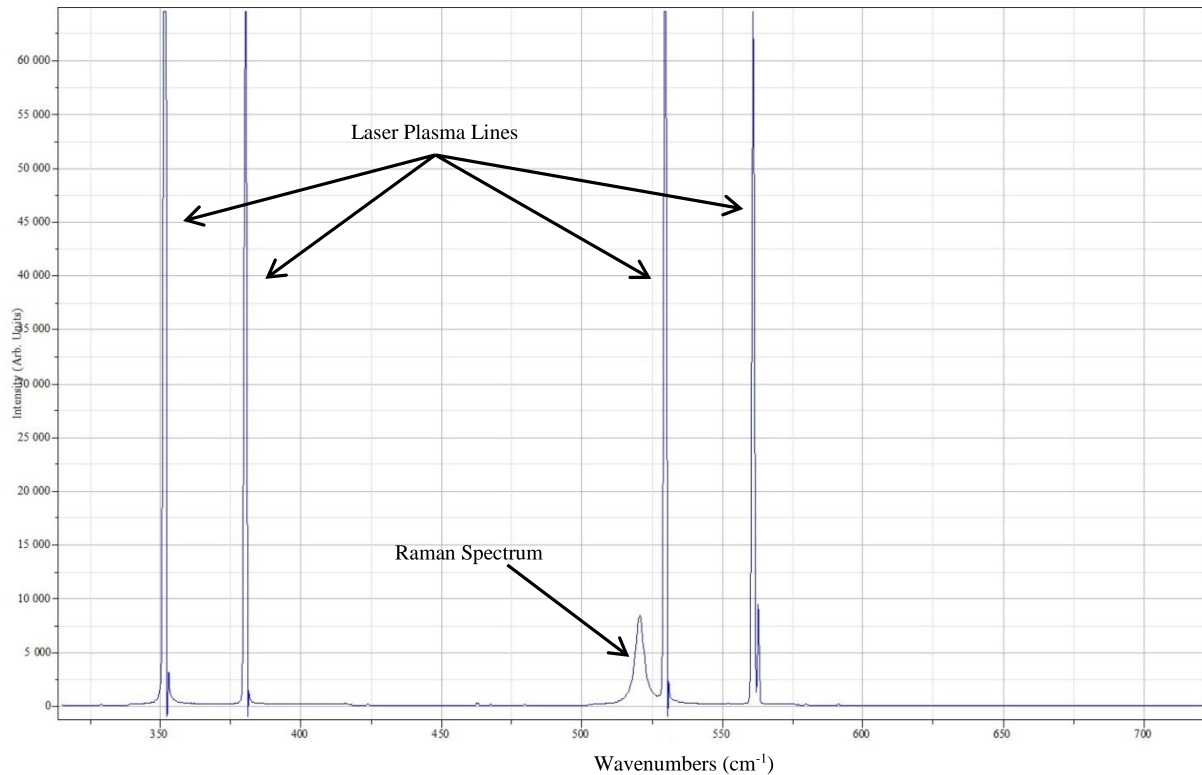

Figure 6.3: Raman Spectrum from a 600mN indent (Sample 9_Indent 1). Both the Raman spectrum from the indent and the laser plasma lines are visible

The laser plasma lines are Rayleigh scattered and so are insensitive to any strain in the sample [1]. The plasma lines are then plotted over the length of the scan and the drift, due to the external factors, can be calculated. This drift can then be subtracted from the Raman spectra over the length of the scan to provide error compensation.

Another source of possible error can be due to laser heating of the sample. The laser is focused to a spot of ~1µm in diameter and as such will cause localised heating of the sample. Due to thermal expansion the silicon TO phonon shifts to a lower energy (~0.025 cm^{-1}/K), which would erroneously imply the presence of a tensile strain. This shift is less than the resolution of the spectrometer used in this study [2] and thus is of no concern.

6.4 Raman Results

The Micro Raman Spectroscopy data were acquired using both 1D Line Scans and 2D Map Scans, both of which will be explained in the following sections. As mentioned in section 6.3 a reference spectrum from unstrained silicon is taken before every set of measurements and the µRS results are then referenced to this reference spectrum. All the strain measurements are estimated assuming biaxial strain and calculated using:

$$\sigma_{xx} = \sigma_{yy} = -\frac{\Delta\omega}{4}\ GPa \qquad 5.1$$

$$\Delta\omega = \omega_1 - \omega_0 \qquad 5.2$$

where σ_{xx} and σ_{yy} are stress components in the X – Y plane, ω_1 is the Raman spectral line from the sample under test and ω_0 is the Si-Si Transverse Optical (TO) spectrum line at ~520 cm^{-1} [1] and $\Delta\omega$ is in units of cm^{-1}.

6.4.1 Line Scan

A Line scan comprises a series of individual scans or spots taken sequentially in a line across the area of interest as shown in fig. 6.4.

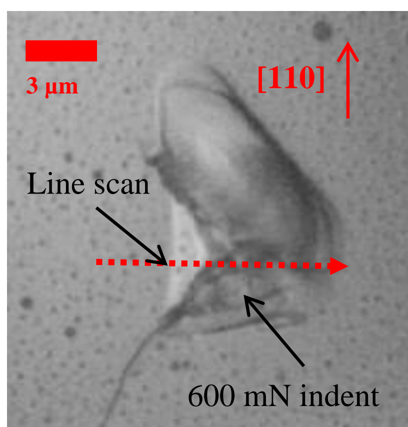

Figure 6.4: Optical micrograph of a 600 mN indent (Sample 9). The dashed red line shows the progression of a 1D line scan across the indent. This was accomplished by taking individual spectra in 0.5 µm steps over the length of the scan.

Using this data it is possible to create a graph of the strain against position across the indent.

Line scans were obtained using both the 325nm He-Cd UV laser giving a penetration depth d_p of ~9nm and the 488nm Ar^+ visible laser with a penetration depth, d_p ~569nm, thus giving data from both the top surface of the sample and down into the bulk of the sample, as shown in fig. 6.5.

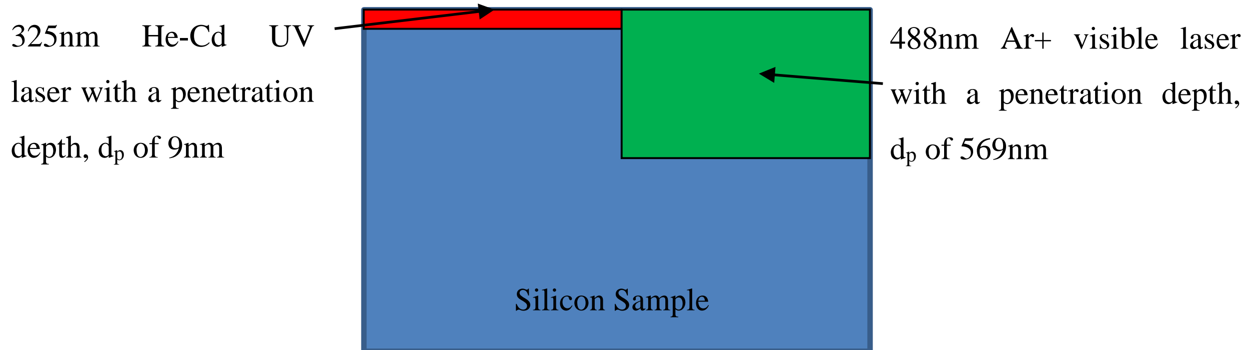

Figure 6.5: Schematic showing the penetration depths of the different lasers (not to scale)

Individual line scans obtained from 600mN and 500mN indents are shown below. Individual line scans for other indents are in the attached DVD.

Data obtained from both scans were compared. Scans taken with the 325nm UV laser, d_p~9nm, showed only compressive stress with the maximum stress observed at or near the centre of the indent. Figs. 6.6 and 6.7 show data from a 600mN and a 500mN indent respectively, with figs. 6.8 and 6.9 showing results from indents ranging from 600mN to 100mN loads. Data was taken every 0.5µm as shown in fig. 6.6, these points are removed for subsequent figures for ease of visibility.

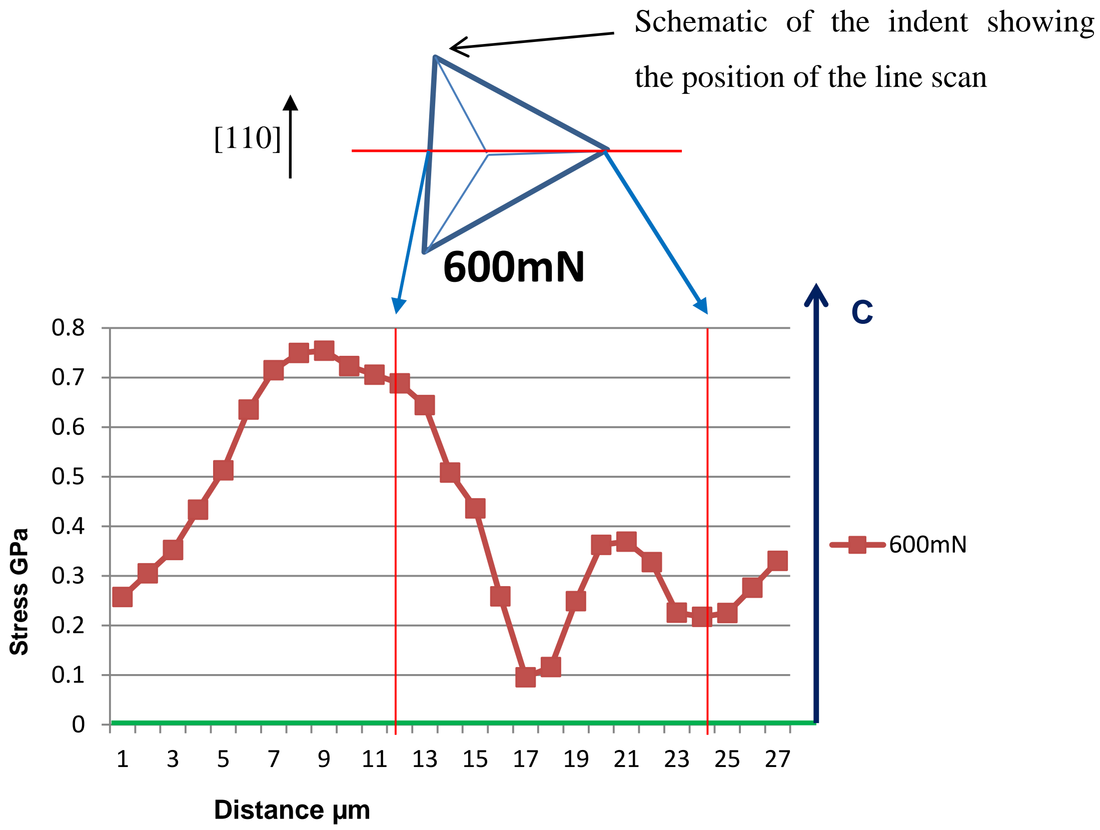

Figure 6.6: Data from line scan taken from a 600 mN indent (Sample 9, Indent 1), showing only compressive stress. Data taken with a 325nm He-Cd UV laser, d_p ~ 9nm.

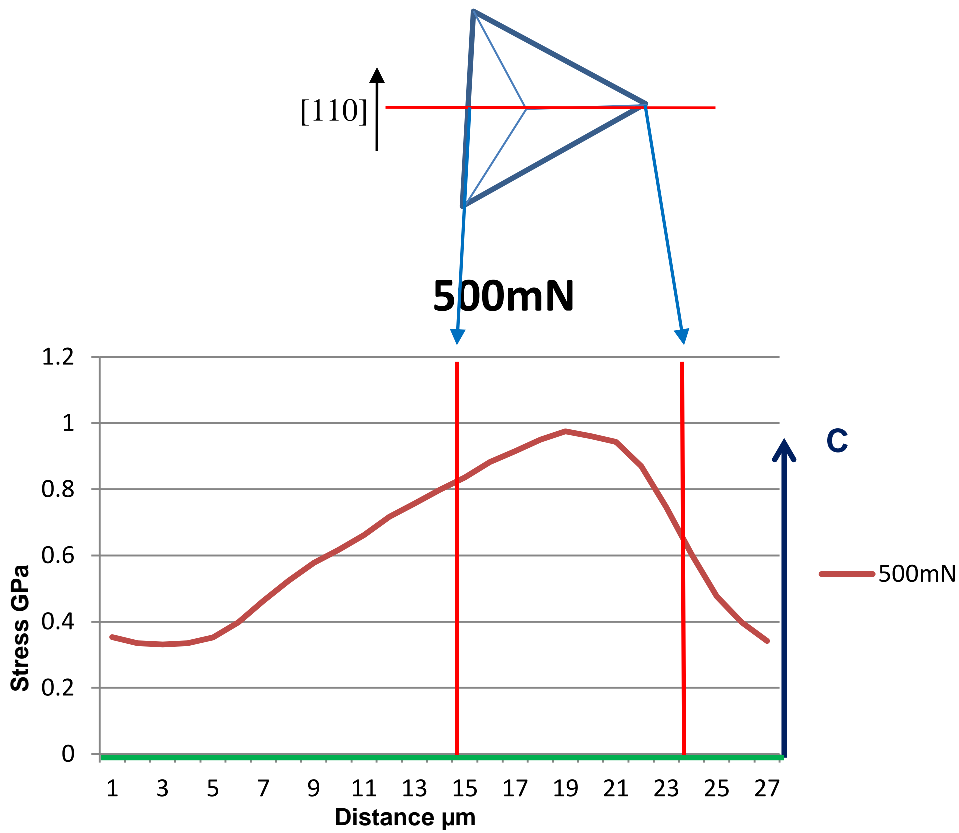

Figure 6.7: Data taken from 500mN indent (Sample 10, Indent 1) showing only compressive stress. Data taken with a 325 nm He-Cd, UV laser, d_p ~ 9nm

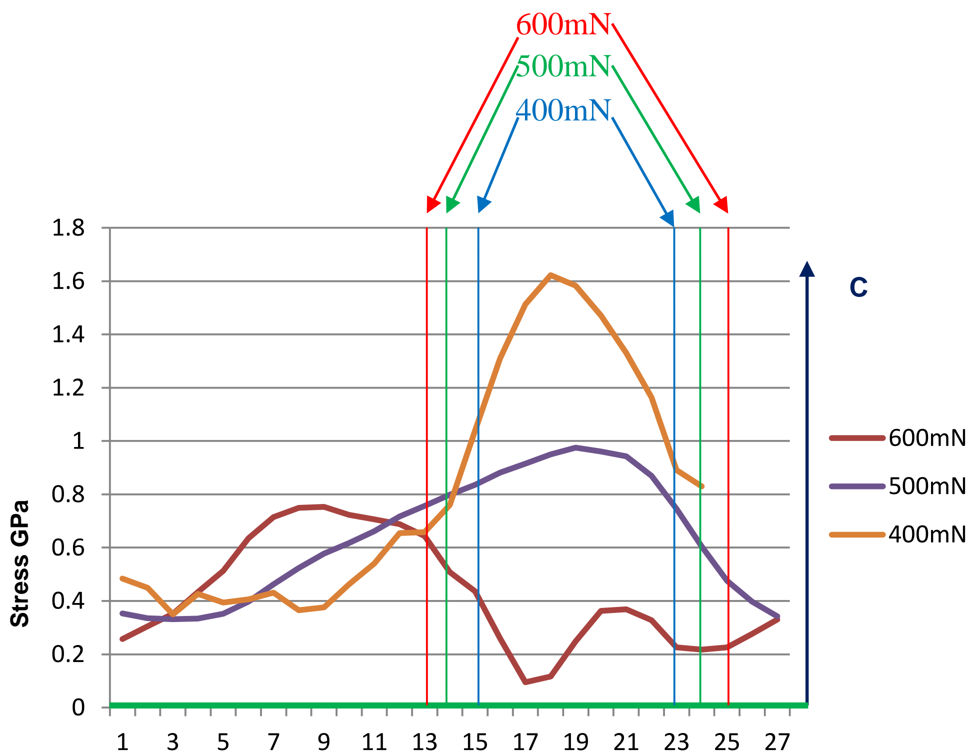

Figure 6.9: Stress data from a 600mN, 500mN and 400mN indent. Data taken with a 325 nm He-Cd, UV laser, d_p ~ 9nm

The anomalous behaviour of the 600mN indent shown in fig. 6.9 correlates with Raman peak broadening data shown in fig. 6.12 below. This behaviour will also be explained below. Compressive stress is denoted by a blue arrow while tensile stress will be denoted by a red arrow on the right hand side of these figures. The value of the stress is derived from eq. 5.1 above with the compressive strain corresponding to an increase in the Raman frequency (blue shift) while tensile strain will cause a decrease (red shift) [1].

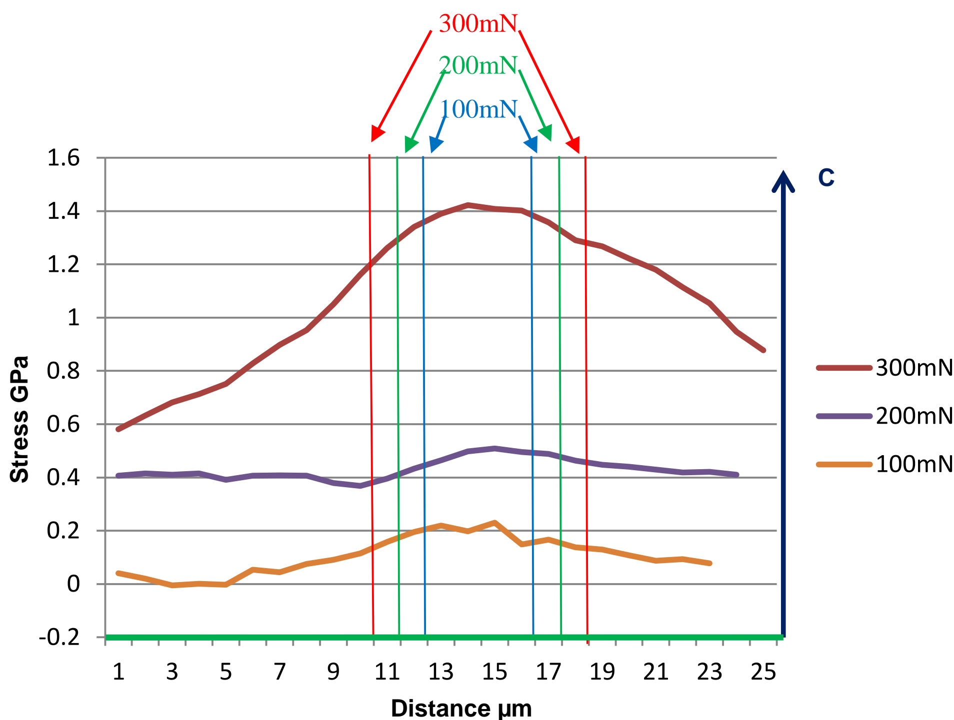

Figure 6.9: Stress data from a 300mN, 200mN and 100mN indent. Data taken with a 325 nm He-Cd, UV laser, d_p ~ 9nm

Analysis of the spectra taken from the centre of the indents created with 500mN to 100mN indents show a sharp peak whereas the peak shape from the 600mN indent shows broadening, fig. 6.10 and 6.11.

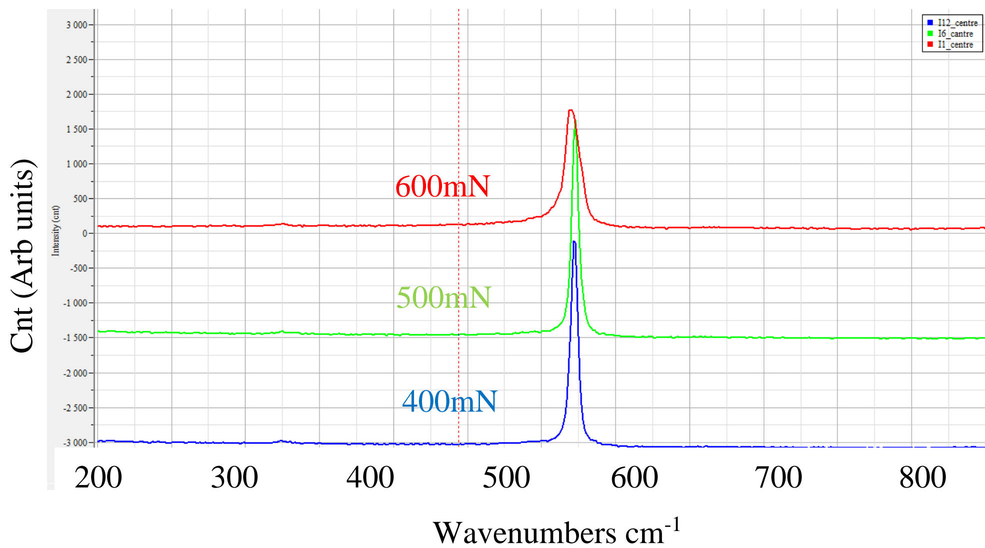

Figure 6.10: Raman spectra taken from the centre of a 600mN, a 500mN and a 400mN indents showing only Si-I. Data obtained using 325nm He-Cd laser, d_p~9nm

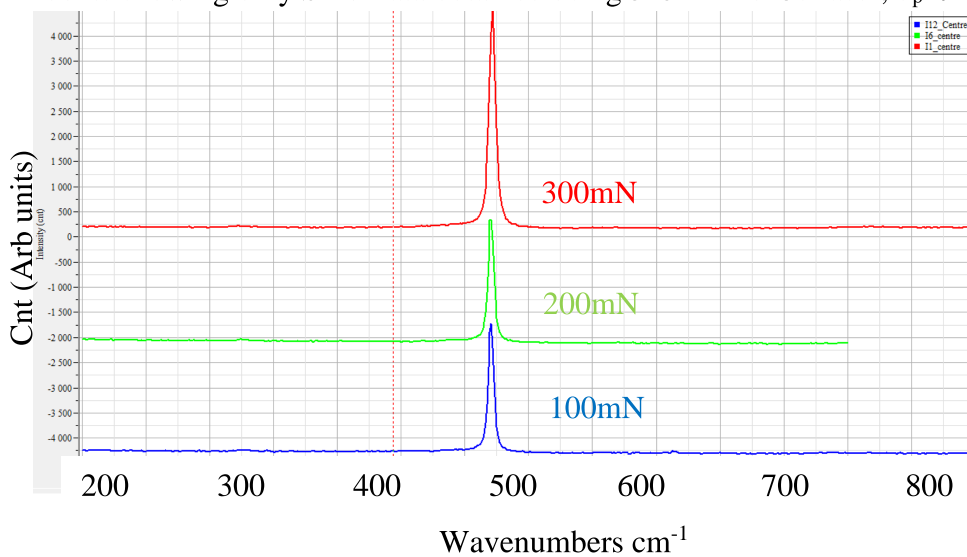

Figure 6.11: Raman spectra taken from the centre of a 300mN, a 200mN and a 100mN indents showing only Si-I. Data obtained using 325nm He-Cd laser, d_p~9nm

Figures 6.12 and 6.13 show graphs of the full width at half maximum (FWHM) of the Raman peak spectra taken across the indents. For indents ranging from 100mN to 500mN there is little change in FWHM across the indents, whereas the 600mN indent does show an increase in FWHM towards the centre of the indent.

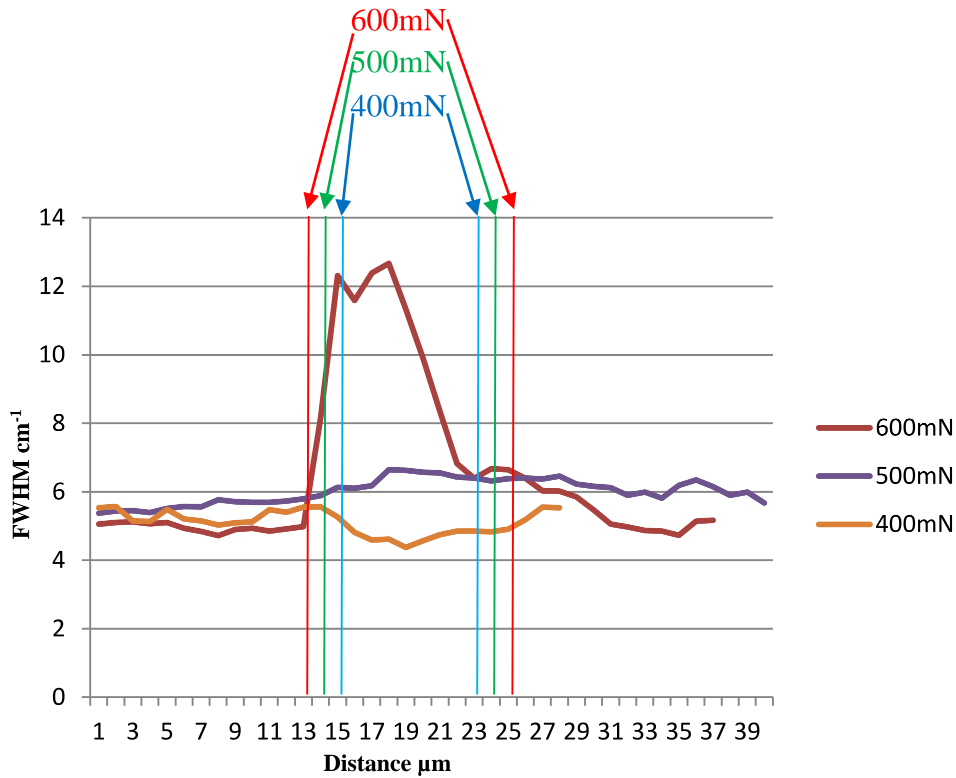

Figure 6.12: Raman peak FWHM data taken from indents 600mN, 500mN and 400mN. Data taken with a 325nm UV He-Cd laser, d_p ~9nm

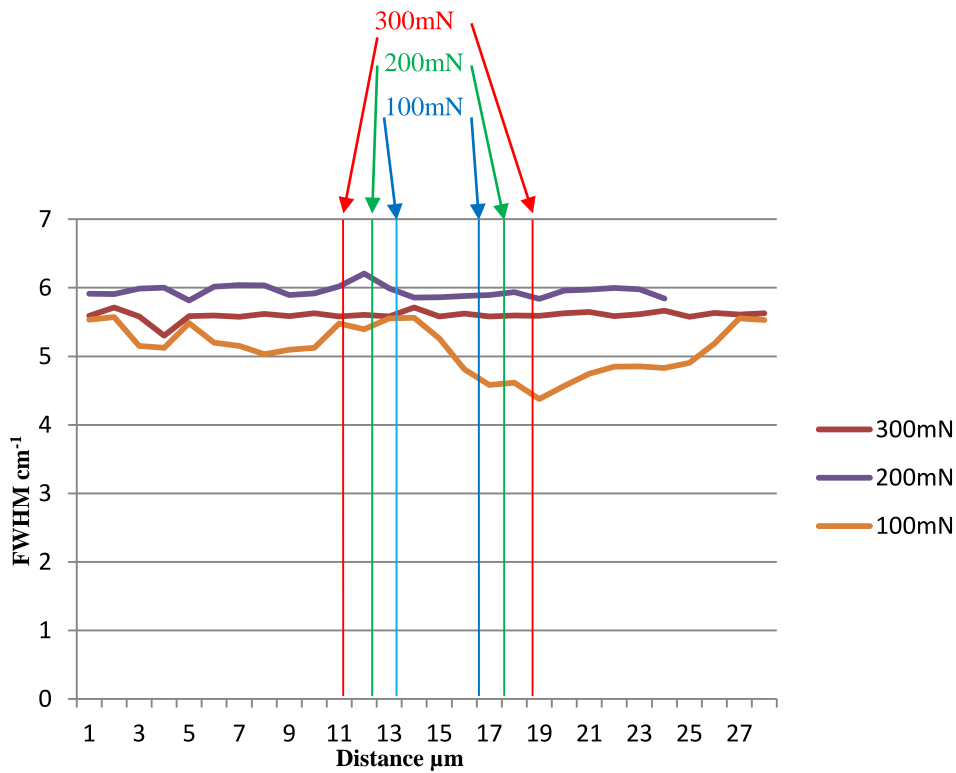

Figure 6.13: Raman peak FWHM data taken from indents 300mN, 200mN and 100mN. Data taken with a 325nm UV He-Cd laser, d_p ~9nm

Table 6.1 shows the average FWHM, plotted in fig. 6.14, across the indents and the standard deviation across the indent from a reference spectrum of 5.50564 cm^{-1}.

	600mN	500mN	400mN	300mN	200mN	100mN
Average	6.547324	6.013715	5.111653	5.601301	5.949257	5.111653
Std. Dev.	2.428504	0.37371	0.350023	0.0686769	0.120241	0.350023

Table 6.1: Table showing the average peak width in cm^{-1} and standard deviation from the reference spectrum for indents ranging from 100mN to 600mN

Indents from 100mN to 500mN show average peak widths of ~5.1 to 6 cm^{-1} with a standard deviation of less than 1, however the 600mN indent showed an average peak width of ~6.5 cm^{-1} and a maximum peak width of ~12cm^{-1}. This broadening of the peak width, along with the peak shift down to 520.49 cm^{-1} together with the apparent relaxation of compressive stress, shown in fig. 6.9, can be attributed to a breakdown of crystalline order which decreases the phonon lifetime causing an increase in bandwidth caused by the formation of nanocrystalline silicon [3].

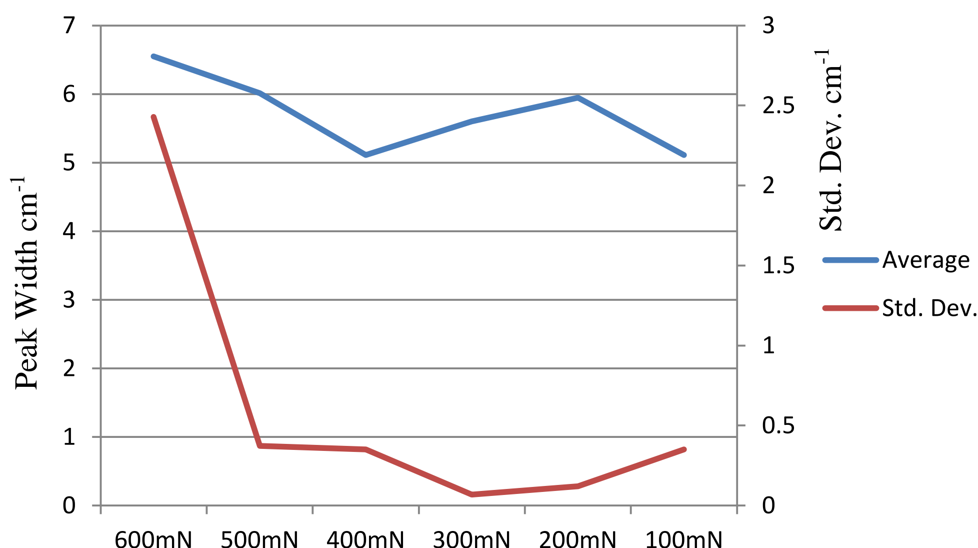

Fig. 6.14: Plot of table 6.1, showing the average peak width and standard deviation from a reference spectrum

Further analysis of the 600mN indent, see fig. 6.15, also shows the presence of peaks at 351cm^{-1} and 435cm^{-1} indicating the presence of Si-XII and Si-III respectively. A weak peak is also visible at ~325cm^{-1}, and a literature search for this peak shows that there is an identified peak at 330cm^{-1} attributed to a new metastable phase of silicon, Si-XIII, by both Domnich [4] and Ge [5] though in both cases this phase was observed at elevated temperatures ~170ºC. The nature of this phase of silicon is currently unknown and is thought to be a hexagonal structure similar to Si-IV or nanocrystalline silicon.

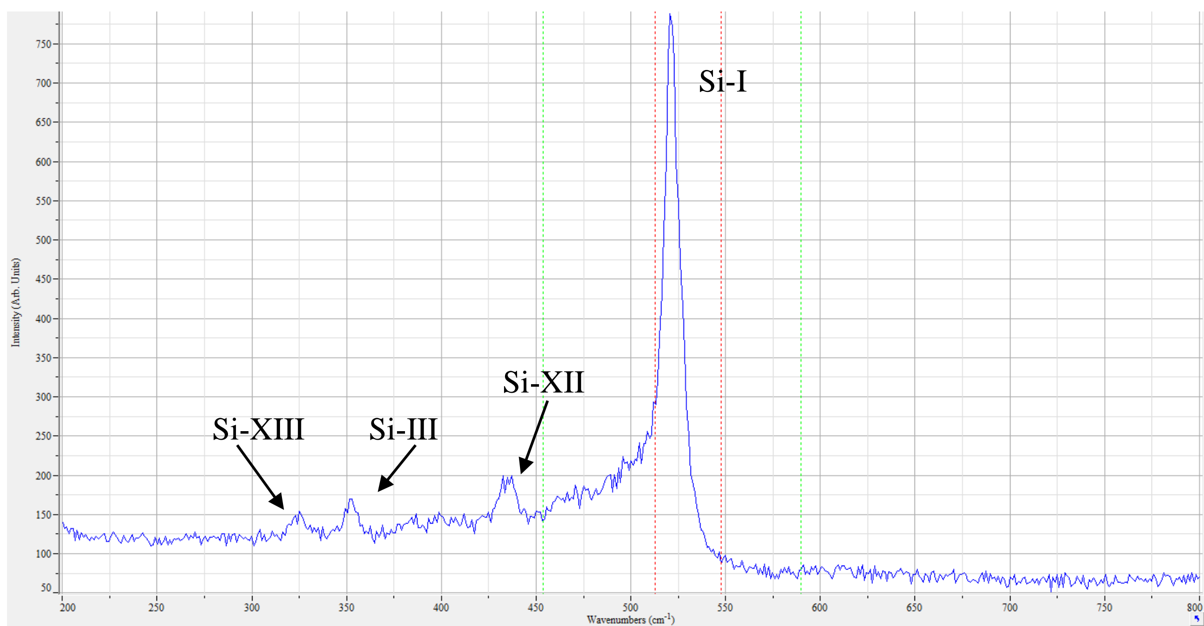

Figure 6.15: Raman spectrum taken from the centre of a 600mN indent showing Si-I peak at 521cm^{-1} with Si-III peak at 351 cm^{-1} and a Si-XII peak at 435cm^{-1}. There is also a peak at 325 cm^{-1} that could be attributed to Si-XIII

The same indents were next analysed using the 488nm Ar^+ laser, with a penetration depth d_p~569nm. This time, instead of a peak compressive strain at the centre, all indents above 100mN showed a tensile strain at the centre.

The data from the 600mN indent shows compressive strain at the edges of the indent up to a maximum of ~0.5 GPa, fig. 6.16, however at the centre of the indent a significant tensile peak was also observed with a maximum strain of ~1.5 GPa.

Similar behaviour graph can be seen in fig. 6.17 which represents data taken from a line scan across a 500 mN indent, Sample 10, Indent 1.

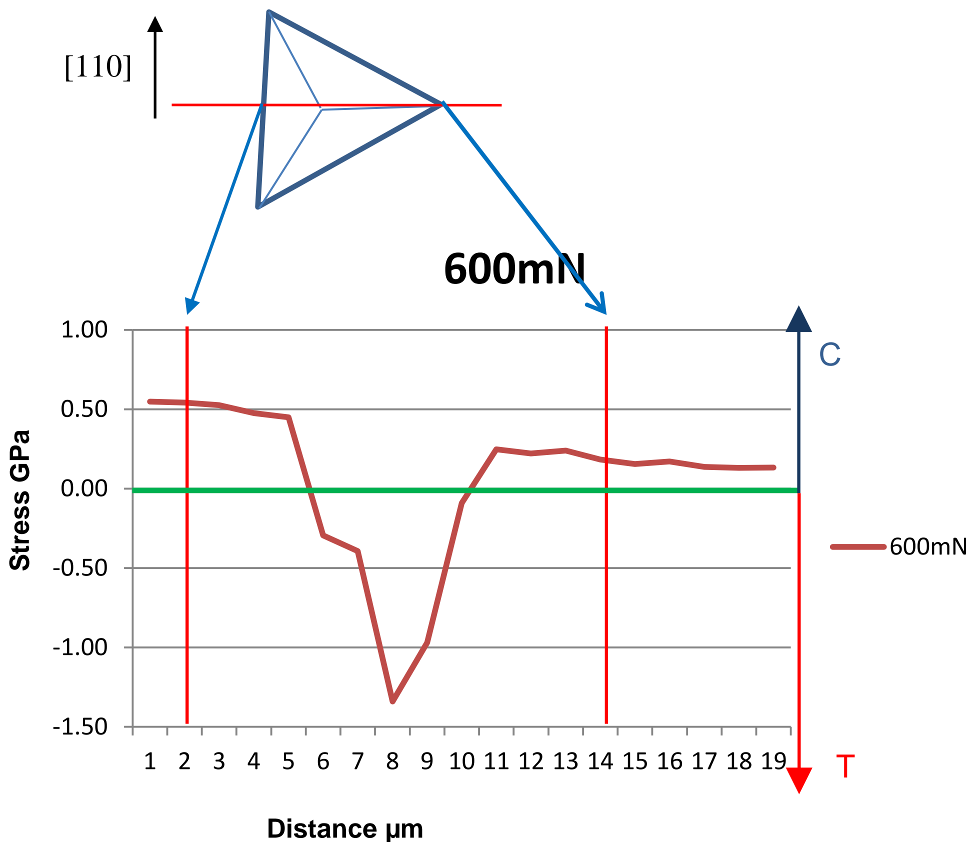

Figure 6.16: Data from the line scan taken from a 600mN indent (Sample 9, Indent 1) showing both compressive (C) and tensile (T) stress using a 488nm Ar^+ laser, d_p ~556nm.

The presence of this sub-surface tensile stress was clearly suggestive of the presence of a sub-surface crack occurring beneath the indent as shown in fig. 6.18. As the UV laser only penetrates through the top 9nm of the silicon, if the crack is sufficiently far below the surface so that the tensile s has no impact on the surface, spectra taken with this laser will only indicate compressive stress throughout the indent.

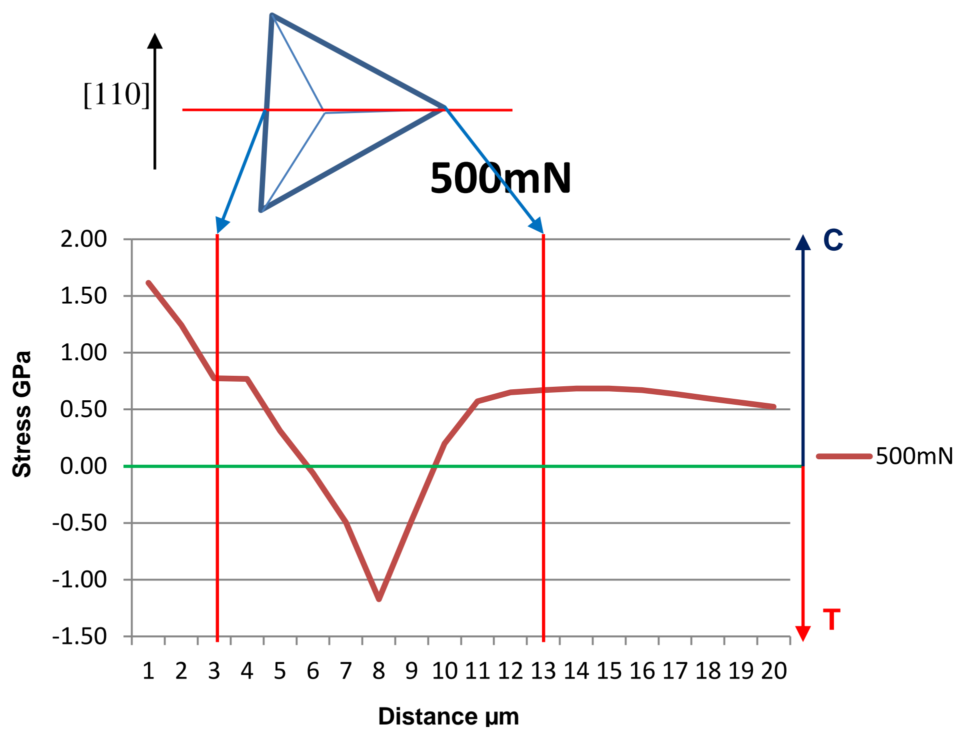

Figure 6.17: Data from the line scan taken from a 500mN indent (Sample 10, Indent 1) showing both compressive (C) and tensile (T) stress, data taken using a 488nm Ar^+ laser, d_p ~556nm.

These results agree with and confirm the theory developed by Lawn *et al*. [6-9]. Lawn postulated that a sharp indenter would create an elastic/plastic zone beneath the indent and that the area of maximum stress is at the base of the plastic zone as shown in figs. 6.18 and 6.19.

Lawn's theory that a sharp indenter, such as a Berkovich tip, can cause a sub-surface crack to form was later confirmed by Lloyd *et al*. [10] and Kailer *et al*. [11] who predicted the formation of lateral or horizontal cracks as well as the median cracks.

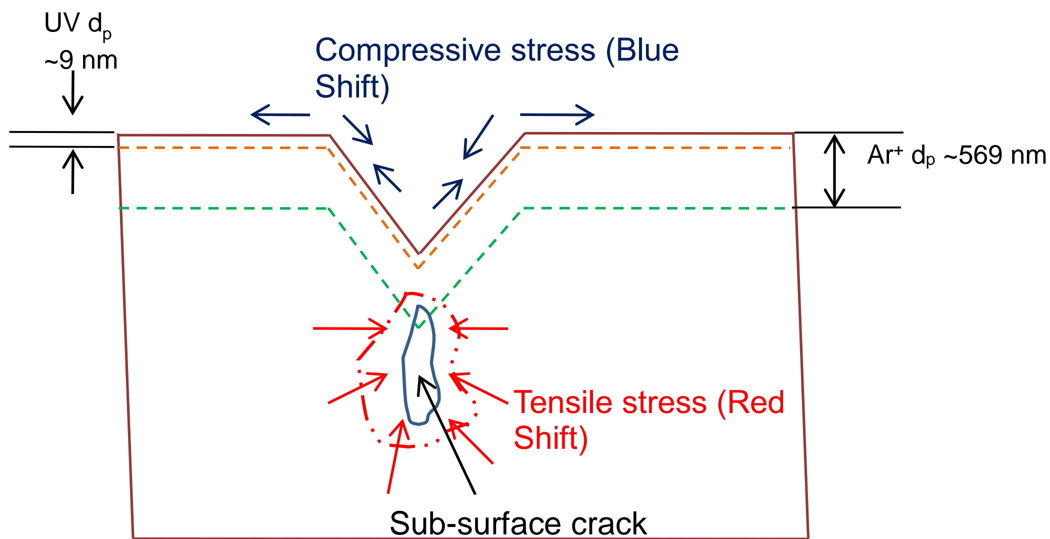

Figure 6.18: Schematic showing the proposed reason for tensile stress observed in figs. 6.16 and 6.17

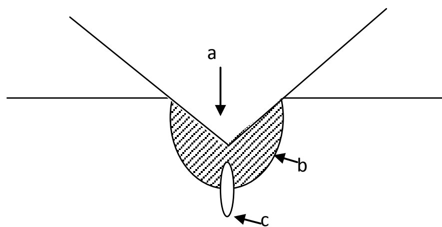

Figure 6.19: Model showing the elastic/plastic region under an indent. (a shows the indenter, b the plastic field and c the area of maximum stress) [4]

Physical confirmation of the existence of such cracks was established by use of Transmission Electron Microscope (TEM) micrographs performed on a 200mN indent, fig. 6.20. The observed cracks lie ~160nm below the surface of the indent. Two types of crack can be seen in the TEM micrograph, a 'horizontal crack' which extends across the width of the micrograph and a 'median crack', which normally develops in a plane normal to the surface and is aligned with the vertices of the indent [12]. Spectra from indents below 200mN loads show only compressive strain within the indent as shown in fig. 6.23 below.

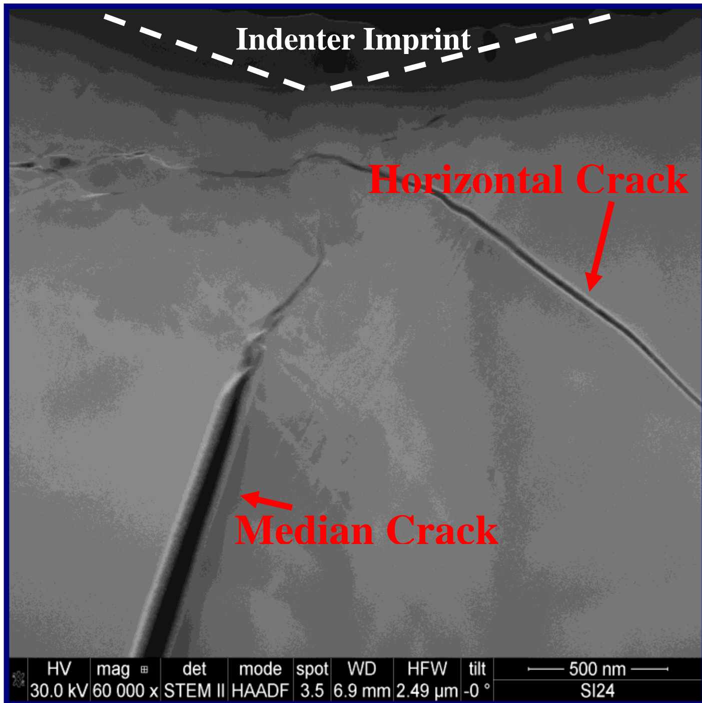

Figure 6.20: TEM micrograph of a 200mN indent. Both median and horizontal cracks are visible. Image courtesy of J. Garagorri, CEIT, Spain

This data is consistent across all indents down to 200mN loads as shown in figs. 6.21 and 6.22 below.

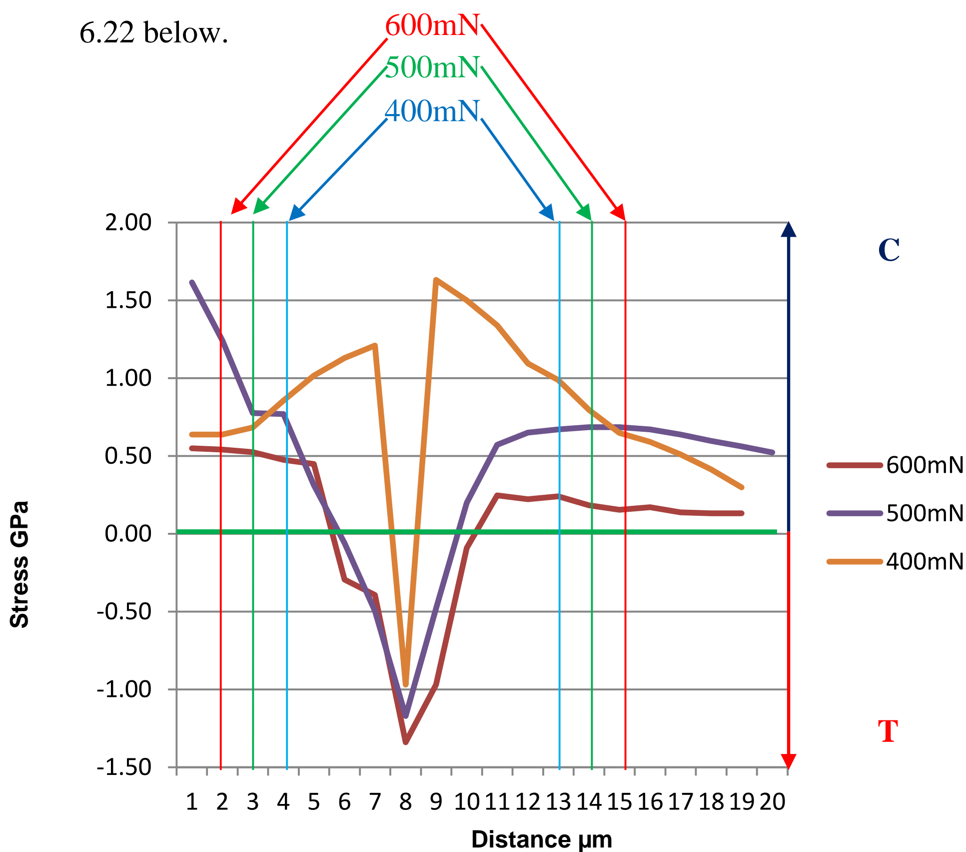

Figure 6.21: µRS stress data for 600mN, 500mN and 400mN indents. Ar^+ laser, d_p~556nm

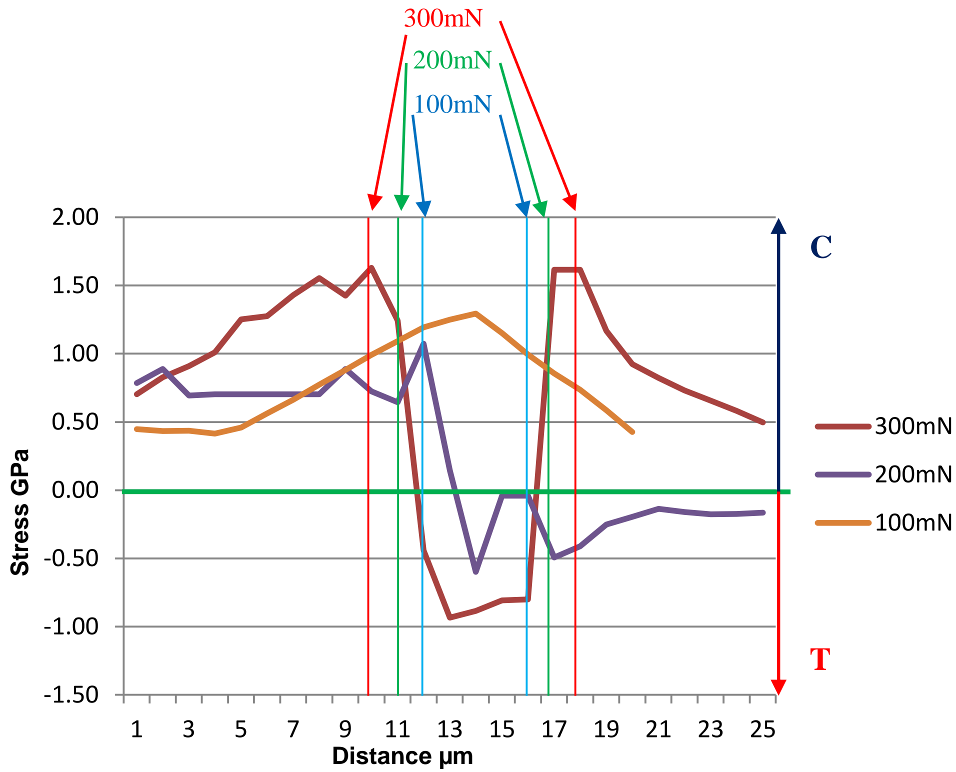

Figure 6.22: µRS stress data for 300mN, 200mN and 100mN indents. Ar^+ laser, d_p ~556nm

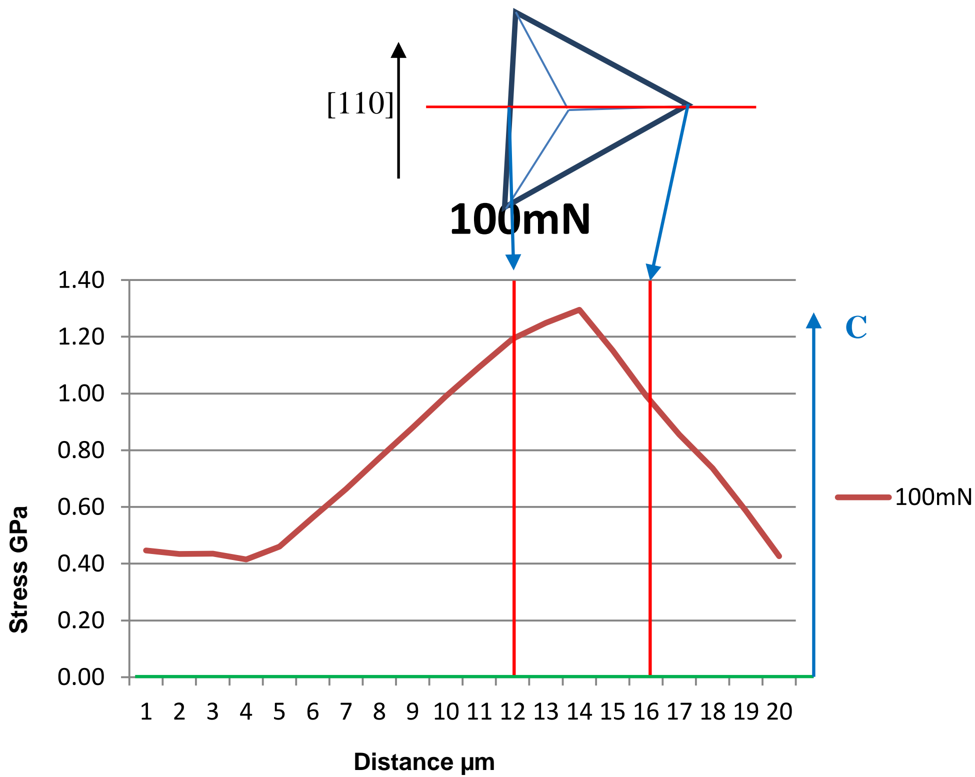

Figure 6.23: Data from the line scan taken from a 100mN indent (Sample 10, Indent 12) showing only compressive (C) stress, data taken using a 488nm Ar^+ laser, d_p ~556nm.

The lack of any observable tensile stress in indents of loads less than 200mN, see fig. 6.23, suggests that there is a minimum load required to initiate cracking beneath the indent. This supposition is in agreement with work performed by Cook and Pharr in 1990 [13] and Chen in 2012 [14], and would appear to agree with analysis of the high pressure polymorphs observed within the indents. The Raman FWHM peak data for each of the indents are shown in figs. 6.24 and 6.25 below.

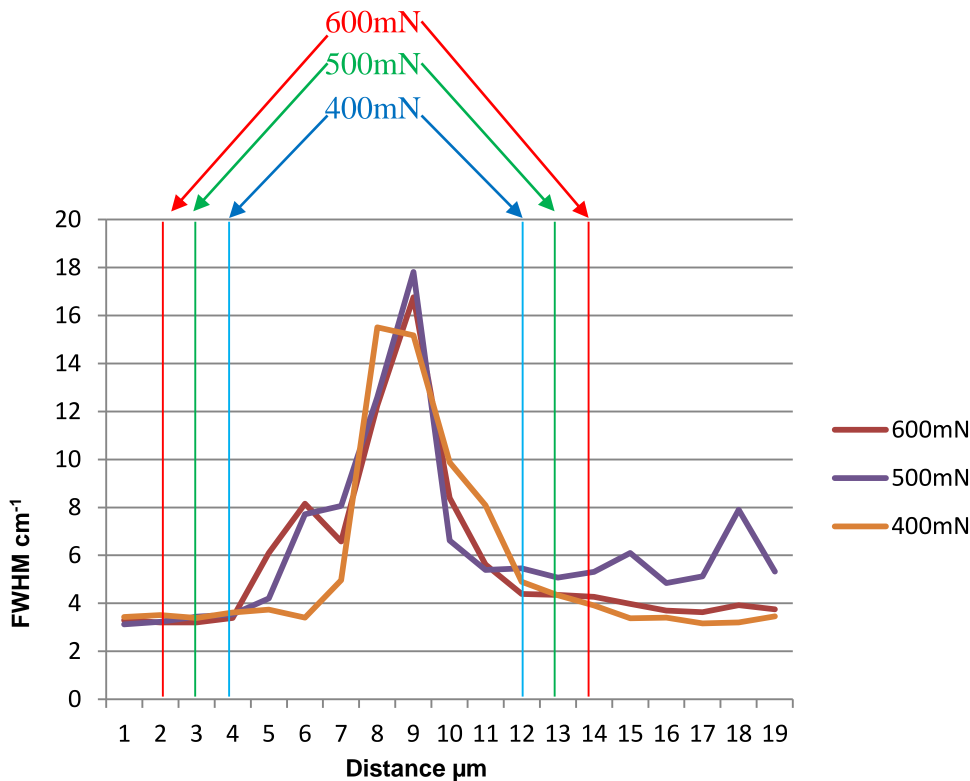

Figure 6.24: Raman peak FWHM data for 600mN, 500mN and 400mN indents. Ar^{+} laser, d_p~556nm

It can be seen from figs. 6.24 and 6.25 that there is a marked increase in the peak FWHM for each of the indents. The average FWHM is shown in table 6.2 below, and plotted in fig. 6.26, along with the standard deviation from the calibration spectrum of 3.54704 cm^{-1}. As can be seen there is broadening of each of the peaks indicating an increase in crystalline disorder. This increase in crystalline disorder, especially via the generation of multiple Si phases is further confirmed in figs. 6.26 and 6.27, which show Raman spectra taken from the centre of

the 600, 500, 400, 300 and 200 mN indents, which clearly indicate the presence of the high pressure polymorphs of silicon, primarily Si-III and Si-XII. The observed phases are in good correlation with literature, as noted in chapter 4 and references therein.

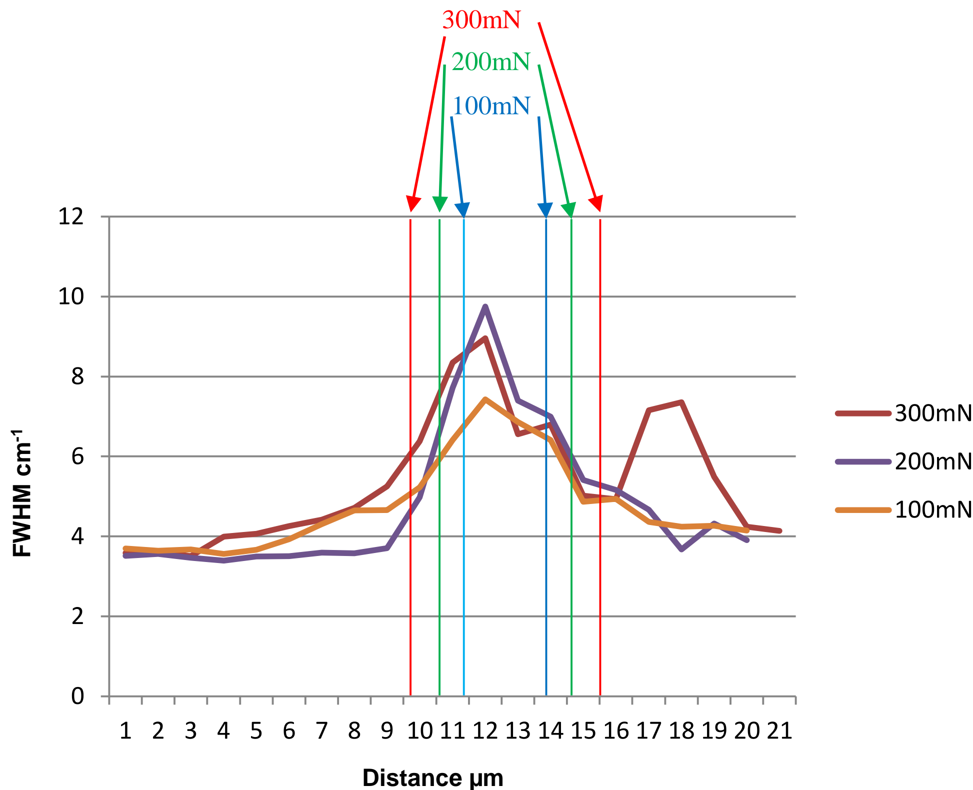

Figure 6.25: Raman peak FWHM data for 600mN, 500mN and 400mN indents. Ar^+ laser, d_p~556nm

	600mN	500mN	400mN	300mN	200mN	100mN
Average	5.734621	6.361536	5.49693	5.494596	4.835879	4.747198
Std Dev	3.400558	3.433385	3.709694	1.625697	1.77016	1.128809

Table 6.2: Table showing the average peak width in cm^{-1} and standard deviation from the reference spectrum for indents ranging from 100mN to 600mN

When the spectrum taken from the 100mN indent, as shown in fig. 6.29 below along with a calibration spectrum taken from non-indented reference sample, was examined it showed none of the high pressure polymorphs but it still showed an average broadening of ~4.7cm^{-1} with a standard deviation of ~1.1 cm^{-1} with a maximum broadening of ~ 6.9 cm^{-1}.

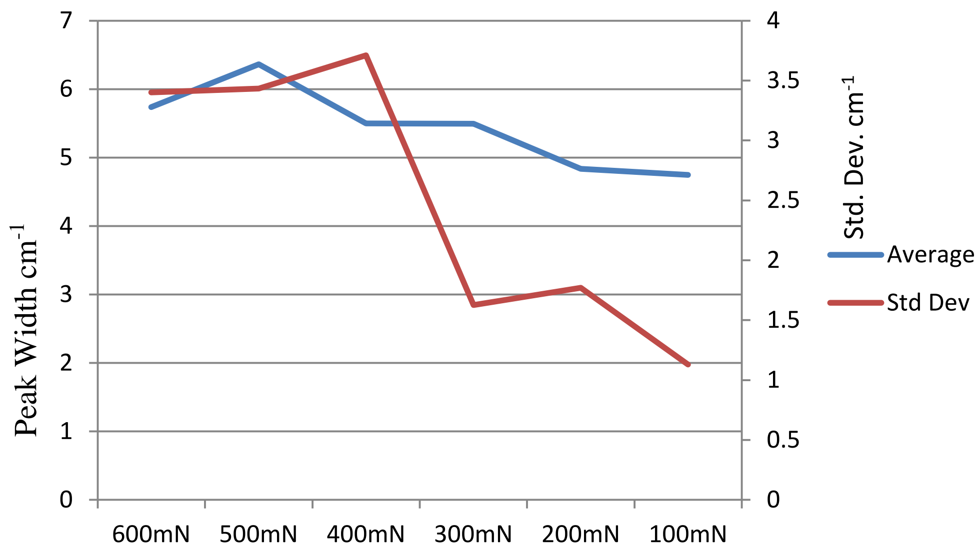

Figure 6.26: Plot of table 6.2, showing the average peak width and standard deviation from a reference spectrum

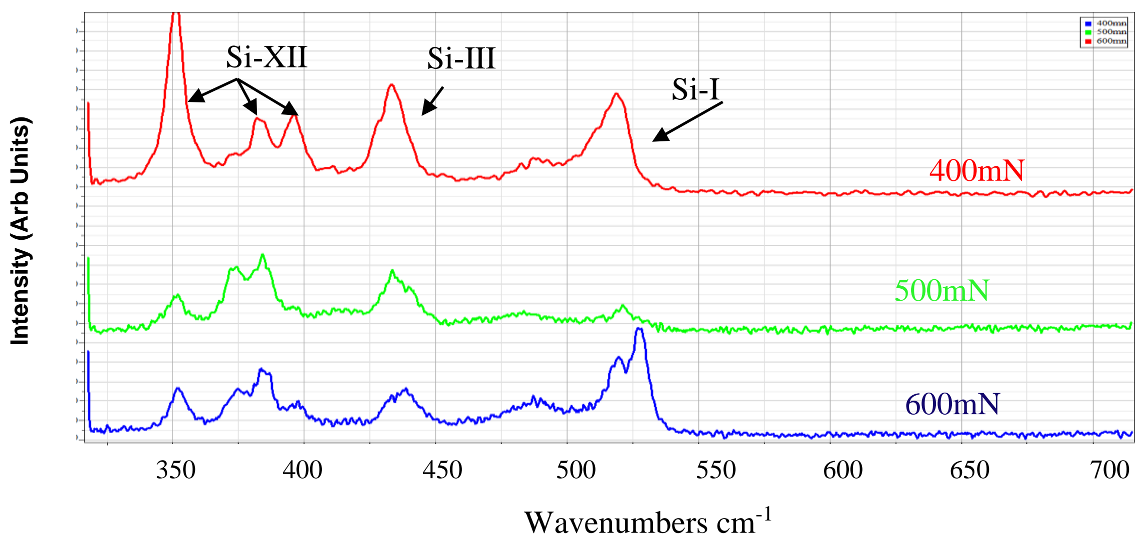

Figure 6.27: Raman spectra taken from a 600mN, a 500mN and a 400mN indent showing the presence of Si-III and Si-XII. Data obtained using 488nm Ar^+ laser, d_p~556nm

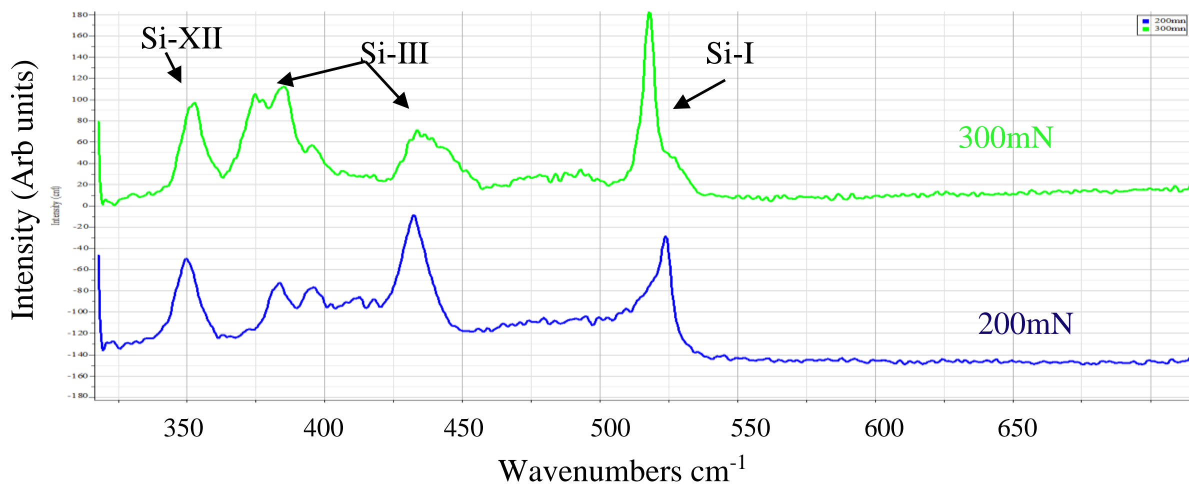

Figure 6.28: Raman spectra taken from a 300mN and a 200mN indent showing the presence of Si-III and Si-XII. Data obtained using 488nm Ar+ laser, d_p~556nm

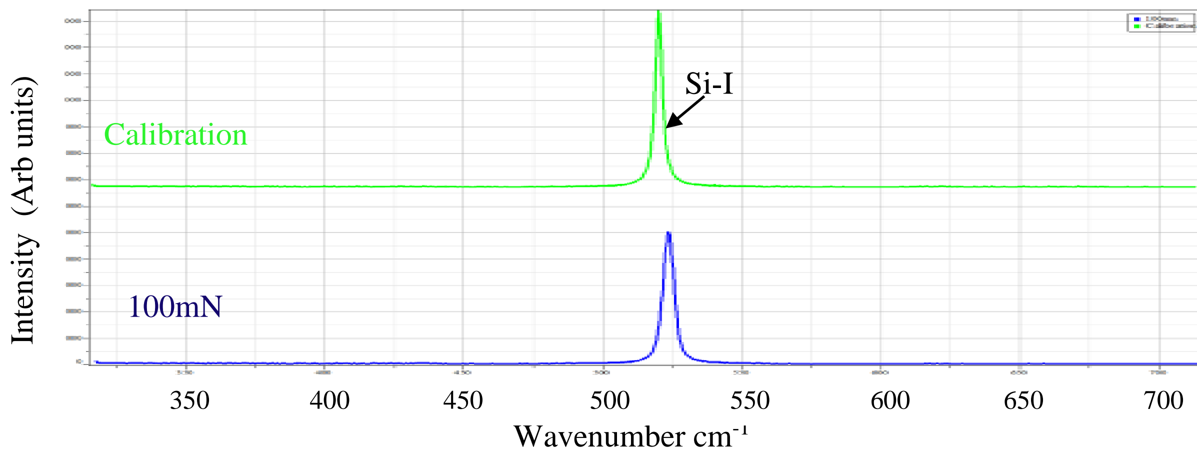

Figure 6.29: Raman spectra taken from a 100mN indent along with a calibration spectrum taken from a reference sample. No evidence of high pressure polymorphs was observed. Data obtained using a 488nm Ar^+ laser, d_p ~556nm

It has been shown in the literature that polymorphs can only form from the β-Sn or Si-II phase [15] of silicon and the absence of the polymorphs indicate that within the 100mN indent the applied pressure did not reach the ~10 to 12 GPa required to initiate the Si-I to Si-

II transformation [4,16,17]. Analysis of the 520cm^{-1} Raman peak from the 600, 500, 400, 300 and 200mN indents show that along with an increase in the crystalline disorder there is also an asymmetric broadening of the 520 cm^{-1} Si peak. This data would indicate that nc-Si is being formed in these areas [3] alongside the high pressure phases of Si-III and Si-XII. Although fig. 6.29 shows a broadening of the 520cm^{-1} Si peak it is symmetric unlike that expected from the formation of nc-Si and this broadening is most likely caused by crystal deformation caused by compressive strain being applied by nanoindentation.

Analysis of the spectra taken from the 600mN indent shows no evidence of high pressure polymorphs at either the edge or the apex of the indent. The spectrum from the centre of the indent shows some evidence of high pressure phases, wherein all spectra have been normalised, figs. 6.30 – 6.33

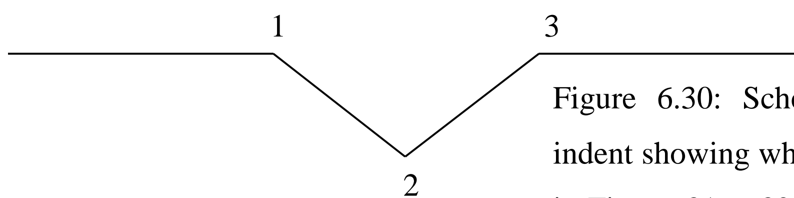

Figure 6.30: Schematic of a 600mN indent showing where the spectra shown in Figs. 6.31, 6.32 and 6.33 below were taken

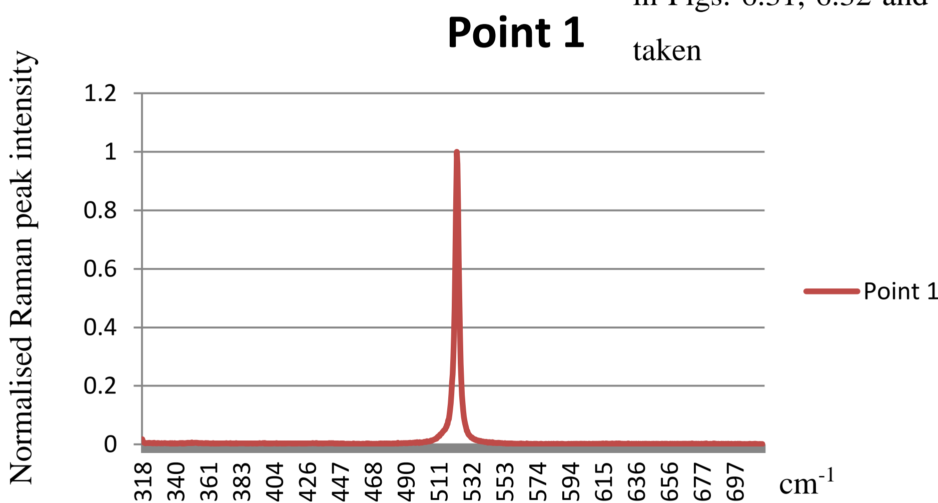

Figure 6.31: Normalised Raman spectrum taken from point 1, the left edge of a 600mN indent

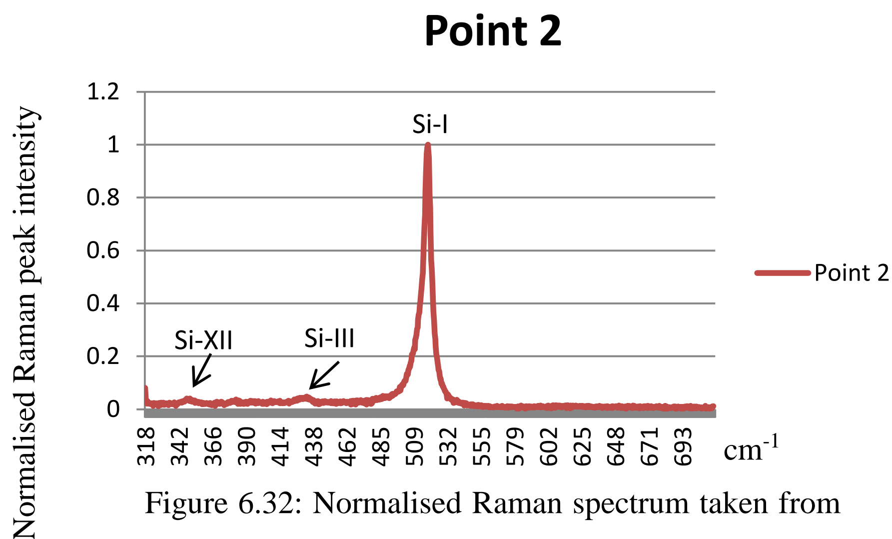

Figure 6.32: Normalised Raman spectrum taken from point 2, the centre of a 600mN indent

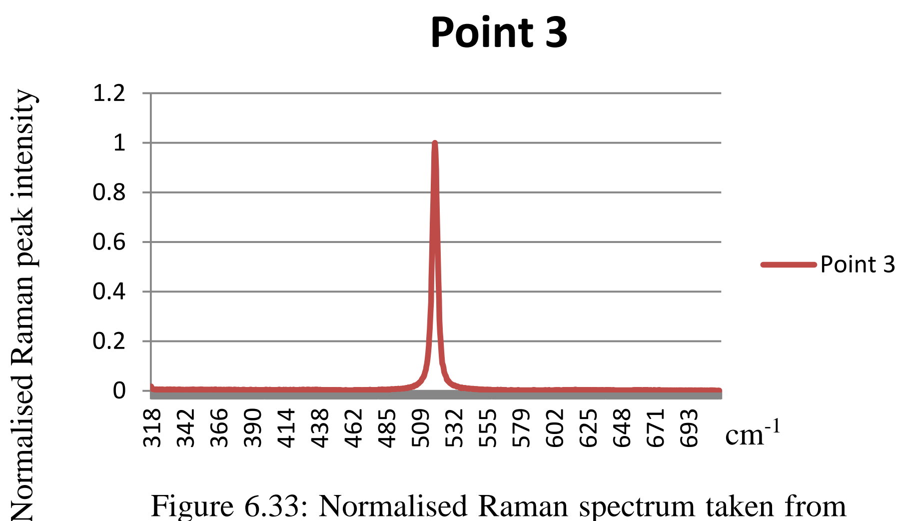

Figure 6.33: Normalised Raman spectrum taken from point 3, the apex of a 600mN indent

Spectra taken from the indent side wall confirm the presence of high pressure polymorphs commencing approx. 2µm in from the edge of the indent as shown in figs. 6.35, 6.36 and 6.37 below.

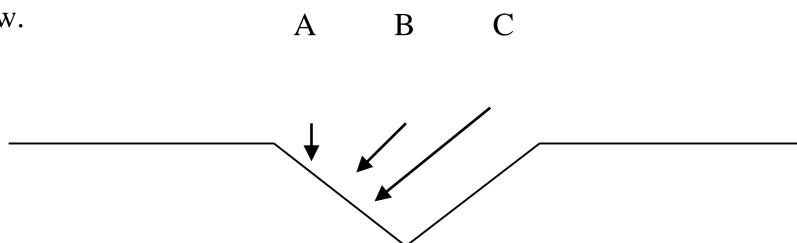

Figure 6.34: Schematic of a 600mN indent showing where the spectra shown in Figs. 6.35, 6.36 and 6.37 below were taken

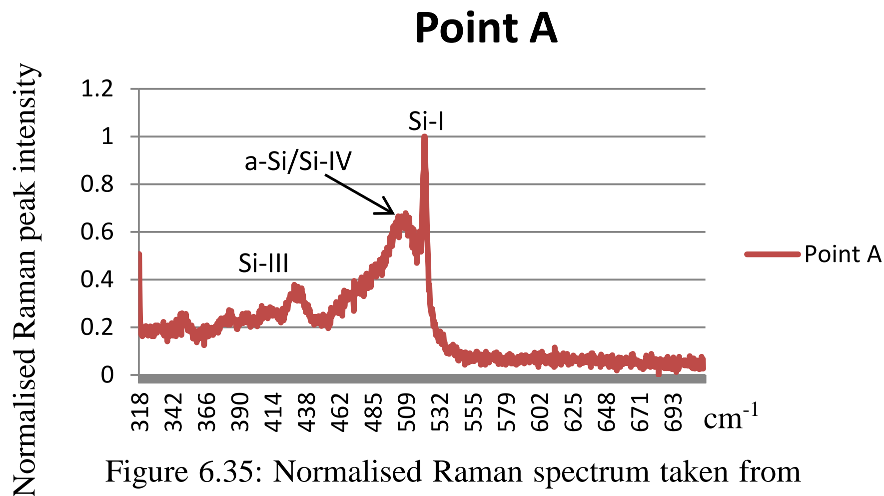

Figure 6.35: Normalised Raman spectrum taken from point A, 2µm in from the edge of a 600mN indent

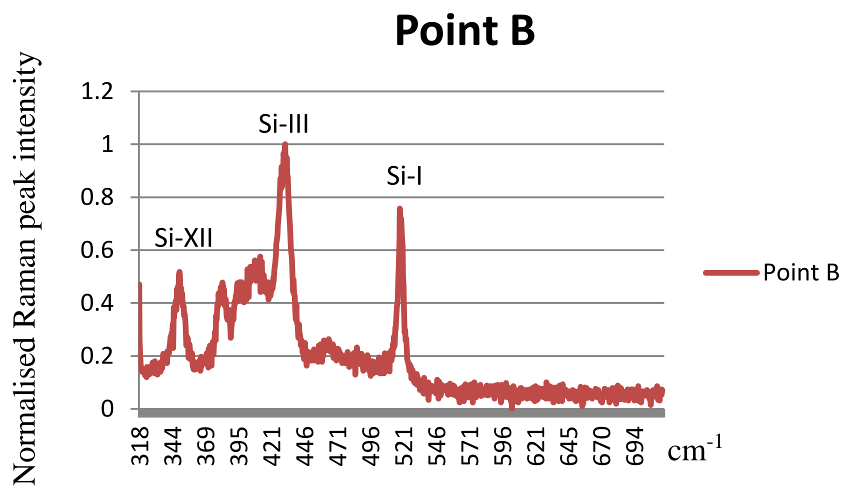

Figure 6.36: Normalised Raman spectrum taken from point B, 3µm in from the edge of a 600mN indent

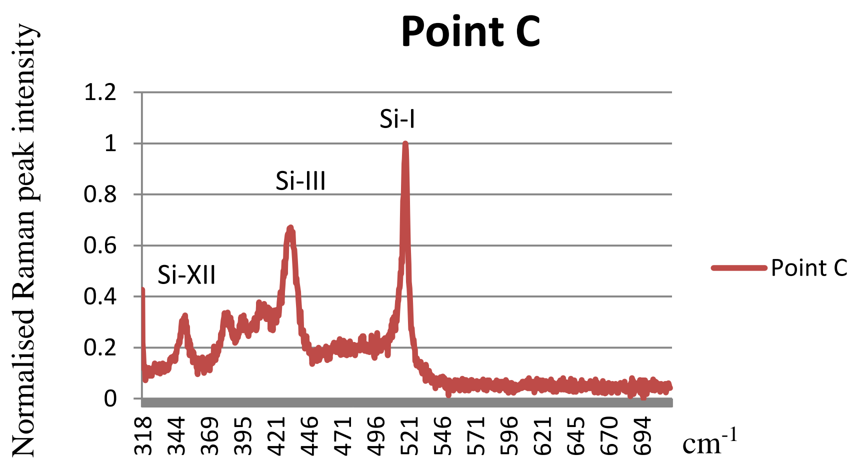

Figure 6.37: Normalised Raman spectrum taken from point C, 4µm in from the edge of a 600mN indent

The spectra shown above confirm the presence of high pressure phases, principally Si-III and Si-XII, in a 600mN indent and that these appear principally along the side wall of the indent. When the centre of the indent is studied the high pressure phases are present but in very low concentrations when compared to the side walls and with spectra taken from the centre of indents created with lower loads.

However, when the spectra of indents from 200mN to 500mN are analysed high pressure polymorphs can be seen throughout the indent. By the way of example figs. 6.38, 6.39, 6.40 and 6.41 are normalised spectra taken from the centre of 200mN, 300mN, 400mN and 500mN indents, respectively.

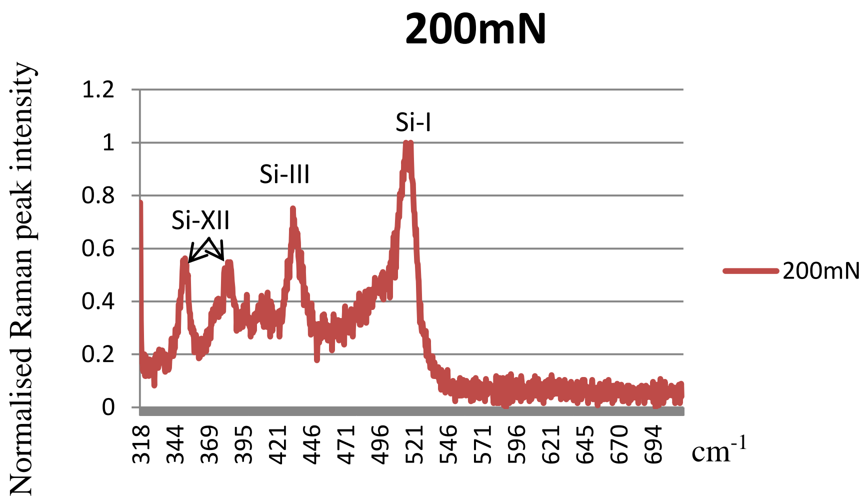

Figure 6.38: Normalised Raman spectrum taken from the centre of a 200mN indent

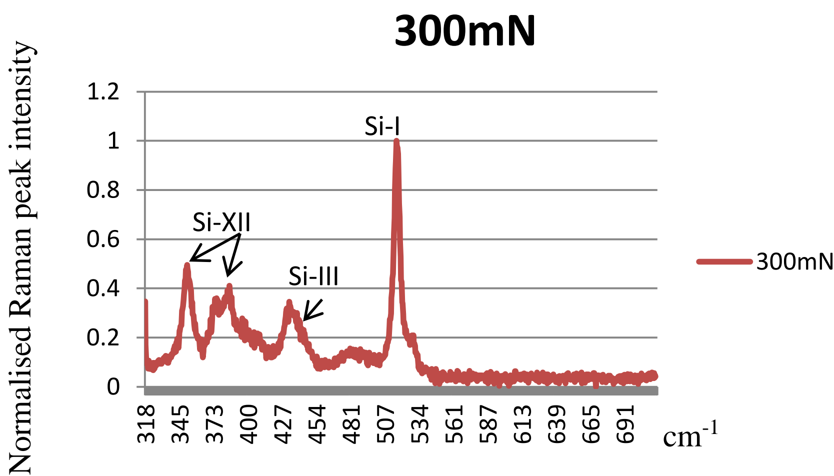

Figure 6.39: Normalised Raman spectrum taken from the centre of a 300mN indent

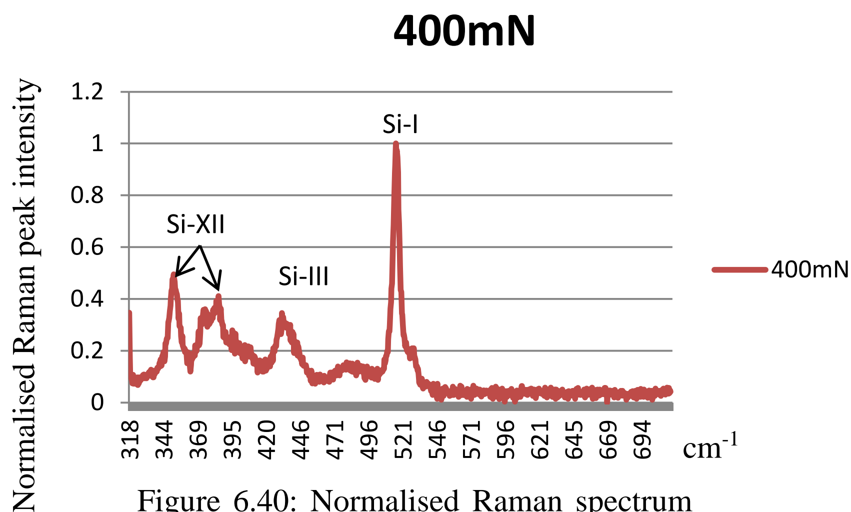

Figure 6.40: Normalised Raman spectrum taken from the centre of a 400mN indent

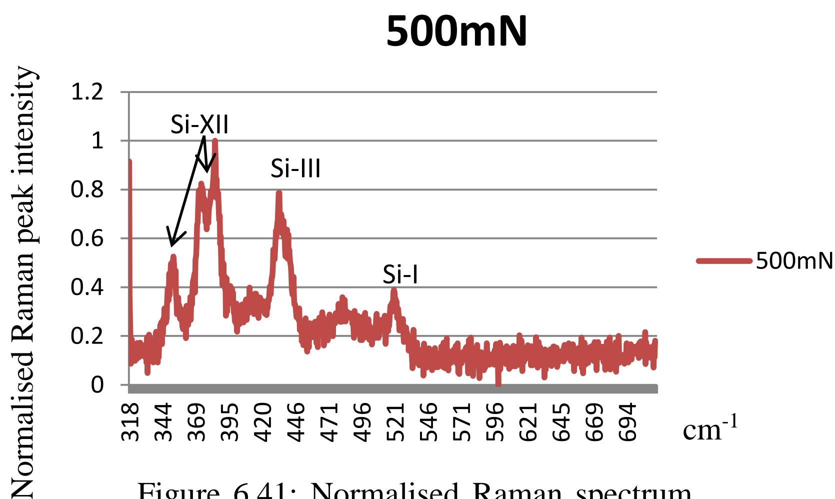

Figure 6.41: Normalised Raman spectrum taken from the centre of a 500mN indent

6.4.2 Map Scan

A map scan is a 2 dimensional scan of an indent consisting of a series of Raman point scans taken as the laser is stepped both horizontally and vertically across the area of interest.

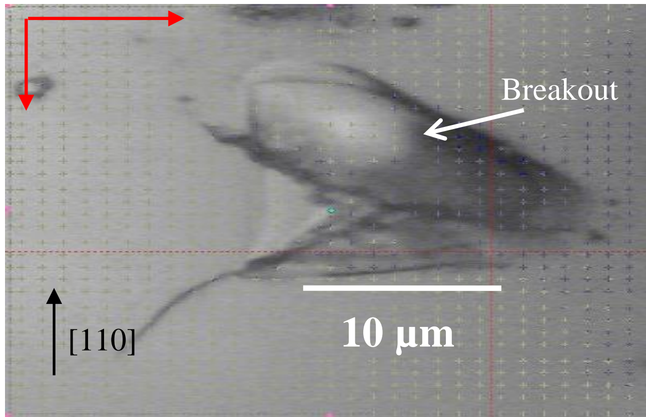

Figure 6.42: Overlay of mapping acquisition scan positions for a 600mN indent. Map size is 30x50µm. The red arrows show the direction of the scan.

The scan pattern shown in fig. 6.42 comprises of 3000 individual steps across an area of 30x50µm utilising a 0.5µm step size in both the x and y directions. The total acquisition time for this scan was ~30hrs; therefore laser drift due to environmental factors must be accounted for. This was accomplished using the laser plasma line based offset cancellation scheme as described in section 6.3.2.

An Excel spread sheet can then be used to calculate and correct for any shift due to environmental factors. These corrections are then applied to the TO phonon peak to ensure that any movement of the peak is due to strain only. Fig. 6.43 shows a 2D Raman map scan of a 600mN indent, Sample 9, Indent 1 wherein the indent is outlined in white.

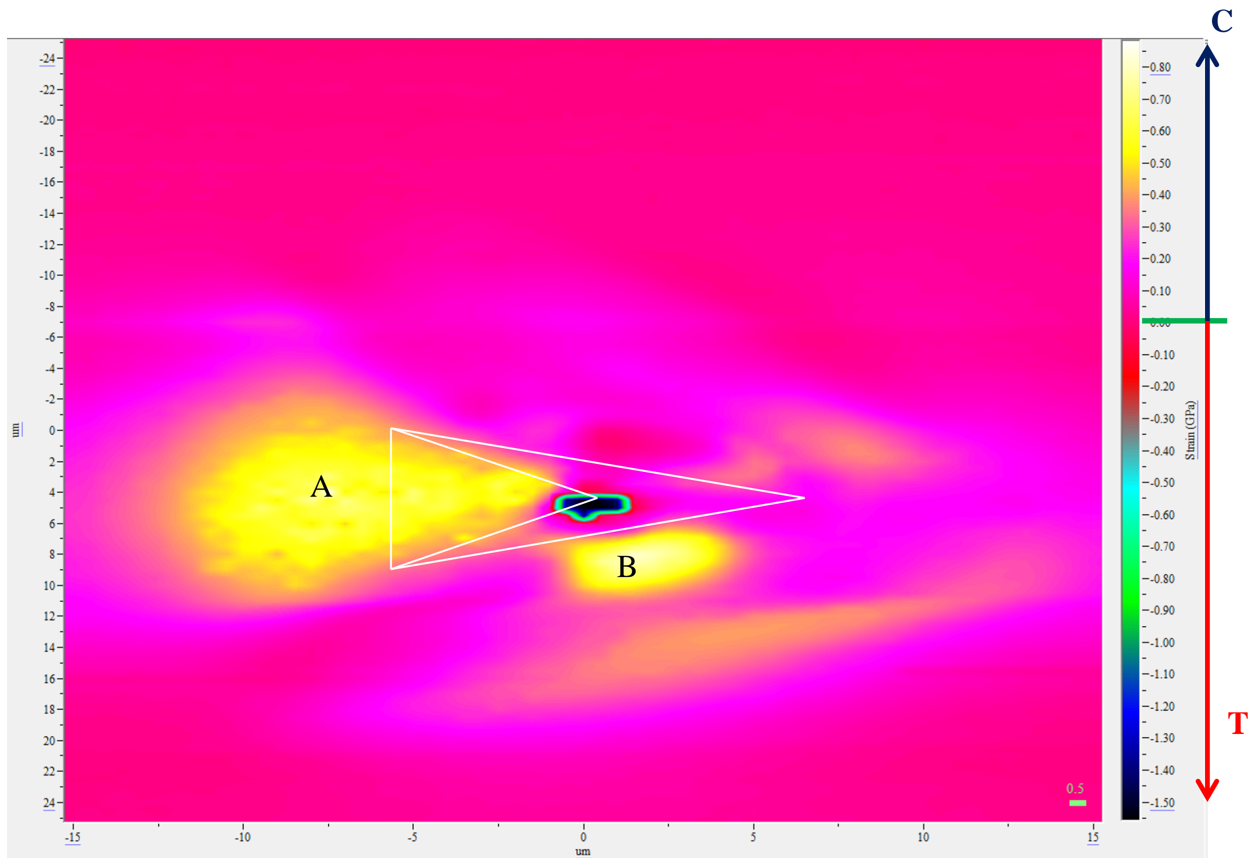

Figure 6.43: 2D Raman map scan of a 600mN indent (Sample 9, Indent 1). Scan taken with a 488nm Ar^+ laser, d_p~556nm.

Two lobes of compressive strain, labelled 'A' and 'B', can be seen at the back and the bottom of the indent with tensile strain observed at the centre of the indent. This is in agreement with the data shown in figs. 6.15 and 6.21 above. Of interest is the absence of strain at the top of the indent. This is due to the presence of a "breakout" indicated in fig. 6.42, which provides strain relief in this area; the breakout observed is a region where the top layer of silicon has cleaved away from the bulk silicon underneath thus acting as a method of relieving strain. This is borne out when a smaller indent is observed. Fig. 6.44 shows an optical micrograph of a 350mN indent (Si_0_Cr9, Indent 6) with no visible indications of breakouts. Fig. 6.45 shows a 2D map scan of this 350mN indent. On this sample no breakouts were observed and compressive strain can be seen on all three sides of the indent with tensile strain at the centre of the indent.

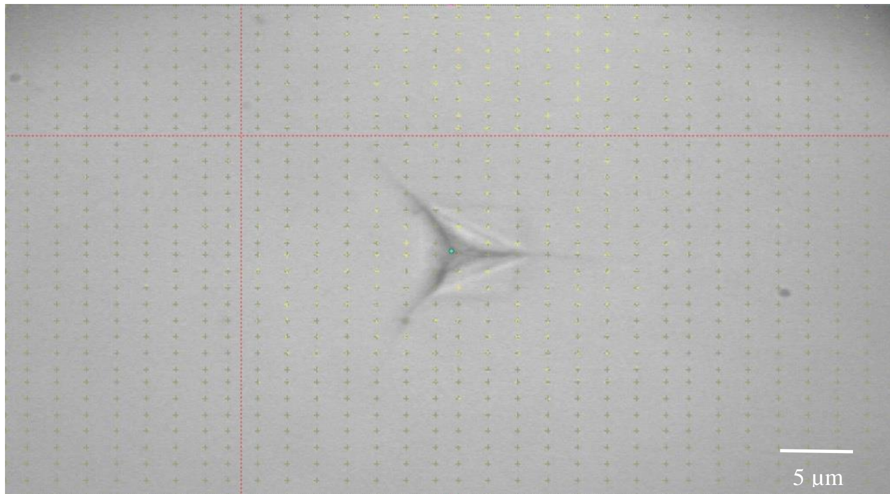

Figure 6.44: Image of a 350mN indent (Si_0_Cr9, Indent 6)

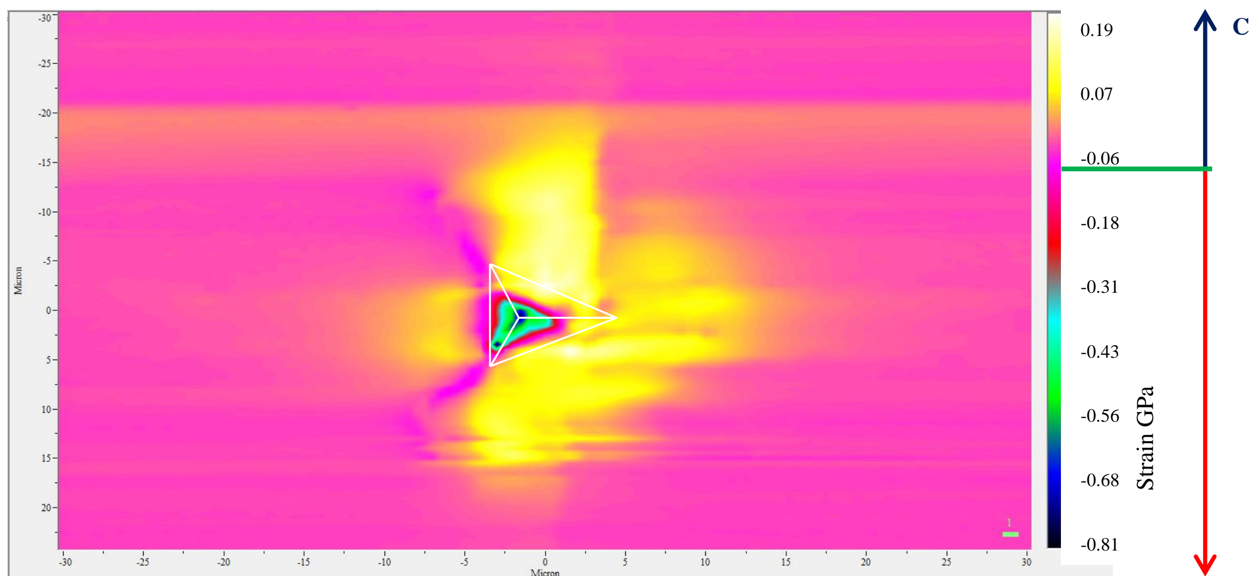

Figure 6.45: 2D map scan of a 350mN indent (Si_0_Cr9, Indent 6) showing only compressive stress at the edges of the indent. Data taken with a 488nm Ar^+ laser, d_p~556nm

This can also be confirmed via examination of the Raman FWHM maps. Fig. 6.46 shows the FWHM map of a 600mN indent. Comparing that with the 2D FWHM map of a 500mN indent fig. 6.47, it can be seen that, while the strain relief produced by the breakout in the 600mN indent reduces crystalline disorder, for the 500mN indent with no breakout, as shown in fig. 6.48, there is crystalline disorder extending outside the confines of the indent.

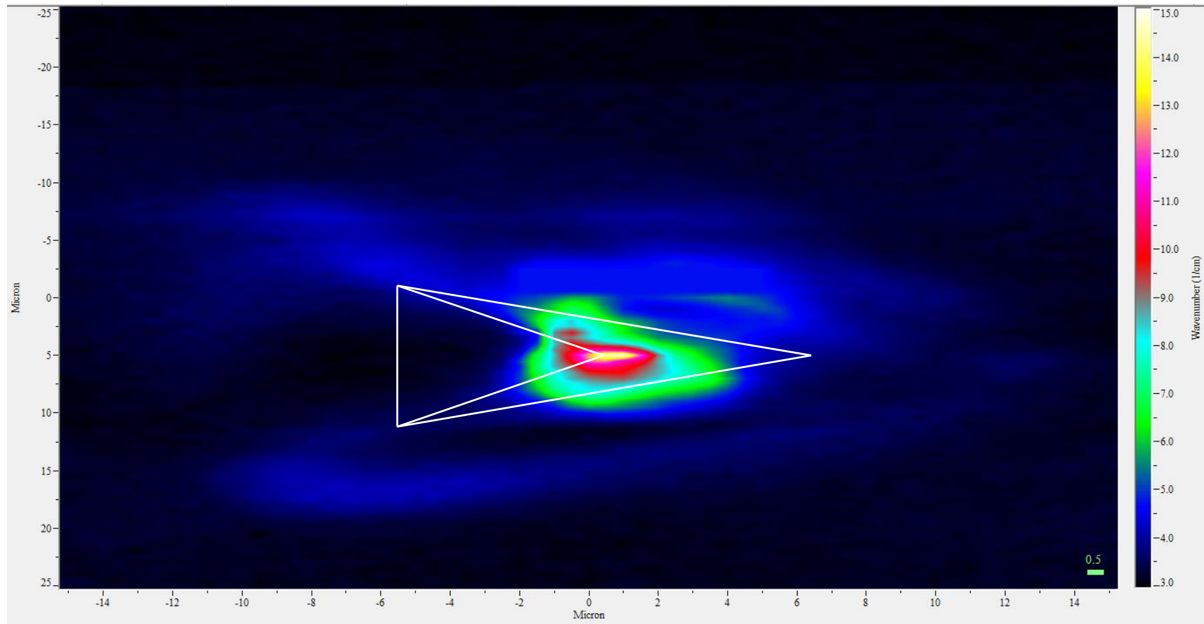

Figure 6.46: 2D Raman map scan showing the FWHM of the 520 cm^{-1} TO raman peak from a 600mN indent (Sample 9, Indent 1). Scan taken with a 488nm Ar^{+} laser, d_p~556nm.

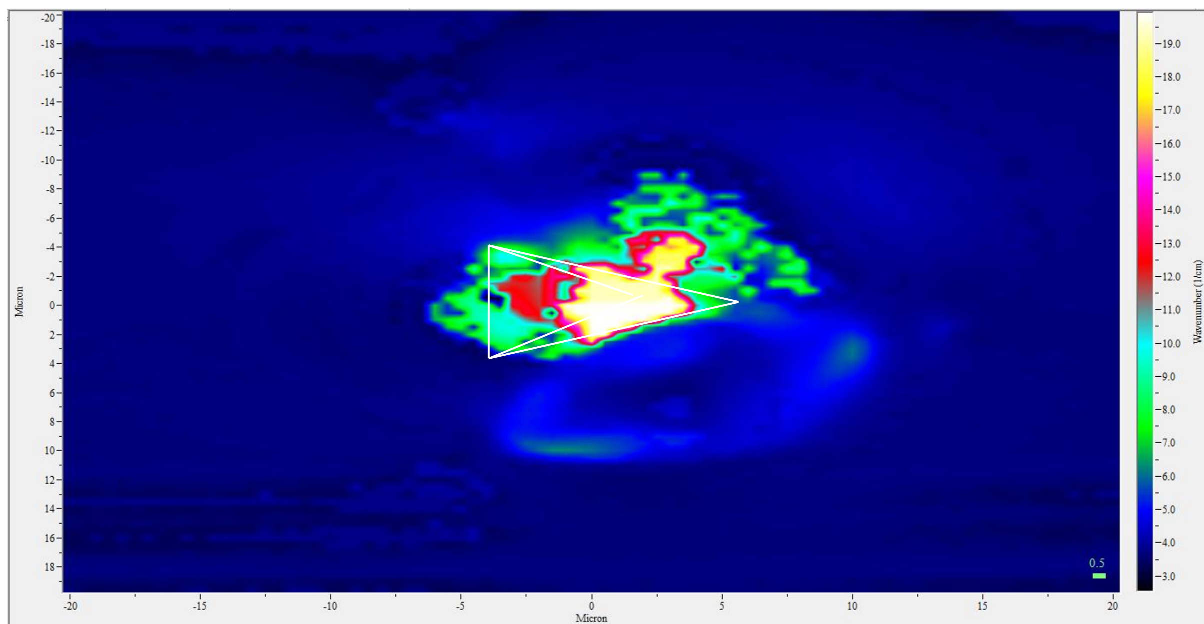

Figure 6.47: 2D Raman map scan showing the FWHM of the 520 cm^{-1} TO Raman peak from a 500mN indent (Sample 7, Indent 6 Row 5). Scan taken with a 488nm Ar^{+} laser, d_p~556nm.

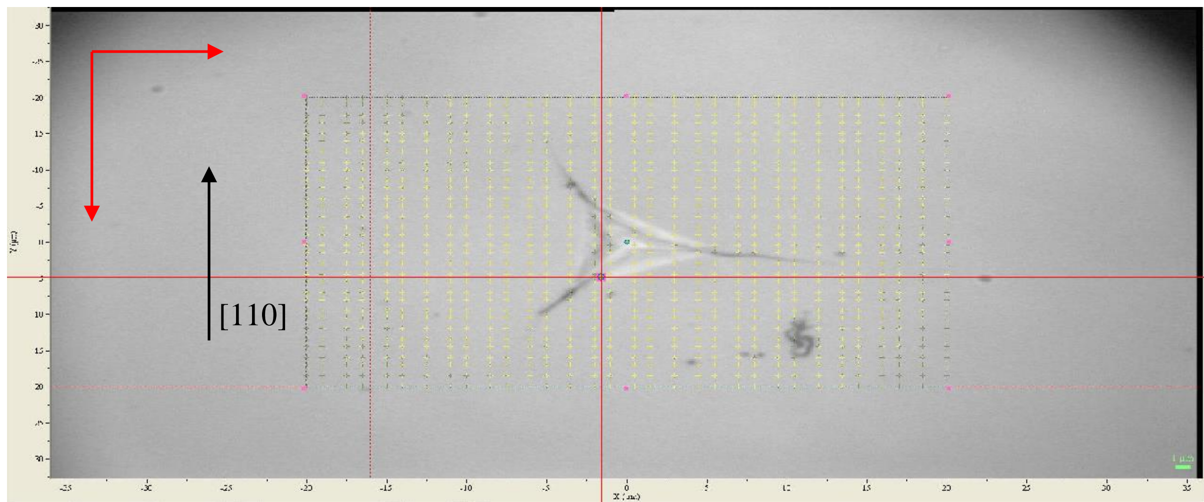

Figure 6.48: Optical micrograph of a 500mN indent (Sample 7, Indent 6 Row 5), indicating the overlay of Raman scan positions. Map size is 40 x 40 µm. red arrows indicate the scan directions

This data would seem to show a relationship between strain relief and crystalline order. While this is true when the samples were annealed, which will be explored later in this chapter, there does also appear to be a relationship between the relief provided by the breakouts and crystalline order. Whether the breakouts occur before the formation of the nc-Si or the breakout allows for the reconstitution of c-Si from nc-Si is unclear.

Figure 6.49 below shows a 2D Raman peak intensity map of Sample 9, Indent 1, and this the data represents the spatial dependence of the 350cm^{-1} Si-XII peak. It can be seen that the positions of peak intensities correlate with those taken from the line indents shown earlier. The peak intensities increase from ~2µm from the edge of the indent and reach a maximum towards the centre of the indent. Fig. 6.50 shows the same 350cm^{-1} Si-XII peak data for a 500mN indent. It can be seen that the peak intensity is at a maximum along the edges of the indent. This agrees with the model postulated by Lawn *et al.* [6,7,9] as shown in fig. 6.19 above. The bottom of the plastic zone contains the region of maximum strain leading to the formation of a crack with the plastic zone extending out from the centre of the indent allowing for the formation of high pressure phases along the edges of the indent.

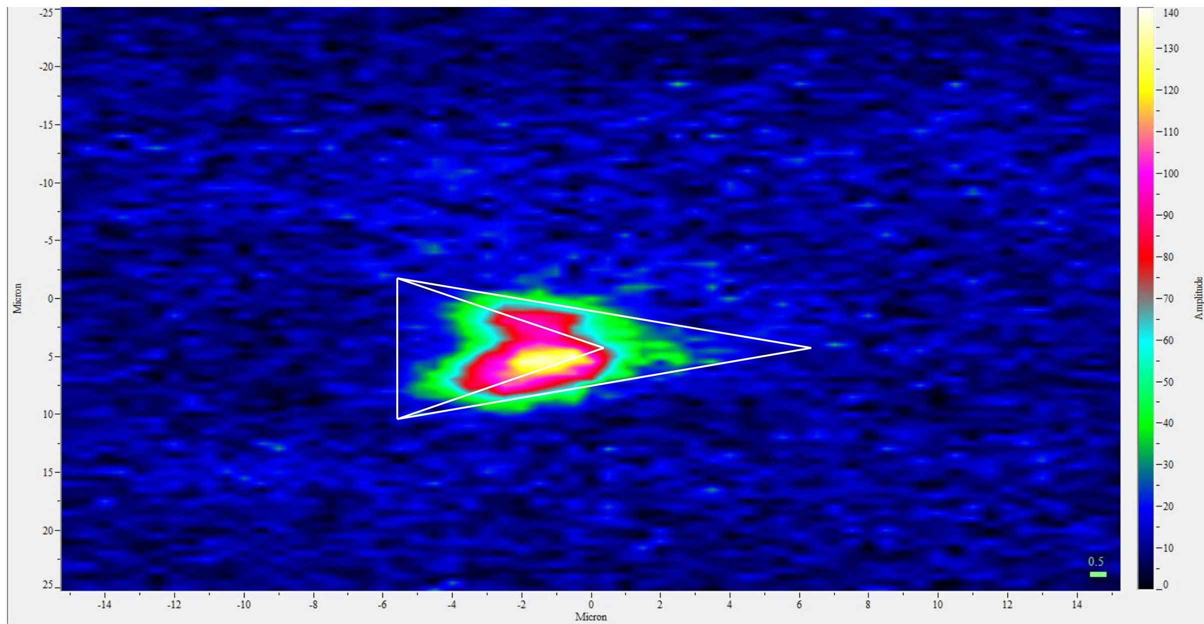

Figure 6.49: 2D Raman map of the 350cm^{-1} Si-XII peak intensity from a 600mN indent Sample 9, Indent 1. Spectra taken using a 488nm Ar^{+} laser, dp ~556nm

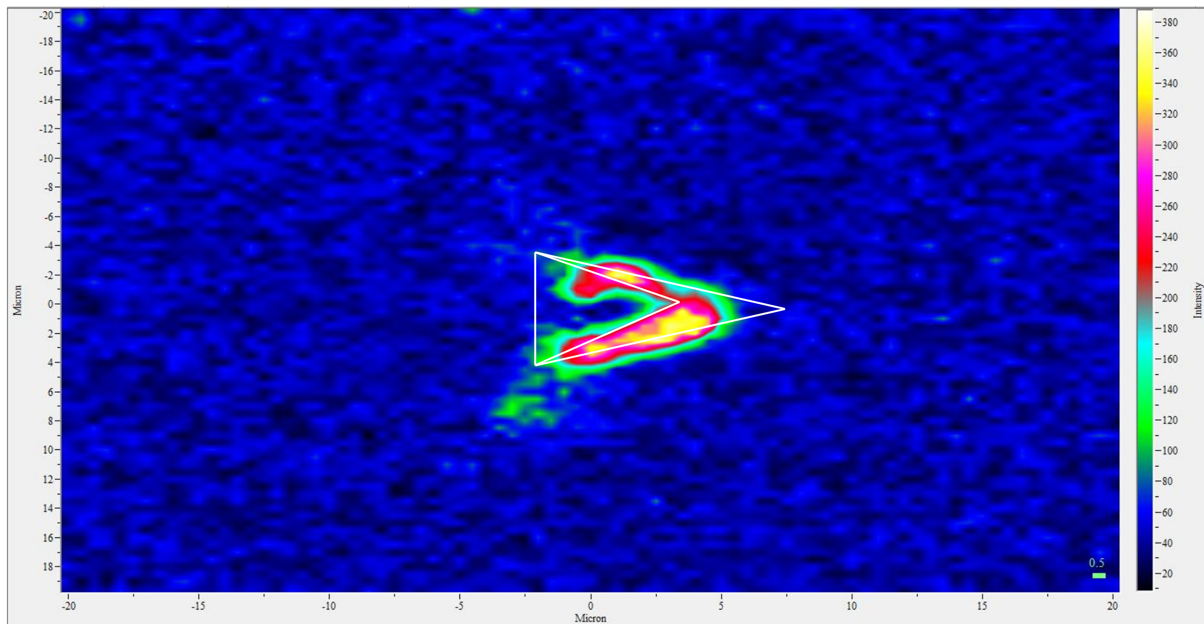

Figure 6.50: 2D Raman map of the 350cm^{-1} Si-XII peak intensity from a 500mN indent Sample 7, Row 5 Indent 6. Spectra taken using a 488nm Ar^{+} laser, dp ~556nm

When a 150mN indent (Si_0_Ar1, Indent 6) is examined however, only compressive stress is observed towards the centre of the indent, fig. 6.51

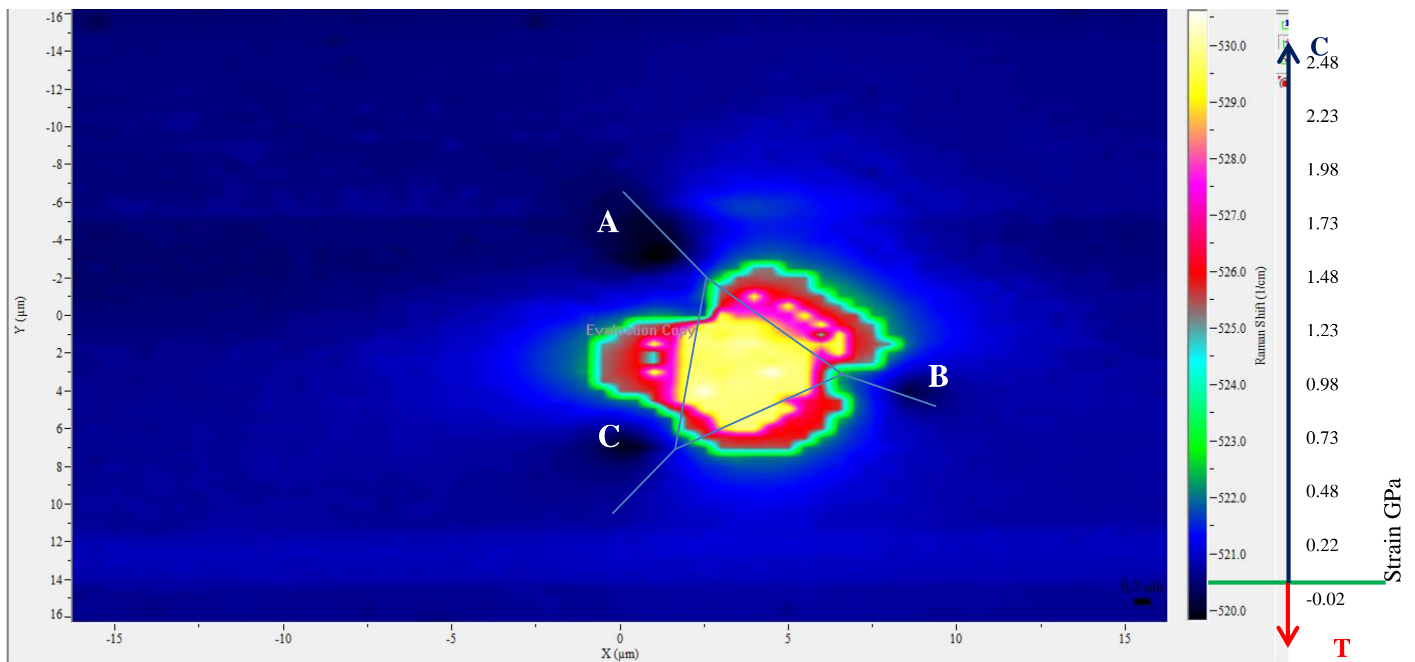

Figure 6.51: 2D map scan of a 150mN indent (Si_0_Ar1, Indent 6) with indent shape added. Compressive stress is seen within the indent peaking at the centre. 3 areas of tensile stress are observed at points A, B, and C.

In fact, three areas of tensile stress were observed at points A, B and C, exterior to the nominally indented zone. The cause of this tensile stress can be found from a Scanning Electron Microscope (SEM) image of this indent, fig. 6.52.

The corresponding points A, B and C are at the vertices of the indent and are due to radial cracks emanating from the indent vertices [14]. This data, along with the earlier TEM micrograph shown in fig. 6.20, significantly supports the supposition that areas of tensile stress observed within indents are due to cracks forming in the silicon.

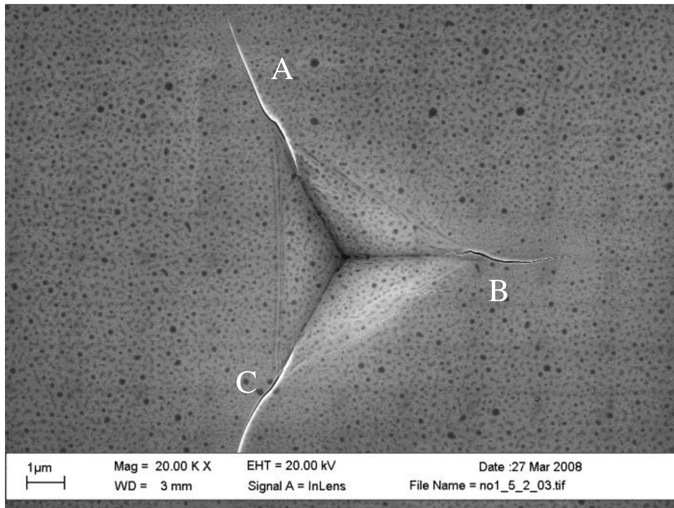

Figure 6.52: SEM image of a 150mN indent (Si_0_Ar1, Indent 6). Points A, B and C are radial cracks emanating from the vertices of the indent. These areas map onto the Raman map as areas of tensile stress.

6.4.3 Impact of Thermal Annealing

A selection of the samples were submitted to *in situ* thermal anneals as described in section 5.2.1 and re-examined. The samples were submitted to a Rapid Thermal Annealing process as described by J. Wittge [18]. The samples were plateau annealed to 1000ºC for 60 s. Analysis of the post anneal spectra show that the high pressure polymorph phases of silicon have all reverted to Si-I, as shown in fig. 6.53 and 6.54 below.

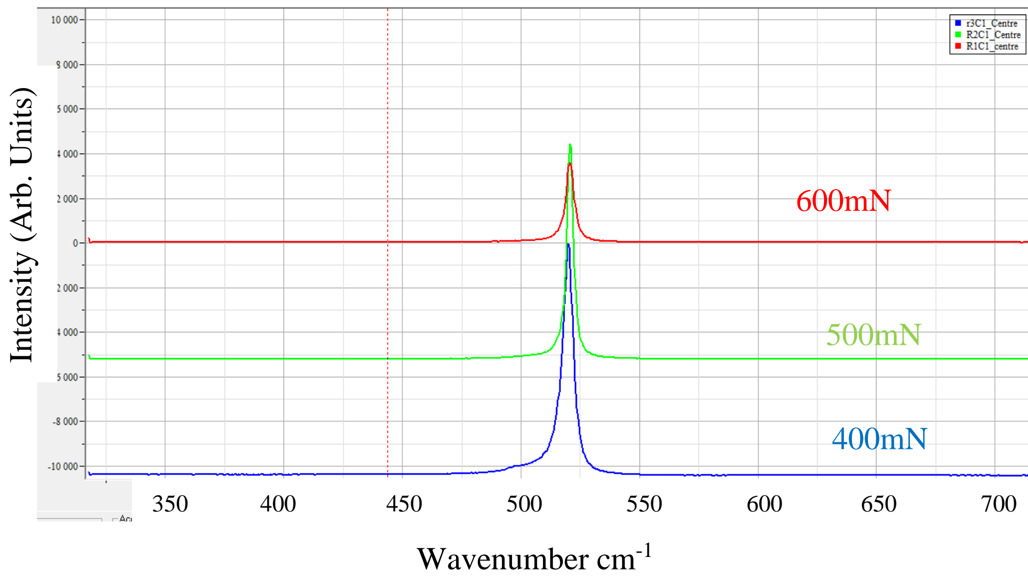

Figure 6.53: Post anneal Raman spectra taken from the centre of a 600mN, a 500mN and a 400mN indent showing only Si-I with no evidence of high pressure polymorphs. Data obtained using 488nm Ar^+ laser, d_p~556nm

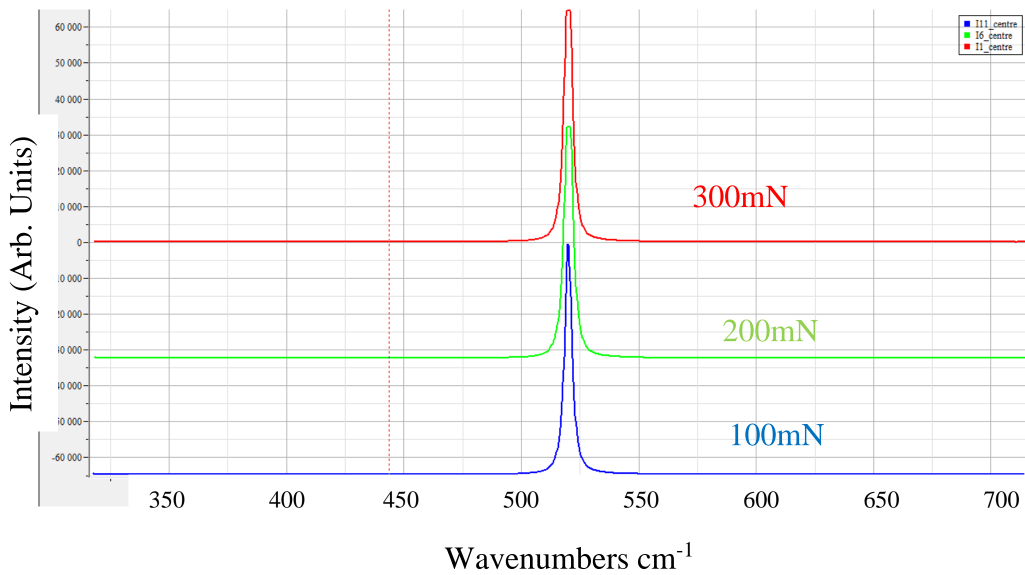

Figure 6.54: Post anneal Raman spectra taken from the centre of a 300mN, a 200mN and a 100mN indent showing only Si-I with no evidence of high pressure polymorphs. Data obtained using 488nm Ar^+ laser, d_p~556nm

Analysis of the strain data extracted from the Raman spectra show evidence of strain relief upon annealing in both the tensile and compressive strain regimes.

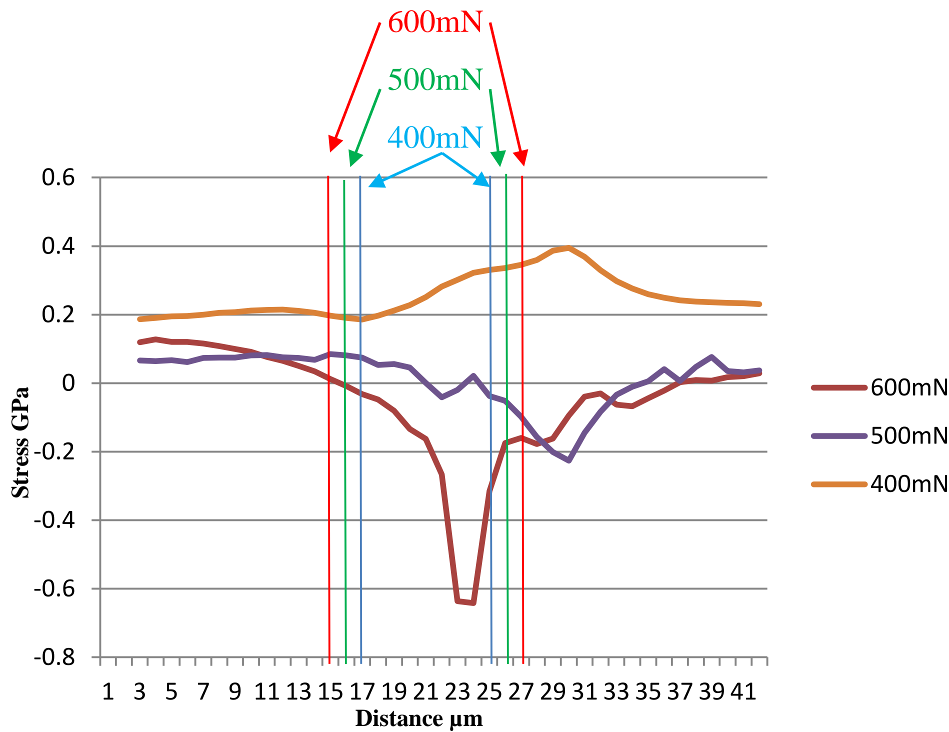

Figure 6.55: µRS stress data for 600mN, 500mN and 400mN indents. Ar^+ laser, d_p~556nm. Post Annealed

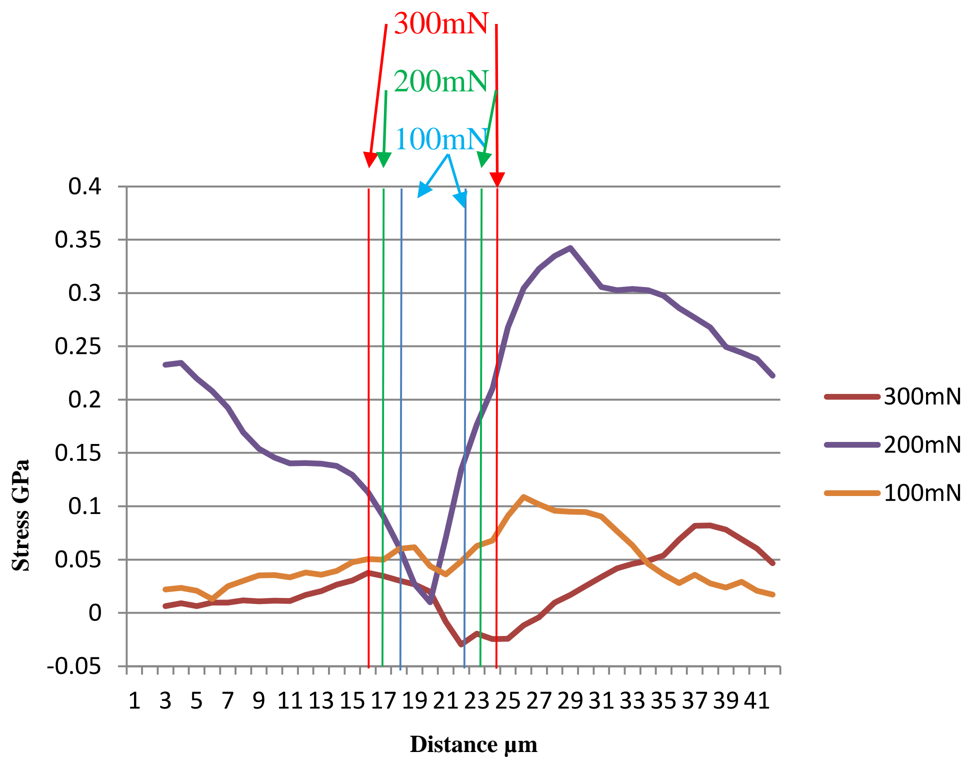

Figure 6.56: µRS stress data for 300mN, 200mN and 100mN indents. Ar^+ laser, d_p~556nm. Post Anneal

Figs. 6.55 and 6.56 show data for a range of indents from 600mN to 100mN taken after the samples have been plateau annealed to 1000°C for 60 seconds with a 30s heating time and a fast cooling. In sharp contrast to the data shown in figs. 6.21 and 6.22, there is a marked decrease in the observed stress both compressive and tensile. This difference averages out to an 86% reduction in compressive stress and an 83% reduction in tensile stress.

	Peak Comp	Peak Tens	Peak Comp	Peak Tens	Peak Comp	Peak Tens
	600mN		500mN		400mN	
Pre Strain (GPa)	0.55	-1.34	1.6	-1.17	1.6	-0.97
Post Strain (GPa)	0.12	-0.64	0.08	-0.22	0.3	0.18
% reduction	78	52	95	81	81	81

Table 6.3: Comparison of the peak Compressive and Peak Tensile stresses for 600mN, 500mN and 400mN indents pre - and post - anneal

	Peak Comp	Peak Tens	Peak Comp	Peak Tens	Peak Comp	Peak Tens
	300mN		200mN		100mN	
Pre Strain (GPa)	1.63	-0.93	1.07	-0.6	1.29	0.41
Post Strain (GPa)	0.05	-0.03	0.3	0.03	0.1	0.03
% reduction	97	97	72	95	92	93

Table 6.4: Comparison of the peak Compressive and Peak Tensile stresses for 300mN, 200mN and 100mN indents pre - and post - anneal

The reduction in tensile stress used in the calculations above ware obtained from line scans across the indent. This may not be quite the peak tensile stress within the indent as is shown in fig. 6.57 below, a 2D Raman map of a 600mN indent (Sample 9, Indent 1) stress. It can be seen that the annealing process has caused the area of peak tensile stress, and the accompanying crack, to shift away from the centre of the indent, though there still is a significant stress reduction of >52%. To accurately compare the effect of the RTA on the crystalline order of the samples another series of line scans was taken post-anneal and the respective FWHM data taken as shown in figs. 6.59 and 6.60 below. The average FWHM is shown in table 6.5 below along with the standard deviation from the calibration spectrum of 3.48811 cm^{-1}. This along with the reduction of stress and the absence of high pressure polymorphs is clear evidence of the recrystallization of the silicon within the indent as a result of the annealing process as predicted by Domnich and Gogosti [4].

When the 2D FWHM map is examined for this indent however, it can be seen that there are still areas of high disorder, correlating well with those areas of peak tensile stress, fig. 6.58. The analysis of these spectra now becomes more difficult as, although the peaks show the asymmetric broadening associated with nc-Si, the heat treatment that the sample underwent could lead to the formation of Si-IV as the transformation of from Si-III to Si-IV occurs at ~200°C [19], though this is unlikely as Wentorf *et al*. suggests that this process takes some hours to accomplish [20].

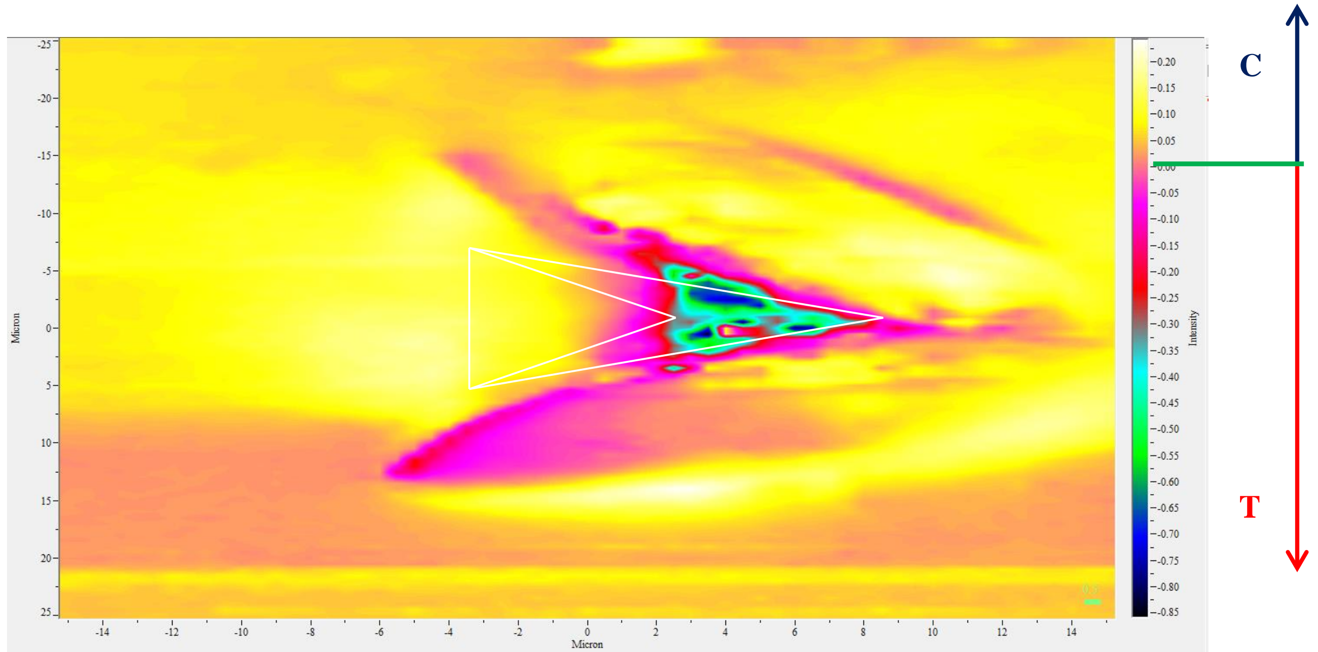

Figure 6.57: 2D Raman stress map of a 600mN indent post thermal anneal (Sample 9, Indent 1). Data obtained using a 488nm Ar^+ laser, d_p~556nm

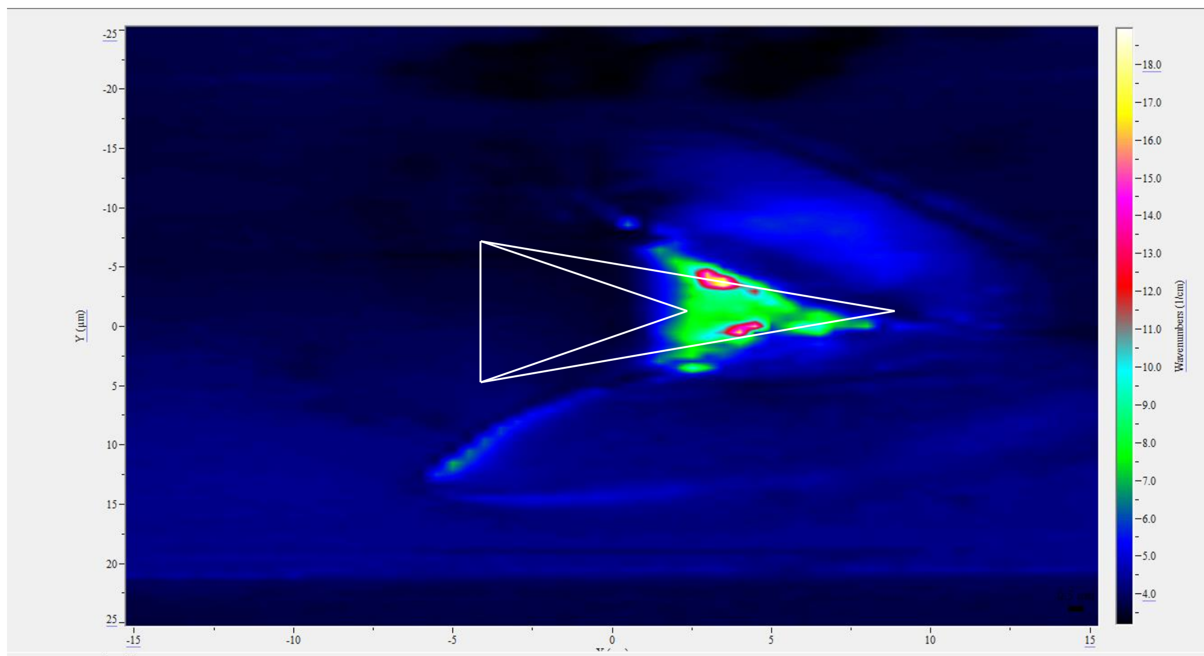

Figure 6.58: 2D Raman map of the FWHM of the 520cm^{-1} TO Si line from a 600mN indent post thermal anneal (Sample 9, Indent 1). Data obtained using a 488nm Ar^+ laser, d_p~556nm

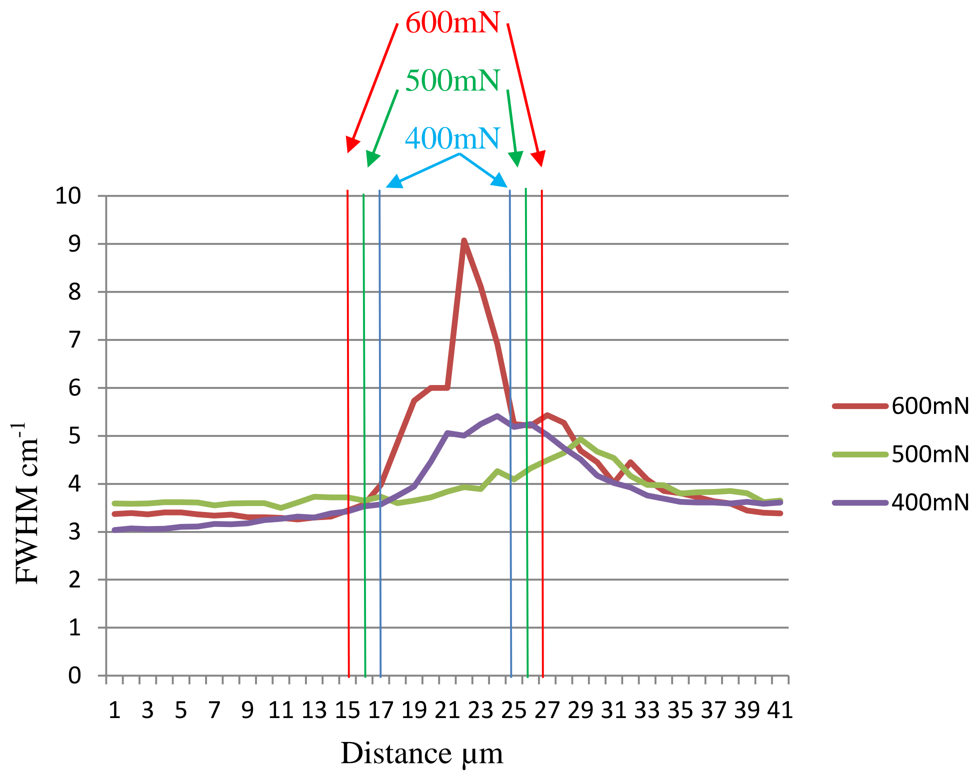

Figure 6.59: Raman peak FWHM data for 600mN, 500mN and 400mN indents post anneal. Ar^+ laser, d_p~556nm

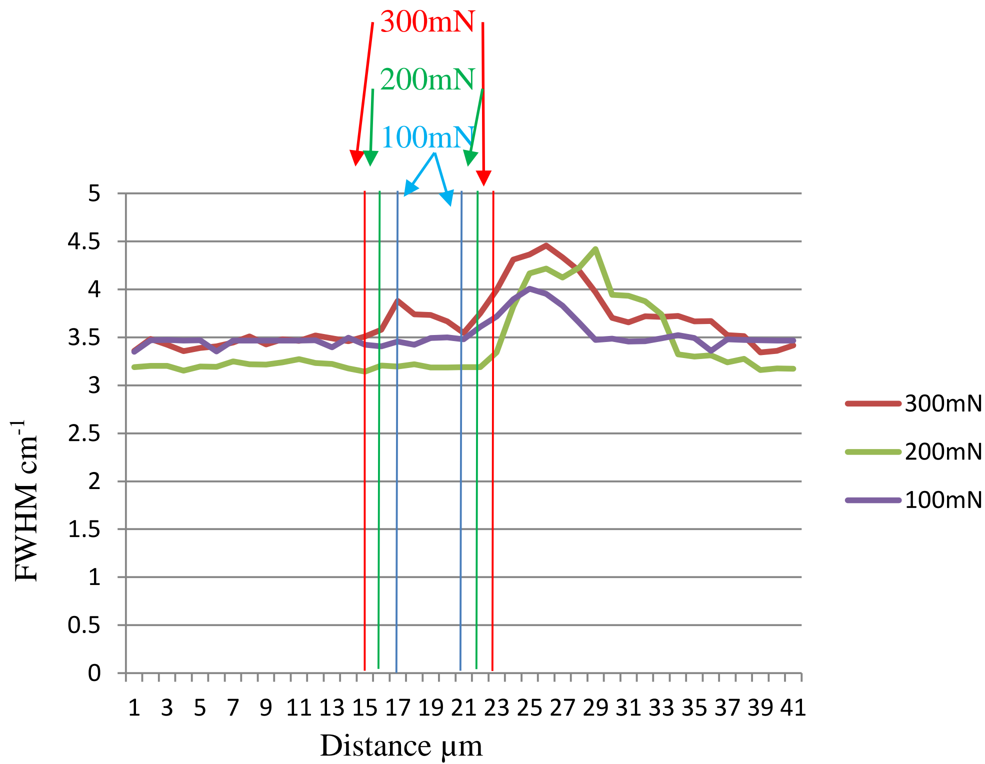

Figure 6.60: Raman peak FWHM data for 300mN, 200mN and 100mN indents post anneal. Ar^+ laser, d_p~556nm

	600mN	500mN	400mN	300mN	200mN	100mN
Average	4.296741	3.87048	3.838968	3.664898	3.420875	3.51766
Std Dev	1.342339	0.353011	0.714898	0.294014	0.367851	0.14766

Table 6.5: Table showing the average peak width in cm^{-1} and standard deviation from the reference spectrum for indents ranging from 100mN to 600mN

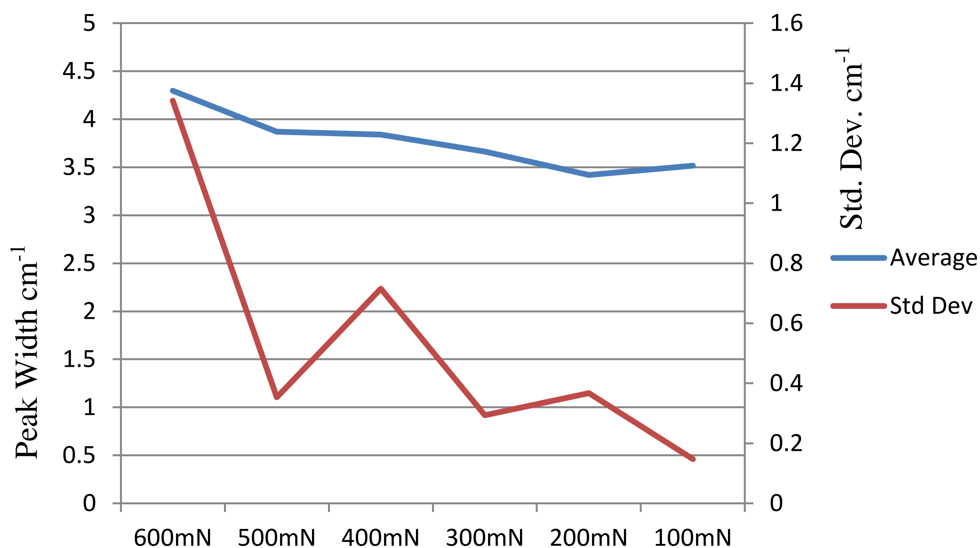

6.5 Correlation with FEM

Finite Element Modelling (FEM) was carried out by our colleagues in CEIT, Spain, and all models are courtesy of E. Gorogostui-Colinas [21]. The modelling was carried out using the ABAQUS 6.10 software package, and was used to correlate with the Raman map scans. Fig. 6.61 shows a FEM model of a 75mN indent, which predicts the expectred Raman shifts of the TO Si peak.

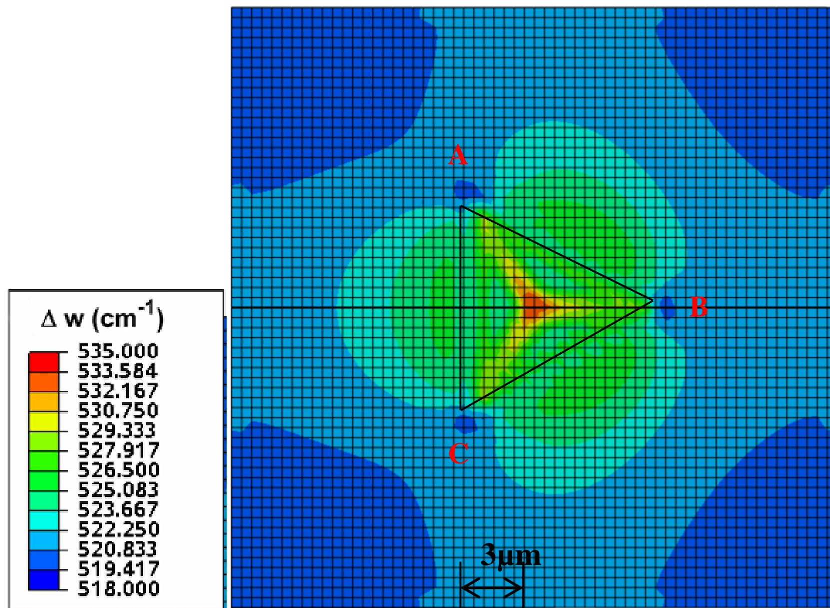

Figure 6.61: FEM model of a 75mN indent showing compressive strain within the indent and tensile strain at the vertices. At zero strain the Raman TO Si peak is 521 cm^{-1}. Red shifted values correspond to compression; blue shifts to tension.

Figure 6.62 below shows a comparison between a 2D Raman map of a 150mN indent experiment and the FEM simulation for the Berkovich loading condition. It can be seen that the simulation agrees very well with the experimental data. Discrepancies between the experimental and simulated data can be attributed to the fact that there was no consideration given to the formation of phase transformations under the indent and that the μRS data from the 488nm Ar^+ laser represents an effective integration of all the Raman peak shifts through to a d_p of ~556nm

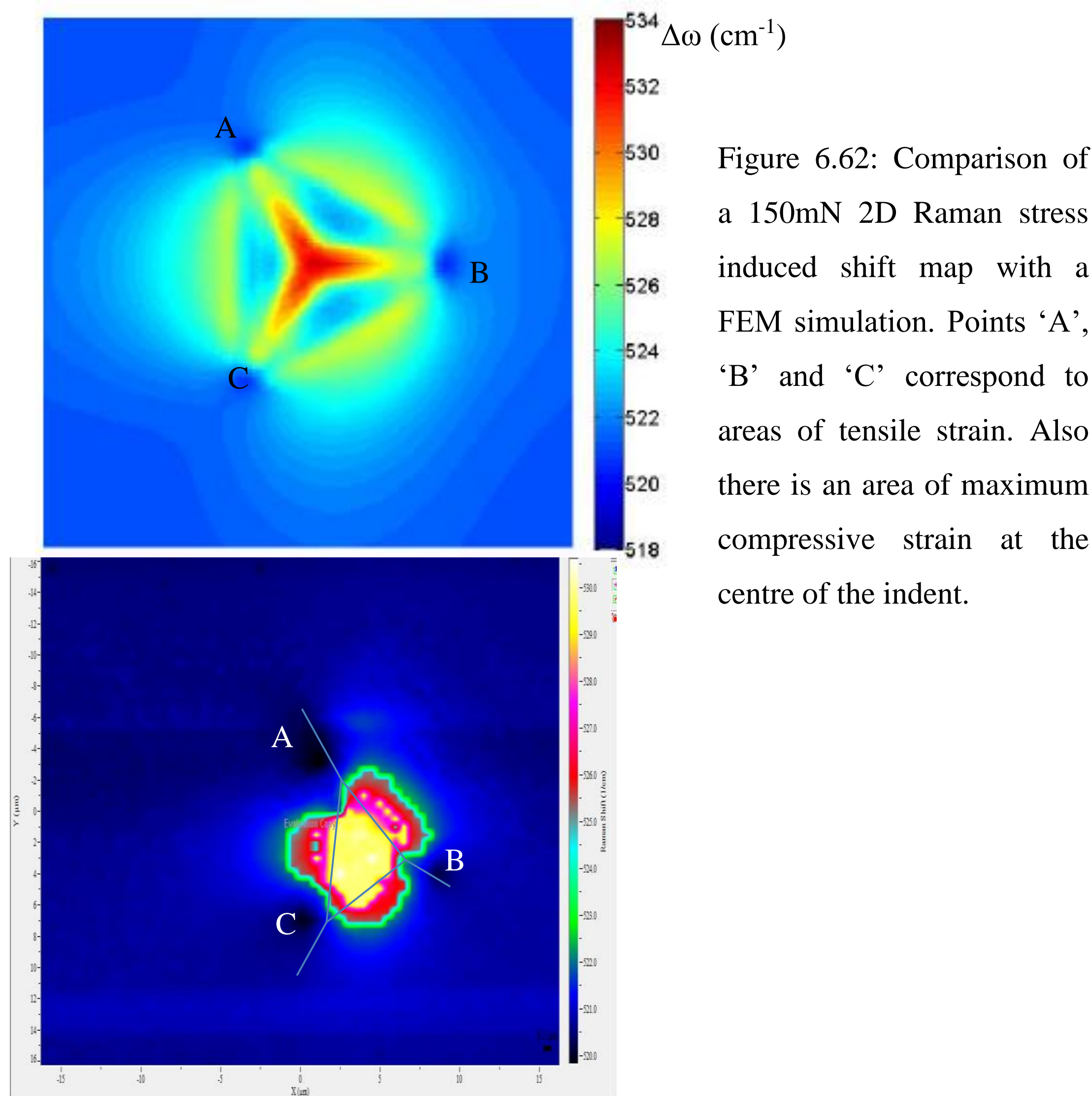

Figure 6.62: Comparison of a 150mN 2D Raman stress induced shift map with a FEM simulation. Points ‘A’, ‘B’ and ‘C’ correspond to areas of tensile strain. Also there is an area of maximum compressive strain at the centre of the indent.

Fig. 6.64 shows the presence of lobes of compressive stress along the vertices of the indent, and tensile stress at the centre of the indent. This is in agreement with the Raman data shown in figs. 6.43 and 6.45. It can also be seen that the strain around the indent is relatively isotropic in nature at a range of ~50 μm from the centre of the indent. This is also confirmed in chapter 7 where data taken from Large Area Back Reflection x-ray topographs also show the strain field around the indent to be isotropic in nature as shown in fig. 6.63. This will be explored further in chapter 7. A model of the expected Raman peak shifts for a 750mN indent was also created, shown in fig. 6.64 and the modelling also included the expected impact of a thermal anneal to ~625°C. The post anneal FEM simulation is shown in fig. 6.65 below.

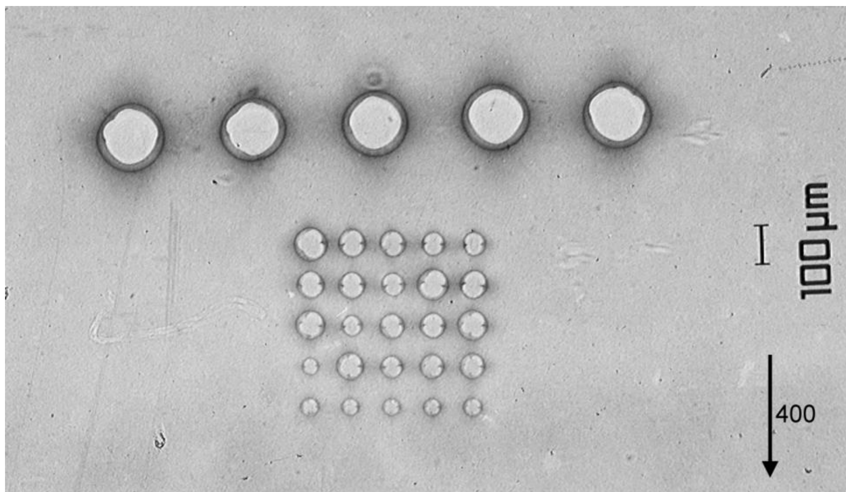

Figure 6.63: Single 0210 Large Area Back Reflection x-ray topograph of Sample 1.

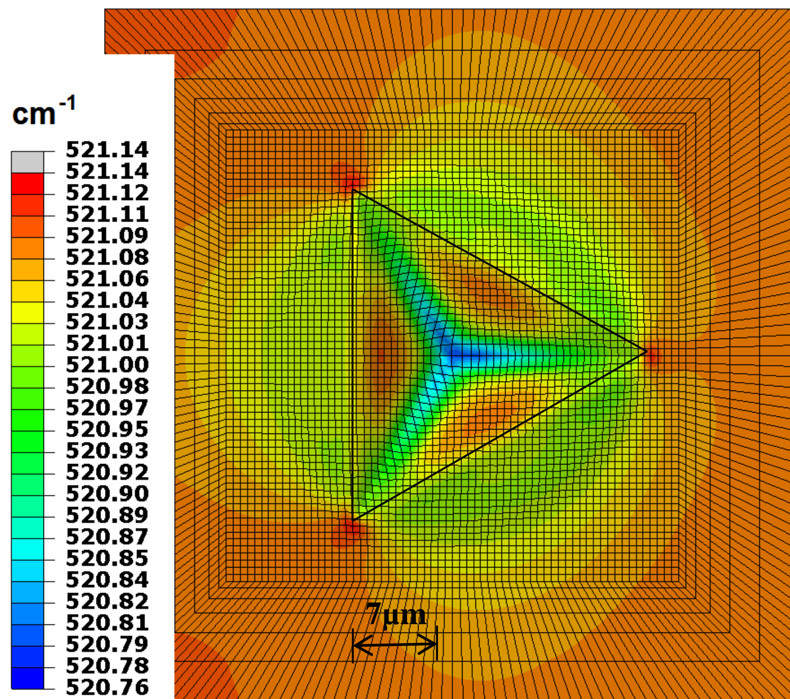

Figure 6.64: FEM model of expected Raman shifts (TO Si) for a 750mN indent before thermal anneal

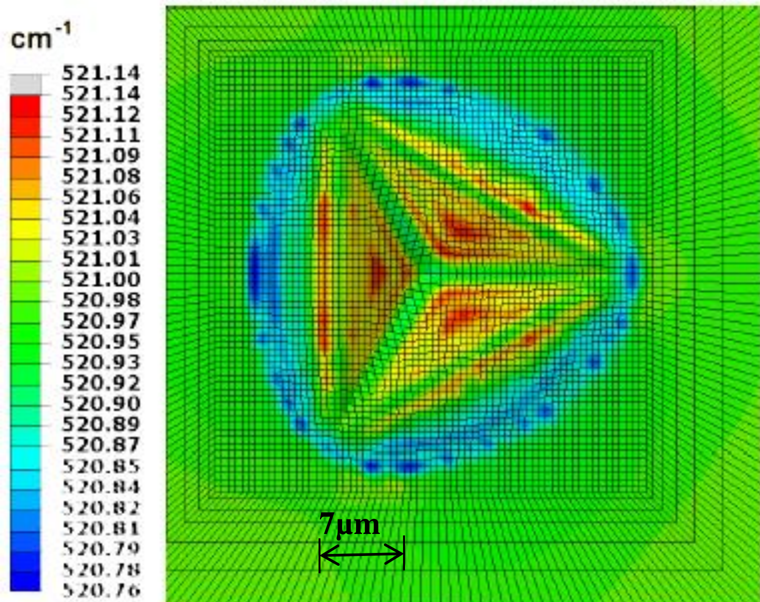

Figure 6.65 FEM model of expected Raman shifts (TO Si) for a 750mN indent post thermal anneal to 625°C

Looking at the centre of the indent it can be seen that the magnitude of tensile stress present within the indent has dramatically reduced. For this simulation the unstressed silicon Raman peak was taken to be 521cm^{-1}. Calculations of the change in the extent of the stress shows a drop of ~80% for this indent which is comparable with the 78% reduction calculated for the 600mN indent as shown in table 6.2 above.

The reduction of the magnitude of the strain fields in annealed crystals is thought to be as a result of dislocation slip and the formation of dislocations. This is confirmed by studying the samples with x-ray topography which confirm the formation of dislocation loops, fig. 6.66, after annealing [22]. This will be explored further in chapter 7. Zeng also noted that the annealing process reduced the observable strain by between 76% and 89% in line with the observations noted in this work. The increase in both tensile and compressive stresses after indentation is due to an increase of the energy within the lattice. This 'deformation energy' that is stored within the material is then released during the annealing process so reducing the strain levels within the material [23].

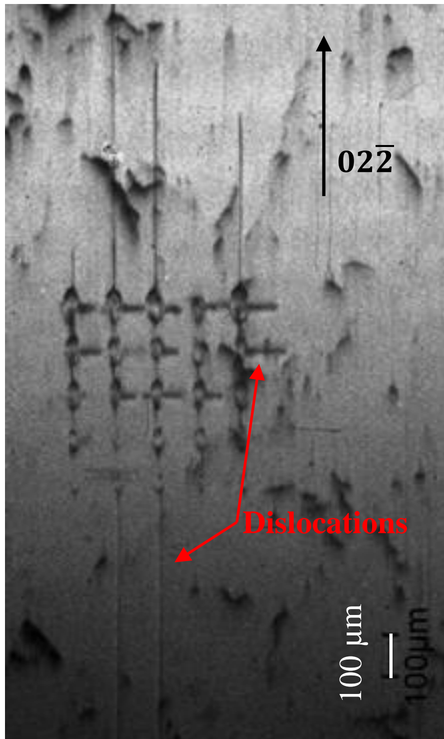

Figure 6.66: LAT x-ray topography of Sample 2, showing horizontal and vertical dislocations

6.6 Summary

The results also show the inherent suitability of Raman spectroscopy to non-destructive defect analysis. As demonstrated above, it is possible to determine the location of sub-surface cracking through the interpretation of the Raman spectra. Raman analysis shows the formation of the high pressure polymorphs and their locations within the defects. The data was correlated with and confirmed by the use of FEM simulations.

6.7 References

[1] I. De Wolf, Semicond. Sci. Tech. **11**, 139 (1996).

[2] K. F. Dombrowski, *Micro-raman investigation of mechanical stress in Si device structures and phonons in SiGe* (Brandenburgische Technische Universitat, 2000).

[3] I. H. Campbell and P. M. Fauchet, Solid State Comm. **58**, 739 (1986).

[4] V. Domnich and Y. Gogotsi, Rev. Adv. Mater. Sci. **3**, 1 (2002).

[5] D. Ge, V. Domnich, and Y. Gogotsi, J. Appl. Phys. **95**, 2725 (2004).

[6] B. R. Lawn and M. V. Swain, J. Mater. Sci. **10**, 113 (1975).

[7] B. R. Lawn and A. G. Evans, J. Mater. Sci. **12**, 2195 (1977).

[8] A. Kailer, K. G. Nickel, and Y. Gogotsi, J. Raman Spec. **30**, 939 (1999).

[9] B. R. Lawn and E. R. Fuller, J. Mater. Sci. **10**, 2016 (1975).

[10] S. J. Lloyd, J. M. Molina-Aldareguia, and W. J. Clegg, J. Mater. Res. **16**, 3347 (2001).

[11] A. Kailer, Y. Gogotsi, and K. G. Nickel, J. Appl. Phys. **81**, 3057 (1997).

[12] D. A. Hills, D. N. Dai, and P. D. Warren, J. Eur. Ceram. Soc. **16**, 1209 (1996).

[13] R. F. Cook and G. M. Pharr, J. Am. Ceram. Soc. **73**, 787 (1990).

[14] J. Chen, J. Phys. D **45**, 203001 (2012).

[15] R. J. Needs and R. Martin, Phys. Rev. B **30**, 5390 (1984).

[16] M. I. McMahon and R. J. Nelmes, Phys. Rev. B **47**, 8337 (1993).

[17] Y. X. Zhao, F. Buehler, J. R. Sites, and I. L. Spain, Solid State Comm. **59**, 679 (1986).

[18] J. Wittge, *In Situ Investigation of Defects in Semiconductors* (Albert-Ludwigs-Universität Freiburg, Germany, 2012).

[19] G. Weill, J. L. Mansot, G. Sagon, C. Carlone, and J. M. Besson, Semicond. Sci. Tech. **4**, 280 (1989).

[20] R. H. Wentorf Jr. and J. S. Kasper, Science **139**, 338 (1963).

[21] E. Gorostegui-Colinas, *Modelling of Silicon Behaviour for Wafer Fracture Assessment during rapid Thermal Annealing* (Centro de Estudios e Investigaciones Tecnicas, Spain, 2012).

[22] D. Zeng, W. Jie, G. Zha, T. Wang, and G. Yang, J. Cryst. Growth **305**, 50 (2007).

[23] R. D. Doherty, D. A. Hughes, F. J. Humphreys, J. J. Jonas, D. J. Jensen, M. E. Kassner, W. E. King, T. R. McNelley, H. J. McQueen, and A. D. Rollett, Mat. Sci. Eng. A **238**, 219 (1997).

Chapter 7 Synchrotron X-Ray Topography Results

7.1 Introduction

X-ray topography experiments were carried out at the ANKA synchrotron light source, Karlsruhe, Germany.

Experiments were carried out on both small 20mm x 20mm silicon samples and on full 300mm wafers. In addition *in situ* heating experiments were carried out at the beamline using a double ellipsoid mirror furnace.

The results of these experiments are detailed below along with FEM simulations of the temperature profiles encountered in an industrial Rapid Thermal Anneal, (RTA) tool.

Using this information, along with both X-ray topography, XRT also referred to as X-ray Diffraction Imaging, XRDI, a parameter κ was determined that can be used to reliably predict wafer breakage.

7.2 Experimental Setup

As mentioned in chapter 3 x-ray topography experiments were carried out at the Topo-Tomo beamline at ANKA, Karlsruhe, Germany. The beamline is operated from a 1.5T bending magnet with the measurement hutch situated ~30m from the beam source. The beam tube itself is held in a vacuum which is isolated from the measurement hutch using a differential pump system. In the beam tube the only optical components present are a Beryllium (Be) window and a slit system used to set the beam size as shown in fig 7.1 [1]. The monochromator (Double Multilayer Monochromator DMM) was removed for all experiments performed.

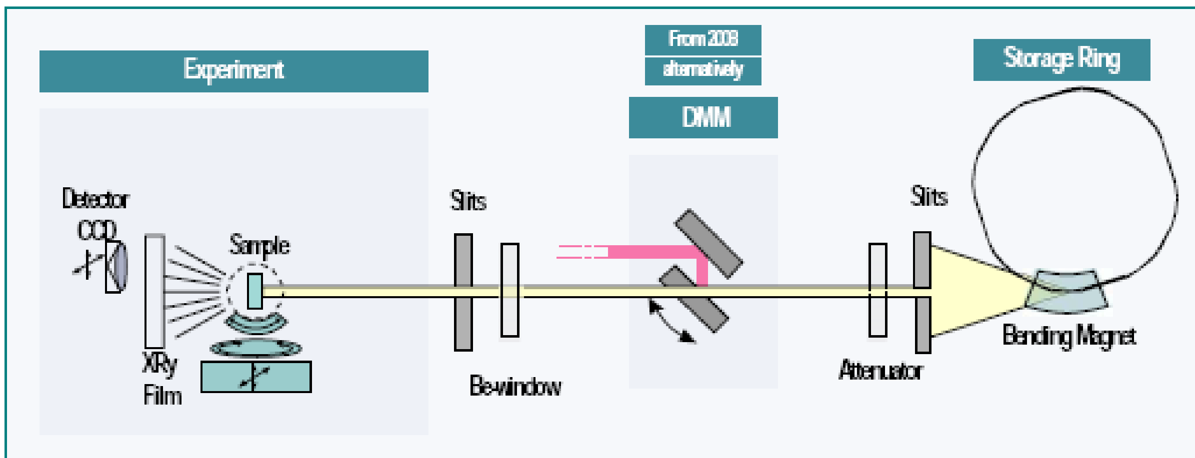

Fig. 7.1 Schematic layout of TOPO-TOMO beamline at the ANKA Facility. [1].

The layout of the experimental hutch is shown in fig. 7.2, which indicates the main physical components [2].

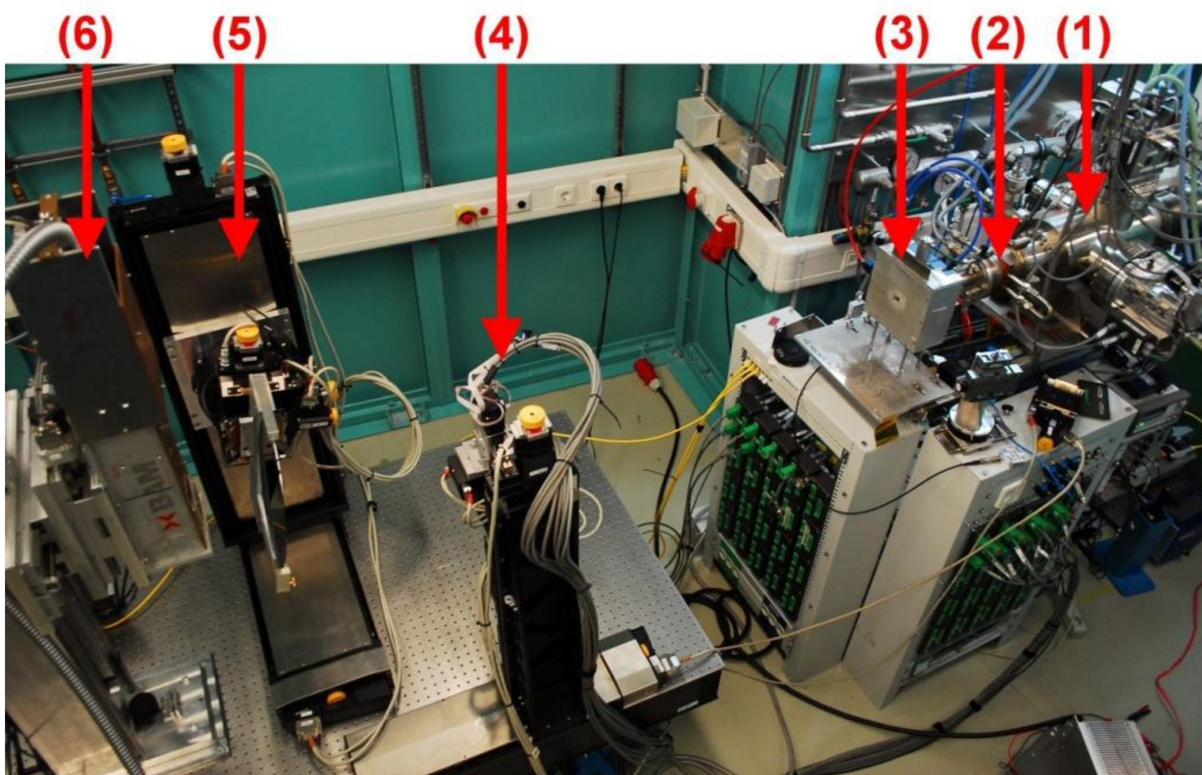

Figure 7.2: Setup of the experimental station at the Topo-Tomo beamline at the ANKA facility.

The components are:

1. Secondary slit system, used to set the beam size both horizontally and vertically.
2. Water cooled Be window
3. Fast shutter for exposure times of ~100ms
4. Tertiary slit system, used for Section Transmission (ST) Topography. Removed for Large Area Transmission (LAT) Topography
5. Translation table with X and Y movement along with goniometer for sample rotation
6. PCO CCD camera system; can be swapped with a film holder for a complete Laue pattern.

The Laue patterns were captured both on normal resolution, Agfa D3sc, and on high resolution, Slavich VPR-M, films while digital images were captured on the CCD system using the various techniques mentioned below. These techniques are also described in Chapter 3 of this work and by Tuomi in 2002 [3].

The techniques that will be discussed in this work are:

I. Large Area Back Reflection (LABR) topography
II. Large Area Transmission (LAT) topography
III. Section Transmission (ST) topography.

7.3 X-Ray Topography Results

7.3.1 Pre Thermal Annealing

7.3.1.1 Large Area Back Reflection Topography

LABR provides images of the strain in the upper regions of the Si wafers to depths of the order of tens of microns. The penetration depth is determined by the wavelength of the diffracted x-rays for a particular reflection as stated in chapter 3.

Figure 7.3 shows an optical image of Sample 1 which possess a range of indents; the top line of indents are due to 2N loads created with a Vickers tip, the remainder range from 500mN to 100mN load indents and were created with a Berkovich tip.

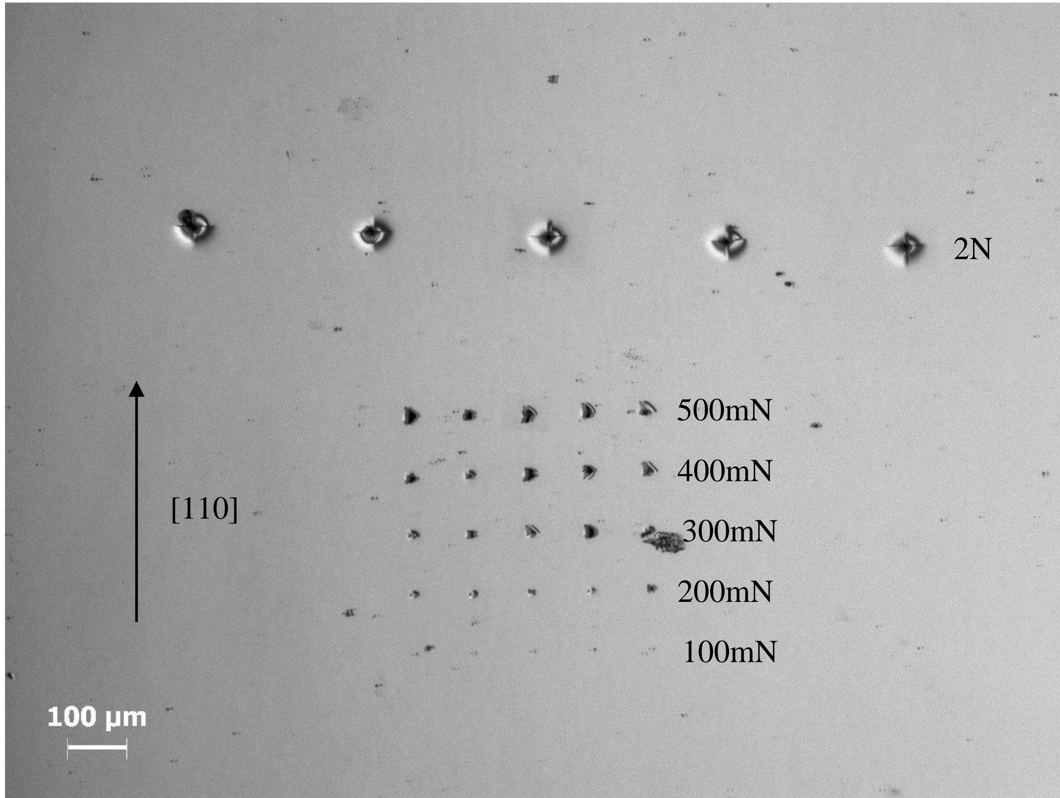

Figure 7.3: Optical image of Sample 1 with a row of 2N indents and an array of indents from 500mN to 100mN below it.

Sample 1 was imaged using LABR as shown in fig 7.4 which is a 0 2 10 topograph with a penetration depth t_p of ~100μm.

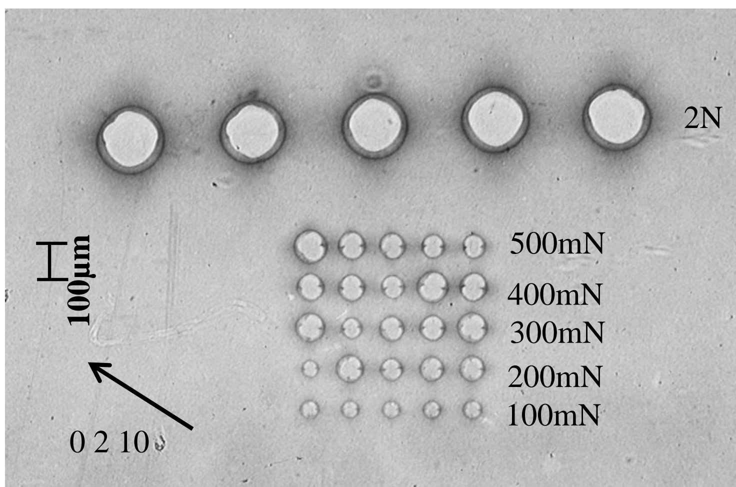

Figure 7.4: Single 0 2 10 Large Area Back Reflection topograph of Sample 1.

Figure 7.4 shows the strain around the indents at distances of the order of 100µm from the indent centres to be isotropic in nature and this isotropy can be observed regardless of the size of the indent. Initially this may look surprising as Silicon, being a cubic crystal, is elastically anisotropic. However silicon is plastically isotropic in nature therefore it can be concluded that, as this LABR topography probes to a t_p of 100µm, that the image is being formed by the plastic zone beneath the indentation, as shown in fig. 7.9 below [4, 5].

This isotropy is confirmed by the use of Finite Element Modelling FEM of the strain around the indents performed at CEIT, Spain [5], fig. 7.5. Though the simulation produced an image that is not as isotropic in nature as the LABR topography, it can be noted from fig 7.5 that the simulation is showing the stresses around the indent out to a distance of 16µm from the indent centre.

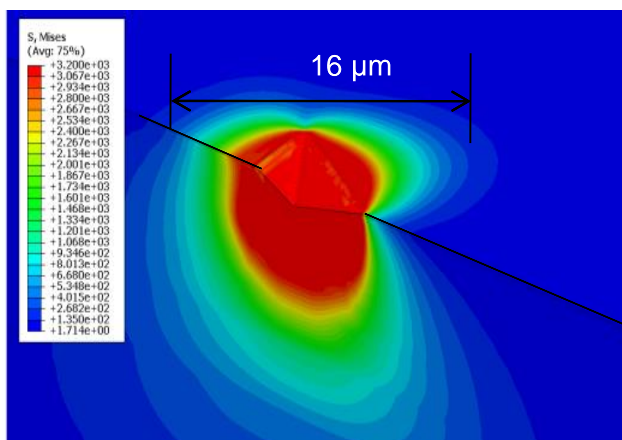

Figure 7.5: FEM simulation of an indent created using a 500mN loading and a Berkovich tip, showing isotropic strain. The simulation shows the resultant von Mises stress.
Courtesy of Eider Gorogosti-Colinas, CEIT, Spain [5]

7.3.1.2 Large Area Transmission Topography

While LABR topography will show the strain from the top 10-100µm of the sample [6], Large Area Transmission (LAT) topography can image the complete volume of the sample using a white beam whose spatial area is several mm^2, and this probed volume is projected onto an x-ray film or a CCD camera system.

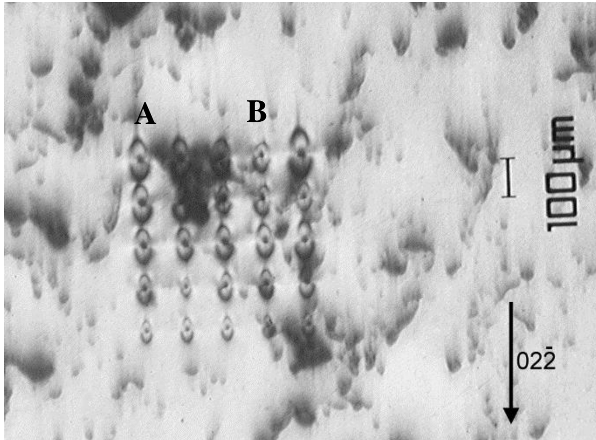

Figure 7.6: $02\bar{2}$ LAT topograph of Sample 2. Five rows of indents are visible ranging from 500mN to 100mN. The strain field reduces in extent between points ‘A’ and ‘B’, both of which were produced with a 500mN load

Fig. 7.6 shows a $02\bar{2}$ reflection of a 200 mm^2 silicon sample, Sample 2. The sample consists of a matrix of indents ranging from 500mN down to 100mN. Of note is that while the size of the strain field diminishes with the size of the indent, there is also a reduction in the size of the strain field within the same indentation load. This can be seen by comparing the spatial extent of the strain fields for the two indents labelled ‘A’ and ‘B’.

The reduction in the extent of the strain field can be explained by the presence of breakouts as observed with micro Raman Spectroscopy (μRS) (Chapter 6). To enable easier visualisation of the phenomena another sample, Sample 7, was analysed. Fig. 7.7 shows a $02\bar{2}$ LAT topograph of the first 3 indents from this sample. There is significant reduction in the extent of the strain field from indents ‘a’ to ‘c’. All the indents were created with a 600mN load from a Berkovich tip.

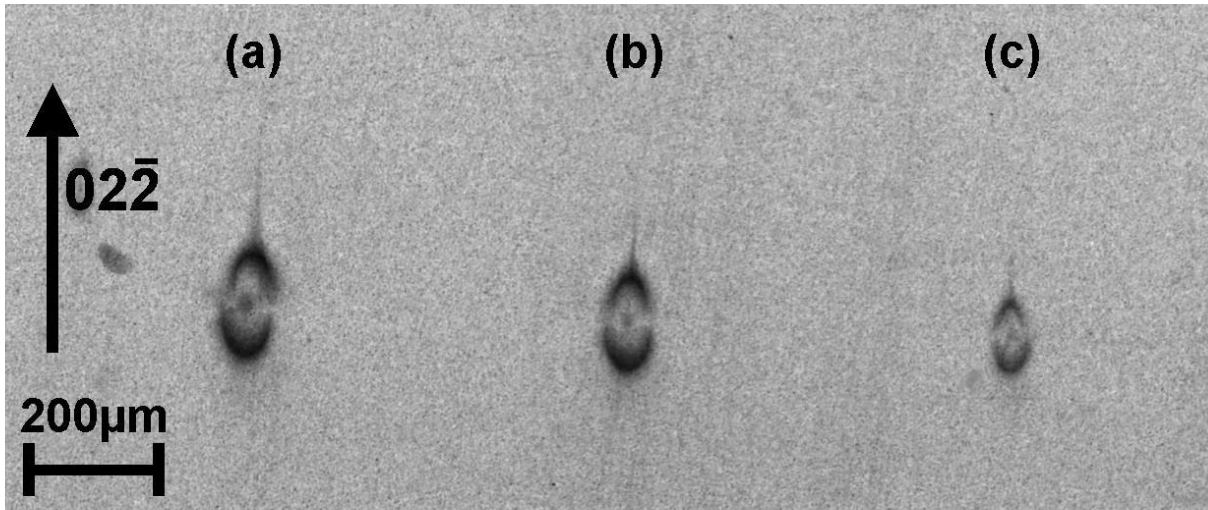

Figure 7.7: $02\bar{2}$ LAT of Sample 7. Image shows three 600mN indents with the extent of the strain field significantly decreasing from indents 'a' to 'c'

Scanning Electron Microscope (SEM) images of the corresponding indents show a correlation between the strain field and the extent of breakouts observed.

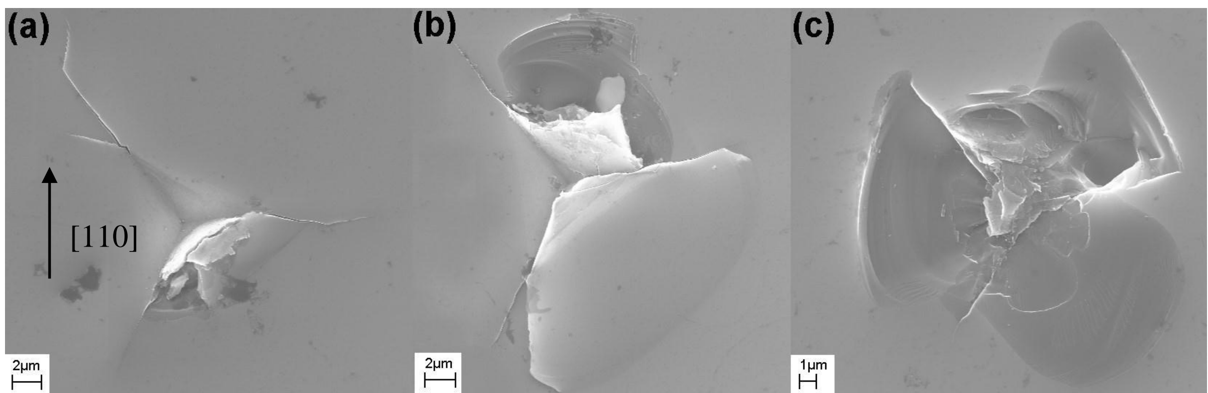

Figure 7.8: SEM images of Sample 7. The SEM images correspond to the indents shown in fig. 7.7. The amount of damage increases from indents 'a' to 'c'.

Analysis of the image shows a drastic reduction in the extent of the strain field for all indents. The reduction in the size of the strain field is approximately 22% in height and 25% in width, the height and width corresponding to the {110} crystallographic directions [2]. Raman data taken from the relevant indents also show a decrease in the magnitude of the compressive stress from ~10GPa for indent 'a' down to ~1.8GPa for indent 'b'. This also correlates well with the 2D Raman stress map data as detailed section 6.4.2. As can be seen by both the

LABR and LAT images, as well as being confirmed by the Raman data of section 6, indentation produces long range strain fields within the crystal lattice, caused by the formation of a plastic zone beneath the indent [7-9].

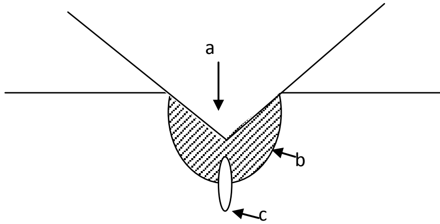

Figure 7.9: Sketch showing the zone of transformation and the plastic zone beneath a nanoindent, (a shows the nano indentation, b the plastic field and c the area of maximum stress) [9]

One of the issues noted upon examination of the LAT topographs was the lack of any dislocation images which are visible in TEM cross sections of indents. Fig. 7.10 shows the TEM images of two indents with the introduced dislocations highlighted with red arrows.

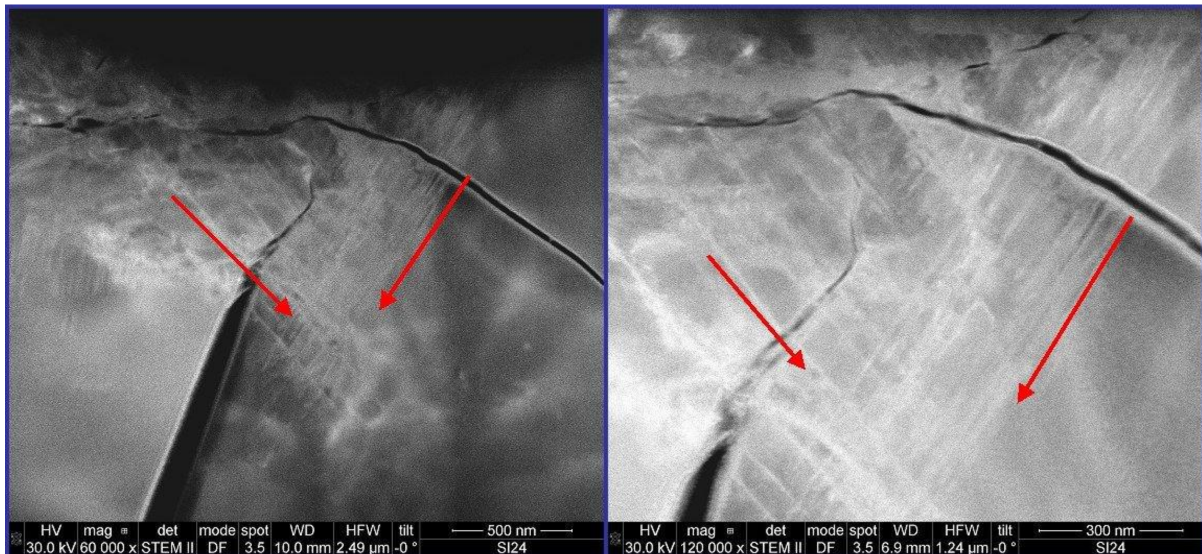

Figure 7.10: TEM cross section images of two nanoindents showing introduced dislocations beneath the indents.

When the LAT topographs are studied, however, no dislocations can be observed as can be seen in fig. 7.11.

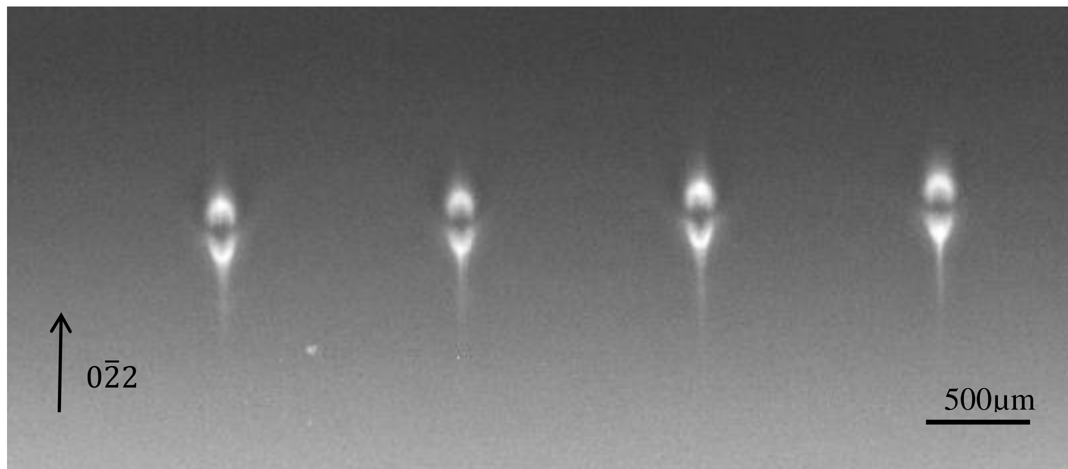

Figure 7.11: A $0\bar{2}2$ LAT topograph of the first 4 indents from sample Si_0_Cr4. All indents produced with a Vickers indenter produced with a 2N force.

The explanation for the apparent differences between the topographs and the TEM images was explained by Raghothamachar. Whereas the resolution limit of the TEM is ~1 – 2 nm [10], there is no magnification involved with topography and the spatial resolution is due to geometric factors which give a resolution limit of ~ 10^5 – 10^6 dislocations per cm^2. Above this limit single dislocations are no longer visible and the dislocations form a large blurred image [11, 12].

7.3.2 Post Thermal Annealing

Sample 2 subsequently underwent a thermal anneal using the double ellipsoid sample heater as described in section 5.2.1. LAT topographs taken post anneal show the appearance of vertical dislocations from the 500mN and 400mN indents. Fig. 7.12 was captured when the sample had reached 729°C. Further annealing gives rise to additional vertical dislocations running in the $[01\bar{1}]$ direction along with the appearance of horizontal dislocations which run

along the $[0\bar{1}\bar{1}]$ direction, fig. 7.13. The formation of the dislocations provides strain relief within the crystal lattice [13-16], due to the release of the deformation energy, as mentioned in chapter 6 and can also be seen in the LABR topograph of the same sample, fig. 7.14.

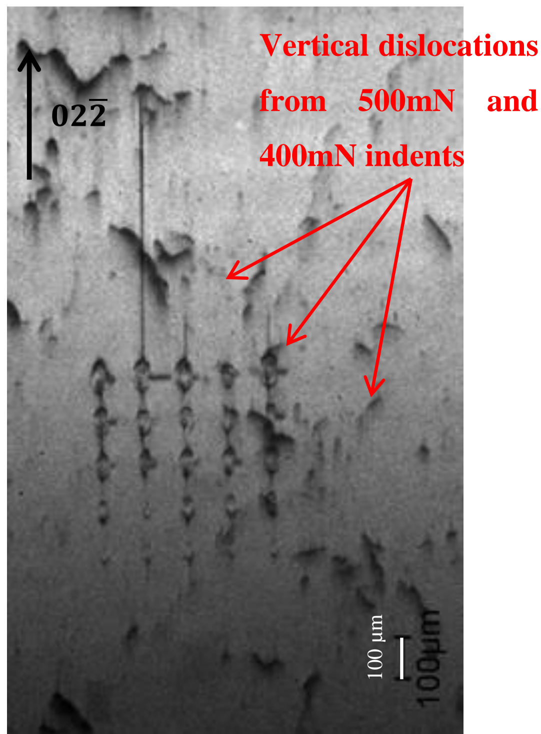

Figure 7.12: $02\bar{2}$ LAT x-ray topograph of Sample 2. Image captured when the sample had reached 729°C and shows the initial formation of “vertical” dislocations running along $[01\bar{1}]$.

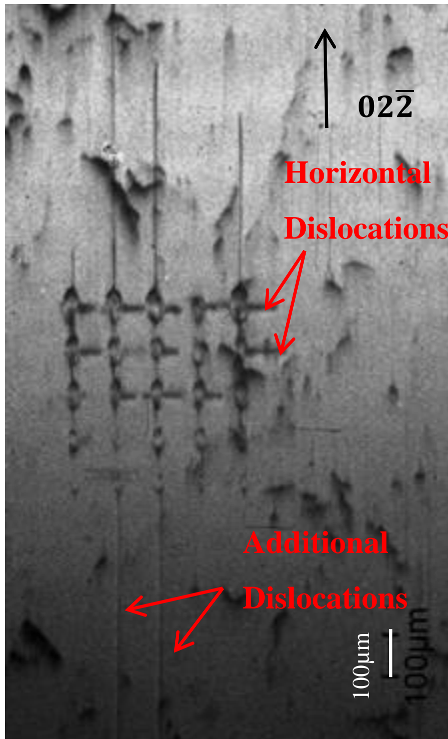

Figure 7.13: $02\bar{2}$ LAT x-ray topograph of Sample 2. Image captured when the sample had reached 790ºC and shows the formation of "vertical" and "horizontal" dislocations running along $[01\bar{1}]$ and $[0\bar{1}\bar{1}]$, respectively

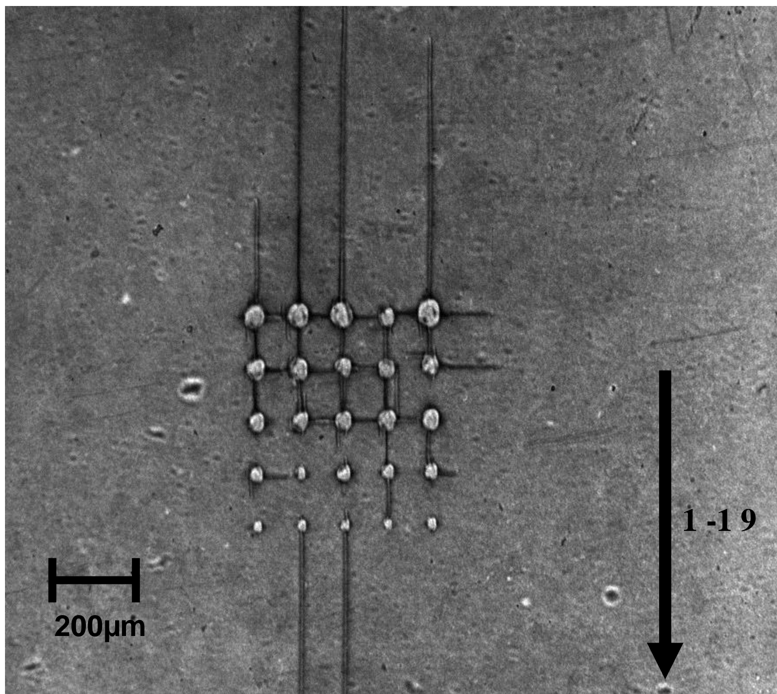

Figure 7.14: 1 -1 9 LABR x-ray topograph of Sample 2 taken post thermal anneal to ~1000ºC

7.3.3 Plateau Annealing

A selection of 20 x 20mm nano-indented samples were subjected to thermal annealing within a double ellipsoid heater as described in section 5.2.1. The samples were mounted in the heater with the indents aligned in a horizontal direction in the heater. The samples were then subjected to a plateau anneal consisting of a 60 second heating with a 60 second holding time at the maximum temperature before being rapidly cooled, fig. 7.15.

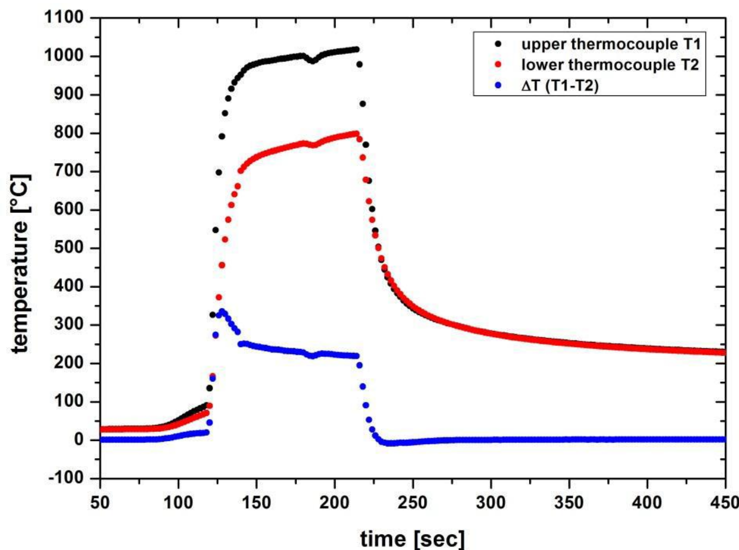

Figure 7.15: Heating timeline and resulting temperature difference between thermocouples on the back side of sample 2 during RTA. [2]

The heater was set up with two thermocouples positioned at the back of the sample to record the sample temperature. Two thermocouples were utilised as the double ellipsoid heater had a temperature differential of 18K/mm in the vertical and 8K/mm in the horizontal directions [17-19] resulting in a stress gradient that is two times higher in the vertical direction [2], the result of this can be observed in figs. 7.12 to 7.14 above, where the vertical dislocations appear first and are of a larger magnitude than the horizontal dislocations. This can be further observed when observing the dynamics of the strain field during thermal anneal. Figures 7.16 to 7.18 show the visible extent of the contrast related to the strain field within the crystal lattice (for ease of communication this will be referred to as the extent of the strain field in the rest of this discussion) around 2N, 10N and 50N indents measured before annealing and

then ~ 28seconds later. At this point dislocation loops began to form masking any further decrease in the extent of the strain field. Tables 7.1 and 7.2 tabulate the differences observed.

Force (mN)	Strain Field Height(μm)	Error (μm)	Strain Field Width (μm)	Error (μm)
2000	275.20	11.58	133.95	7.16
10000	419.55	9.02	195.80	6.82
50000	1117.00	32.57	688.00	18.87

Table 7.1: Extent of the strain field around a 2N, 10N and 50N indent before annealing

Force (mN)	Strain Field Height(μm)	Error (μm)	Strain Field Width (μm)	Error (μm)	% Reduction in Strain Field Height	% Reduction in Strain Field Width
2000	170.36	7.15	94.88	5.02	38	29
10000	190.05	3.99	120.15	4.08	55	38
50000	852.28	24.72	657.19	17.74	24	4

Table 7.2: Extent of the strain field around a 2N, 10N and 50N indent after annealing

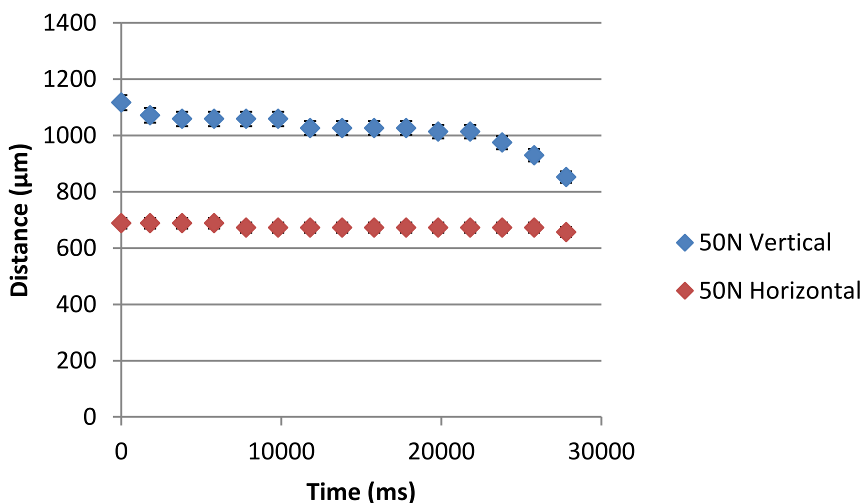

Figure 7.16: Graph of the reduction of the extent of the strain field around a 50N indent with time during annealing

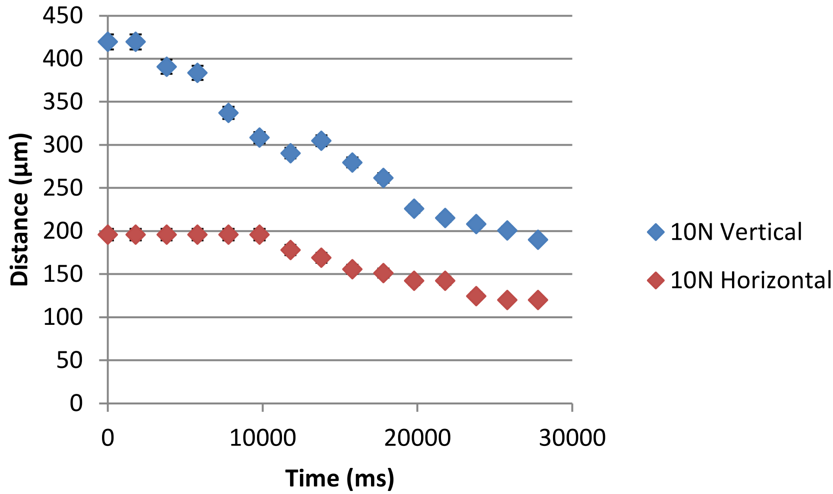

Figure 7.17: Graph of the reduction of the extent of the strain field around a 10N indent with time during annealing

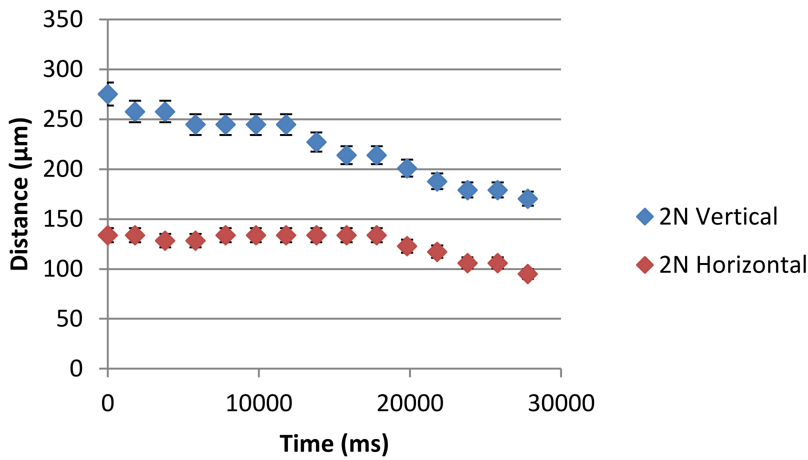

Figure 7.18: Graph of the reduction of the extent of the strain field around a 2N indent with time during annealing

Based on the recording in the topographs of the spatial extent of contrast due to the existence of strain fields surrounding the nanoindents the data show that there is a reduction of up to 55% in the vertical strain field extent while in the horizontal strain field this reduction is only up to 38% and is as a result of the annealing process relaxing the introduced strain fields. This relaxation of the strain fields was also observed by micro-Raman spectroscopy as noted in section 6.4.3. It was also noted in this earlier section that, after thermal annealing the position of the peak tensile strain observed had moved horizontally with respect to the indent, and at the time it was unclear as to the reason for this. The data shown above could offer an

explanation for this effect as the vertical strain field experienced by the indent reduces at a greater rate than the horizontal one resulting in an added stress value due to the temperature gradients within the mirror furnace. This effect becomes more pronounced when the formation of the dislocation loops and slip bands are studied and will be discussed later in section 7.3.4. Figure 7.12 and 7.13 above show that the temperature differential has an effect on the growth of the dislocations. More significantly, the effect of the temperature differential can be noticed when sample Si_0_Cr4 is studied. This sample consisted of a row of seven 2N Vickers indents that were subjected to a plateau anneal of ~970ºC, fig. 7.19.

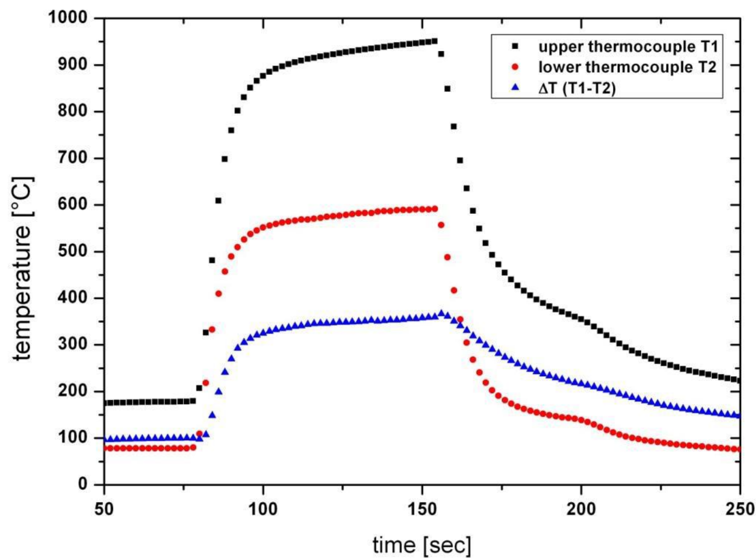

Figure 7.19: Plateau anneal of sample Si_0_Cr4 showing the temperature from both thermocouples and the resulting temperature difference. [2]

Fig. 7.20 shows a sequence of $0\bar{2}2$ LAT topographic images from this sample showing the indents before heating (a), the first appearance of the dislocation loops (b). Image c was taken 30s later, the dislocation lops are more pronounced with only two of the {111} planes activated. Finally image (d), taken after 60s shows the activation of the secondary pair of {111} planes. Not only is there a significant difference in the extent of the dislocation loops progressing from indent 1 to indent 7 but when the average velocities are calculated it can be

seen that they too are different across the indents. The average velocity for indent 1 is between 20 - 25 μm/s and for indent 5 the average velocity is 17 - 19 μm/s [2].

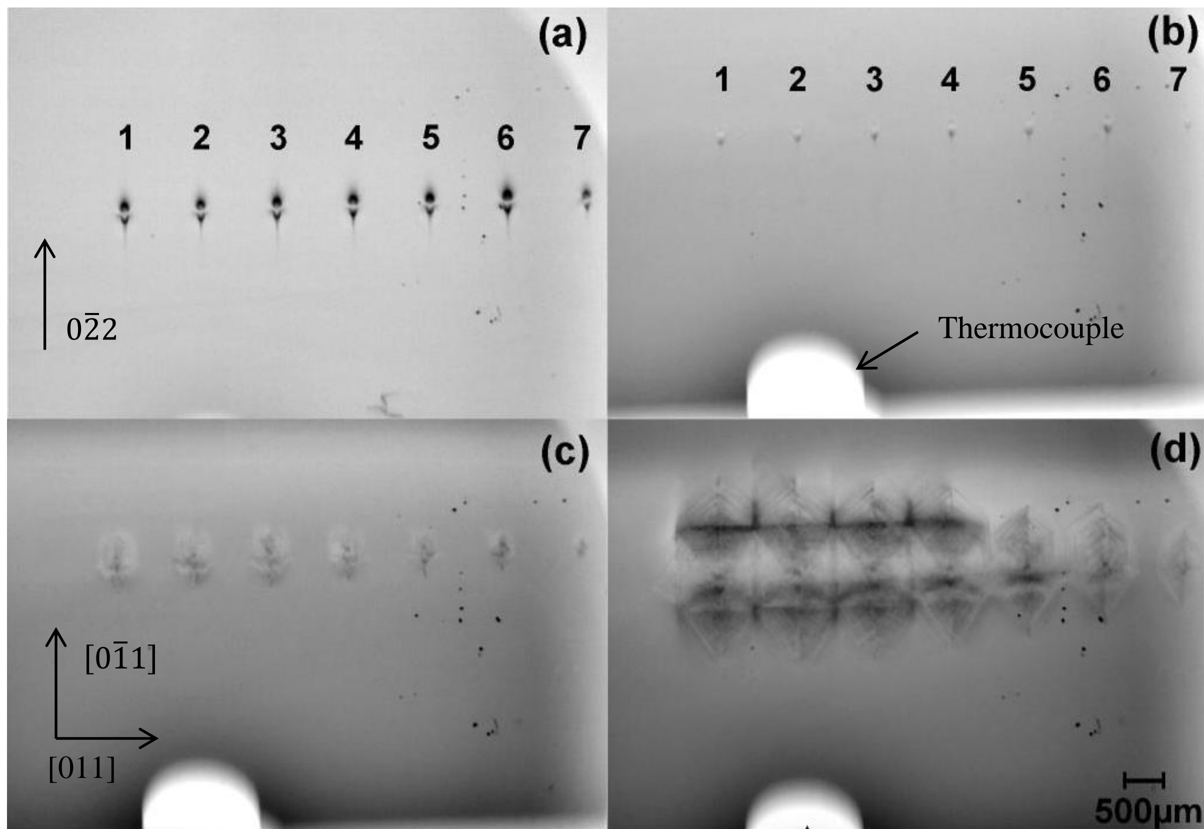

Figure 7.20: Sequence of transmission topographs taken of sample Si_0_Cr4 showing the formation of dislocation loops. [2]

Tables 7.3 and 7.4 tabulate the change in the extent of the strain field around 6 of the 2N indents from sample Si_0_Cr4. It can be seen that while the reduction of the extent of the vertical strain field remains constant across the indents, the size of the horizontal strain field reduces by ~29% for indent 1 to ~54% for indent 6.

Vertical Strain Field (μm)					
Indent 1	Indent 2	Indent 3	Indent 4	Indent 5	Indent 6
275.20	275.20	275.20	275.20	275.20	275.20
170.36	170.36	170.36	170.36	170.36	170.36

Table 7.3: Reduction in the size of the vertical strain field around 2N indents, sample Si_0_Cr4

Horizontal Strain Field (µm)					
Indent 1	Indent 2	Indent 3	Indent 4	Indent 5	Indent 6
133.95	133.95	133.95	133.95	133.95	133.95
94.88	94.88	83.72	83.72	83.72	61.39

Table 7.4: Reduction in the size of the horizontal strain field around 2N indents, sample Si_0_Cr4

7.3.4 Slip Band Development

Using the data taken from XRT images of dislocation loops combined with the 3D-XRDI data extracted from the ST topographs, as discussed in chapter 5, it is possible to produce a three dimensional model of the formation of the dislocation loops. Fig. 7.21 shows a schematic of the formation of dislocation loops in sample Si_0_Cr4. Initially the loops appear on the (111) and $(1\bar{1}\bar{1})$ planes, fig 7.21b. During the heat treatment the second glide system is then activated on the $(1\bar{1}1)$ and $(11\bar{1})$ glide planes until finally the loops progress through to the back of the sample forming slip bands. Fig. 7.22 shows a comparison of the model to a 3D reconstruction of ST topographs taken on sample Si_0_Cr4 where the features predicted by the model can be observed on the rendered image.

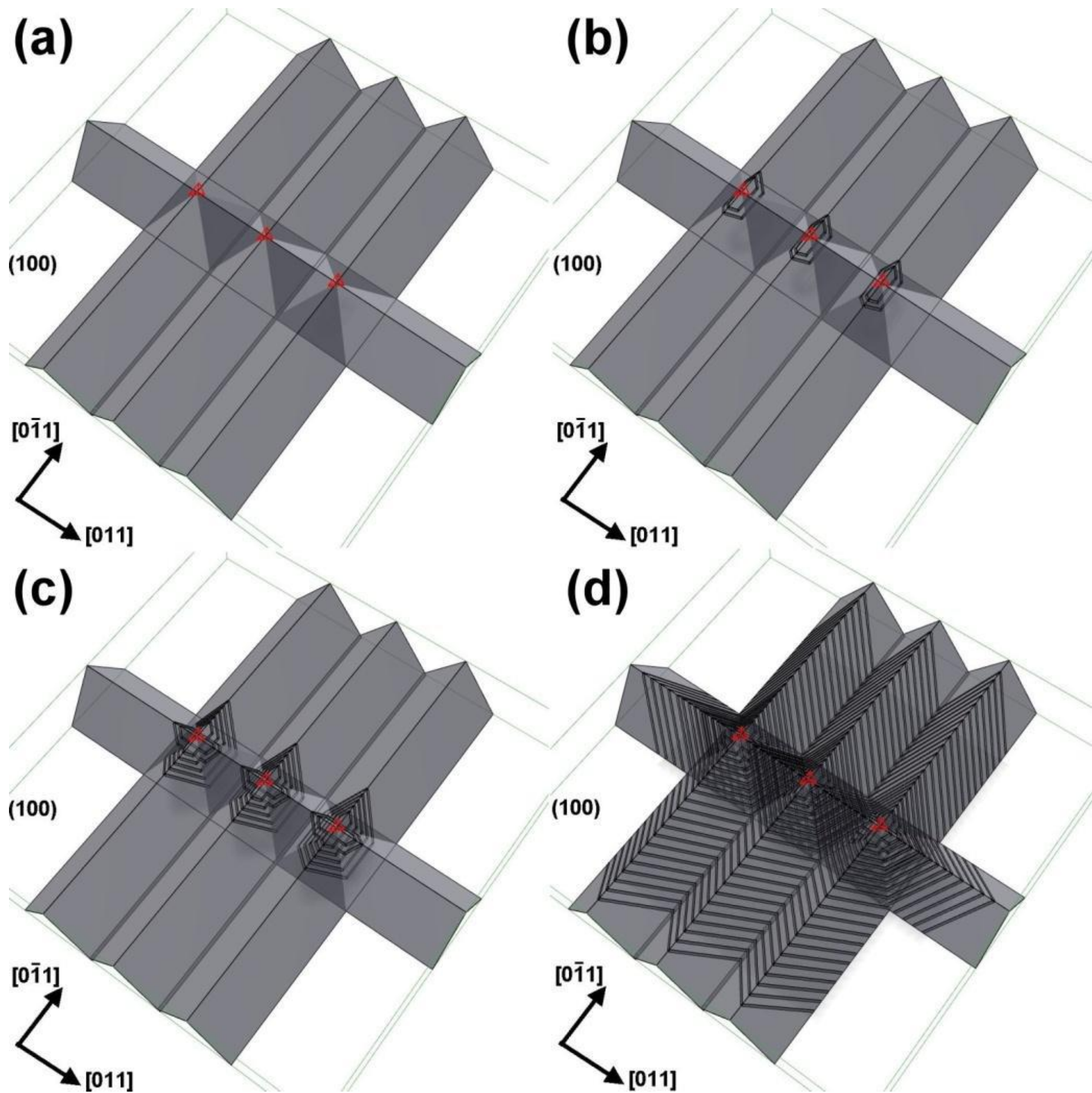

Figure 7.21: Model of the propagation of dislocation loops through a silicon sample. (a) only the indent is visible, (b) dislocation loops begin to form, (c) the secondary glide system is now activated and (d) the dislocation loops have propagated through the sample. [2]

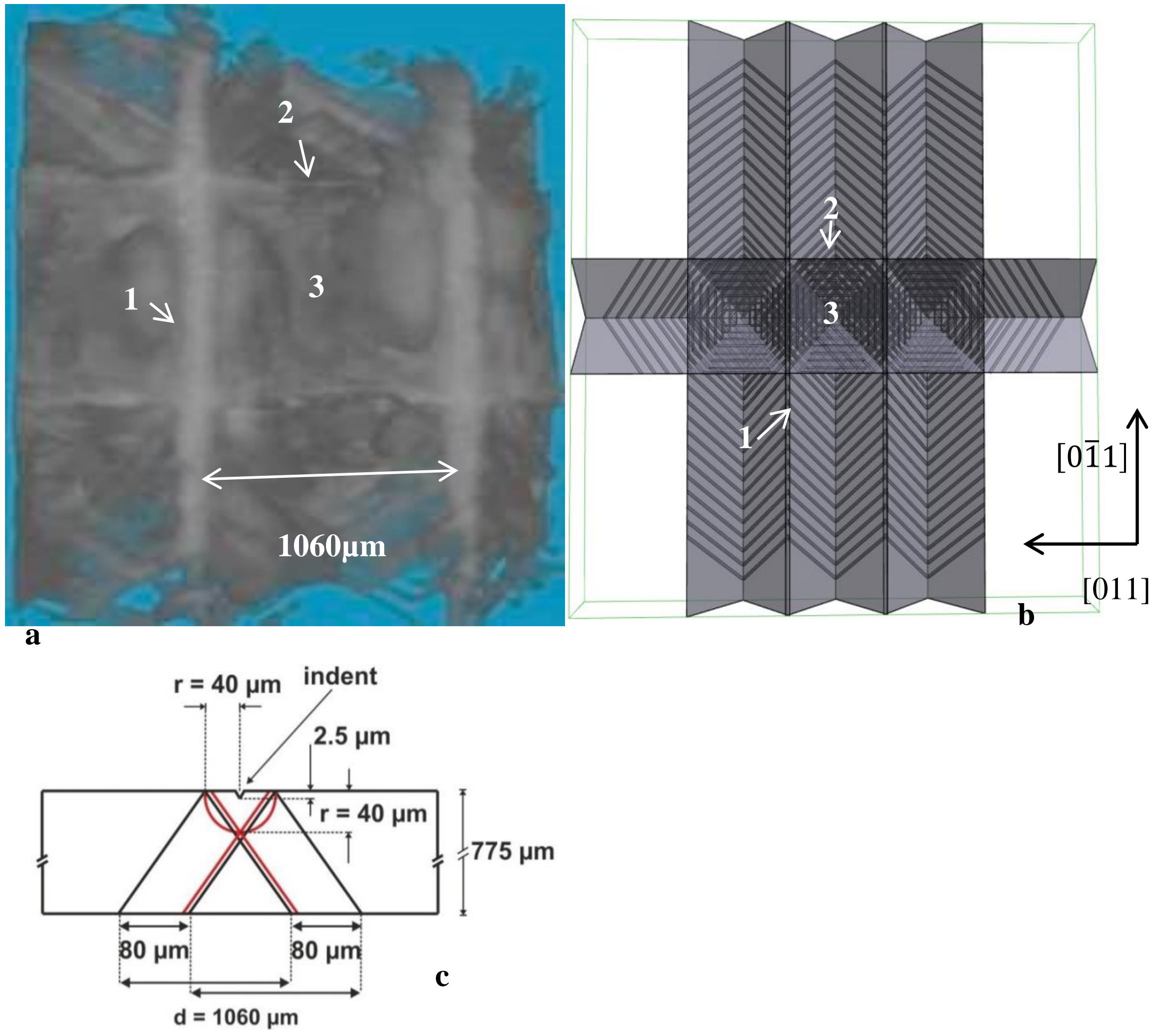

Figure 7.22: (a) is a still image from a 3D reconstruction showing the back side of sample Si_0_Cr4 compared to (b) the model of dislocation propagation, (c) shows a schematic sketch of the development of slip planes around an indent produced by J. Wittge [2]. The image shows (1) the overlapping slip bands from two adjacent indents, (2) single slip band and (3) dislocation free area under the indent

It is known that the preferred glide plane for (100) silicon is along the {111} series of glide planes [20]. This means that there should be no preferential direction for the formation of the dislocation loops between the [111] planes and any apparent difference must be due to the addition of stress to the sample. These differences can be attributed to the temperature gradients within the mirror furnace providing a stress value of between 0.12 to 0.68 MPa/m along the direction of the temperature gradient [17]. This internal stress could also be a contributing factor to the phenomenon observed by micro Raman Spectroscopy in section

6.4.3. The *in situ* thermal annealing process also showed that below a critical temperature of 900°C only single straight dislocations could be observed [17] and that when the temperature rose to above 900°C the density of the dislocations increased giving rise to longer slip bands [21]. Although no Si samples broke during the *in situ* study, it could be argued that the temperature differentials acting on the samples were insufficient to produce enough strain to cause the samples to break. The data does indicate that these internal stresses do exist and are acting on the samples during annealing.

This becomes more obvious during thermal annealing of whole wafers. For this study whole wafers were subjected to *ex situ* thermal annealing at CEIT, Spain. Finite element modelling showed that the temperature differential between the edge and the centre of a 300mm wafer was in the order of 50°C which gives rise to shear stresses in the order of a few MPa acting along the wafer edge [21]. The study took 48 commercial grade 200mm wafers and subjected them to either plateau or spike anneals. The wafers were indented with various loads and a matrix of the indent loads and annealing processes can be seen in appendix 3. Figure 7.23 shows an image of wafer 45 taken on the Bedescan™ XRDI tool, a commercially available x-ray metrology tool as described by Bowen *et al.* [22]. Wafer 45 was indented with a Vickers indent to a load of 3N before being plateau annealed to 1000°C for 30 seconds. The image showed a multitude of slip bands, virtually all of them originating at or near the wafer bevel edges.

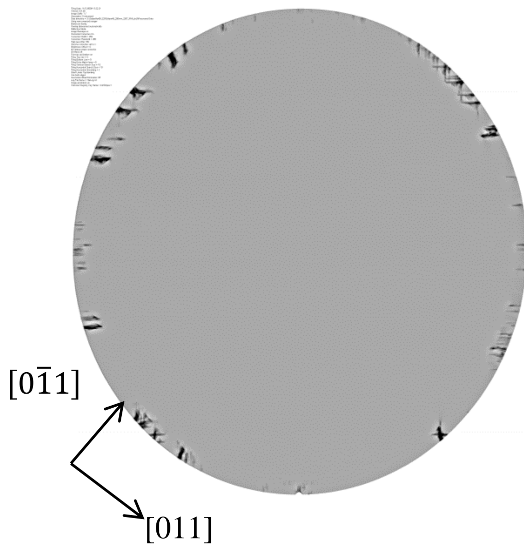

Figure 7.23: Bedescan™ XRD image of a 200mm wafer, wafer 45, and plateau annealed to 1000°C for 30 seconds showing slip from the edge. MoKα radiation, wavelength 0.708Å. Wafer was indented with 3N loads at 45° and 275° from notch.

It was interesting to note that the slipbands observed appeared to be originating in places other than those that had been indented. As the wafers had a [100] surface orientation the dislocation lines are all orientated in the <011> set of directions [13]. Detailed SXRT analysis of the wafer confirmed that, while there were slipbands originating from the indents, fig. 7.24 there were also many slipbands which originated from the wafer edge and from the notch, fig. 7.25.

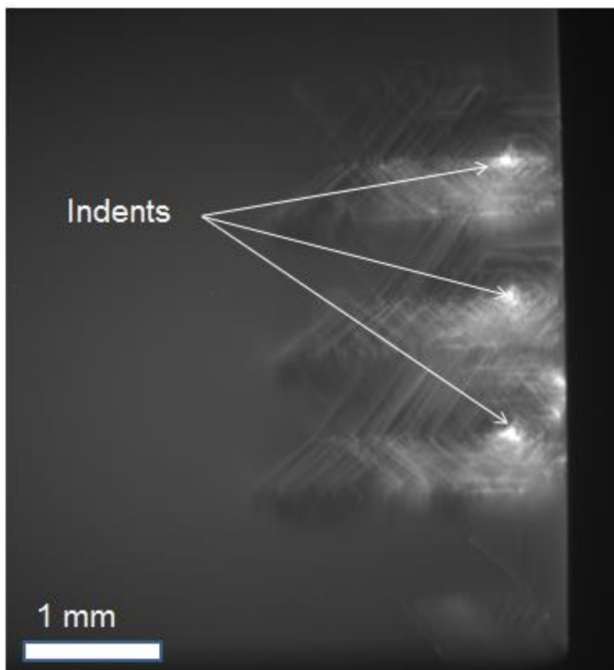

Figure 7.24: 220 X-ray topograph of wafer 45 showing three indents. Image taken at 180° to the notch

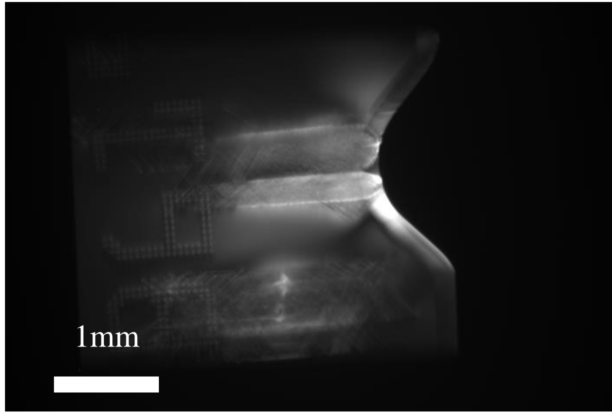

Figure 7.25: 220 X-ray topograph of wafer 45 showing slip bands emanating from the notch

SXRT analysis was also performed on wafers that had not undergone thermal annealing. The images showed evidence of localised defects, mainly at the wafer edge which can act as sources for the formation of dislocation loops, fig. 7.26. This evidence is supported by work performed by Chen *et al*. in 2009. Chen discovered, in a study of ~10,000 production line wafers, that the wafers that broke had unequal bevel edge lengths [23]. This study complemented the work of Wang in 2005 where he found that both the protruding SiC nodules protruding from the backside of a wafer contact between the wafer and its supports can cause damage that will result in the formation of dislocation loops and ultimately slipbands [24].

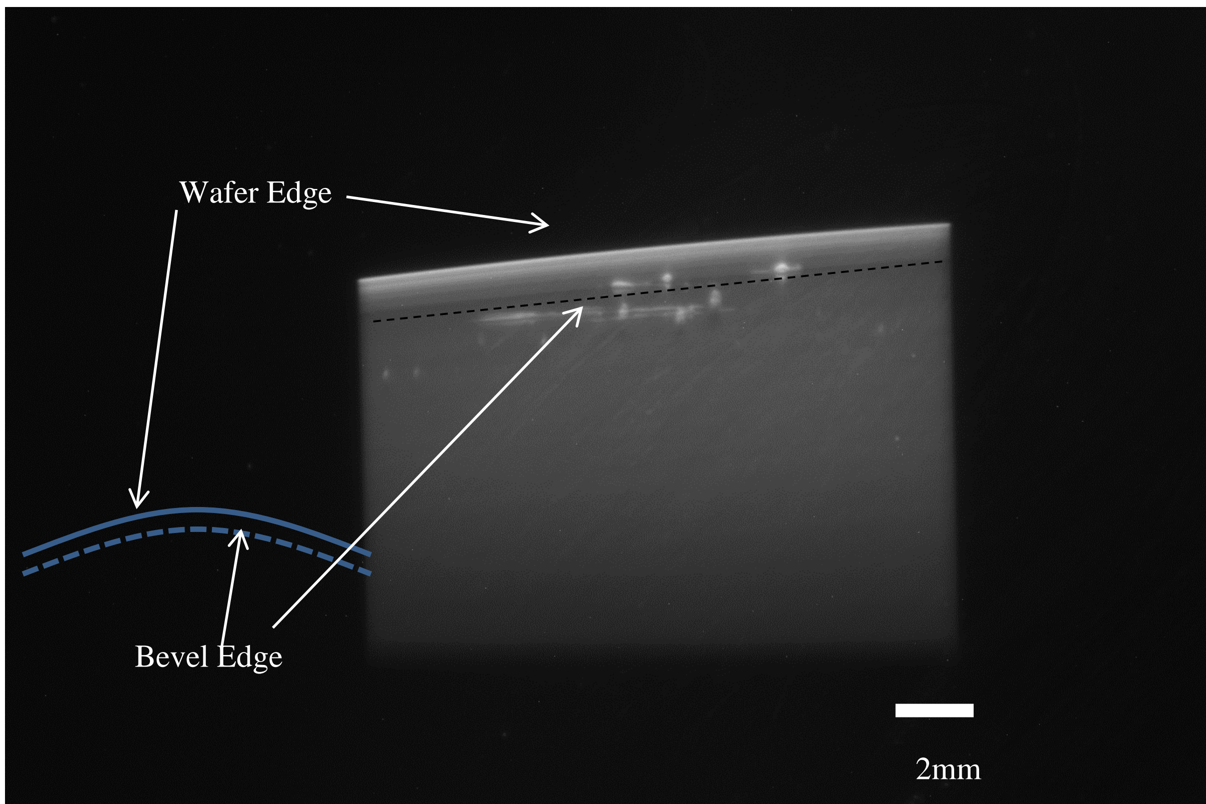

Figure 7.26: 220 X-Ray topograph of Wafer 55 showing areas of localised damage and strain along the bevel edge

Therefore it can be clearly stated, both from the data of Chen *et al*. and Wang, and based on the data shown in this study that slip bands can start from regions where there are no defined indents but will propagate from both the wafer edge and bevel edge. As this was true for all observed annealed wafers it can be concluded that the presence of these 'unobservable ' strain centres is common among silicon wafers.

The knowledge that differences in temperature provide a source of internal stress becomes more significant when the problem of cracks within wafers were studied. The development of cracks in the wafers examined in this study is comprehensively covered by J. Wittge in his doctoral thesis [2] wherein he found that, unlike the dislocation loops, cracks not only run along the {110} series of planes but can also run along the {111} and {112} series of planes. During the course of this study wafer breakage of 200mm wafers was observed during the cooling phase of the thermal anneal and modelled by J. Garagorri [10]. The data showed that

cracks introduced into a wafer would propagate when the edge of the wafer was in tensile stress and the centre was in compressive stress. Figure 7.27 shows the FEM simulation while fig. 7.28 shows the wafer with the compressive and tensile strain areas overlaid.

Along with the stress applied to the wafer due to thermal differences within the RTA tool, Yoo *et al*. also observed elastic deformation of wafers subjected to annealing with a maximum wafer deformation of ~10mm at 800°C returning to the flat position at 950°C, this being due to radiation heat transfer being more efficient at the edge as opposed to the wafer centre [25].

In order to mathematically model an XRDI image of a surface crack, the strain at the crack tip can be approximated to that of a super-edge dislocation [26] with a Burgers vector of $N\boldsymbol{b}$, where $\boldsymbol{b}$ the Burgers vector associated with the smallest lattice translation, and N is a number given by the crack width d such that

$$N\boldsymbol{b} = d \qquad (7.1)$$

In 1921 Griffith proposed what is known as the Griffith criterion whereby he showed that for a crack to open then the stresses σ must be greater than the back stress due to the edge dislocation [27]

$$\sigma > \frac{GN\boldsymbol{b}}{\alpha(1-v)L} \qquad (7.2)$$

where G is the shear modulus, α is a parameter approximately equal to unity, v is Poisson's ratio.

This was then applied to XRDI images of cracks by our research team; see Tanner *et al*. in 2012 [26]. Using the semi-kinematic theory of XRDI Tanner *et al.* showed that image formation only occurs when the effective misorientation of the crystal lattice associated with the defect $\delta(\Delta\theta)$ equals the FWHM of the crystal reflecting range for a perfect crystal, known

as the Darwin Width [28] and that within this area the defect will diffract kinematically with a scattering power given by

$$\delta(\Delta\Theta) = -\frac{1}{\kappa sin2\Theta_B}\frac{\partial}{\partial \boldsymbol{S_g}}\bar{g}\cdot\bar{u} \qquad (7.3)$$

where $\kappa = 1/\lambda$, θ_B is the Bragg angle, $\bar{u}$ is the long range displacement and $\boldsymbol{S_g}$ is a vector in diffracted beam direction. Tanner *et al.* then went on to show that a crack will propagate when

$$\sigma > \beta G\delta\omega\left(\frac{d_0}{L}\right) \qquad (7.4)$$

where β is a numerical parameter between 5 and 10, $\delta\omega$ is the Darwin width and σ is the thermal stress within the RTA chamber. This is in accordance with work published by Cramer *et al.* where he showed that an external stress or force acting upon a wafer with a crack in it will exert a driving force upon the crack, which in the case of this study is the thermal stress applied to the wafers [29].

Thus the stability of a crack is dependent on a single parameter, namely the crack length divided by the width of the XRDI image at the crack tip, giving a parameter κ where

$$\boxed{\frac{L}{d_0} > \kappa_c} \qquad (7.5)$$

where κ_c is the critical value of κ in a given stress state, L is the crack length and d_o is the width of the XRDI image at the crack tip. This infers that when a crack has a large width to length ratio it will not propagate whereas those with a large length but a narrow width can cause breakage, though cracks with a long length can be benign if the crack tip is sufficiently blunted [26]. This can be seen in fig. 7.29 below where two cracks were studied. C1 had a κ_c value of 0.9 while C2 had a κ_c value of 30 this being where the sample broke.

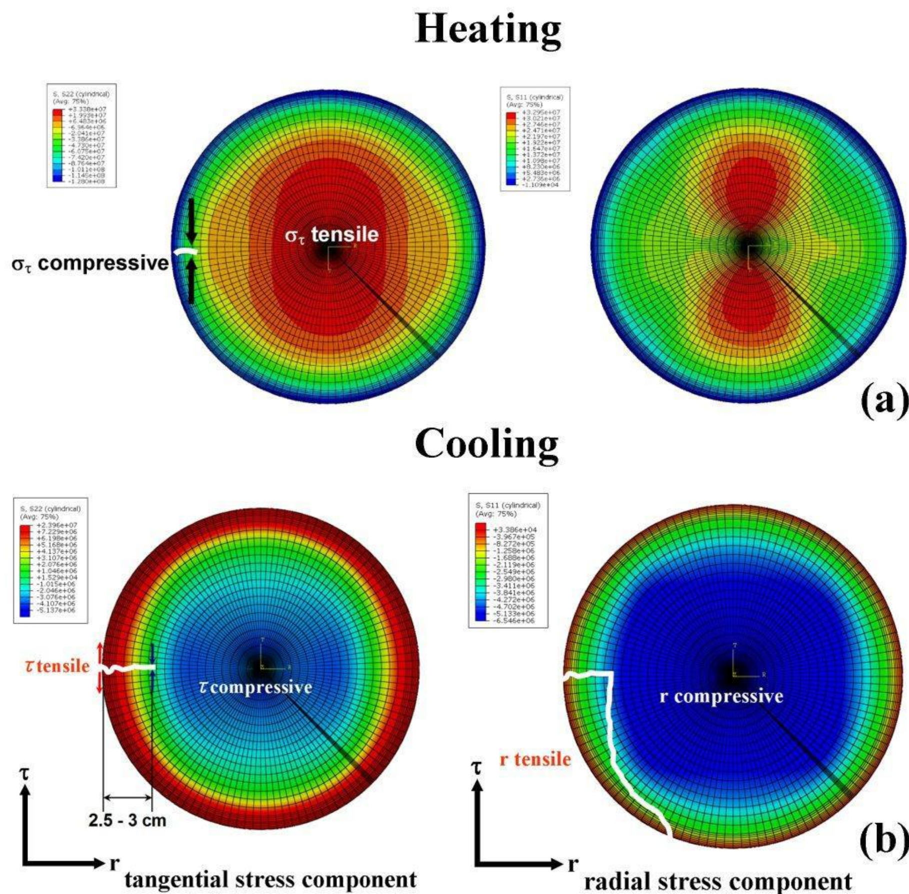

Figure 7.27: FEM simulation results of the thermal stress distribution during a spike anneal in an RTA furnace during heating (a) and cooling (b) along with a crack path indicated in white. Images courtesy of J. Garagorri CEIT Spain.

Figure 7.27 shows the FEM simulation of the stresses experienced by the wafer during a spike anneal along with the crack path that was observed in fig 7.28. During heating (fig. 7.27 a) the edge of the wafer experiences compressive stress both tangentially and radially. This has the effect of closing any cracks caused by near edge indents; however during a forced cooling (fig. 7.27 b) both the tangential and radial stresses are tensile at the edge while the centre is in compression. Thus any crack it a κ value greater than κ_c will open and propagate towards the centre of the wafer. After a certain distance, typically 2.5 – 3cm the crack will enter a region where the stress experienced are compressive in nature. At this point the radial stresses are still tensile so the crack direction will change so the crack will propagate

circumferentially back to the wafer edge [30]. This phenomenon has been observed experimentally and is shown in fig 7.28 below. This is an image of a 200mm wafer that fractured during an RTA cool down. The image is overlaid with colours showing the areas of tensile (Red) and compressive (Blue) stresses.

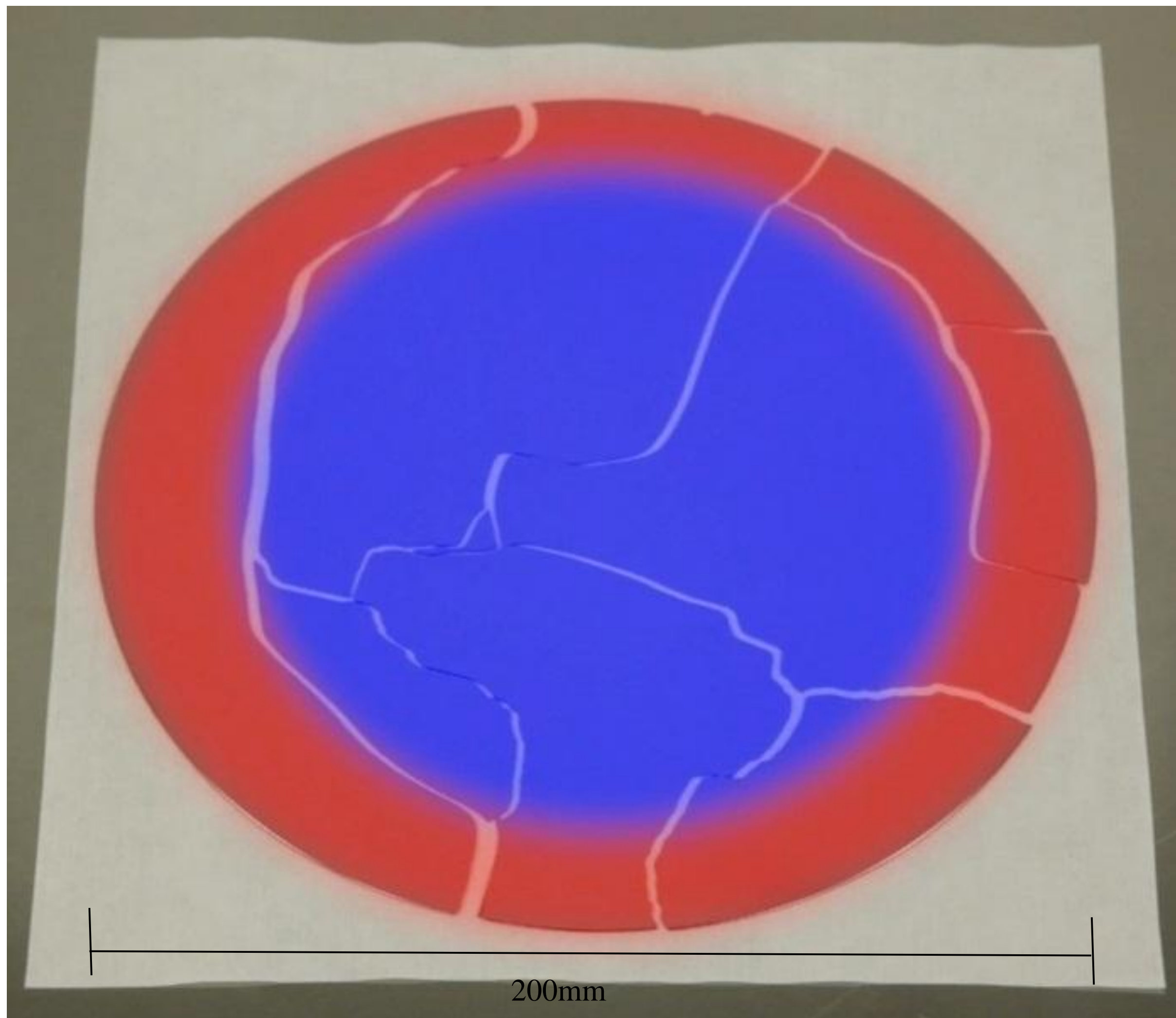

Figure 7.28: Image of broken wafer with the FEM stress results overlaid

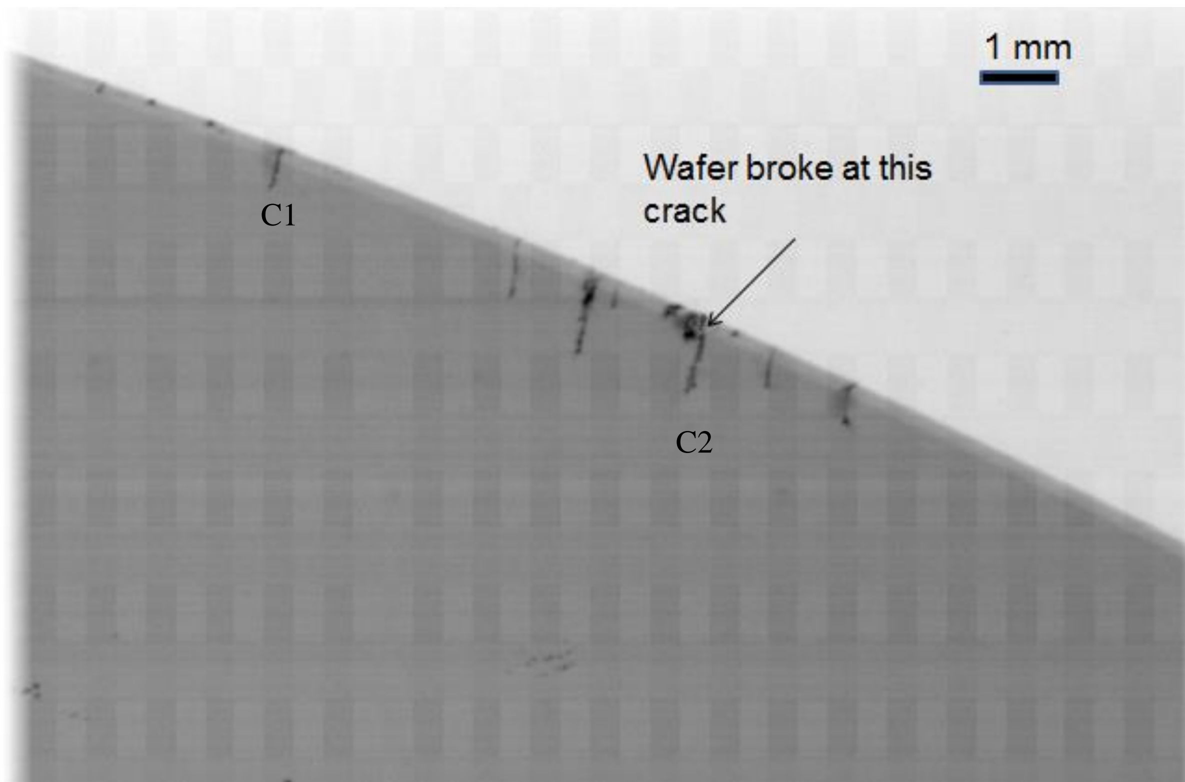

Figure 7.29: Bedescan™ XRDI image 115 reflection showing a series of cracks along the wafer edge. The wafer fractured along C2.

7.4 Summary

In has been shown that XRDI is a powerful tool for the non-destructive analysis of silicon. The reduction in the extent of the strain field due to RTA has been measured and shown that temperature gradients within RTA tools can and do lead to the movement of dislocation loops. It has also been shown that under the correct conditions the temperature gradients will allow for the movement of cracks within a wafer. A parameter κ_c was formulated that can be used to predict the likelihood of a crack propagating and causing a wafer to shatter.

7.4 References

[1] M. Cholewa and A. Rack, *ANKA Instrumentation Book* (ANKA Angstroemquelle Karlsruhe, Germany, 2007), 2009, p. 84.

[2] J. Wittge, *In Situ Investigation of Defects in Semiconductors* (Albert-Ludwigs-Universität Freiburg, Germany, 2012).

[3] T. Tuomi, J. Synchrotron Rad. **9**, 174 (2002).

[4] M. A. Hopcroft, W. D. Nix, and T. W. Kenny, J. Microelectromech. S. **19**, 229 (2010).

[5] E. Gorostegui-Colinas, *Modelling of Silicon Behaviour for Wafer Fracture Assessment during rapid Thermal Annealing* (Centro de Estudios e Investigaciones Tecnicas, Spain, 2012).

[6] A. Authier, *Dynamical Theory of X-Ray Diffraction* (Oxford University Press, Oxford, 2004), p. 674.

[7] V. Domnich and Y. Gogotsi, Rev. Adv. Mater. Sci. **3**, 1 (2002).

[8] P. Grau, D. Lorenz, and A. Zeckzer, Radiat. Eff. Defect S. **157**, 863 (2002).

[9] A. Kailer, K. G. Nickel, and Y. Gogotsi, J. Raman Spec. **30**, 939 (1999).

[10] J. Garagorri (private communication).

[11] M. J. Hill and D. J. Rowcliffe, J. Mater. Sci. **9**, 1569 (1974).

[12] B. Raghothamachar, G. Dhanaraj, J. Bai, and M. Dudley, Microsc. Res. Technique **69**, 343 (2006).

[13] J. Wittge, A. N. Danilewsky, D. Allen*, et al*, J. Appl. Cryst. **43**, 1036 (2010).

[14] J. Wittge, A. N. Danilewsky, D. Allen*, et al*, Powder Diffr. **25**, 99 (2010).

[15] D. Zeng, W. Jie, G. Zha, T. Wang, and G. Yang, J. Cryst. Growth **305**, 50 (2007).

[16] R. D. Doherty, D. A. Hughes, F. J. Humphreys, J. J. Jonas, D. J. Jensen, M. E. Kassner, W. E. King, T. R. McNelley, H. J. McQueen, and A. D. Rollett, Mat. Sci. Eng. A **238**, 219 (1997).

[17] A. N. Danilewsky, J. Wittge, A. Croell, D. Allen, P. J. McNally, P. Vagovic, T. dos Santos Rolo, Z. Li, T. Baumbach, and E. Gorostegui-Colinas, J. Cryst. Growth **318**, 1157 (2010).

[18] A. N. Danilewsky, J. Wittge, A. Hess*, et al*, Nuc. Instrum. Meth. Phys. Res. B **268**, 399 (2010).

[19] A. N. Danilewsky, J. Wittge, A. Hess, A. Cröll, A. Rack, D. Allen, P. J. McNally, T. dos Santos Rolo, P. Vagovič, and T. Baumbach, Phys. Stat. Sol. A **208**, 2499 (2011).

[20] F. Vallino, A. Jacques, and A. George, Phys. Stat. Sol. **222**, 51 (2000).

[21] B. K. Tanner, J. Wittge, D. Allen, M. C. Fossati, A. N. Danilewsky, P. J. McNally, J. Garagorri, M. R. Elizalde, and D. Jacques, J. Appl. Cryst. **44**, 489 (2011).

[22] D. K. Bowen, M. Wormington, and P. Feichtinger, J. Phys. D **36**, A17 (2003).

[23] P. Y. Chen, M. H. Tsai, W. K. Yeh, M. H. Jing, and Y. Chang, Jpn. J. Appl. Phys. **48**, 1 (2009).

[24] T. Y. Wang, J. Cryst. Growth **280**, 16 (2005).

[25] W. S. Yoo, T. Fukada, I. Yokoyama, K. Kang, and N. Takahashi, Jpn. J. Appl. Phys. **41**, 4442 (2002).

[26] B. K. Tanner, M. C. Fossati, J. Garagorri, M. R. Elizalde, D. Allen, P. J. McNally, D. Jacques, J. Wittge, and A. N. Danilewsky, *Prediction of the propagation probability of individual cracks in brittle single crystal materials*, 2012).

[27] A. A. Griffith, Phil. Trans. Roy. Soc. **221**, 163 (1921).

[28] D. K. Bowen and B. K. Tanner, *X-Ray Metrology in Semiconductor Manufacturing* (CRC Press, USA, 2006), p. 270.

[29] T. Cramer, A. Wanner, and P. Gumbsch, Phys. Rev. Lett. **85**, 788 (2000).

[30] B. K. Tanner, M. C. Fossati, J. Garagorri, M. R. Elizalde, D. Allen, P. J. McNally, D. Jacques, J. Wittge, and A. N. Danilewsky, Appl. Phys. Lett. **101**, 041903 (2012).

Chapter 8 Summary

This thesis presents work performed to examine the effects of induced defects into silicon by way of nano-indentation. The tools used were primarily micro-Raman Spectroscopy and White Beam Synchrotron X-Ray Topography (also known as X-Ray Diffraction Imaging). The intent of the project was to enable a breakthrough methodology for wafer inspection.

Chapter 1 provided an introduction to the thesis explaining the problem, that there existed, at the present time, no method to reliably predict if and when a wafer would break. It detailed the contribution to the project by Dublin City University and introduced the two tools that were used during the project.

Chapter 2 described the history and makeup of silicon crystal and derived the equations that would be used later in the thesis to correlate the Raman data to strain in silicon

Chapter3 and 4 described the tools used in detail and described the setups utilised to capture the data.

Chapter 5 described the development of 3D XRDI. While the concept of creating 3D images from topographs was not new the utilisation of medical tomographic algorithms along with the use of a public domain image processing tool were shown to be able to produce high quality images in relatively short periods of time. Initial reconstructions were obtained from 45 images that took 3hrs to capture, towards the end of the project this had expanded to reconstruction being obtained from >600 images within the same time period. The 3D images could then be examined from any angle and a process was developed where it became possible to step through a sample and observe the progression of the slip bands through the silicon. A K-Means clustering technique was also demonstrated where the extension of the strain fields could be examined and shown. It was also shown how these images could be transferred to physical models and for the first time a physical representation of the slip bands could be created.

Chapter 6 described the micro-Raman Spectroscopy results. It showed how μRS is used to gain quantative information about the strain fields within a silicon sample after nano-indentation. It showed how this technique can detect sub surface cracks which was confirmed by taking a TEM micrograph of the area under an indent. It showed the predicted presence of high pressure polymorphs of silicon resulting from the indentation process and the impact of thermal annealing upon these polymorphs. It showed how thermal annealing reduces the size of the strain field within the sample and allows for the recrystallization of the silicon.

Chapter 7 showed experimental setup and results from the XRDI experiments. It showed the reduction of the apparent strain field around indents after annealing and the growth of slip bands. It also showed how slip bands can originate from areas of the wafer that had no defined defects in particular from the wafer edge and the bevel edge. The chapter finished by showing the development of the Tanner criterion which related the crack length to the width of the XRDI image at the crack tip to derive a single parameter that could be used to determine the probability of wafer breakage.

Future Work

It has been shown that it is possible to predict the possibility of wafer breakage through the analysis of cracks present in the wafer. In order for this to be of use to the semiconductor industry at large, the analysis needs to be automated as part of either an *in situ* process monitoring tool or off line analysis tool. This will need to be coupled with image processing software with the correct analysis algorithms. This parameter, κ_c, has also only been applied to silicon in general and to industrial wafers in particular. There is a body of work leading on from this study that could be applied to thin silicon wafers, in particular the thinned wafers used with through silicon vias to see if the parameter still holds valid. It will also be important to look at different materials, e.g. GaAs to see if the parameter is still valid for these wafers.

With regard to 3D-XRDI work can be carried out to optimise the algorithms used. Currently the algorithms are very memory intensive and these can be optimised to reduce both memory load and processing time required to generate the images. Further work can also be carried out on real time 3D-XRDI imaging. This can be accomplished through the use of multiple slits where more than one ST topograph can be taken at a time or through the use of retilography. It may also be possible to use lower resolution camera within the beamline to speed up the process of image capture.

Publications

The results of much of this thesis can be found in the following publications:

D. Allen, J. Wittge, A. Zlotos, E. Gorostegui-Colinas, J. Garagorri, P. J. McNally, A. N. Danilewsky, and M. R. Elizalde, Nuc. Instrum. Meth. Phys. Res. B **268**, 383 (2010).

J. Stopford, D. Allen, O. Aldrien, M. Morshed, J. Wittge, A. N. Danilewsky, and P. J. McNally, Microelectron. Eng. **88**, 64 (2010).

A. N. Danilewsky, J. Wittge, A. Croell, D. Allen, P. J. McNally, P. Vagovic, T. dos Santos Rolo, Z. Li, T. Baumbach, and E. Gorostegui-Colinas, J. Cryst. Growth **318**, 1157 (2010).

A. N. Danilewsky, J. Wittge, A. Hess, A. Croll, D. Allen, P.J. McNally, P. Vagoic, Z. Li, T. Baumbach, E. Gorostegui-Colinas, M.R. Elizalde, Nuc. Instrum. Meth. Phys. Res. B 268, 399 (2010).

J. Wittge, A. N. Danilewsky, D. Allen,P.J. McNally, Z. Li, T. Baumbach, E. Gorostegui-Colinas, J. Garagorri, M.R. Elizalde, D. Jacques, M.C. Fossati, D.K. Bowen, B.K. Tanner, J. Appl. Cryst. **43**, 1036 (2010).

J. Garagorri, E. Gorostegui-Colinas, M. R. Elizalde, D. Allen, and P. J. McNally, An. Mec. Frac. **2**, 559 (2010).

J. Wittge, A. N. Danilewsky, D. Allen, P.J. McNally, Z. Li, T. Baumbach, E. Gorostegui-Colinas, J. Garagorri, M.R. Elizalde, D. Jacques, M.C. Fossati, D.K. Bowen, B.K. Tanner, *et al*, Powder Diffr. **25**, 99 (2010).

D. Allen, J. Wittge, J. Stopford, A. N. Danilewsky, and P. J. McNally, J. Appl. Cryst. **44**, 526 (2011).

T. Jauß, A. N. Danilewsky, J. Wittge, A. Cröll, J. Garagorri, M. R. Elizalde, D. Allen, and P. J. McNally, Cryst. Res. Tech. (2011).

A. N. Danilewsky, J. Wittge, A. Hess, A. Cröll, A. Rack, D. Allen, P. J. McNally, T. dos Santos Rolo, P. Vagovič, and T. Baumbach, Phys. Stat. Sol. A **208**, 2499 (2011).

B. K. Tanner, J. Wittge, D. Allen, M. C. Fossati, A. N. Danilewsky, P. J. McNally, J. Garagorri, M. R. Elizalde, and D. Jacques, J. Appl. Cryst. **44**, 489 (2011).

J. Stopford, A. Henry, D. Allen, N. Bennett, D. Manessis, L. Boettcher, J. Wittge, A. N. Danilewsky, and P. J. McNally, arXiv preprint arXiv:1204.1466 (2012).

B. K. Tanner, M. C. Fossati, J. Garagorri, M. R. Elizalde, D. Allen, P. J. McNally, D. Jacques, J. Wittge, and A. N. Danilewsky, *Prediction of the propagation probability of individual cracks in brittle single crystal materials*, 2012).

B. K. Tanner, M. C. Fossati, J. Garagorri, M. R. Elizalde, D. Allen, P. J. McNally, D. Jacques, J. Wittge, and A. N. Danilewsky, Appl. Phys. Lett. **101**, 041903 (2012).

A. N. Danilewsky, J. Wittge, K. Kiefl, D. Allen, P. J. McNally, J. Garagorri, M. R. Elizalde, T. Baumbach, and B. K. Tanner, J. Appl. Cryst. **46** (2013).

B. K. Tanner, J. Wittge, P. Vagovič, T. Baumbach, D. Allen, P. J. McNally, R. Bytheway, D. Jacques, M. C. Fossati, and D. K. Bowen, Powder Diffr. **28**, 1 (2013).

Appendix 1

Dynamical Theory

This is a brief overview of the dynamical theory of x-ray diffraction. It was not included within the main body of this thesis as it was not utilised in the analysis of the results.

In the dynamical theory the interaction between scattered or diffracted rays [1] and must be taken into account when dealing with diffraction from large crystals [2,3]. The main theories will be discussed here.

Darwin's Dynamical Theory

In Darwin's second paper of 1914 [4], he took into account the interaction between the lattice planes and the propagating waves. He concluded that, at each lattice plane the incident wave generates both a reflected and a transmitted wave, which, in turn generate more waves each time they cross a lattice plane, fig. 3.5 [5,6].

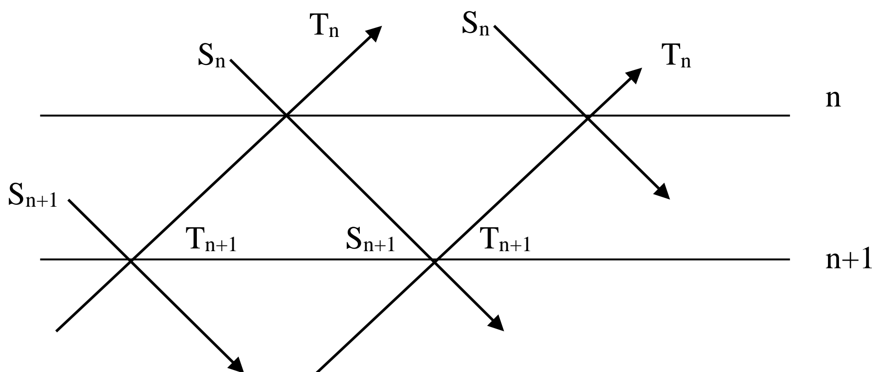

Figure 3.5: Representation of Darwin's Theory. S_n and T_n are the amplitudes of the incident and reflected waves

Darwin worked out the phases and amplitudes of the transmitted and reflected waves as a set of recurrent equations, and in so doing he found the coefficients of reflection and transmission on a single atomic plane and only in symmetric Bragg conditions [7]. If the nth

and (n+1)th planes are considered then let S_n and T_n be the amplitudes of the incident and reflected waves, Darwin showed that

$$S_n = jqT_n + (1 - jq_0)e^{(-j\phi)S_{n+1}} \quad (3.14)$$

and

$$T_{n+1}e^{j\phi} = (1 - jq_0)T_n - j\bar{q}e^{(-j\phi)S_{n+1}} \quad (3.15)$$

where

$$q = Nd_{hkl}R|F_{hkl}|/sin^2\theta_B \quad (3.16)$$

is the ratio of the reflected to the incident amplitude on an atomic plane,

$$\phi = 2\pi d_{hkl}sin\theta_B/\lambda \quad (3.17)$$

is the phase factor, R is the classical radius of the electron, d_{hkl} is the reflecting plane spacing, N the number of scattering units per unit volume, λ the wavelength, θ_B the Bragg angle and F_{hkl} the structure factor. $\bar{q}$ and q_0 are given by eqn. (3.13) with F_{hkl} replaced by $F_{\bar{h}\bar{k}\bar{l}}$ and F_{000} respectively. The imaginary terms are introduced by diffraction. Darwin also showed that in the symmetric Bragg case, total reflection occurs only over a small angular range, ~10 seconds of arc, and that the centre of the region is shifted slightly from the position as indicated by Bragg's law. This is due to the fact that λ must be replaced with λ_0/μ, where λ_0 is the X-ray wavelength in free space and μ is the linear absorption coefficient for X-rays in the body [1].

In 1914 and later in 1917 both Darwin [4,8] and Compton [9] produced an equation for the integrated intensity of reflection from a mosaic crystal. This equation is given as [10]:

$$\rho = \frac{N^2\lambda^3}{2\mu}|F|^2\left(\frac{e^2}{mc^2}\right)^2\frac{1+\cos^2 2\theta}{2\sin 2\theta} \quad (3.18)$$

This theory was later modified by Prins to include absorbing crystals in 1930 [11] when he produced a modified form of eqn. 3.15 to deal with perfect crystals

$$\rho = \frac{8}{3\pi} N\lambda^2 |F| \frac{e^2}{mc^2} \frac{1 + |\cos 2\theta|}{2 \sin 2\theta} \qquad (3.19)$$

and then again by Borie in 1966 and 1967 to take into account transmission geometry [12,13].

Extinction Theory

Darwin noticed, after experimenting with rock salt that the measured value of intensity differed significantly from that predicted from eqn. 3.15 [5,10] and showed that there were two distinct effects to be considered: primary and secondary extinction.

Primary extinction occurs when the angle of incidence has a value that falls within the range of total reflection. In this case the primary beam energy is wholly reflected into the reflected beam and the primary beam energy decreases rapidly in intensity as it passes through the crystal. This occurs due to the fact that there is a phase lag of $\pi/2$ at each reflection, so the twice reflected wave, which travels in the same direction as the primary is out of phase and so reduces the intensity of the primary, fig. 3.6 [10,14]; the effect is now known as the Borrmann-Campbell effect [15-18]. Darwin also noted that, due to primary extinction, the intensity calculations given in eqn. 3.15 and 3.16 need to be adjusted and a correction factor applied to obtain the true intensity. This factor is [5,6,10]:

$$\frac{\tanh pq}{pq} \qquad (3.20)$$

where *p* is the number of reflecting planes and *q* is amplitude reflected from a single plane of atoms.

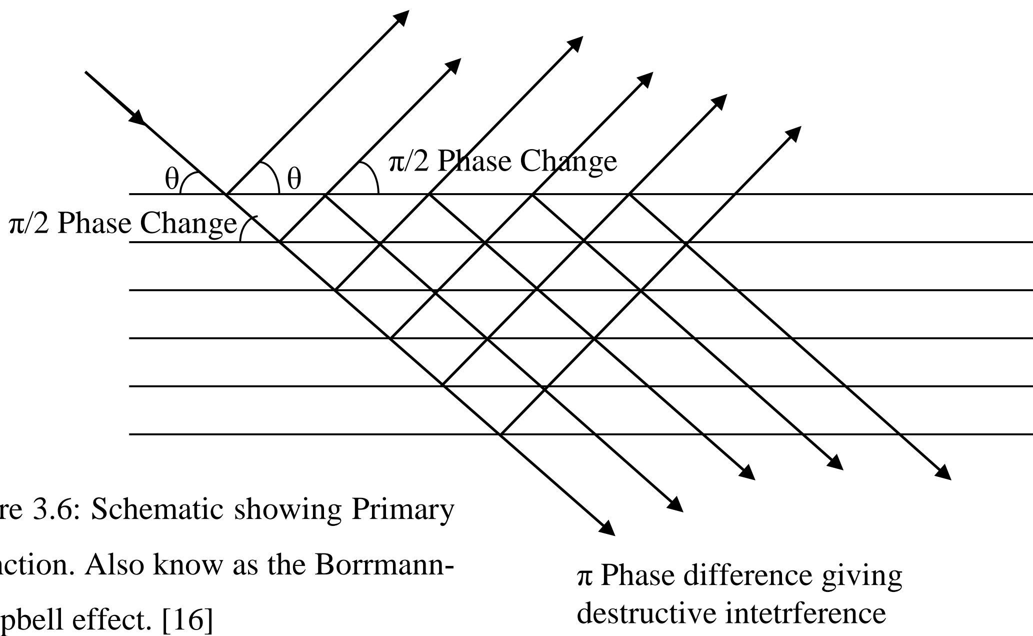

Figure 3.6: Schematic showing Primary extinction. Also know as the Borrmann-Campbell effect. [16]

Secondary extinction is used to describe the anomaly seen when the layers of crystal are thin enough that primary extinction can be neglected. When this happens, the reflection intensity observed from such a crystal is observed to be less than what should be expected from eqn. 3.15 [10,19] and is used to describe the process of extinction that occurs in imperfect crystals. An imperfect crystal is seen to be composed of independent layers which have their atomic planes parallel to each other, thus there is no regular phase relationship between the reflected rays and it is equivalent to an increase in the absorption coefficient of the crystal. The correction for this can be found by increasing the value of μ [5,6,10]. This theory was later improved by Hamilton [20] and then by Zachariasen [21,22] to give more realistic models [6].

<u>Ewald's Dynamical Theory</u>

In his dynamical theory, Ewald, working on a microscopic scale [23] introduced the notion of wavefields, i.e. the optical field that propagates through a crystal is a sum of plane waves whose wavevectors can be deduced by translations in reciprocal space:

$$\boldsymbol{E} = \sum_{m} \boldsymbol{E_m} e^{(-2\pi j \boldsymbol{K_m} \cdot \boldsymbol{r})} \qquad (3.21)$$

where $m = o,h,g...$, $\boldsymbol{h} = \boldsymbol{OH}$ and $\boldsymbol{g} = \boldsymbol{OG}$ are reciprocal lattice vectors as shown in fig.3.7. The wavefield is characterised by its tiepoint P so that $\boldsymbol{K_o} = \boldsymbol{OP}$, $\boldsymbol{K_h} = \boldsymbol{HP}$ and $\boldsymbol{K_g} = \boldsymbol{GP}$ [5],

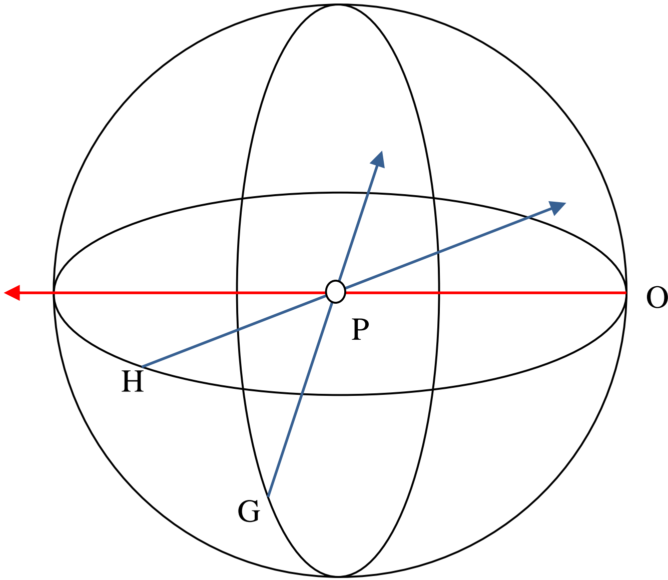

Figure 3.7. Ewald Sphere. O,H and G are the reciprocal lattice nodes, P is the tie point of the wavefield, $\boldsymbol{OP}$ is the incident wavevector and $\boldsymbol{HP}$ and $\boldsymbol{GP}$ are the reflected wavevectors.[23]

Ewald postulated that each lattice point of a crystal was occupied by a dipole that would be set into oscillation by the radiation field of an electromagnetic field passing through the crystal [10]. Each dipole would then radiate a spherical wave which propagates through the crystal and that the exciting wave is a superposition of the waves emitted by all the other dipoles, which has a propagation velocity given by [6]:

$$v = \frac{c}{n} \qquad (3.22)$$

where n is the refraction index.

von Laue's Dynamical Theory

Von Laue differed from Ewald in that he took a macroscopic picture of the dynamical theory [23]. Laue's assumption was to consider that the crystal is made up of a continuous

distribution of positive and negative charges [6] with positive charges concentrated at the atomic centres [10]. Laue assumed that charges were distributed in such a way that, in the absence of an external electromagnetic field, the charges would neutralise each other at every point. If an electromagnetic field is then applied to the crystal a relative displacement of the positive and negative charges is observed [10], though, as the relative mass of the proton to the electron is in the order of 1836 times greater, the interaction with the positive charges can be ignored for a first order approximation [5]. The magnetic interaction with the charged particles is similarly ignored as it is extremely weak [24]. Maxwell's equations locally relate $\boldsymbol{E}$, the electric field, $\boldsymbol{D}$, the electric displacement, $\boldsymbol{H}$, the magnetic field and $\boldsymbol{B}$, the magnetic induction by

$$\boldsymbol{D} = \varepsilon \boldsymbol{E} \qquad (3.23)$$

$$\boldsymbol{B} = \mu \boldsymbol{H} \qquad (3.24)$$

where ε and μ are the dielectric constant and the magnetic permeability respectively.

In the absence of local electric charges, and neglecting magnetic interaction, Maxwell's equations become [24]

$$\nabla \times \boldsymbol{E} = \frac{-\partial \boldsymbol{B}}{\partial t} \qquad (3.25)$$

$$\nabla \times \boldsymbol{H} = \frac{\partial \boldsymbol{D}}{\partial t} \qquad (3.26)$$

$$\nabla \cdot \boldsymbol{D} = 0 \qquad (3.27)$$

$$\nabla \cdot \boldsymbol{B} = 0 \qquad (3.28)$$

These equations can then be used to calculate the propagation of an electromagnetic wave through the crystal.

First the propagation through a vacuum is obtained by using the relationships

$$\nabla \times \boldsymbol{B} = \mu_0 \varepsilon_0 \frac{\partial \boldsymbol{E}}{\partial t} \qquad (3.29)$$

$$\mu_0 \varepsilon_0 = \frac{1}{c^2} \qquad (3.30)$$

$$\nabla \cdot \boldsymbol{E} = 0 \qquad (3.31)$$

Taking the *curl* of both sides of eqn. 3.25, and using the vector identity

$$\nabla \times (\nabla \times \boldsymbol{V}) = \nabla(\nabla \cdot \boldsymbol{V}) - \nabla^2 \mathbf{V} \qquad (3.32)$$

where $\boldsymbol{V}$ is any vector, it can be shown that

$$\nabla^2 \boldsymbol{E} = \frac{\partial}{\partial t}(\nabla \times \boldsymbol{B}) \qquad (3.33)$$

Substituting from eqn. 3.29, eqn. 3.33 can be rewritten as

$$\nabla^2 \mathbf{E} = \frac{\partial}{\partial \mathrm{t}}\left(\mu_0 \varepsilon_0 \frac{\partial \mathbf{E}}{\partial \mathrm{t}}\right) \qquad (3.34)$$

and rearranging gives

$$\nabla^2 \boldsymbol{E} = \epsilon_0 \mu_0 \frac{\partial^2 \boldsymbol{E}}{\partial t^2} = \frac{1}{c^2} \frac{\partial^2 \boldsymbol{E}}{\partial t^2} \qquad (3.35)$$

The simplest solution to eqn 3.34 is that of a plane wave given by [5,24--26]

$$\boldsymbol{E} = \boldsymbol{E_0} e^{j(\omega_0 t - 2\pi \boldsymbol{k} \cdot \boldsymbol{r})} \qquad (3.36)$$

One can rearrange eqn. 3.23 knowing that in a medium:

$$\varepsilon = \varepsilon_0 (1 + \chi) \qquad (3.37)$$

where χ is the electrical susceptibility. As χ is very much smaller than 1, it can be shown that

$$\boldsymbol{E} \approx \frac{\boldsymbol{D}}{\varepsilon_0}(1 - \chi) \qquad (3.38)$$

An equation for the propagation of an electromagnetic field in a crystalline medium can then be found

$$\nabla^2 \boldsymbol{D} + \frac{(1 + \chi)}{c^2} \frac{\partial^2 \boldsymbol{D}}{\partial t^2} = 0 \qquad (3.39)$$

[1] P. P. Ewald, *50 Years of X-ray Diffraction* (International Union of Crystallography - http://www.iucr.org/publ/50yearsofxraydiffraction, Scotland, 1960), p. 733.

[2] D. K. Bowen and B. K. Tanner, *High resolution X-ray Diffractometry and Topography* (Taylor & Francis, London, 1998), p. 252.

[3] B. W. Batterman and C. Henderson, Rev. Mod. Phys. **36**, 681 (1964).

[4] C. G. Darwin, Phil. Mag. **27**, 675 (1914).

[5] A. Authier, *Dynamical Theory of X-Ray Diffraction* (Oxford University Press, Oxford, 2004), p. 674.

[6] A. Authier and C. Malgrange, Acta Cryst. A **54**, 806 (1998).

[7] W. Yashiro and T. Takahashi, Acta Cryst. A **56**, 163 (2000).

[8] C. G. Darwin, Phil. Mag. **27**, 675 (1914).

[9] A. H. Compton, Phys. Rev. **9**, 29 (1917).

[10] R. W. James, *The Optical Principles of the Diffraction of X-rays*, edited by W. L. Bragg (Ox Bow Press, USA, 1948), p. 664.

[11] J. A. Prins, Z. Phys. **63**, 477 (1930).

[12] B. Borie, Acta Cryst. **21**, 470 (1966).

[13] B. Borie, Acta Cryst. **23**, 210 (1967).

[14] A. A. Balachin and C. R. Whitehouse, Phys. Educ. **9**, 53 (1974).

[15] G. Borrmann, Z. Phys. **42**, 157 (1941).

[16] G. Borrmann, Z. Phys. **127**, 297 (1950).

[17] H. N. Campbell, Acta Cryst. **4**, 180 (1951).

[18] I. A. Vartanyants and M. V. Kovalchuk, Rep. Prog. Phys. **64**, 1 (2001).

[19] M. Kuriyama and T. Miyakawa, Acta Cryst. A **26**, 667 (1970).

[20] W. C. Hamilton, Acta Cryst. **10**, 629 (1957).

[21] W. H. Zachariasen, Acta Cryst. A **24**, 421 (1968).

[22] W. H. Zachariasen, Acta Cryst. **23**, 558 (1967).

[23] H. Wagenfeld, Acta Cryst. A **24**, 170 (1968).

[24] A. Authier, S. Lagomarsino, and B. K. Tanner, *X-Ray and Neutron Dynamical Diffraction Theory and Applications* (Plenum Press, USA, 1996), 357, p. 419.

[25] D. Lowney, *Analysis of the Structural and Optoelectrical Properties of Semiconductor Materials and Devices using Photoacoustic Spectroscopy and Synchrotron X-ray Topography* (Dublin City University, Dublin, 2002).

[26] W. H. Zachariasen, *Theory of X-ray Diffraction in Crystals* (Dover Pheonix, USA, 2004), p. 255.

Appendix 2

List of 20mm x 20mm samples

	Location					Status												
	DCU	Freiburg	ANKA	CEIT	JV	Raman	SEM	BedeScan	ANKA				RTA	ANKA			Raman	Notes
Sample #									LAT	ST	BR	RC		LAT	ST	BR		
1			x			Done	Done	Done	Done	Done	Done	Done	Done	Done		Done	Done	Rocking Curves
2	x					Done	Done	Done	Done	Done	Done		Done	Done	Done	Done	Done	
7	x					Done	Done	Done	Done		Done	Done						LAT also done in DESY
9					x	Done	Done	Done	Done	Done	Done	Done	Done	Done	Done	Done	Done	Rocking curves
10	x					Done	Done	Done	Done	Done	Done		Done	Done	Done	Done	Done	
11		x				Done	Done		Done	Done	Done						Done	
12		x				Done	Done		Done		Done						Done	BR and LAT also done in DESY
Sidam_0_Ar1	x					Done	Done											
Sidam_0_Ar2	x					Done	TBD											
Sidam_0_Ar4	x																	Break Test @ 204.0781 N
Sidam_0_Ar5	x																	Break Test @ 176.1953 N
Sidam_0_Ar6	x																	Break Test @ 173.0239 N
Sidam_0_Ar7	x																	Break Test @ 25.7191 N
Sidam_0_Ar19	x																	Break Test @ 241.3487 N
Sidam_0_Br1	x																	
Sidam_0_Br2	x					Done	Done		Done		Done		Done	Done	Done	Done	In Progress	
Sidam_0_Br4	x					Done	Done		Done		Done		Done	Done	Done	Done		
Sidam_0_Br5	x					Done	Done		Done		Done		Done	Done	Done	Done	In Progress	
Sidam_0_Br6		x				Done	TBD		Done		Done							
Sidam_0_Br7		x				Done	TBD		Done				Done	Done	Done	Done	TBD	
Sidam_0_Br8		x				Done	TBD		Done				Done	Done	Done	Done	TBD	
Sidam_0_Br9		x				Done	Done		Done		Done							
Sidam_0_Br10		x				Done	Done		Done		Done							
Sidam_0_Br11		x				Done	TBD		Done		Done							
Sidam_0_Cr1		x				Done	TBD		Done		Done							
Sidam_0_Cr2	x					Done	TBD		Done		Done							
Sidam_0_Cr3		x				Done	TBD		Done		Done							
Sidam_0_Cr4		x				Done	TBD	TBD	Done	Done	Done		Done	Done	Done	Done		
Sidam_0_Cr7		x				Done	TBD		Done	Done	Done		Done	Done	Done	Done		
Sidam_0_Cr8		x				Done	TBD		Done	Done	Done		Done	Done	Done	Done		
Sidam_0_Cr9		x				Done	TBD		Done	Done	Done		Done	Done	Done	Done		
Sidam_0_Cr10	x					Done	TBD		Done	Done	Done							
Sidam_0_Cr13		x				Done	TBD		Done	TBD	TBD	TBD						
Sidam_0_Dr1			x			Done	TBD		Done	TBD	TBD	TBD					TBD	
Sidam_0_Dr2	x					Done	TBD		Done	TBD	TBD	TBD					TBD	
Sidam_0_Bl9		x				Done	TBD		Done		Done							
Sidam_0_Dl3	x					Done	TBD		Done	TBD	TBD							
Sidam_0_Dl4	x					In Progress	TBD		Done	TBD	TBD							
SiDam_0_Er5		x				In Progress	Done	TBD				TBD	Done	Done	Done	Done	TBD	
Sidam_0_Er6		x				In Progress	Done	TBD	Done	Done	Done	TBD						

LAT Large Area Topography
ST Section Topography
BR Back Reflection
RTA Rapid Thermal Anneal
RC Rocking Curve

Appendix 3

List of 200mm wafers

Wafer	Max. Load [N]	Indenter	Side	Rapid Thermal Annealing Mode (plateau annealing / spike annealing)	Bede	LA	Section
Sidam 01	0.2	B	front	Plateau Annealing[1] (1000°C)	x[8]	x	
Sidam 02	0.5	B	front	Plateau Annealing [1] (1000°C)	x[8]		
Sidam 04	10	V	front	Plateau Annealing [3] (850°C)	x	x	
Sidam 05	10	V	front	Plateau Annealing [1] (1000°C)	x	x	
Sidam 06	-	-	-	Plateau Annealing [3] (850°C)	x	x	
Sidam 07	-	-	-	Plateau Annealing [1] (1000°C)	x	x	
Sidam 08[5]	10	V	front		x[8]		
Sidam 09[7]	50-100-200	V	front		x[8]		
Sidam 10	50	V	front	Plateau Annealing[1] (1000°C)	x[8]	x[9]	x[9]
Sidam 11	50	V	front		x[8]	x[9]	x[9]
Sidam 27	0.2	B	front	Plateau Annealing [1] (1000°C)	x[8]	x	
Sidam 28	0.2	B	back	Plateau Annealing [1] (1000°C)	x	x	
Sidam 29	0.2	B	back	Plateau Annealing[4] (1091°C)	x[8]	x	
Sidam 30	0.2	B	back	Spike Annealing (941°C)	x	x	
Sidam 31	0.2	B	back	Plateau Annealing [1] (1000°C)	x[8]	x	
Sidam 32	0.2	B	back	Plateau Annealing[4] (1086°C)	x[8]		
Sidam 33[5]	0.2	B	front		x[8]		
Sidam 34	0.2	B	back		x[8]	x	
Sidam 35	0.2	B	front		x[8]		
Sidam 36	0.5	B	back	Plateau Annealing [1] (1000°C)	x	x	x
Sidam 37	0.62	B	front	Spike Annealing (1019°C)	x[8]		
Sidam 38	0.62	B	front	Plateau Annealing [2] (1000°C)	x[8]		
Sidam 39	0.62 Bevel	B	front	Plateau Annealing [2] (1000°C)	x[8]		
Sidam 40	0.62 Bevel	B	front	Spike Annealing	x[8]		
Sidam 41	0.5	V	front	Spike Annealing	x[8]		
Sidam 42	-	-	-		x[8]	x	
Sidam 43	1	V	front	Spike Annealing (1014°C)	x	x[9]	x
Sidam 44	2	V	front	Spike Annealing (996°C)	x	x	x
Sidam 45	3	V	front	Plateau Annealing [2] (1000°C)	x	x	x
Sidam 46	20	V	front	Plateau Annealing [2] (1000°C)	x[8]	x[9]	x[9]
Sidam 47	20	V	front	Spike Annealing (1008°C)	x[8]	x	x[9]
Sidam 48[6]	20	V	front	Plateau Annealing [2] (1000°C)	x[8]		
Sidam 50[6]	20	V	front		x[8]	x	x
Sidam 51	2	V	front	Spike Annealing (900°C)[11]	x[8]	x	
Sidam 52	2	V	front	Spike Annealing (925°C) [11]	x[8]	x	

Wafer	Max. Load [N]	Indenter	Side	Rapid Thermal Annealing Mode (plateau annealing / spike annealing)	Bede	LA	Section
Sidam 53	2	V	front	Spike Annealing (950°C) (11)	x(8)	x	
Sidam 54	2	V	front	Spike Annealing (975°C) (11)	x(8)	x	
Sidam 55	2	V	front	Spike Annealing (1000°C) (11)	x	x	
Sidam 56	2	V	front	Spike Annealing (1075°C) (11)	x	x	
Sidam 57	2	V	front	Spike Annealing (1050°C) (11)	x	x	
Sidam 58	2	V	front	Spike Annealing (1025°C) (11)	x	x	
Sidam 59	2	V	front	Spike Annealing (1100°C) (11)	x	x	
Sidam 62	-	-	-	-	x(8)		
Sidam 63	-	-	-	Spike Annealing (950°C)	x	x	
Sidam 64	-	-	-	Spike Annealing (1000°C)	x	x	
Sidam 65	-	-	-	Spike Annealing (1050°C)	x	x	
Sidam 76	-	-	-	Plateau Annealing (1000°C), Wafer rotated by 45° clockwise in the furnace to the normal alignment	x(10)		
Sidam 77	-	-	-	Plateau Annealing (1000°C), Wafer rotated by 45° anti-clockwise in the furnace to the normal alignment	x(10)		
300mm Wafer	Cracks	-	-	Several unknown steps in the same machine.	x	x	x

(1) Ramping at 100-150 °C/s and a 60 seconds plateau at 1000 °C

(2) Ramping using 100% power for the ramping and a 30 seconds plateau

(3) Ramping at 130-150 °C/s and a 60 seconds plateau at 850°C

(4) High Temperature treatment, heating up to ~1100°C in 15 seconds

(5) Broken during manipulation

(6) Broken during shipping

(7) Broken during adhesive removal at 150-175 °C/s due to heavy loads on indents

(8) Bede Scan of wafer without indentation and annealing.

(9) Measurement in process

(10) Bede Scan of wafer without indentation but annealing (transmission mode)

(11) Spike Annealing Study